WINTER IS COMING

THE GLOBAL COOLING AND THE NEXT LITTLE ICE AGE



FRANK DOSK

Winter Is Coming — The Global Cooling and the Next Little Ice Age

sciknow

Book version 569 — exported 2026-10-28 12:13 UTC

Contents

Contents **v**

1 Introduction: The Case for an Incoming Little Ice Age **1**
1.1 A climate that has always changed . . . 1
1.2 Why now — weakening cycles 24 and 25 . . . 4
1.3 Ocean modes turning cold — AMO and PDO . . . 7
1.4 Echoes of the pre-Maunder configuration . . . 9
1.5 Why this book, and how it argues . . . 12

2 History of Past Cold and Warm Periods **17**
2.1 Cosmogenic isotopes as a solar proxy . . . 17
2.2 Pre-Maunder grand minima . . . 19
2.3 The Maunder and Dalton Minima up close . . . 22
2.4 Grand maxima and societal abundance . . . 24
2.5 The long cycles — Hallstatt, Eddy, Bray . . . 27

3 Solar Science Foundations **33**
3.1 From Galileo to the photoheliograph . . . 33
3.2 Cycle metrics — Schwabe, Hale, butterfly . . . 38
3.3 Sunspot numbers and their recalibration . . . 41
3.4 The satellite-era TSI record . . . 43
3.5 F10.7 and the modern activity index . . . 47

4 The Grand Solar Cycles: Zharkova's Two-Wave Dynamo **49**
4.1 The solar background magnetic field . . . 49
4.2 PCA and the two-wave decomposition . . . 52
4.3 Isotope validation . . . 55
4.4 The 2020–2053 Modern Grand Solar Minimum prediction . . . 57
4.5 Flare physics — the same magnetic field . . . 61

5 The Sun's Inertial Motion **65**
5.1 How exoplanets reveal stellar wobble . . . 65
5.2 Solar inertial motion (SIM) . . . 68
5.3 The Jose cycle and longer beats . . . 71
5.4 Harmonic analysis — Yndestad and Abdussamatov . . . 75
5.5 How planetary forcing reaches Earth's climate . . . 77

6 The Cloud Hypothesis: Cosmic Rays and Climate **81**
6.1 How cosmic rays reach the lower atmosphere . . . 81
6.2 Forbush decreases — the natural experiment . . . 83
6.3 Chamber evidence — SKY and CLOUD . . . 86
6.4 Heliospheric modulation and global temperature . . . 89
6.5 Shaviv and the spiral-arm record . . . 90

7 The Underground Connection: Volcanism and the Sun **95**
7.1 When the Sun goes quiet, the Earth gets loud 95
7.2 The Maunder-era eruptions 100
7.3 Tambora and the Year Without a Summer 102
7.4 Hunga Tonga — the eruption that warmed the world 107
7.5 Mechanisms — why might the Sun affect the Earth's crust? 109
7.6 What if the next minimum brings the next big eruption? 111

8 There Is No Such Thing as Settled Science **117**
8.1 Warming happened — but who did it? 117
8.2 The natural CO_2 budget 119
8.3 The surface temperature record under a magnifying glass 123
8.4 TSI vs. CO_2 — the Connolly–Soon attribution 126
8.5 Natural cycles as confounders — Scafetta, AMO, PDO 129

9 What Can We Do? Preparation for the Next Minimum **133**
9.1 The historical baseline — what cold periods look like 133
9.2 Grid and energy resilience 135
9.3 Food security and agriculture 138
9.4 Water, sanitation, and the built environment 140
9.5 Household and regional preparedness 142
9.6 The precautionary closing argument 144

Bibliography **145**

Chapter 1

Introduction: The Case for an Incoming Little Ice Age

The climate is cooling, weakening solar cycles 24–25 echo the pre-Maunder pattern, and a public-facing precautionary case is overdue.

1.1 A climate that has always changed

Before asking where the climate is heading, it helps to know where it has been. Across the Holocene — the warm stretch since the last ice age, the whole span in which human civilisation happened — change is the normal condition, not the exception. [1] The Greenland Ice Sheet Project 2 (GISP2) offers a clear window into that past. This American deep-drilling campaign recovered a continuous ice core from the summit of the Greenland ice sheet. Its annual layers preserve a year-by-year archive of past climate. It took five years and over 3 km of drilling to reach bedrock in 1993. [1] Analysis of Dansgaard–Oeschger (D–O) events in the GISP2 ice core revealed a striking pattern. These were abrupt warmings of the last glacial period. Greenland temperatures leapt by roughly 8–16 °C within decades before gradually cooling again. The data showed a prominent frequency at 1470 years. Stefan Rahmstorf argued this periodicity had less than 1% probability of being due to chance. [1] The result was not so clear in similar ice cores. The European GRIP (Greenland Ice Core Project) was completed in 1992. GISP2 was considered to have better resolution. [1] The GISP2 record of ^{18} serves as a proxy for Greenland temperature. It has been placed on the new GICC05 timescale. [1] Dividing the 48–10 kyr BP period in boxes of approximately 1500 years helps display the periodicity of the D–O cycle. The abrupt start of the Holocene in the North Atlantic is considered the most recent D–O warming. [1] A new reconstruction of temperature variability in the extratropical Northern Hemisphere during the last two millennia shows a distinct Roman Warm Period c. AD 800–1300. This work utilized many palaeotemperature proxy records never previously included in any large-scale temperature reconstruction. [2]

This reconstruction demonstrates that decadal mean temperatures seem to have reached or exceeded the 1961–1990 mean temperature level during substantial parts of these earlier warm periods. [2] During the Medieval Climate Anomaly, spanning the 10th to 13th centuries CE, temperature and hydrological shifts were not uniform. [3] Peatland water-table reconstructions from the North Atlantic Region show that the onset of drier conditions varied temporally and spatially, with some sites recording contradictory hydrological conditions despite their proximity. [4] This high degree of spatial variability suggests that the Medieval Climate Anomaly was characterized by strong regional differences rather than uniform global warmth. Furthermore, global temperature composites indicate that peak Northern Hemisphere warmth during the Middle Ages was less than or at most comparable to the mid-20th-century warm period, as Medieval temperature peaks were not synchronous in all records. [5][6][4][1] The inherent ambiguities in defining this feature underscore the complexity of paleoclimate data. [1] Specifically, the Neoglacial cooling trend averaged approximately -0.2 °C per millennium, a rate that demonstrates the profound impact of even modest temperature changes on global systems. This gradual cooling, which culminated in the Little Ice Age, caused considerable glacier expansion and biome changes, such as the reduction of tropical forests and the expansion of tundra. [1] While short-term fluctuations of 0.4 °C can occur over just a few years, they are transient compared to these millennial-scale trends. [1] Understanding this deep historical context is crucial, as it challenges the assumption that recent warming is entirely anomalous. [1]

The usual story casts climate change as one crisis, without precedent, caused by industry alone. That story leaves out the long record behind it. The Earth's climate was never steady in the first place. [1] Freeman Dyson put it plainly: Change is part of the normal order of things. It was already happening before humans arrived. This intrinsic variability sets a baseline of natural fluctuation that predates our current era of concern. [1] Recognizing that Climate has always changed helps us see the whole picture. We move beyond a narrow focus on emissions. We consider the profound effect of natural cycles and events that shaped the planet's past. [1] This broader perspective is essential. It addresses unanswered questions in natural climate change. Those questions usually live in highly specialized scientific works. [1] The Intergovernmental Panel on Climate Change (IPCC) presents a specific view of the past 10000 years. Some researchers argue that this depiction of temperature history is selective and incorrect.

This contention arises from discrepancies between official records

and independent data analyses. [7][1] For instance, critiques suggest that the IPCC's temperature history is contradicted by the actual data record, pointing to figures that reveal a more nuanced picture than the "approved" storybook narrative implies. [7] The reliance on smoothed global proxy reconstructions, which depend heavily on researcher choices and limited low-precision proxies, introduces significant uncertainty. [1] Consequently, alternative reconstructions, such as those correcting for proxy re-dating and smoothing issues, present a different trajectory. This evidence supports the view that the standard IPCC depiction may be flawed, suggesting that our understanding of past climate stability requires revision. [8] While the Mauna Loa series is frequently cited as the gold standard for pristine measurements, significant disputes exist concerning the accuracy of broader atmospheric CO2 records and the true significance of human emissions over the past 150 years. Critics argue that the objections raised against ice-core data are mysteriously not applied to surface temperature measurements, creating an asymmetry in scientific scrutiny. [9][7][10][1]

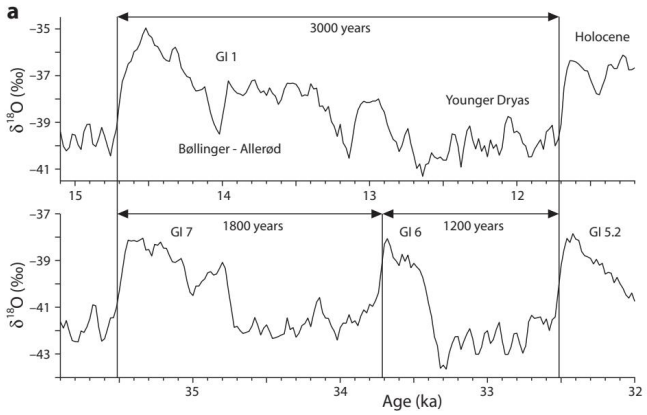


Figure 1.1: This figure displays two 60-year averaged GISP2 ^{18}O records, a proxy for Greenland temperature, on the GICC05 timescale, covering the periods 11.2–15.1 ka and 32–35.9 ka. The top panel shows the Holocene and the Bøllinger–Allerød (GI 1) events, while the bottom panel highlights the Younger Dryas (GI 6) and the preceding GI 7 event. Horizontal arrows indicate the common 3000-year periodicity between Dansgaard–Oeschger (D–O) events, along with instances of 1800-year and 1200-year spacing. The plots illustrate the characteristic sawtooth pattern of rapid warming phases followed by gradual cooling, with the ^{18}O values ranging from approximately -43‰ to -35‰. [1]

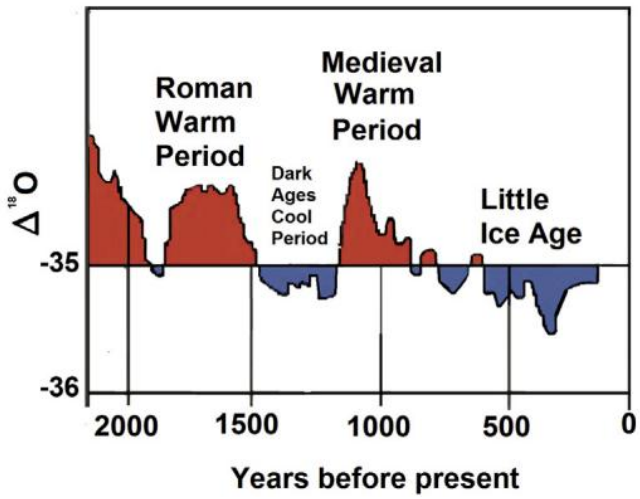


Figure 1.2: This figure displays the oxygen isotope (^{18}O) record from the GISP2 Greenland ice core, plotted as a time series spanning 2000 years before present. The data, derived from Grootes and Stuiver (1997), shows variations in ^{18}O values, with red regions indicating warmer periods and blue regions indicating cooler periods. The graph highlights major climatic intervals including the Roman Warm Period, Dark Ages Cool Period, Medieval Warm Period, and Little Ice Age, illustrating Holocene climate variability with millennial-scale resolution. [8]

1.2 Why now — weakening cycles 24 and 25

The Sun's magnetic activity waxes and wanes in a roughly 11-year rhythm known as the solar cycle, tracked most directly in the rise and fall of sunspot numbers; astronomers have numbered these cycles consecutively since 1755. Solar cycle 24 exhibited lower intensity than cycle 23, and forecasters across the solar-minimum literature projected that cycle 25 would be weaker still. This decline is not merely a fluctuation in sunspot counts but reflects a substantial weakening of the Sun's magnetic field, as evidenced by a 51% reduction in integrated solar magnetic energy density from cycle 23 to cycle 24. [11][12][13]

Magnetic disturbances travel through the solar wind at a rate called the Alfven speed. That speed fell below 57 km/s in cycle 24. This was a marked drop from the range seen in cycles 22 and 23. At the same time, the magnetosonic Mach number — the ratio of wind speed to magnetic sound speed — showed a higher lower bound for cycle 24. These shifts weakened the energy coupling parameter. The result was a 15%–38% decrease in the average strength of current systems. These currents flow in the high-latitude ionosphere, the low-latitude magnetosphere, and the equatorial ionosphere. [12] Consequently, high-latitude Joule heating — the warming of the upper atmosphere by electrical currents — dropped by about 30% during cycle 24. This pattern supports the prediction of a modern grand solar minimum. That quiet period is expected to span from 2020 to 2053. [14] As we move deeper into this predicted phase, the data suggests the Sun is entering a period of diminished output. This could have important implications for our Earth's atmosphere-ionosphere-magnetosphere system. [15]

The Sun's energy output is not static. It fluctuates with the solar cycle. Recent data reveals a troubling trend. [16] Total Solar

Irradiance — the measure of solar energy reaching Earth — has shown an increasing rate of decline from cycle 22 through cycle 24. This decline continues into cycle 25. The acceleration is stark. The average annual decrease rate in the 22nd cycle was approximately 0.007 Wm^2/yr. It rose to ˜0.02 Wm^2/yr in the 23rd cycle. [16][12] In the current cycle, this rate has jumped to almost 0.1 Wm^2/yr. This trajectory is consistent with a deepening solar dimming. [16] The 11-year component of TSI in the current cycle has decreased by almost 0.7 Wm^2 with respect to cycle 23. The average cyclical values were lower by ˜0.15 Wm^2 in the 23rd cycle than in the 22nd. [16] Furthermore, the TSI value at the minimum between cycles 23 and 24 was lower by ˜0.23 Wm^2 compared to the 22/23 minimum. This observed trend of increasing TSI decline suggests that the current solar behavior mirrors the analogous TSI decline of the Maunder Minimum period. This sets the stage for a new era of reduced solar heating. [16] This level was 0.32 $/^2$ lower than the minimum of the 21st cycle in October 1986. It was 0.25 $/^2$ lower than the 22nd cycle minimum in June 1996. [17] The value of TSI at the minimum between 23/24 cycles (1365.27 ś 0.02 ^{2}) was lower by ˜0.23 and ˜0.30 ^{2} than at the minima between 22/23 and 21/22 cycles, respectively. [16]

The TSI minimum between cycles 23 and 24 sat lower than the minima between cycles 21/22 and 22/23. This suggests the solar irradiance during that specific trough was anomalously low compared to recent historical precedents. [18][16][17][19][20] This decline matches analyses of the solar background magnetic field. Those maps, derived from WSO magnetic synoptic charts, indicated that cycle 25 would exhibit smaller activity compared to cycle 24. [11] Such findings align with the prediction of a modern grand solar minimum spanning 2020 to 2053. [14] Furthermore, predictions based on the Layman's Sunspot Count indicated that cycles 24 and 25 would remain below 50 SSN. This method uses SIDC values while ignoring specks rated lower than 23 pixels. It quantifies AMP events to provide a platform for future sunspot prediction out to 3000 AD. [21] The current AMP group, which began with solar cycle 20, failed to generate a full grand minimum. This failure stemmed from a weak AMP event. That weakness arose from the late timing of the Uranus/Neptune conjunction and a failed Wilson's Test. [21] The results indicate that a solar minimum is in progress during cycle 24. Cycle 24 is smaller than Cycle 23. In that projection, Cycle 25 is smaller than Cycle 24. [22] This pattern suggests continued weakness through cycle 27, around 2050. It is consistent with a Dalton-type solar minimum.

The Dalton Minimum serves as a useful benchmark. It suggests the current solar quietude matches that historical low. This similarity marks a clear break from the stronger cycles of the

mid-twentieth century. [22][23] Models had already flagged Cycle 24 as moderate or low. They pointed to a negative power anomaly. They also noted the negative phase of the 120-year solar magnetic pattern. These signals implied Cycle 25 could not be high. [23] We can check this energy balance directly. The Clouds and the Earth's Radiant Energy System, Energy Balanced And Filled data (CERES EBAF 2.8) offers a precise ledger. It reveals a small but negative trend in the net Top Of Atmosphere (TOA) energy imbalance over the past decade. This finding challenges earlier claims that external radiative forcing was unimportant during the climate hiatus. [24] The drop in net radiation tracks the falling Total Solar Irradiance (TSI). Incoming solar radiation has decreased as we approach the Centennial Gleissberg Cycle (CGC) minimum. Meanwhile, the Outgoing Longwave Radiation (OLR) has stayed largely flat. This stability reflects the lack of a global temperature trend during the hiatus. The Reflected Shortwave (RSW) radiation, determined by albedo, did not change significantly either. [24] Consequently, the Earth is projected to maintain a negative average annual energy balance. This deficit may last for 53 to 75 years. Such a prolonged state suggests a sustained cooling phase. It points away from a temporary fluctuation.

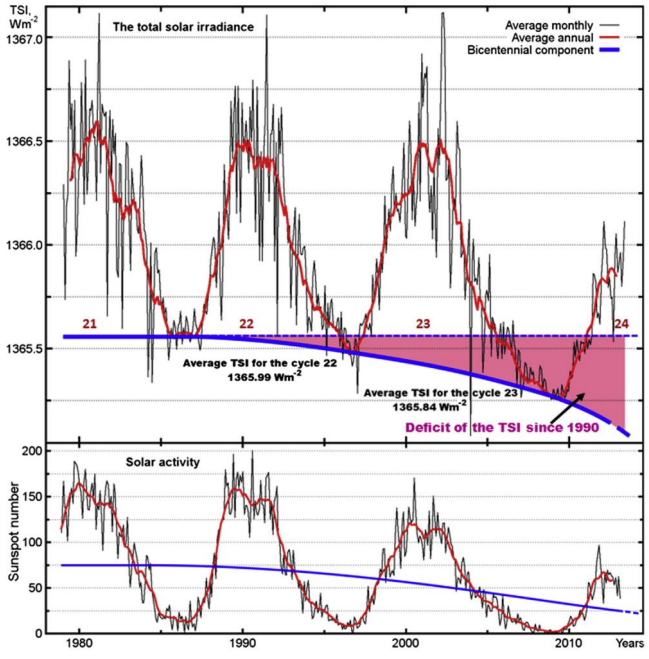


Figure 1.3: The figure displays two time series from 1978 to 2013: total solar irradiance (TSI) in W/m^2 (top panel) and sunspot number (bottom panel), both showing solar activity variations. The TSI data, derived from daily measurements, exhibit a clear 11-year cycle with a long-term decline, highlighted by a blue line representing the bicentennial component and a shaded region indicating the TSI deficit since 1990. The sunspot number, based on monthly data, follows a similar cyclical pattern, with the average annual values smoothed into a red line. The plot compares the average TSI for solar cycles 22 (1365.99 W/m^2) and 23 (1365.84 W/m^2), illustrating a slight decrease over time. [8]

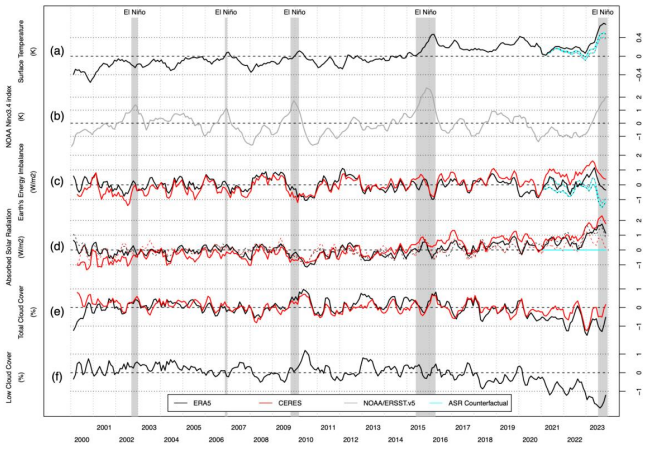


Figure 1.4: This figure displays six panels showing three-month running-mean anomalies of key climate variables from 2001 to 2023, relative to the 2001–2022 mean. Panels (a) through (f) plot surface temperature, Niño 3.4 index, Earth's top-of-atmosphere (TOA) energy imbalance, TOA net solar radiation, total cloud cover, and low-cloud cover, respectively. Red curves represent satellite observations from CERES, black curves show reanalysis data from ERA5, and cyan curves depict a counterfactual model assuming zero absorbed solar radiation (ASR) anomalies after December 2020. Gray shaded regions indicate El Niño events with anomalies exceeding +1 K. The data reveal strong interannual variability, particularly in surface temperature and the Niño 3.4 index, with notable correlations between cloud cover and TOA radiation anomalies, and a clear divergence between observed and counterfactual ASR trends post-2020. [25]

1.3 Ocean modes turning cold — AMO and PDO

Before asking where the climate is heading, it helps to look at the engines driving it. The Atlantic and Pacific basins have shifted recently, moving away from the warm phases that dominated the late twentieth century. [8] This suggests a departure from recent norms. Simulations using the MPI-ESM-P Earth system model show that this system can undergo abrupt, self-sustaining shifts. These shifts can lock the region into prolonged cold states. An ensemble of millennium-long simulations reveals the mechanism. An abrupt weakening of the subpolar gyre — the counterclockwise loop of cold surface currents circulating the North Atlantic south of Greenland and Iceland — can trigger multicentennial cold climate regimes. These regimes resemble the Little Ice Age. The mechanism does not rely on a permanent collapse of the broader overturning circulation. Instead, it relies on localized feedbacks involving sea ice and freshwater export. [26][27] This weakening was driven by anomalous freshening in the upper Labrador Sea. Cold conditions in the Nordic Seas also played a role. These conditions enhanced sea ice growth and export through the Denmark Strait. [26] The resulting reduction in poleward heat transport cooled the Nordic Seas further. This created a positive feedback loop that

stabilized the weaker gyre regime. [26] The simulated post-shift climate featured expanded sea ice. It also showed reduced subpolar meridional heat transport. Persistent blocking-like sea level pressure anomalies appeared. These conditions broadly agree in magnitude and duration with paleoclimate reconstructions of the Little Ice Age.

While the timing of the simulated shift around 1600 CE differs from reconstructed anomalies in the thirteenth and fourteenth centuries, this discrepancy is attributed to the dominance of internal climate variability rather than a failure of the mechanism. [26] Simulations from the MPI-ESM-P model, specifically the Past1000-R3 ensemble, provide a mechanistic understanding of how such cold regimes stabilize. In this simulation, an abrupt weakening of the subpolar gyre around 1600 separates two stationary regimes, with the post-shift cold regime persisting for at least 250 years. [26] First, reduced poleward heat transport cools the Nordic Seas, which enhances sea ice growth and export through the Denmark Strait, further freshening the Labrador Sea. [26] Second, reduced salt transport sustains this upper-ocean freshening. [26] These feedbacks demonstrate that the post-shift cold regime is stabilized by interactions between freshened upper Labrador Sea waters and expanded sea ice. Although the Atlantic Meridional Overturning Circulation (AMOC) does not exhibit a long-lasting shift, it temporarily weakens during the transition, contributing to the broader cooling signal. [27] In one specific millennium-long simulation (Past1000-R3), the SPG weakened by 0.72 Sv over two decades around 1600, separating two stationary regimes with the post-shift state persisting for at least 250 years. [26] Two positive feedbacks stabilized this weaker regime: reduced poleward heat transport cooled the Nordic Seas, enhancing sea ice growth and export through the Denmark Strait, which further freshened the Labrador Sea; simultaneously, reduced salt transport sustained upper-ocean freshening. [26]

The Atlantic Meridional Overturning Circulation — the great vertical conveyor of heat and salt in the Atlantic — does not break. It weakens only briefly, during the transition itself. The simulations establish that these abrupt shifts in the subpolar gyre are not associated with persistent changes in the strength of that overturning circulation. [28][26] The climate that follows the shift looks very different. Sea ice expands. The transport of heat toward the pole drops. High-pressure systems block the weather, lingering for decades. These features agree broadly in magnitude and duration with paleoclimate reconstructions of the Little Ice Age. [28][26] Historical analogs provide a stark warning about the potential magnitude of such shifts. [1] The model shows how the cascade begins. Freshwater exports from the Arctic freshen

the upper Labrador Sea. This rapid weakening of the subpolar gyre triggers a chain reaction. It alters oceanic and atmospheric circulation. It changes sea ice extent. It reshapes upper-ocean salinity. [26] The timing discrepancies are not a flaw in the model. They reflect the chaotic nature of internal climate variability. [26] Preconditioning by that internal variability explains why the simulated shifts do not line up perfectly with the reconstructed onset of the Little Ice Age. This finding is pivotal. It demonstrates that the ocean can spontaneously enter a cold state. It does so due to its own internal dynamics. It does not require a persistent external forcing, like a grand solar minimum. [26] The ocean is not just a passive recipient of solar energy. It is an active participant in the climate system. It stores and releases heat in ways that can override short-term atmospheric trends. [29]

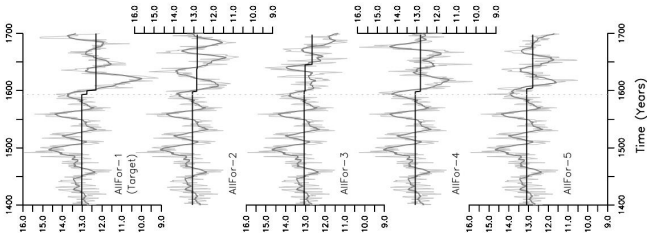


Figure 1.5: The figure displays time series of the Subpolar Gyre (SPG) strength in Sverdrups (Sv) for five sensitivity experiments (AllFor-1 to AllFor-5), with thin lines representing annual averages and solid lines showing 11-year running means. Each panel illustrates the SPG strength over time, with vertical dotted lines marking the start of each integration and horizontal dashed lines indicating discrete reference levels. The data reveal interannual variability and long-term trends in SPG strength across the experiments, with notable shifts in mean strength and variability between runs. [27]

1.4 Echoes of the pre-Maunder configuration

To gauge where the Sun is heading, we first need a baseline from the past. The Maunder Minimum, spanning 1645 to 1715, serves as our best historical analogue for today's solar behavior. [30] During those decades, the Sun grew remarkably quiet. Observers recorded very few sunspots, and the total solar irradiance — the total energy output reaching Earth — dropped measurably. [31][32][33][34][35][36] This quietude was not just visual. Isotopic records from that era show a distinct maximum, a chemical signature preserved in ice and tree rings. That spike indicates the Sun's magnetic field had weakened so much that it could no longer deflect cosmic rays effectively. [37] The Maunder Minimum proves the Sun can enter extended periods of low activity. Such shifts carry significant consequences for global climate, reminding us that solar variability is a real driver of earthly change. [38]

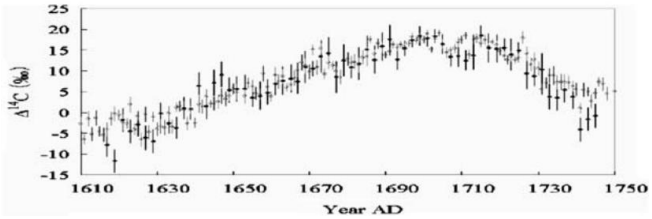


Figure 1.6: The image displays a time series plot of radiocarbon (^{14}C) concentration anomalies (^{14}C, in ‰) from 1610 to 1750 AD, showing a distinct peak around 1650 AD followed by a decline. This data illustrates the enhancement of ^{14}C during the Maunder Minimum, a period of low solar activity, as a consequence of increased cosmic ray flux (CRF), with the data sourced from Miyahara et al.. [47]

The Maunder Minimum — that quiet stretch from 1645 to 1715 — offers a vital baseline for understanding the climate effects of prolonged solar hibernation. [38] Temperatures plummeted across the continent. The growing season shrank by more than a month. This was not a statistical blip. It was a tangible crisis that reshaped daily life and agricultural viability. [39] In the Paris region, the average monthly temperature fell below freezing eight times between 1691 and 1697. That pattern has never repeated. Further north, in Finland, long winters and early night frosts destroyed the harvest in both 1695 and 1696. The result was a demographic catastrophe, with population losses in some areas exceeding 40 per cent. [39] The natural archive on climate indicates that average temperatures in 1687–1700 were 1.5°C lower than in the preceding decade. Climatologists christen this period the climax of the Little Ice Age. [39] These oscillations seem small, but their impacts were outsized. Each change of 0.1°C in global temperature advances or retards the ripening of crops by one day. The cooling of the 1690s delayed harvests by an average of two weeks in temperate zones. [39]

The Thames River and Dutch canals froze solid, a tangible demonstration of how solar quiescence reshapes regional hydrology. [8] The winter of 1657–58 stands out as a landmark event in the northern hemisphere. The canal between Haarlem and Leiden stayed frozen for two months. The Baltic Sea froze so hard that the Swedish army marched over the ice to launch a surprise attack on Copenhagen. [39] John Evelyn judged that he and his compatriots had just lived through 'the severest winter that man alive had known in England.' He noted that even crow's feet froze to their prey. [39] Later, during the Great Frost of 1683–84, the River Thames was completely frozen for two months. Ice reached 11 inches thick at London. [40] Solid ice extended for miles off the coasts of the southern North Sea. It may have prevented the use of many harbors and caused severe problems for shipping. [40]

The cold did not just freeze rivers; it starved people. Harvest

failures during the Maunder Minimum triggered mass famines across Europe. [41][42][39] The temperature dropped by 1 C to 2 C worldwide. This cooling came from weak solar activity in the early and mid-seventeenth century, combined with major volcanic eruptions. [41][42][39] A single degree centigrade may seem small, but it seriously shortens growing seasons. Crop yields fell catastrophically across the world. [39] In seventeenth-century Europe, a 30 percent drop in grain harvest often doubled the price of bread. A 50 percent drop quintupled it. [42] The most densely populated areas of the early modern world relied on a single crop. Wheat or rye sustained Europe. Rice fed Asia. Maize supported the Americas. [42]

These staple crops made up as much as 75 percent of the diet. That dependence turned climate shifts into starvation. [39] The food crises of the seventeenth century, and the deep crisis of the 1690s, have been connected to the Maunder Minimum. [43] This was a period of low solar activity between 1645 and 1715. Low solar output likely contributed to the long-term cooling. But the sudden summer drops look different. The sharp temperature falls and crop failures across northern Eurasia resemble the signature of volcanic eruptions more than the signal of solar activity. The case of Southern Ostrobothnia shows the reach of this forcing. It fundamentally challenged human lives more than ten thousand kilometres away from the physical source of the eruption. [41]

The late seventeenth century serves as a critical baseline analogue for understanding current solar behavior, particularly the period known as the Maunder Minimum (approximately 1645-1715). [38] Such dramatic reductions, extending beyond a single eleven-year cycle, are classified as grand solar minima. [44] During these periods, the Sun exhibits specific physical traits that distinguish it from active phases. [45]

The historical record provides a critical baseline for understanding the potential climatic consequences of prolonged solar quiescence, particularly when examining the Maunder Minimum period that spanned approximately 1645 to 1715. [38] This era is widely regarded as the most prominent recent instance of reduced solar activity, characterized by a distinct lack of visible sunspots as documented by Eddy 1976, alongside increased concentrations of cosmogenic isotopes such as carbon-14 and beryllium-10 that indicate a more quiescent heliospheric magnetic field. [46] Paleoclimate reconstructions, including tree-ring data from northern North America analyzed by Jacoby and D'Arrigo 1989, reflect the general coldness associated with the Little Ice Age during this seventeenth-century window, suggesting that global or Northern Hemisphere temperatures were approximately 0.5 degrees Celsius colder than today, with extratropical regions experiencing cooling

closer to 1 degree Celsius. [46] Even the multiproxy reconstructions of Mann et al. 1999 and Mann et al. 2003, which suggest the hemispheric-average cooling was only a few tenths of a degree, register a discernible cold anomaly during this window.

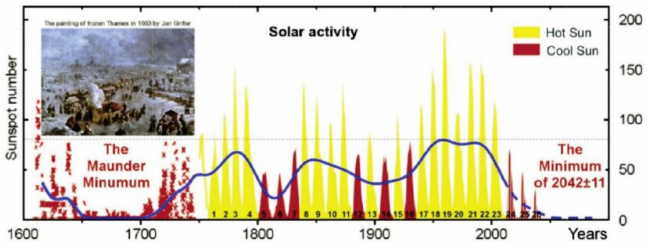


Figure 1.7: The figure displays a time series of solar activity from 1600 to 2020, showing sunspot number (left y-axis) and a proxy for total solar irradiance (TSI) as a blue line, with yellow bars indicating periods of high solar activity ("Hot Sun") and red bars indicating low activity ("Cool Sun"). The graph highlights historical solar minima, including the Maunder Minimum (1645–1715) and the predicted minimum around 2042ś11, with a dashed line forecasting future solar activity trends. A small inset image depicts the frozen Thames in 1603, illustrating the cold climate conditions associated with the Maunder Minimum. [48]

1.5 Why this book, and how it argues

This book lays out the evidence and the argument for this approach, challenging the current narrative of anthropogenic global warming. [49]

The book asserts that IPCC temperature and CO2 records are selective, inaccurate, or based on discarded data. This critique establishes that the Intergovernmental Panel on Climate Change's depiction of the temperature history over the past 10,000 years is selective and plain wrong, contradicting the actual data record. [7] Furthermore, serious questions regarding the accuracy of the IPCC's claimed record of atmospheric CO2 over the past 150 years demonstrate that many measurements have been discarded because they do not agree with the approved story. Additionally, the study identifies significant errors in the IPCC reports, showing that the 39 computer models used by the panel fail validation against measured surface temperature changes. [48]

The author argues that the Sun is entering a hibernation — a prolonged cold spell — and that this solar variability drives our current climate. This drop in energy output marks the end of warming. It signals the start of a new, potentially dangerous cold climate. [49] The evidence suggests this shift is coming. The most likely outcome involves widespread global loss of life. Social, economic, and political disruption would follow. [49] We must

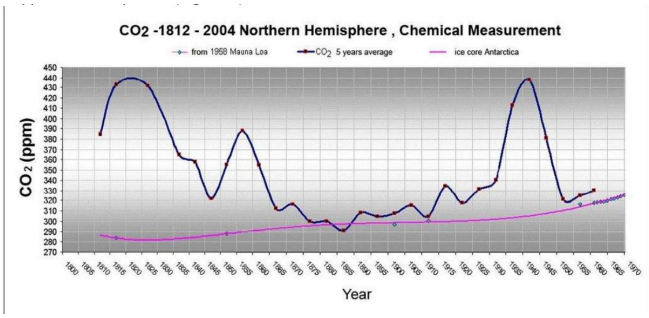


Figure 1.8: This line graph displays atmospheric CO_2 concentrations (ppm) in the Northern Hemisphere from 1812 to 2004, based on chemical measurements. It compares three datasets: CO_2 values from Mauna Loa (1958–2004), a 5-year average of CO_2 measurements, and ice core data from Antarctica. The graph shows significant year-to-year variability in the chemical measurements, with peaks around 1815 and 1940, while the ice core data exhibit a gradual, long-term increase. [7]

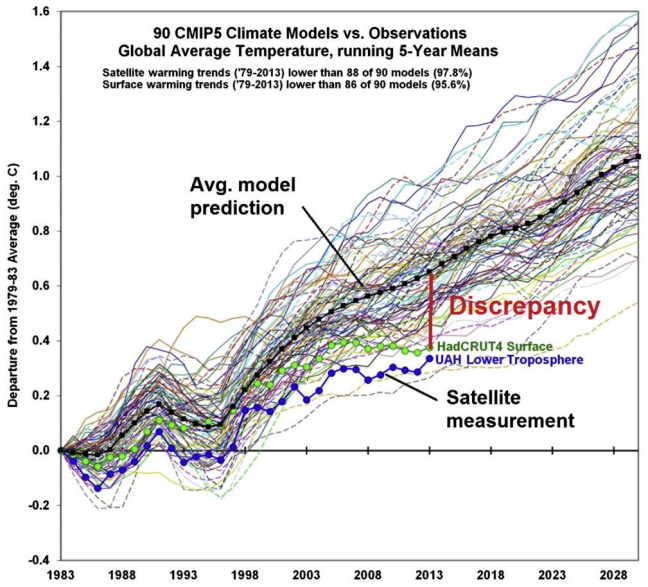


Figure 1.9: This line graph compares 90 CMIP5 climate model predictions against satellite and surface temperature observations from 1979 to 2013, plotting the departure from the 1979–83 average in degrees Celsius. The graph shows numerous model projections (colored lines) and an average model prediction (black line) that generally trend above the observed data from HadCRUT4 surface measurements (green dots) and UAH lower troposphere satellite measurements (blue dots), with a highlighted discrepancy indicating that most models overestimate warming trends. [8]



Figure 1.10: This line graph compares observed global mean temperature change (1990–2016) from RSS+UAHv6 satellite data against IPCC FAR projections, showing a 0.42°C over-prediction (1.60°C/century) relative to the observed trend of +0.31°C/century ($r^2 = 0.195$). The observed data (black line) fluctuates around the projected trend (red line), with the projected warming (0.73°C/-century) falling outside the observed range, indicating a significant divergence between historical observations and the IPCC FAR projection. [8]

understand this change to prepare for the inevitable cold and difficult years ahead. [49] Adaptation means practical adjustments. We would change our clothing and transportation. We would redesign homes and businesses. We would also learn more about cold-weather health hazards. [52] Little Ice Age conditions could strangle food production. Famines might result. The plan therefore emphasizes techniques for long-term food storage. [53]

Massive ice storms and blizzards can knock out the power grid. Modern electric heating systems then stop working. The strategy highlights the critical need for backup heat sources that do not rely on electricity. [49] This failure of infrastructure forces a harder truth. Individuals and communities must prepare for a scenario where they cannot rely on external aid. That aid might come from their own national governments or from foreign powers. The text demonstrates this necessity clearly. [49] The book's mission, therefore, is to alert readers to this reality before it becomes an immediate crisis. [49] Staying silent about these discoveries would be a disservice to the public. The narrative emphasizes this point strongly. The cooling trend could trigger a "long depression" or severe economic recession. [49] Thus, the text proves that a shift toward self-reliance is not just advisable but essential for navigating the upcoming decades.

The chapters that follow build the case in sequence. Chapter 2 traces the rhythm of past cold and warm periods, showing that abrupt climate swings are the historical norm rather than the exception. Chapter 3 lays out the tools of solar science — how sunspots are counted and the Sun's output is measured. Chapter 4 turns to Zharkova's two-wave dynamo and its forecast of a grand minimum. Chapter 5 follows the Sun's own motion about the solar system's centre of mass, the planetary clock behind those cycles. Chapter 6 examines the cloud hypothesis — how cosmic rays, modulated by solar activity, may seed the clouds that cool the Earth. Chapter 7 explores the underground connection between a quiet Sun and a restless crust. Chapter 8 confronts the attribution question head-on, weighing the Sun against carbon dioxide. And Chapter 9 asks what a prudent society should do now to prepare for a colder few decades.

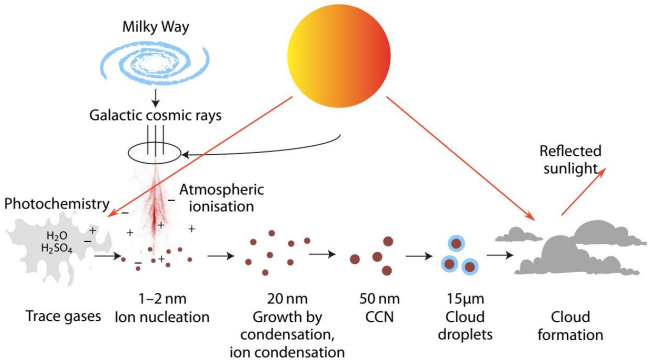


Figure 1.11: The diagram illustrates a proposed physical mechanism linking solar activity to climate change through cosmic ray modulation of cloud formation. It shows galactic cosmic rays, influenced by the Milky Way's magnetic field and solar activity, entering the atmosphere and causing ionization. This ionization initiates a chain of processes: photochemistry of trace gases like H_2O and H_2SO_4 leads to ion nucleation (1–2 nm), followed by growth via condensation and ion condensation to form 20 nm and 50 nm cluster condensation nuclei (CCN). These CCN grow into 15 m cloud droplets, ultimately leading to cloud formation that reflects sunlight, thereby affecting Earth's albedo and climate. [55]

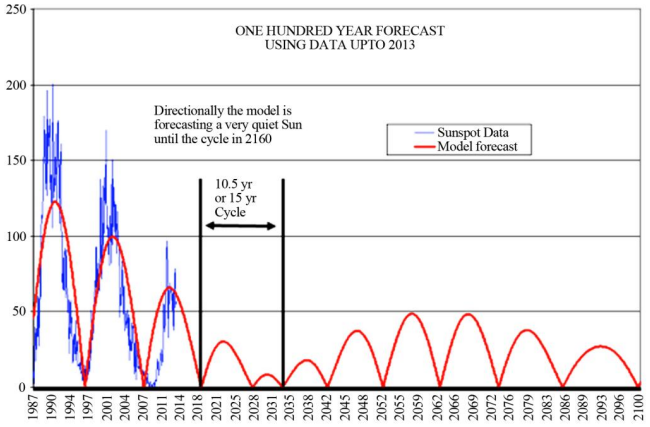


Figure 1.12: The figure displays a time-series plot comparing monthly sunspot numbers from 1987 to 2013 (blue line) against a model forecast of the absolute value of solar activity (red line) extending to 2100. The x-axis spans years from 1987 to 2100, with the y-axis representing sunspot numbers up to 250. The model forecast, derived using data up to 2013, predicts a prolonged period of low solar activity, indicating a very quiet Sun until a cycle in 2160, with a cycle duration of 10.5, 15, or 15 years. [54]

Chapter 2

History of Past Cold and Warm Periods

Reconstructed solar activity shows ˜5 deep minima and ˜4 sustained maxima since antiquity, each tracking documented climate and societal impact.

2.1 Cosmogenic isotopes as a solar proxy

We cannot watch the Sun directly for most of history. To fill that gap, scientists use cosmogenic isotopes — atoms created when cosmic rays hit the atmosphere — as natural archives of cosmic-ray flux. [44] Beryllium-10 (^{10}Be) is one such proxy. Researchers measure its concentrations in Greenland ice cores, such as the Dye-3 core. These cores hold a continuous record of atmospheric deposition. That archive allows us to trace variations in solar modulation over millennia. [56][57][58][59][60][61] The precision of these records is crucial. It helps us understand the long-term behavior of the Sun and its impact on Earth's climate system. [62]

The solar wind carries a magnetic field that pushes galactic cosmic rays away from Earth. This shielding varies with solar activity. When the Sun is active, the shield is strong. Fewer cosmic-ray protons reach the atmosphere. Consequently, less beryllium-10 (^{10}Be) is produced. The isotope thus records the strength of that magnetic shield. [59] We can test this link against direct measurements. Neutron monitors count cosmic rays as they arrive at the surface. Ice from Law Dome in East Antarctica preserves the same signal in frozen layers. The two datasets track each other closely. The correlation between ^{10}Be concentrations and the monitor data is $= 0.64$. [63] This sensitivity proves useful when visual counting fails. During the Maunder Minimum, sunspots all but vanished. Counting them yields almost no information about solar strength. The Greenland Ice Core Project data tells a different story. The ^{10}Be time series can still distinguish a deep solar minimum from a shallow one. It does so even when sunspot numbers drop to near zero. This capability confirms that ^{10}Be records the open solar magnetic field continuously. It avoids the

threshold effects that obscure sunspot observations during grand minima. [59] The isotope record therefore registers solar variability on centennial timescales. It offers a critical tool for studying long-term solar-climate interactions. These interactions extend far beyond the limited span of direct sunspot observations.

Ice-core archives from Antarctica and Greenland preserve beryllium-10 (^{10}Be), a cosmogenic isotope whose atmospheric production is modulated by solar activity. [34] These temperature anomalies, derived from various paleoclimate records, show a remarkable correlation with cosmic-ray variations inferred from isotopic data. [64] The resulting ^{14}C production rate (p ^{14}C) reflects the flux of incoming cosmic ray particles, which are modulated by the solar magnetic field. [65] This inverse relationship establishes ^{14}C production rates as a robust indicator of solar variability. [66] For instance, the maximum ^{14}C production rate in the last millennium occurred between AD 1645 and 1715, coinciding with the Maunder Minimum when sunspots were almost lacking. [33] In contrast, ^{14}C concentration in tree rings can be influenced by changes in the global carbon cycle, complicating the isolation of solar signals. The first principal component explains 69% of the total variance, implying that ^{14}C production changes throughout the Holocene are very similar to the ^{10}Be changes found in polar ice cores from two different hemispheres. [56] Simulations starting at 500 BC using ^{10}Be-derived production from Antarctic ice show a good match with IntCal04 atmospheric ^{14}C variations in both amplitude and phase, with correlation coefficients (^{2}) close to 0.9. [67] Consequently, long-term reconstructions rely on proxy evidence from natural archives, specifically cosmogenic isotope concentrations preserved in dendrochronologically dated tree rings and ice cores.

Carbon-14 (^{14}C) offers a distinct window into the past. We extract this isotope from ancient tree rings, creating a reliable archive of solar activity. This record spans years, centuries, and even millennia. It shows that radiocarbon production in the atmosphere, and subsequently in wood, stems from cosmic rays. That cosmic ray flux has varied significantly over time. It moves in inverse relationship with solar activity. [68][69][70][71] The longest and most precise annual ^{14}C dataset comes from Brehm et al. They used 13 oak timbers from buildings in the UK and Switzerland. These samples cover the period 969–1933 CE. The data demonstrates the persistence of the 11-year Schwabe cycle throughout the last millennium. [69] These annually resolved proxies come from the same calendar-dated tree-ring sequence. They confirm a direct influence of the Schwabe cycle on climate. This reaffirms that ^{14}C in tree-ring chronologies provides robust information on solar variability. [69] Longer cycles show less

regularity. The 178.7-year cycle is sometimes disturbed. Patterns of solar minima, like the Spörer and Maunder types, recur in steps of approximately 2402 years. To see the Sun clearly, we must correct for obfuscating variables. The strength of the geomagnetic field is one such variable. This correction yields a function called the solar modulation potential. It reveals solar activity over time via changes in cosmogenic isotope production. [68] This method confirms that the radiocarbon record in tree rings is a reliable archive of past solar activity. It allows researchers to reconstruct solar behavior far beyond the reach of instrumental records. [44]

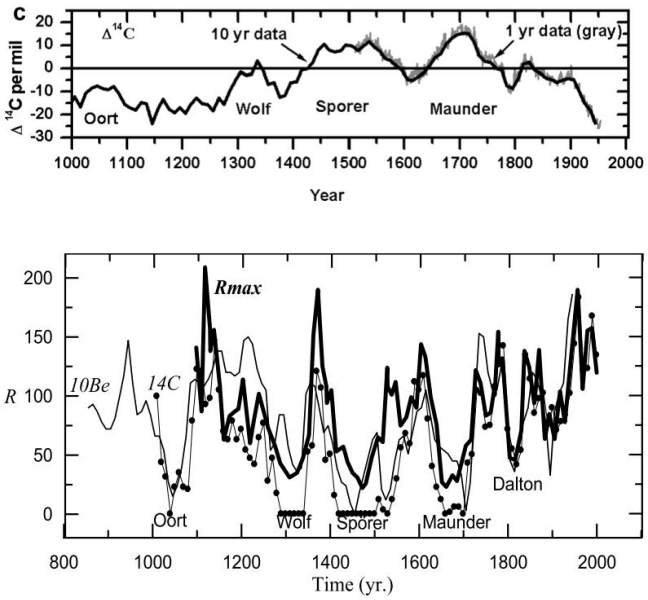


Figure 2.1: This graph displays the variation of ^{14}C (in per mil) over the last 1000 years, with data presented as 10-year averages (black line) and 1-year data (gray line). The plot spans from 1000 to 2000 CE and highlights major solar activity minima, including the Oort, Wolf, Spörer, and Maunder minima, which are marked on the timeline. The data, sourced from Stuiver et al., shows fluctuations in radiocarbon levels that correlate with changes in solar activity, with lower ^{14}C values indicating periods of higher solar output. [72]

The figure plots reconstructed solar activity from 800 to 2000 CE. It shows annual sunspot numbers derived from radiocarbon (^{14}C, solid dots) and beryllium-10 (^{10}Be, thin line) data.

2.2 Pre-Maunder grand minima

Auroral records provide further support for this view. Continuous Chinese observations from 900 A.D. to 1200 A.D. show that auroral activity was relatively weak during 1010–1050 A.D. This quietness is consistent with the grand minimum conditions of the Oort Minimum. [73] The lack of auroral evidence in "The Poetic Edda," assembled in southern Norway between 1000 and 1100

A.D., also aligns with the reconstructed auroral zone. Such silence fits the weak solar activity characteristic of the Oort Minimum. [73]

Solar activity reconstructions reveal distinct periods of prolonged low output, or grand minima, scattered across the historical record. [44] 1050, a signal inferred to indicate a period of minimum solar activity known as the Oort Minimum. This specific interval, spanning roughly from 1010 to 1070 or 1080, is identified in adjustment-free solar activity reconstructions as one of four grand minima since the year 1000 A.D., alongside the Wolf, Spörer, and Maunder events. The elevated ^{14} levels during this time confirm reduced solar modulation, as higher radiocarbon production corresponds to lower sunspot numbers in the inverted scale of the record. While some extratropical Northern Hemisphere temperature reconstructions do not explicitly highlight the Oort Minimum as a distinct cold anomaly, the cosmogenic isotope data establishes the solar quiescence. The timing of this minimum aligns closely with grand perihelion coincidences of Saturn, Uranus, and Neptune near the year 1050, suggesting a planetary association with Oort-type solar activity. These independent lines of evidence from radiocarbon dating and orbital mechanics suggest that the Oort Minimum was characterized by significantly reduced solar activity. Although the direct temperature signal in some proxy records is less pronounced than in later minima like the Maunder, the solar reconstruction confirms the event's occurrence and duration. The consistency between the ^{14} peak and the solar activity reconstruction is consistent with the existence of this early grand minimum in the Holocene record. [32][19][2][67][74] The resulting ^{10} record spans approximately from year 840 AD to year 1980 AD, offering a near-decadal resolution with an average of 8 years per sample. [67]

The ice piles up at a steady pace, roughly 7 cm of water equivalent each year. [67] This accumulation rate sets the rhythm for the entire record. We use it to reconstruct — the solar modulation potential, a measure in megavolts of how strongly the heliospheric magnetic field shields Earth from incoming galactic cosmic rays. Our method stacks multiple records and assumes constant mixing. The result matches the reconstruction by McCracken et al. quite well. They used the South Pole record and their mixing model "M3". But three marked differences stand out. First, the Spörer Minimum corresponds to the weakest activity in our reconstruction. This holds true even after removing the lowest values around year 1456 AD. [67] Second, the South Pole reconstruction shows a secondary maximum centered around year 1220 AD. That bump does not exist at all in our stack. [67] Third, the rank of the minima shifts. In our stack, the Spörer is

the lowest minimum. It is followed by the Maunder, Wolf, Oort, and Dalton Minima. That means the Oort and Maunder Minima are higher than in the McCracken et al. reconstruction. [67] The maximum of appears during the 20th century in the raw values. But it shifts to the 8th century in the smoothed values. [67] As discussed in Sect. 3.3, trends in snow accumulation have probably biased the relative values of . This bias would affect the rank of the reconstructed solar Minima and maxima. [67] In particular, the expected decrease in snow accumulation during the 16th and 17th centuries would have increased ^{10}Be concentration. That concentration spike would have biased towards lower values. [67]

However, this bias would not (or less) apply to our reconstructed Spörer Minimum and would even lower the Maunder Minimum. Specifically, large volcanic eruptions caused short-term climatic effects, including cooler temperatures over several months due to reduced solar irradiation. This distinction is vital because stratospheric aerosols affect the global radiation budget by absorbing and, more importantly, backscattering incoming solar radiation, which causes a cooling of the lower atmosphere and the surface. [75][1][76] Statistical studies using superposed epoch analysis have identified a statistically significant average temperature decrease of about 0.2 to 0.5°C for 1 to 3 years following the times of known nineteenth and twentieth century eruptions. [75] However, this volcanic signal is transient; surface temperatures recover in a few years as the aerosols decay, meaning that volcanic forcing cannot account for the multi-decadal or centennial cooling trends observed during the Sumerian, Egyptian, or Roman minima. The volcanic signal expected in hemispheric or zonal surface temperature records in historical times is about the same as the background interannual variations in temperature, requiring careful compositing to isolate the signal from noise. [75] Therefore, when we observe sustained cooling periods that align with low solar activity in ^{10}Be and ^{14}C records, we are not looking at the aftermath of volcanic winters, which are brief and intense, but rather at the prolonged dimming of the Sun itself. Thus, the pre-Maunder record stands as a testament to solar dominance on decadal to centennial scales, independent of the short-term volcanic noise that punctuates the instrumental era.

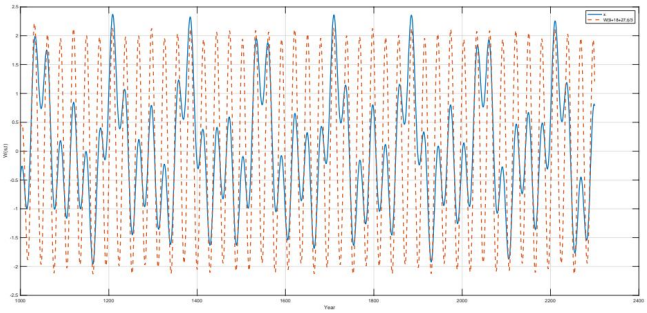


Figure 2.2: The plot displays two time series from year 1000 to 2100: the sum of perihelion coincidences for Saturn, Uranus, and Neptune (Asun(t) = Asa(t)+Aur(t)+Ane(t), solid blue line) and the contribution from Saturn alone (Asa(t), dotted red line), both measured in W/m^2. The blue curve shows a complex, high-frequency oscillation with amplitude modulated by a slower, lower-frequency envelope, while the red dotted line exhibits a similar but less pronounced oscillatory pattern, indicating Saturn's dominant influence on the combined signal. [19]

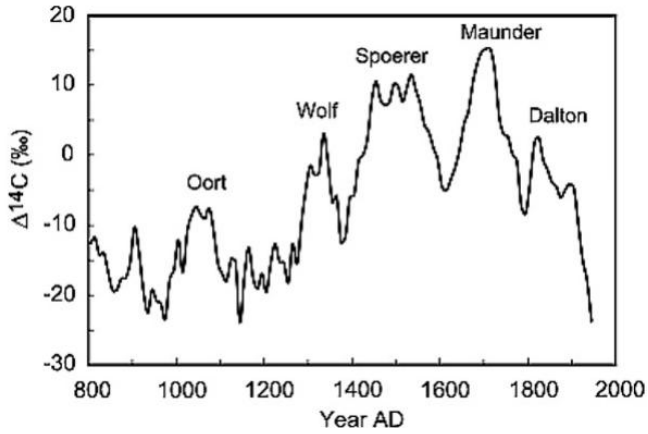


Figure 2.3: This line graph plots radiocarbon concentration (^{14}C, in ‰) against calendar year AD, showing decadal variations in solar activity over the past two millennia. Higher ^{14}C values, which are inversely proportional to solar activity, indicate periods of low solar output. The plot highlights several historical minima: the Oort, Wolf, Spoerer, Maunder, and Dalton events, with the Maunder Minimum (164 [77]

2.3 The Maunder and Dalton Minima up close

The cosmogenic record — the isotope archive — detects the Hallstatt 2,400-year cycle across the Holocene. This suggests a deep, rhythmic structure to solar output that predates the instrumented era.

Chapter 7 tells the full Tambora story, covering the 1815 eruption, the 'year without a summer,' and the failed harvests from New England to Finland. Here we note only one thing. The Dalton Minimum's most infamous years were a volcanic exclamation point set inside an already sun-starved climate.

The Dalton Minimum was not a quiet time for volcanoes. [85] We already know about the massive Mount Tambora eruption. But La Soufriere on Saint Vincent also erupted, in 1812. These events happened at the same time. [49][83] That overlap complicates the story. It challenges the idea that any single driver explains climate change. Instead, solar hibernation and volcanic particulates likely worked in tandem. They probably depressed global temperatures together. [86] The historical record thus suggests a deeper truth.

The Dalton Minimum was not merely a solar phenomenon. It was a time of compounded climatic stress. That stress came from both celestial and terrestrial sources. [87] Post described this era as the "last great subsistence crisis in the Western world." The sun went quiet during this interval. The Earth began to slowly cool. That cooling delayed the start of the planting season. It also limited the harvest with early frost in the fall. [88]

Computer models disagree on how much the Sun cools the Earth. Some simulations blame volcanoes for most of the chill. Others argue that solar cooling played a major role during the Dalton Minimum. Shindell and colleagues found that volcanic eruptions hit hard, but only for a short time. The drop in solar irradiance — the energy reaching Earth from the Sun — lasts much longer. [88][85][46][1][49] That difference matters for what comes next. Archibald in Australia, Duhau in Argentina, and Theodor Landscheidt in Germany forecast a new quiet period. They predicted the Sun might enter a phase like the Dalton Minimum. Some even suggested a more severe "Grand Minimum" could arrive in Solar Cycle 25. This forecast covers the 2020–2053 window this book uses. [89] These predictions warn of future solar minima. They suggest risks to global temperatures and societal stability. The echoes of the Dalton era remain loud. [49] Volcanoes and low solar output together could shift global mean temperatures. Wagner and Zorita showed changes of up to several tenths of a degree. [85] Yet we do not know the exact solar forcing used in some models. This uncertainty makes it hard to separate solar impacts from other factors.

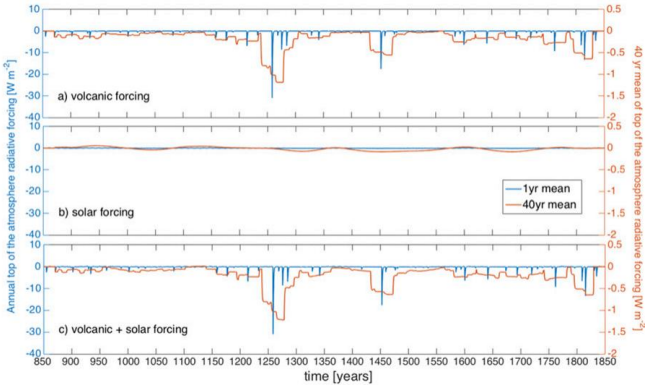


Figure 2.4: This figure displays three time series plots of top-of-atmosphere radiative forcing in W m^2 from 850 to 1850 CE, showing annual average volcanic forcing (a), solar forcing (b), and their sum (c). The blue lines represent 1-year running means, while the orange lines show 40-year running means, with the right y-axis corresponding to the 40-year mean values. Volcanic forcing exhibits large, short-term negative spikes, particularly around 1250 and 1800 CE, while solar forcing remains relatively stable with minor fluctuations. The combined forcing (c) reflects the sum of both components, with the 40-year mean (orange) smoothing out short-term variability. [90]



Figure 2.5: This black-and-white painting depicts Napoleon Bonaparte on horseback at the center of a desolate, snow-covered landscape, surrounded by a retreating army. Soldiers are shown falling, lying dead or wounded in the snow, with military equipment scattered around, conveying the harsh conditions of the retreat from Moscow. The composition emphasizes the scale of the disaster, with a dark, stormy sky ov [49]

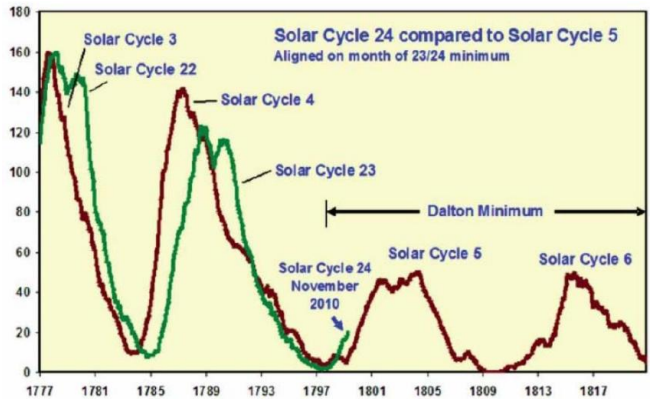


Figure 2.6: The graph plots solar cycle amplitude (in arbitrary units) over time, comparing Solar Cycle 24 and Solar Cycle 5, which are aligned on the month of their respective 23/24 minimums. It also overlays data for Solar Cycles 3, 4, 22, and 23, showing the relative timing and magnitude of solar activity peaks and troughs, including the prominent Dalton Minimum between Cycles 5 and 6. [91]

2.4 Grand maxima and societal abundance

The region did not simply warm in a single, steady trend. Instead, it experienced a sharp seesaw in rainfall. The western basins often dried out during positive North Atlantic Oscillation periods. The NAO is a dominant mode of atmospheric variability in the North Atlantic. Meanwhile, the east sometimes grew more humid. This happened despite the broader NAO impact. [92] This regional divergence was driven by the interplay of multiple climate patterns. One key driver was the North Sea-Caspian Pattern. This pattern is defined by the pressure difference between the North Sea and the Caspian Sea. When the pattern was positive, it brought cool and dry winter conditions to the central and eastern Mediterranean. When negative, it delivered warm and wet conditions. [92] Furthermore, a strong Siberian High could channel unusually cold airflow from Inner Eurasia. This air moved into the eastern Mediterranean and the Middle East. It contributed to rare phenomena such as snowfall and frost in Baghdad. These events were described several times during the Oort Minimum of the 11th century. These specific meteorological dynamics demonstrate that the Medieval Climate Anomaly in the Eastern Mediterranean was spatially and temporally incoherent.

It was punctuated by recurring anomalies.

Such variability underscores the necessity of examining regional climate drivers rather than relying on hemispheric averages, as local socio-political dynamics in the Byzantine Empire were likely shaped by these fluctuating environmental conditions rather than a steady thermal trend. [92][93] Elena Xoplaki and co-authors combined evidence of economic and demographic growth in Byzantium between 850 and 1300 CE with new findings from palynology, alongside documentary textual evidence and natural proxies for the Balkans and Asia Minor. [92] Their analysis identified potential links between climatic and societal changes, specifically noting correlations between a long-term trend towards wetter conditions in western Anatolia around AD 850–1000 and stable, relatively warm-wet conditions in northern Greece during AD 1000–1100. [92] Based on a marine record from the Athos basin in Northern Greece, they reconstructed changes in sea surface temperatures and other palaeoenvironmental factors. [92] Their data suggests a cooling trend from ca. [94] 500 to 850 CE, followed by a warming trend from ca. [92] 850 to 950 CE in the Northern Aegean. [92]

Pollen from Asia Minor and the Southern Balkans confirms a farming boom in the Byzantine Empire. It began in the late 9th and 10th centuries, after a quiet decline between the 6th and 8th. [92] Farmers grew more cereals, olives, and grapes. They also shifted toward pasturage and animal husbandry, adapting to local land. [92] Alexander Olson's study of oak and olive cultivation offers a deeper explanation. He argues that this economic upsurge was driven by elite pressure for surplus, not just by demographic growth alone. [92] The data shows that modest landscape modifications and slow agricultural growth characterized the 10th and 11th century Aegean provinces. More significant economic dynamics emerged only in the late 11th century. [92]

The Komnenian-led Byzantine state demanded higher tax revenue, while an emerging class of big landowners sought rent and Italian merchants traded across the Aegean's waters. These combined pressures forced peasants to produce a surplus that garnered coins on the market. [92] The climate offered no relief. In 1069, a harsh and long winter hit Germany, freezing rivers solid and causing a significant shortage of wine and fruit due to the extreme cold. [40] These concurrent extremes demonstrate the global reach of climatic anomalies during this period. [3] England suffered too. The year 1069 saw a great dearth there, exacerbated by Norman conquests, where peasants resorted to cannibalism and sold themselves into slavery to survive. [40]

The Oort Solar Minimum (ca. 1010–1080) was characterized by

reduced solar activity and cooler global average temperatures. An adjustment-free reconstruction of the solar activity over the last three millennia confirms four Grand minima since the year 1000A.D, including the Oort (1010–1070) period. The smoothed reconstruction — built from tree-ring data by ensemble empirical mode decomposition with variance matching — exhibited a general agreement with the variation of the reconstructed total solar irradiance, with a significant correlation ($r = 0.498$, $edf = 34$, $p<0.01$) during the common period 849–2000 AD. The relatively cold conditions between the two warm peaks around AD 1000 and 1100 seemed to be related to the Oort Minimum. Several of the periods with especially low solar activity are also visible in the reconstruction, such as the Wolf Minimum (c. [19][95][2][96] This complex climatic backdrop did not necessarily cause societal collapse in Byzantium or neighbouring polities; instead, it appears to be consistent with long-term economic expansion for certain times, suggesting that the empire possessed significant resilience against exogenous shocks. [92] A detailed examination of the winter of 927–28 illustrates this dynamic clearly. [92] Rather, the long winter was later connected with what the state and the peasants perceived as a socioeconomic crisis, serving as a lens through which contemporaries understood the reasons for social transformation. [97]

The environmental stressor, even if it was not the harshest winter of the tenth century in physical terms, impinged upon the complex web of crop ecologies, social relations, and the state's interests. [97] It added new momentum to extant social dynamics, specifically the trend of office-holding elites accumulating wealth to become an increasingly powerful social group. [92] While Byzantine society as a whole proved resilient, surviving the crisis, the price for this resilience was a significant shift in the balance of socioeconomic relations. [97] The winter offered an opportunity for the more affluent to exploit peasants whose livelihoods depended on ecological niches incapable of withstanding prolonged cold spells. [97] Thanks to buffers such as existing estates, accumulated gold, and local connections, elite groups could exploit local subsistence crises across the provinces to improve their situation relative to both the producing population and the state. [97] This suggests that environmental stressors stimulated social evolution rather than causing direct collapse. [97] Recent regional studies, including pollen data from Lake Belevi and Bafa Gölü, alongside written records like the 1073 charter for Andronikos Dukas regarding flood-damaged estates in the Maeander delta, support this nuanced view. [92] These archives inform us about short-term localised events and long-term trends, allowing for a more detailed description of the resilience of rural and urban communities. [92]

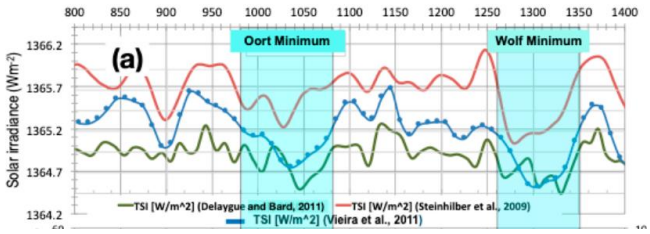


Figure 2.7: This line chart displays solar irradiance (W/m^2) over time, with the x-axis representing years from approximately 800 to 1400 and the y-axis showing irradiance values. Four distinct time series are plotted: TSI (W/m^2) from Delaygue and Bard (2011) in green, TSI (W/m^2) from Steinhiber et al. (2009) in red, and TSI (W/m^2) from Vieira et al. (2011) in blue and dark blue. The data reveals periodic flu [93]

2.5 The long cycles — Hallstatt, Eddy, Bray

This view shifts the worry away from rapid warming in the 21st century. Instead, it points toward a possible ice age in several thousand years. [8] If Vinós' analysis holds, our faith in controlling climate by cutting CO_2 emissions might prove to be the greatest folly of the 21st century. [1] That possibility demands a wider debate on what truly drives climate change.

Climate models employing reductions in total solar irradiance of 0.4%, 0.25%, 0.12%, and 0.08% indicate that even a 'grand' minimum state would only partly reduce global mean temperature by 0.1 K, or delay the projected rise. [98] More moderate scenarios result in an even weaker signal, while recent experiments with a 0.12% reduction apportioned across the spectrum, or a larger 0.85% reduction in UV irradiance alone, show regional responses in the Northern Hemisphere that do not appear to scale linearly with the forcing magnitude. [98] These simulations suggest that a hypothetical grand solar minimum would offset only approximately 0.2 K of anthropogenic warming. Consequently, such a solar downturn is unlikely to significantly alter the long-term warming trend driven by greenhouse gas emissions. [99] These higher estimates imply that solar forcing could be important for climate variability, particularly if the irradiance from the quiet Sun varies significantly over time. [100] Some studies utilizing these high solar variability TSI estimates argue that solar forcing dominated long-term warming since the 19th century, suggesting that the solar contribution to observed temperature increases may be larger than previously thought. [101] Consequently, the relative importance of solar forcing in recent warming trends continues to be a subject of significant scientific debate.

The Sun warms the Earth through two distinct routes. The simplest is direct heating, driven by changes in the total radiative output that reaches our atmosphere. [102] We currently believe these variations are too small to dominate surface climate. Yet they may have been larger in the past. [103] The second route is

indirect. Solar activity can alter the transparency of the atmosphere, which shifts the planet's overall radiative budget. [102] One specific mechanism involves ultraviolet (UV) radiation — the high-energy part of the solar spectrum. This UV light is absorbed by ozone in the stratosphere, heating that upper layer. The resulting temperature changes can then ripple downward, influencing the large-scale dynamics of the troposphere below. [102] During solar maxima, the energy in the UV spectrum can be several percent higher than during solar minima. [64] This chain of effects adds to natural climate fluctuations. But it remains a minor factor compared to anthropogenic greenhouse gas emissions.

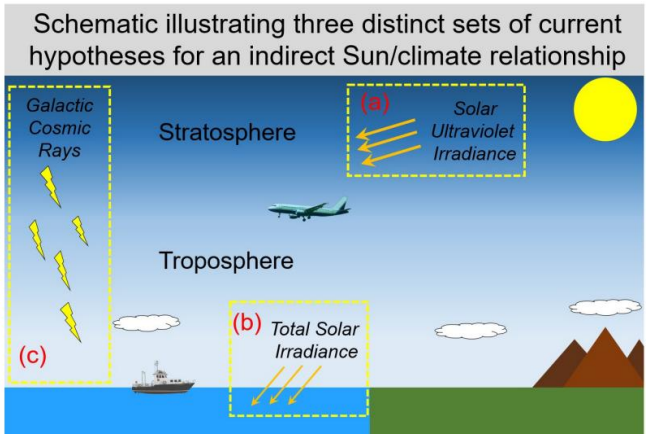


Figure 2.8: This schematic illustrates three proposed mechanisms for indirect solar influence on Earth's climate. Panel (a) shows solar ultraviolet irradiance affecting the stratosphere, with a top-down pathway to the troposphere and surface. Panel (b) depicts total solar irradiance impacting the troposphere and oceans, representing a bottom-up mechanism. Panel (c) illustrates galactic cosmic rays modulated by solar activity, with a proposed influence on the troposphere and stratosphere. The diagram contrasts the vertical pathways of solar forcing across atmospheric layers. [101]

Porter demonstrates that sulfur-rich aerosols generated by volcanic eruptions are a primary forcing mechanism of glacier fluctuations and climate on a decadal scale, suggesting volcanic impacts as a dominant driver of interannual-to-decadal Northern Hemisphere temperature variability. The study shows that episodes of glacier advance consistently associate with intervals of high average volcanic aerosol production, inferred from acidity variations in a Greenland ice core. [104][79][56] Specifically, advances occur whenever acidity levels rise sharply from background values to reach concentrations 1.2 $^{+}$/ above background. [104] A phase lag of about 10–15 yr, equivalent to reported response lags of Alpine glacier termini, separates the beginning of acidity increases from the beginning of subsequent ice advances. [104] The amount of surface cooling attributable to individual large eruptions or episodes of eruptions is similar to the probable average temperature reduction during these advances, ca. 0.5 1.2, as inferred from depression of equilibrium-line altitudes. [104] This climatic shock coincided with the political transition from the Roman Republic and Ptolemaic Kingdom to the Roman Empire, a period marked by unusual climate, crop failures, famine, disease,

and unrest in the Mediterranean, suggesting significant vulnerability to hydroclimatic shocks in ancient states. These findings imply that such environmental stressors may have exacerbated existing political tensions, potentially accelerating the collapse of established regimes. [105][106][107][108]

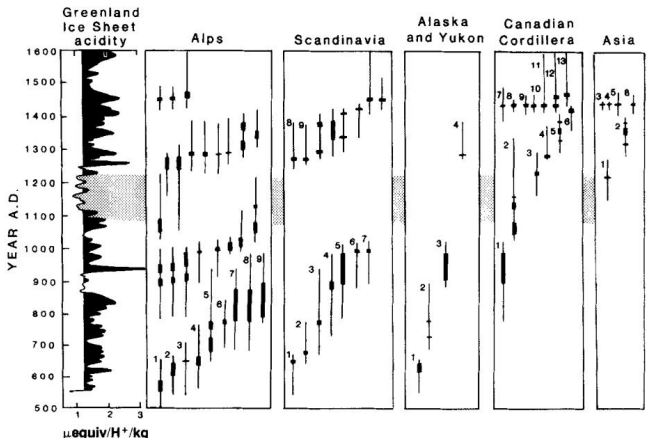


Figure 2.9: The figure displays a composite time series comparing a filtered Greenland Ice Sheet acidity record (in equiv H^+/kg) with calibrated radiocarbon dates of glacier advances across the Northern Hemisphere, including the Alps, Scandinavia, Alaska and Yukon, Canadian Cordillera, and Asia. The Greenland record, plotted on the left with years A.D. on the vertical axis, shows fluctuations in acidity over time, while the other regions are represented by vertical bars indicating the timing of glacier advances. A shaded interval from approximately 1090 to 1230 A.D. highlights the Medieval Optimum, a period marked by reduced acidity and a lack of dated glacier advances. [104]

The MPI-ESM-P ensemble simulations suggest the subpolar gyre weakened abruptly around 1600. This shift stemmed from unusual Arctic freshwater export into the Labrador Sea. The Past1000-R3 simulation captures this change clearly. Gyre strength dropped by 0.72 Sv over two decades, separating two stationary regimes. [26][27] Positive feedbacks appear to stabilize this new state. Reduced poleward heat transport cools the Nordic Seas. That cooling enhances sea ice growth and export through the Denmark Strait. The added ice further freshens the upper ocean. [26] These simulated changes, including expanded sea ice and reduced subpolar meridional heat transport, are consistent with paleoclimate reconstructions of Little Ice Age-type episodes. The timing does not line up perfectly, but internal climate variability may explain those gaps. [26]

By the 1940s, researchers had refined the postglacial zonation. They established a summer vegetation-based temperature scale for the Scandinavian Holocene. [1] These efforts produced climate reconstructions that closely mirror current understanding. They reveal that the Holocene climate subdivides into periods of distinct conditions. A diagram by Rutger Sernander from 1912 illustrates this structure. [1] The resulting vegetation stages allow for the distinction of a 2500-year cycle in plants and animals. Some botanists, like Sernander, proposed that transitions between periods were abrupt rather than gradual. [1] Sernander linked the last transition between the Sub-Boreal and the Sub-Atlantic

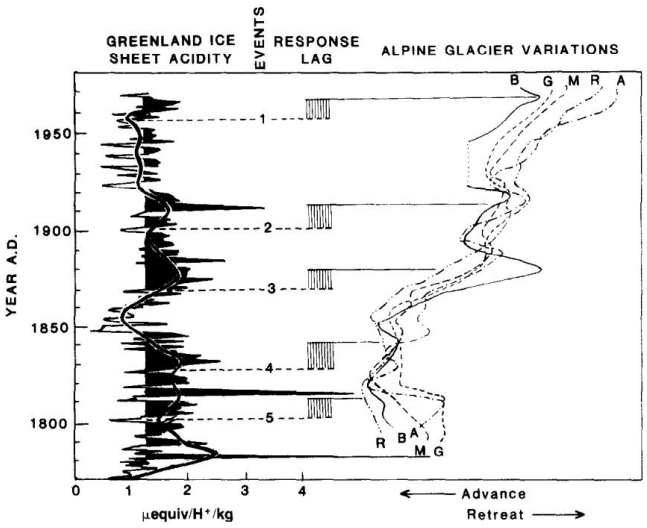


Figure 2.10: The figure displays a time series comparing the 2-year average acidity profile of the upper Greenland Ice Sheet, with a 11-point Gaussian filtered curve and shaded regions indicating values above background levels, against five Alpine glacier variations (Argentière, Brenva, Unter Grindelwald, Mer de Glace, Rhone) from 1800 to 1950 A.D. Dashed horizontal lines mark the onset of acidity events exceeding 2.4 equiv H^+/kg, and shaded zones to the right of the Greenland acidity curve illustrate the response lag, showing that glacier advances lag behind acidity peaks by 1–2 decades. [104]

to a specific event. It occurred around 650 BC. He connected it to the "Fimbulvintern," or Great Winter of the Sagas. This marks the end of the Nordic Bronze Age. It rendered the Nordic countries a colder place. [1]

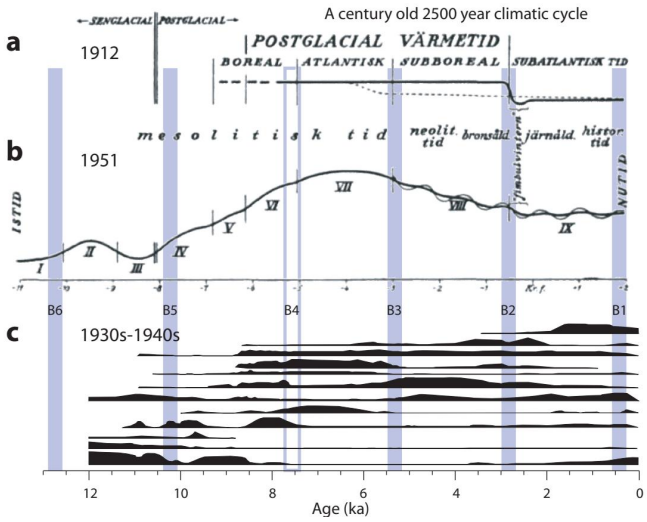


Figure 2.11: This figure presents three historical reconstructions of postglacial climate and vegetation in southern and central Sweden from the early 20th century. Panel (a) shows Rutger Sernander's 1912 model of abrupt climate degradation at the Sub-Boreal/Sub-Atlantic transition, labeled "fimbulvintern," contrasted with G. Andersson's gradual temperature evolution. Panel (b) displays Magnus Fries' 1951 diagram of temperature evolution based on pollen zones (I–IX), with a thin line indicating a near-millennial humidity oscillation. Panel (c) illustrates analytical pollen zones from the 1930s–1940s, confirming Sernander's climatic framework, with blue vertical bars marking the 2500-year Bray cycle. All panels use a common age scale in thousands of years before present (ka), with dates in CE calendar years. [1]

Chapter 3

Solar Science Foundations

The instrumented solar record — sunspot counts, magnetic indices, F10.7, TSI — is the toolbox every later chapter draws on.

3.1 From Galileo to the photoheliograph

The story of solar observation starts with glass, not the naked eye. [44] Telescopes brought the Sun's surface into sharp focus, revealing dark patches that drifted across its face. These were sunspots. By the late seventeenth century, astronomers such as Cassini and Flamsteed were counting them with growing regularity. [109] Cassini observed that spots appeared more often in 1676 than in the twenty years before. Flamsteed, working later, complained about how rare they had become. [109] The modern sunspot number — a standard metric for solar activity — traces its roots directly to these early counts. [62] The legacy of 1610 is therefore not merely a historical curiosity. It marks the beginning of the continuous solar record that supports our current understanding of solar variability. [44] This optical method produced reasonably clear images of the Sun. It remained the standard tool for solar observation until the late 18th century. [44]

Kepler projected the Sun's image through a tiny hole in May 1607, using a camera obscura — a darkened chamber that casts a picture of the star onto a screen. He saw a dark mark on that disk and thought it was Mercury passing in front of the Sun. That interpretation was wrong. [44] Such careful looks were rare at first. They usually happened only when something dramatic was due, like an eclipse or a planetary transit. But people did watch the Sun regularly this way, too. In Bologna, observers logged their views in the cathedral of San Petronio. They kept doing this from 1655 to 1736. Eustachio Manfredi published about 300 pages of those logs in 1736. [44] Those drawings and notes count as instrumental data. They were made with a device, not just the naked eye. This matters because it fills the gap between casual sightings and the later telescope surveys. It gives us a continuous record of solar activity. [110][111][109][112]

The sunspot number stands as the most common and longest available index of solar activity, serving as a synthetic index useful for the quantitative representation of overall solar activity outside the grand minimum. [44] However, this series has big uncertainties before 1900, and fragmentary non-instrumental observations of the sun before 1610, while giving a possible hint of relative changes in solar activity, cannot be interpreted in a quantitative manner. Daily records of sunspot observations have formed an essential basis for evaluating long-term solar activity since 1610, a data series often considered one of the longest ongoing scientific experiments in modern science. [110] After the initial modern compilation of the comprehensive data set of sunspot group number in Hoyt & Schatten (1998a, 1998b), recent studies have continuously recalibrated and improved these data series to revise the overall long-term trends. [110] Investigations of the original observational records have formed the basis for these analyses, offering a ground truth for further recalibrations using sophisticated methods. [110] The standard sunspot number index is available from 1610 AD onward, though data quality degrades significantly in earlier periods.

Consequently, interpretations of solar activity prior to the twentieth century should be treated with caution due to these inherent observational limitations. [113][110][111][114][115][116] This adjustment, attributed to Max Waldmeier, significantly altered the Relative Sunspot Number, creating a discontinuity in the ratio between the Group Sunspot Number and the Standard Sunspot Number around 1945. [117] However, systematic searches of historical drawings from the Greenwich Photoheliographic Programme suggest that the earlier observer, Wolfer, did not apply this weighting scheme, as no such spots were found in the records for which weighting was allegedly applied at Zürich. This finding is consistent with the absence of any mention of a weighting scheme in Wolf's and Wolfer's meticulous yearly reports in the *Mittheilungen über Sonnenflecken* series. [62] Consequently, the apparent continuity of the record masks a fundamental shift in observation protocols, where the Locarno Station, serving as the modern reference site, continues to apply Waldmeier's weighting, thereby carrying the effect fully into the current sunspot number maintained by SIDC in Brussels. Thus, the recovery of lost notebooks is not an antiquarian exercise but a necessary step to establish a reliable baseline for comparing modern satellite-era measurements with pre-telescopic reconstructions.

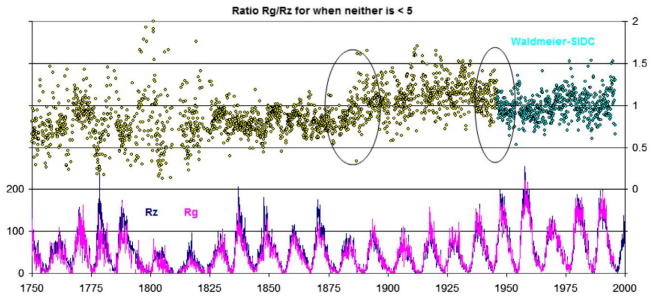


Figure 3.1: The figure displays a scatter plot of the ratio between monthly Group Sunspot Numbers (Rg) and Wolf (Zürich, International) Sunspot Numbers (Rz) from 1750 to 2000, with the ratio plotted against time. The top panel shows the Rg/Rz ratio, where data points are color-coded by time: yellow-green for earlier periods and teal for later periods, with the ratio generally clustering around 1.0 after ˜1900. Two oval regions highlight periods of notable deviation. The bottom panel shows the individual Rg (magenta) and Rz (blue) time series, both exhibiting the characteristic 11-year solar cycle, with Rg values generally higher than Rz. The caption indicates the data excludes months where either Rg or Rz is less than 5. [117]

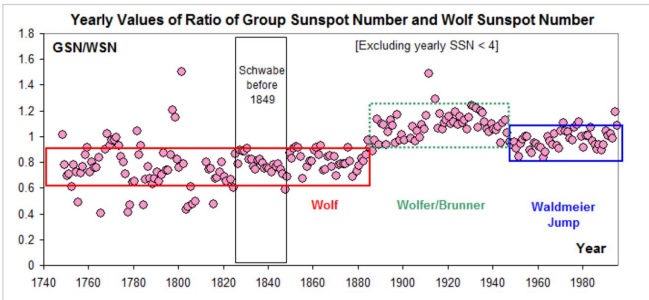


Figure 3.2: This scatter plot displays the yearly ratio of Group Sunspot Number (GSN) to Wolf Sunspot Number (WSN) from 1740 to 1990, excluding years where the Wolf Sunspot Number is less than 4. The vertical axis represents the GSN/WSN ratio, while the horizontal axis shows the year. The data points reveal a distinct shift in the ratio over time: values are clustered around 0.8–1.0 prior to 1849, with a notable increase beginning around 1849, followed by a more stable period from approximately 1900 onward. The plot highlights the "Waldmeier Jump" and labels historical periods including the Schwabe cycle before 1849, the Wolf era, and the Wolfer-/Brunner era. [62]

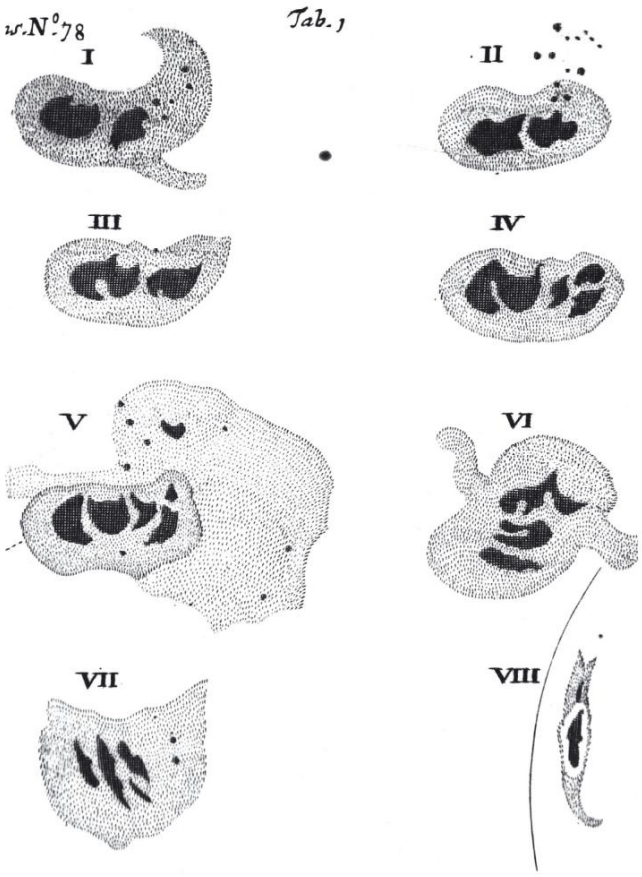


Figure 3.3: This figure presents eight numbered illustrations of sunspot observations from 1671, attributed to G. D. Cassini and published in Oldenburg (1671c). The drawings depict the Sun's surface with varying configurations of dark sunspots and penumbral structures, rendered in stippled detail to represent brightness and texture. The illustrations, labeled I through VIII, show different solar disk views, i [118]

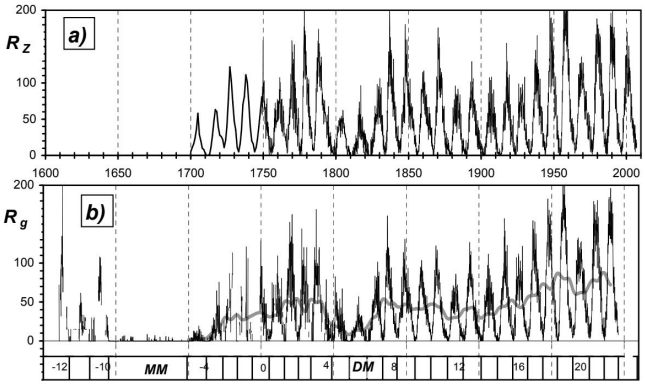


Figure 3.4: This figure displays two time series of solar activity from 1610 to 2000: panel (a) shows the Wolf sunspot number (Rz) with monthly data from 1749 and yearly data from 1700–1749, while panel (b) presents the group sunspot number (Rg). Both plots exhibit the characteristic 11-year solar cycle, with a clear 11-year running mean (grey line) applied after the Maunder minimum. The lower panel indicates [44]



Figure 3.5: The image displays a hand-drawn illustration of the Sun, showing a circular solar disk with a pale yellow surface and a thin blue-green outer ring, consistent with 18th-century astronomical drawings. Several dark, irregularly shaped spots are visible on the solar surface, clustered in two groups, representing sunspots observed on February 15, 1760. Handwritten annotations below the disk include "d [62]

3.2 Cycle metrics — Schwabe, Hale, butterfly

The Schwabe cycle anchors this variability. It is an approximately 11-year period of solar activity. This rhythm serves as the primary heartbeat of the solar dynamo. [119] Space-borne measurements of total solar irradiance (TSI) and spectral solar irradiance (SSI) clearly establish this 11-year cycle. The overall energy output varies by only about 0.1%. The ultraviolet spectrum fluctuates by several percent. This happens particularly in the 200–250 nm range. This modulation is not merely a surface phenomenon. It is deeply tied to the Sun's magnetic structure. [120][121][122][123] This longer magnetic cycle is evident in the modulation of galactic cosmic rays. These rays exhibit a 22-year pattern. The tilt of the heliospheric neutral current sheet influences this pattern. This sheet is the vast, rippled surface winding through interplanetary space. It separates the two magnetic polarities of the Sun's field. The drift of charged particles through the interplanetary magnetic field also plays a role. [122] Observations of the Ca II H and K emission lines further confirm the connection between magnetic activity and irradiance. Magnetic processes in the chromosphere heat the cores of these lines. The chromosphere is the thin layer of the Sun's atmosphere just above its visible surface. [120] These lines serve as a quantitative proxy for stellar magnetic activity. They reveal that more active stars possess more vigorous cycles. This implies that the younger Sun likely experienced stronger irradiance variability than it does today. [120]

Together, these cycles create a complex, asymmetric environment that modulates the flow of cosmic rays and shapes the space weather experienced by Earth. The ˜11 yr cycle itself was discovered by Heinrich Schwabe in 1844 through tracking the variation in the sunspot number. [44] This ˜11 yr cycle is considered a fundamental feature of solar activity originating from the solar dynamo process. It is currently believed that these quasi-periodic changes in solar irradiance and sunspot number, known as the Schwabe cycle, are the result of solar differential rotation as modeled in hydromagnetic solar dynamo models. [124][125][126][127][128] Half a century later, E. W. Maunder identified the butterfly diagram, a pattern progressing from ˜30° latitude to the equator over the ˜11 yr period. [129] Later, G. E. Hale demonstrated that sunspots were sites of intense magnetism protruding through the Sun's photosphere and that the polarities of the butterfly's wings alternated in sign with a period of about 22 yr. [126] The variability of solar cycle amplitudes from decadal to millennial timescales can be understood as the natural behaviour of the solar dynamo itself — a weakly driven, noisy oscillator. [124] No intrinsic periodicities apart from the

11-year cycle are required to understand this variability, although the possible existence of such periodicities cannot be strictly excluded. [124]

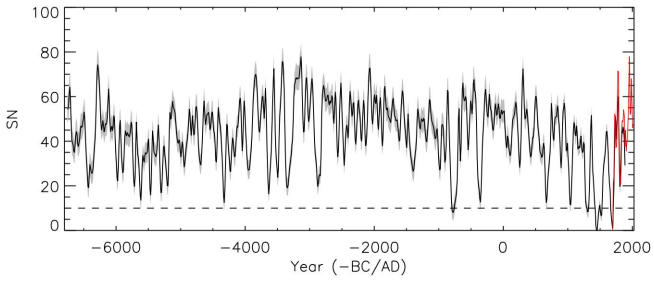


Figure 3.6: The chart displays a time series of reconstructed sunspot numbers (SN) from –6000 to 2000 years (–BC/AD), with the y-axis showing SN values up to 100 and the x-axis representing time. A black line plots the reconstructed SN, accompanied by a gray shaded region indicating the 68% confidence interval. A red line shows the decadally resampled international sunspot number (version 2, scaled by 0.6) from Clette et al., and a dashed horizontal line at SN = 10 marks a reference threshold. The data reveal significant variability in solar activity over millennia, with periods of high and low SN, including a notable minimum below SN = 10 around 0 AD. [143]

Sunspot counts remain the standard tool for tracking this rhythm. [130] But the count is only a surface symptom. The deeper driver is magnetic. The true physical period is not 11 years, but 22. [131] The toroidal magnetic field — the component wrapped around the Sun's equator like a belt — flips its sign every cycle. This alternation is captured in Hale's polarity law. [130] The leading magnetic polarity in each hemisphere switches from one sunspot cycle to the next. Consequently, the 22-year Hale cycle marks the full magnetic polarity cycle. Sunspot polarities alternate in sign every 11 years. This reversal suggests that the large-scale organization of the field inside the Sun is mostly toroidal in orientation. It wraps around the rotation axis in belts, rather than running pole to pole. The direction opposes itself on either side of the equator. Active regions adhere to this pattern approximately 92–95% of the time. [132][126][133][134][135][136]

The spot count is only one symptom. The solar cycle is a complex magnetic phenomenon, with distinct spatial and temporal signatures. [130] The butterfly diagram maps this movement. It shows sunspots emerging at roughly 30 degrees latitude. Over the 11-year cycle, they drift toward the equator. E. W. Maunder first mapped this latitudinal migration. [137][126][135][133][133] Hale added the magnetic layer in 1908. He showed that the polarities of these regions alternate in sign. The period of this alternation is about 22 years. This defines the Hale cycle. [44] The Sun's magnetic field does not return to its original state after one 11-year sunspot cycle. It takes two such cycles to complete the 22-year magnetic polarity cycle. [44] The wings of the butterfly

diagram thus represent more than just sunspot locations. They show the visible manifestation of this deeper magnetic rhythm. [129] Surface meridional flow — the slow circulation of plasma from equator to pole — carries the trailing sunspot polarity flux poleward. This creates unipolar magnetic regions at high latitudes. These regions rush to the poles. [135] We now recognize that the 11 yr cycle is part of the more general Extended Solar Cycle or Hale cycle. This cycle averages 22 yr. It encompasses observational elements beyond sunspots. These range from the latitudinal distribution of prominences to coronal X-ray bright point positions. Coronal extreme-ultraviolet intensity is included too. [138][126][139] The dominant periodicity is about 11 yr. The Sun also undergoes longer-term variations. These span multiple cycles and last decades. [44]

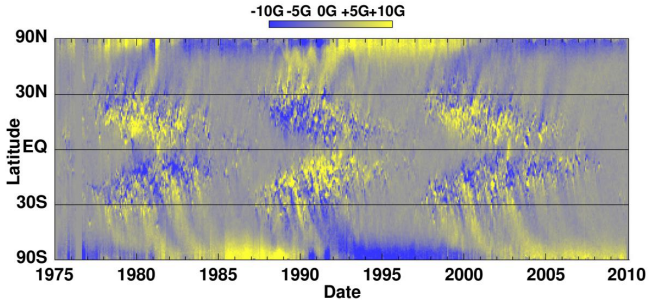


Figure 3.7: This magnetic butterfly diagram displays the longitudinally averaged radial solar magnetic field from 1975 to 2010, derived from Kitt Peak and SOHO observations. The plot shows magnetic polarity (blue for negative, yellow for positive) as a function of latitude and time, illustrating the 11-year solar cycle with alternating bands of opposite polarity emerging at mid-latitudes and migrating toward the equator, while trailing-polarity flux streams poleward to reverse the polar fields. The pattern confirms Hale's Polarity Laws, Joy's Law (tilted active regions), and the gradual reversal of polar magnetic fields, with higher-latitude magnetic features transported toward the poles over time. [130]

The Schwabe cycle varies in both amplitude and duration, rather than being a regularly ticking clock. This variability is evident when examining the time-variant number of sunspots, which can be represented by a simple model where the solar activity period time and phase state fluctuate significantly from one cycle to the next. [19][140][141][57][142] Furthermore, the duration of the total cycle is not merely a sum of hemispheric activities but is influenced by phase asynchrony between the northern and southern hemispheres. During solar cycle 14, the total cycle length was defined by the southern hemispheric cycle, whereas in cycle 20, it was determined by the northern hemisphere, despite large phase asynchrony at the beginning of the 20th cycle. [140] In some cases, such as cycles 15 and 19, the length of the total sunspot cycle can be less than the lengths for the individual hemispheres due to fluctuations in solar activity and phase relationships

around the sunspot minimum. [140] When analyzing the Wolf Sunspot Number and Group Sunspot Number datasets using Empirical Mode Decomposition, the highest amplitude intrinsic mode function corresponds to a period of approximately 9 years, followed by a mode of about 14 years, which together compose the Schwabe cycle. [141] Thus, the solar cycle is not a simple periodic oscillator but a complex system with varying amplitude and duration, shaped by hemispheric asymmetries and internal dynamical processes.

3.3 Sunspot numbers and their recalibration

Sunspots look dark because they are cooler than the rest of the solar surface. Strong magnetic fields suppress the flow of heat, dropping the temperature to about 4000 K. The surrounding photosphere burns at 5800 K. That contrast creates the distinct darkening we see. [44] Counting every individual spot is difficult for early observers. To repair this deficiency, Hoyt and Schatten introduced the Group Sunspot Number. This index counts only groups of spots, not the spots themselves. That choice makes it compatible with earlier, less precise records. It provides a more reliable reconstruction of solar activity back to the early seventeenth century. [62] Methodological debates persist, however. They concern the weighting schemes introduced by Wolf and modified by Waldmeier. These schemes may have introduced systematic biases. Analysis of monthly values suggests that the group count and spot count are constrained to a narrow diagonal band. This indicates that a one-dimensional relationship with the relative sunspot number might be sufficient for correction to an un-weighted value. [144][113][145] Researchers can calculate a logarithmic weight factor from the observed sunspot number. They then divide the International Sunspot Number since 2003 by this computed factor. [144] This supports the assertion that the weight factor function is also valid for the Waldmeier era at Zürich. It allows for the correction of the Zürich sunspot number for the inflation introduced by the weighting scheme. [117] The weight factor varies with the sunspot number itself. One cannot use a constant weight factor throughout. Doing so would be a first, crude approximation at best. [144]

This update confirms that the previous series contained artificial trends that distorted the true amplitude of solar cycles, particularly in the modern era. [62] To resolve this, the solar community undertook a decade-long effort involving four Sunspot Number Workshops from 2011–2014, producing major recalibrations: (1) became (2) by Clette and Lefèvre, and HoSc98 became SvSc16

by Svalgaard and Schatten. [146] To address these issues, researchers have replaced the sunspot number between the years 1639 and 1715 with a reconstruction by Vaquero et al., which accounts for the large amount of missing sunspot number data and the difficulty in calibrating between different observatories. [147] While the International and Group sunspot numbers share similarities, such as indicating low activity during the Dalton minimum and a peak around 1957/58, they diverge sharply for earlier periods, with Group numbers running 25-50% lower than International numbers before 1882. [148] This divergence establishes that different sunspot series agree closely over the twentieth century but diverge significantly for earlier centuries. The consensus among diverse reconstructions since 1900, where underlying data are plentiful and of good quality, confirms that all methods are equally satisfactory provided the reference observer records are stable. [116][116][148][64] However, going back in time to Solar Cycle 11, peaking in 1870, the disagreement persists for all earlier cycles, highlighting the critical need for careful calibration when interpreting long-term solar variability from the limited observational records of the past.

The Wolf series struggles to capture the true magnitude of solar cycles from 1650 to 1700. [62] During this stretch, the fraction of active days is so low that the record suggests very small cycle amplitudes. The data quality simply drops off as we look further back, especially through the Maunder minimum from 1645 to 1715. The Group Sunspot Number offers a sturdier framework for this era. It counts only the number of sunspot groups, rather than individual spots, which stabilizes the record when observations are sparse. Early data interpretation was fraught with pitfalls, as one case shows. Observations by Anton Maria Schyrlaeus Rheita in 1642 were initially misread as showing eight sunspot groups. Later analysis corrected this to report just one group in June. [30] This correction highlights how easily early records can be skewed. The Maunder minimum is therefore not merely a gap in the Wolf record. It is a period where the Group Sunspot Number provides the only reliable window into solar behavior. This approach establishes a clearer picture of solar minima that extends back to the early 17th century.

We use the SILSO Sunspot Number version 2.0 as our reference series. The 2015 recalibration fixed the long-standing Waldmeier discontinuity. It remains the community standard, maintained by the World Data Center in Brussels. Where later analyses dispute particular segments of the record, we flag the disagreement. We do not silently switch series. [146]

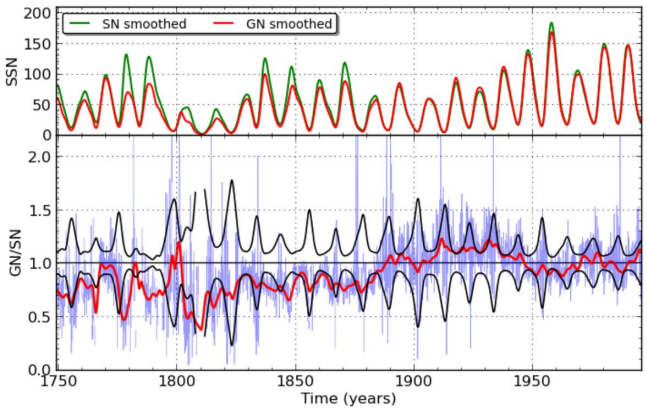


Figure 3.8: The figure displays two panels plotting solar activity indices over time from 1750 to 1960. The top panel shows smoothed sunspot number (SN, green) and group number (GN, red) time series, both processed with a 12-month Gaussian filter, revealing synchronized 11-year cycles. The bottom panel presents the GN/SN ratio (blue) and its smoothed version (red), with black lines indicating confidence intervals derived from Hoyt and Schatten. The ratio deviates significantly and systematically from unity before approximately 1880, indicating a period of differing solar activity metrics. [62]

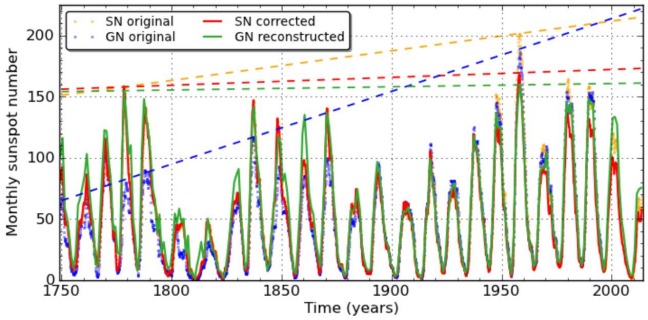


Figure 3.9: This line plot displays monthly sunspot numbers from 1750 to 2015, comparing original and corrected/ reconstructed series for both the SN (Sunspot Number) and GN (Group Number) datasets. The y-axis shows monthly sunspot number, and the x-axis represents time in years. The SN original (orange dots) and SN corrected (red line) series, along with the GN original (blue dots) and GN reconstructed (gree [62]

3.4 The satellite-era TSI record

The satellite-era record of Total Solar Irradiance (TSI), the spatially and spectrally integrated radiant energy from the Sun at one astronomical unit, represents the primary energy input to the Earth's climate system, dwarfing all other sources by a factor of three thousand. [149] These measurements rely on electrical-substitution radiometers, instruments that achieve high accuracy by modulating heater power to maintain thermal stability, thereby ensuring precise quantification of the incoming solar flux. Early instruments, such as ERB and ACRIM-1, initially measured higher TSI values than subsequent sensors like ERBE, ACRIM-2, and VIRGO, creating a divergence in the long-term record that has fueled ongoing debate regarding decadal trends. [149] The launch of the Total Irradiance Monitor (TIM) onboard the Solar Radiation and Climate Experiment (SORCE) mission introduced significant improvements in measurement accuracy and stability, ultimately establishing a lower, now internationally accepted TSI value of approximately 1361 W m^2. [149]

Despite these advancements, the composite TSI record remains

subject to scrutiny, particularly concerning the gap-bridging methods used to reconcile data from different instruments. [150] This uncertainty is critical for climate studies, as it directly impacts assessments of solar forcing on global temperatures. [150] The launch of the SOlar Radiation and Climate Experiment/Total Irradiance Monitor (SORCE/TIM) helped resolve this offset issue. [149] It confirmed lower TSI values and indicated that predecessor instruments were approximately 0.35% erroneously high. [149] Subsequent corrections were retroactively applied to flight data for ACRIM3 and VIRGO. [149] The lower TSI value established by SORCE/TIM was validated by later missions, including the Total Spectral and Solar Irradiance Sensor (TSIS-1)/TIM, and is now the accepted value by the International Astronomical Union. [149] This recalibration improved uncertainties regarding Earth's energy balance by resolving discrepancies between incoming and outgoing radiation. [149]

The satellite-era record of total solar irradiance — the total power from the Sun reaching Earth — tells different stories depending on how the data are stitched together. [86] The ACRIM composite suggests TSI increased during the 1980s and 1990s. It has slightly declined since then. This upward pattern from 1980 to 2000 stands in stark contrast to the PMOD composite. That dataset indicates a slight downward trend over the same period. [100][101][100] This multi-decadal difference matters for solar models. Those models try to interpret climate changes. [86] If TSI increased from 1980 to 2000, total solar activity could have risen too. That rise might have contributed significantly to the global warming observed from 1980 to 2000. [86] The choice of composite directly impacts assessments of solar forcing. ACRIM data supports the possibility that TSI acted as a primary driver of global temperatures during this interval. PMOD data suggests a different mechanism for the observed warming.

The satellite-era record of Total Solar Irradiance (TSI) reveals significant discrepancies in how long-term trends are reconstructed, particularly concerning the period known as the ACRIM Gap — the roughly two-year hiatus (1989–1991) between the ACRIM1 and ACRIM2 satellite radiometers, which every composite must bridge with lower-precision instruments. [86] During the 1990–1992.5 interval, comparisons between the WSKF06 proxy models and the PMOD composite highlight a fundamental divergence in data processing. [86] While the WSKF06 models show stationarity, the PMOD composite exhibits a significant downward trending difference, largely due to Fröhlich's downward adjustment of the ERB data. [86] This adjustment involved a shift of approximately 0.86 W/m^2, which is more than twice the shift derived from WSKF06 comparisons. [86] Consequently, the resulting PMOD

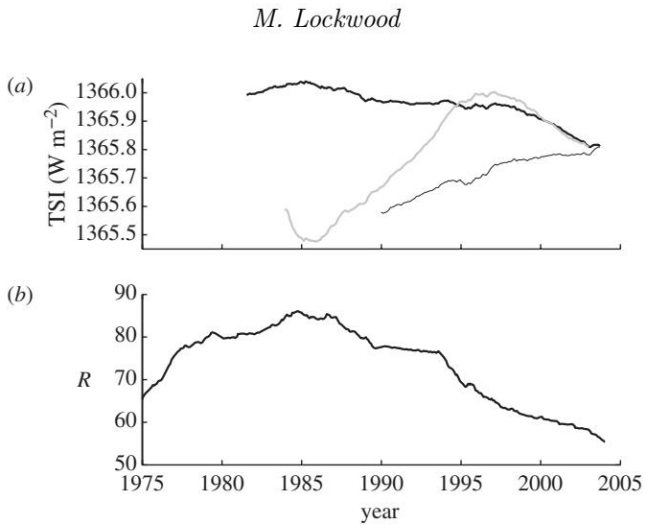


Figure 3.10: The figure presents two panels showing solar-cycle-averaged variations in total solar irradiance (TSI) and sunspot number. Panel (a) plots TSI (W m^2) from 1975 to 2005, comparing three composites: PMOD (thick black line), ACRIM (thick grey line, offset by -0.4 W m^2), and IRMB (thin black line, offset by -1 W m^2), revealing a general decline in TSI over the period with notable divergence during the late 1980s. Panel (b) shows the corresponding solar-cycle-averaged sunspot number (R), which increases from ˜60 in 1975 to a peak near 85 around 1985, followed by a steady decline to ˜50 by 2005. [152]

composite suggests that TSI has been steadily decreasing since at least the late-1970s, a conclusion that stands in contrast to the ACRIM composite, which would require an upward adjustment of ˜0.46 W/m^2 to reconcile the minima trends. This ongoing debate over gap-bridging methods underscores the uncertainty in decadal TSI trends, as the choice of composite directly influences the perceived direction of solar output over recent decades. This methodological sensitivity implies that the magnitude of solar forcing in climate models remains somewhat ambiguous. [51][101][100][100] Consequently, attributing specific temperature variations to TSI fluctuations requires careful consideration of these reconstruction uncertainties.

The ACRIM and PMOD composites diverge because they bridge the ACRIM Gap differently. They rely on conflicting trends from the ERB and ERBE instruments. This suggests that long-term solar trends may be somewhat ambiguous. [86]

Satellites have watched the Sun since 1978. They measure Total Solar Irradiance — the full stream of radiant energy hitting the top of Earth's atmosphere — from Earth-orbiting platforms. [150] The instruments do not last forever. They wear out and must be replaced by new ones. This forces scientists to stitch separate mission records together. They must inter-calibrate the data to bridge gaps and correct for instrument degradation. That stitching is tricky. Inconsistencies in cross-calibration leave the magnitude of secular TSI change uncertain. [64][151][64][149][100][101] We can see the short-term rhythm clearly. TSI varies by 0.05–0.07% over each 11-year solar cycle. But looking beyond that cycle is hard. Combining these experiments is difficult. We cannot yet be confident of any multi-decadal trend in TSI. [150]

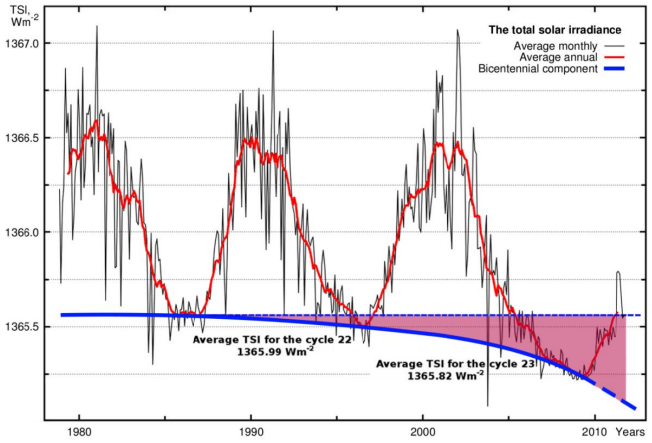


Figure 3.11: The graph displays the total solar irradiance (TSI) from 1978 to 2011, showing daily (black line) and average monthly (red line) variations, with a long-term trend (blue line) representing the bicentennial component. The data reveals a clear 11-year solar cycle, with TSI peaking around 1366.5 W/m^2 and declining to a minimum near 1365.5 W/m^2. The average TSI for solar cycle 22 is 1365.99 W/m^2, while for cycle 23 it is 1365.82 W/m^2, indicating a gradual decrease in solar output over the period. [153]

The satellite era began in late 1978. It gave us the only direct observations of Total Solar Irradiance — the integrated radiant energy arriving from the Sun at the top of Earth's atmosphere. [86] The instruments wear out. Data gaps appear. Scientists must stitch the records together. They disagree on the precise calibration needed to bridge them. This leads to divergent composites. Early instruments like ERB and ACRIM-1 measured higher TSI values than subsequent instruments. The SORCE/TIM launch helped resolve this discrepancy. International calibration workshops established a lower accepted TSI value of approximately 1361 W m^2. [149] We can see the short-term rhythm clearly. TSI varies by as much as 0.05–0.07% over an 11-year solar cycle. This amounts to around 1 W/m^2 at the top of the atmosphere. It reaches only 0.2 W/m^2 at the surface after accounting for geometry and albedo. [150] The critical question for climate science is whether there is a trend in the TSI data beyond this 11-year cycle. Such a trend could have implications for estimates of TSI changes on long timescales. [150] The debate over whether TSI has increased or decreased over the multi-decadal scale remains unresolved. Reconstructions from different groups disagree on the ma

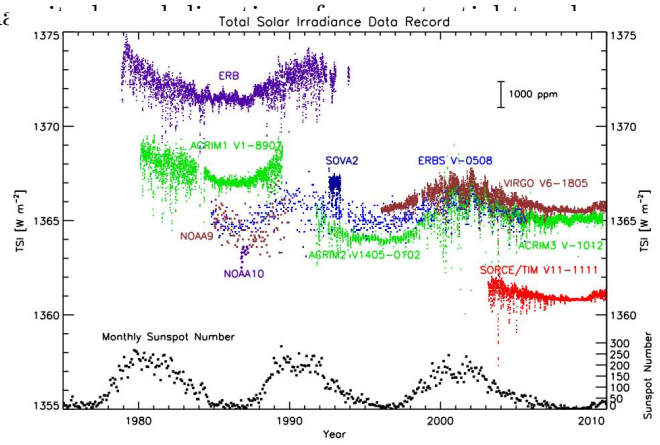


Figure 3.12: The figure displays a time series of total solar irradiance (TSI) measurements from multiple satellite instruments, including ERB, ACRIM1, SOVA2, and SORCE/TIM, plotted against year from 1980 to 2010. The data points, color-coded by instrument, show TSI values in W m^2 on the primary y-axis, with a secondary y-axis showing the monthly sunspot number. The plot illustrates the consistency among diff [149]

3.5 F10.7 and the modern activity index

The F10.7 index tracks the Sun's radio emission at a 10.7 cm wavelength. That signal rises and falls with the amount of magnetically heated plasma in the upper solar atmosphere. Observers have recorded it continuously since February 1947. This steady stream of data lets researchers track solar cycles with high precision. [44]

Radio astronomers measure the Sun's flux density at the 10.7 cm wavelength. This reading tracks solar activity, offering a metric distinct from visible sunspot counts. [130]

The Canadian Solar Radio Monitoring Programme has measured the 10.7 cm Solar Flux every day since 1946. [130] This daily routine yields a completely objective record of solar activity. Clouds cannot block these radio waves, so the measurements continue under virtually all weather conditions. The flux tracks the International Sunspot Number closely, but the link is not a simple straight line. The slope of that relationship shifts as the sunspot number climbs toward 30. The Holland and Vaughn formula captures this complexity. [146][130][130][154][148] It accounts for a base level of about 67 solar flux units. It also adjusts for the varying sensitivity at different activity levels. Even so, the two measures are not perfectly synchronized in time. The 10.7 cm radio flux lags behind the sunspot number by about one month. [130] This delay adds a temporal nuance to the correlation.

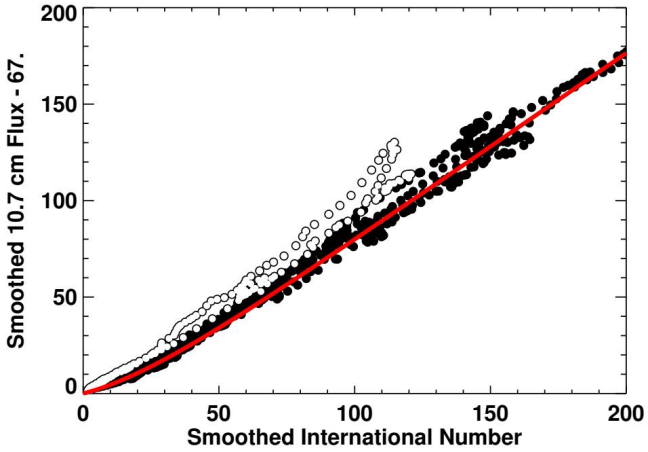


Figure 3.13: This scatter plot shows the relationship between smoothed 10.7 cm radio flux (in solar flux units, S.F.U.) and the smoothed International Sunspot Number from August 1947 to January 2014. Data points are color-coded by observation period: filled black circles represent data prior to cycle 23, and open white circles represent data collected after 1997. A strong positive correlation is evident, with the data points closely following a linear trend line (red) representing the Holland and Vaughn formula, indicating a 99.5% correlation between the two solar activity indices. [130]

The 10.7 cm Solar Flux, measured daily by the Canadian Solar Radio Monitoring Programme since 1946, offers a completely objective measure of solar activity that can be recorded under virtually all weather conditions. [130] Unlike sunspot counts, which rely on visual observation, this radio flux captures disc-integrated emission at 2800 MHz, providing a stable baseline of about 67

solar flux units for a quiet Sun. [130] The relationship between this radio index and the International Sunspot Number is remarkably tight; statistical analysis confirms that the two measures are highly correlated, with a correlation coefficient of r = 0.995. This near-perfect linear alignment demonstrates that F10.7 serves as a robust proxy for overall solar variability, tracking the rise and fall of solar cycles with precision. [155][146][130][156][157][158]

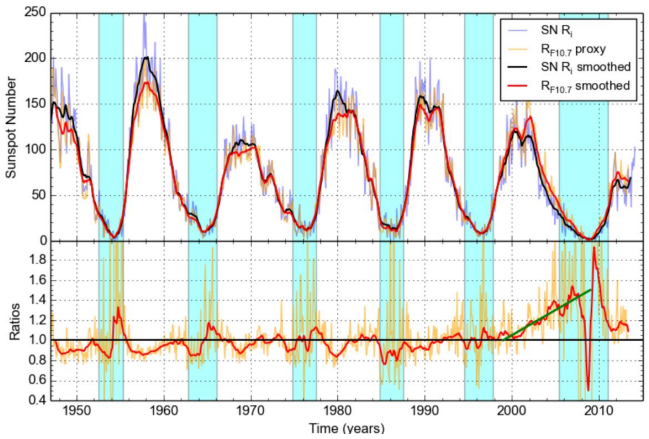


Figure 3.14: This figure plots the sunspot number (SN) R (blue line) and the SN proxy R_F10.7 (red line), derived from the $F_{10.7}$ radio flux, against time from 1950 to 2010. The upper panel shows the raw and smoothed time series, with the smoothed curves computed using the classical 13-month Zürich smoothing function. The lower panel displays the ratio of the proxy to the observed sunspot number, revealing a g [159]

Chapter 4

The Grand Solar Cycles: Zharkova's Two-Wave Dynamo

Zharkova's PCA of synoptic magnetograms reveals two magnetic waves whose beating predicts a Modern Grand Solar Minimum running ~2020–2053.

4.1 The solar background magnetic field

Sunspots and flares are local, intense concentrations of magnetic flux. The solar background magnetic field is the opposite. It is the weak, large-scale field that pervades the whole solar surface. This field exists between and beneath those active regions. We measure it across the full disk. We use synoptic magnetograms from observatories like the Wilcox Solar Observatory. Recent analyses have applied Principal Component Analysis (PCA) — a statistical method that distills complex data into a few dominant patterns — to these low-resolution full-disk measurements. The goal is to derive the dominant eigenvalues that cover the maximum variance of the data. [160] This method identifies eigenvectors, or Principal Components (PCs). These PCs come in pairs. They reflect the main dipole dynamo waves produced by the solar dynamo mechanism. [161] Researchers classified these PCs using symbolic regression based on the Hamiltonian principle. They derived mathematical formulae describing their amplitude and phase variations. [160] The summary curve of these two PCs tells a story. It was derived for cycles 21–23. It was predicted for cycles 24–26. The curve shows a noticeable decrease in predicted average sunspot numbers. This drop is linked to a reduction in the amplitudes. It is also linked to an increase in the phases of the principal components of the solar background magnetic field. [162] Extending this prediction thousands of years backward and forward reveals more. It reveals the occurrence of a grand solar cycle of 350–400 years. This cycle successfully reproduces well-known historical events. These include the Maunder, Wolf, Oort, and Homeric Grand Solar Minima.

To isolate the large-scale solar background field from the chaotic noise of active regions, researchers rely on low-resolution magne-

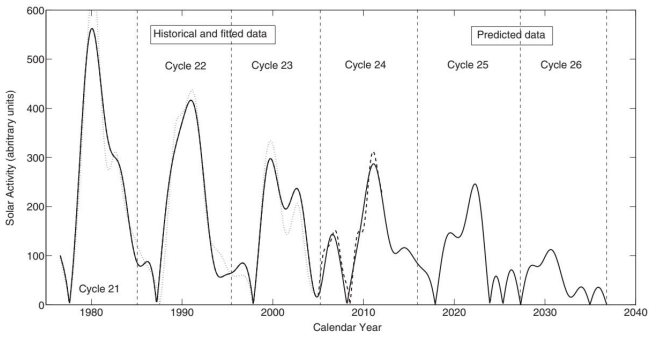


Figure 4.1: This line graph plots solar activity (in arbitrary units) against calendar year from 1970 to 2040, showing the modulus summary principal component for solar cycles 21–26. The solid curve represents the calculated modulus summary PC for cycles 21–23 and its prediction for cycles 24–26, while the dotted curve shows the derived PC from SBMF for cycles 21–23, and the dashed curve shows the SBMF-derived PC for cycle 24. The graph is divided into historical and fitted data (cycles 21–23) and predicted data (cycles 24–26), with vertical dashed lines marking the start of each solar cycle. [162]

tograms from the WSO Babcock solar magnetograph. [163] The Stanford University telescope, equipped with a 22.9m vertical Littrow spectrograph, has provided daily sun-as-a-star integrated light measurements of the mean solar magnetic field since May 1975. [164] The polarity pattern observed in these mean field measurements is essentially identical to the interplanetary magnetic field sector structure seen near Earth, albeit with a four-day lag. [164] These principal components, which come in pairs, are considered a reflection of the main dipole dynamo waves in the solar poloidal magnetic field produced by the dynamo mechanism. [160] By applying symbolic regression based on the Hamiltonian principle, Zharkova et al. derived mathematical formulae describing the amplitude and phase variations of these eigenvectors. [160]

Researchers used the Wilcox Solar Observatory to pull the quiet background field out of the noise. [165] They applied principal component analysis — a statistical tool that breaks complex data into simpler, independent patterns — to full-disk magnetic maps. [11] This method splits the shifting latitudinal waves into eigenvectors. Each eigenvector links to a specific physical process, judged by how much variance it explains. [11] The results show these eigenvectors arrive in distinct pairs. The first pair captures 39% of the observed variance. The second pair accounts for 18%. [11] Together, these four modes explain about 95% of the total magnetic variance. This concentration suggests the solar background field is dominated by a few coherent structures, not random fluctuations. [11][128][166][167][168] These principal components represent the largest symmetric patterns in the field's latitudinal distribution. The model treats the magnetic field as a potential between the photosphere and a source surface. It assumes the field becomes exactly radial at that boundary. [168] Harmonic coefficients are calculated from synoptic maps for every

rotation. The data cadence matches half a Carrington rotation. This is the 27-day period the Sun takes to turn once as seen from Earth. It serves as the standard bookkeeping unit for synoptic solar maps. [169]

The decomposition relies on the assumption that the magnetic field is potential between the photosphere and the source surface, while the field is presumed to be exactly radial at the source surface. [132] This technique allows for the precise extraction of the large-scale magnetic structure from the complex synoptic data. [129] The use of associated Legendre polynomials demonstrates that the solar surface magnetic field can be effectively broken down into its constituent harmonic parts. [132] The harmonic coefficients are derived from the synoptic maps, ensuring that the analysis is grounded in observational data. [169] These models rely on line-of-sight measurements of the photospheric magnetic field, which are mapped up to a hypothetical coronal source surface where the field is assumed to be purely radial. [168] This approach assumes that there are no currents in the corona between the photosphere and the source surface, meaning the curl of the magnetic field is zero. [168] By solving Laplace's equation, the coronal field lines are determined, allowing for the classification of open flux that extends from the photosphere to the source surface. [168] However, the accuracy of these models is affected by several factors, including the assumption of time-invariance of the photospheric boundary and the challenge of resolving polar magnetic fields due to line-of-sight projection.

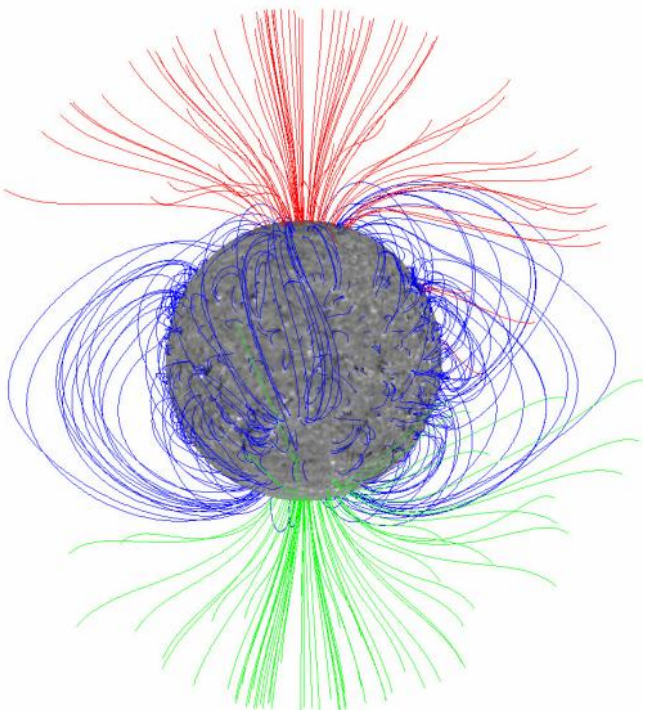


Figure 4.2: This figure displays a Potential Field Source Surface (PFSS) model of the Sun's magnetic field, showing the radial photospheric field strength via grayscale (saturated at 100 G, white for positive, black for negative polarity) and magnetic field lines. Open field lines are color-coded: green for positive polarity, red for negative polarity, and blue for closed field lines. The model illustrates a solar minimum configuration, where the dipole axis is aligned with the rotation axis, resulting in a nearly symmetric distribution of open flux with visible green (positive) and red (negative) field lines extending from opposite poles. The closed field lines (blue) form loops concentrated near the equator, indicating active regions. This configuration contrasts with solar maximum, where the dipole axis is tilted and open flux is asymmetric. [135]

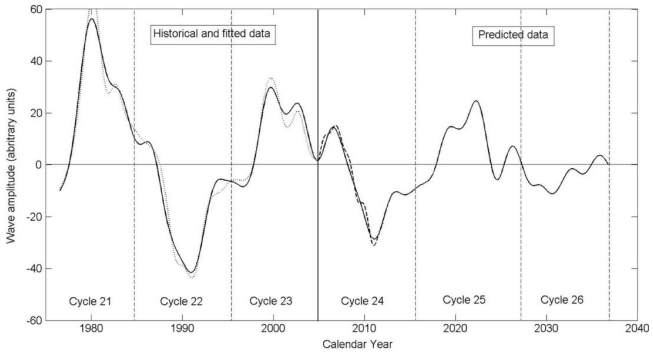


Figure 4.3: The figure displays two plots of solar magnetic field (SBMF) principal components (PCs) over cycles 21–26. The top plot shows historical data (dotted lines) and model fits (solid lines) for cycles 21–23, with predictions for cycles 24–26, where the solid curves represent fits to equations (2) and (3) with over 97% accuracy; vertical lines mark cycle minima at approximately 11-year intervals. The b [160]

4.2 PCA and the two-wave decomposition

Researchers needed to pull the main features out of the solar magnetic data. They applied Principal Component Analysis — a method that finds the dominant patterns in a complex dataset — to low-resolution measurements of the Sun's background magnetic field. [160] This technique performs an orthogonal linear transformation. It squeezes multi-dimensional data into fewer dimensions for easier analysis. The method ensures that the greatest variance in the data projects onto the first coordinate. That first coordinate is the Principal Component. The second Principal Component stands at right angles to the first. It captures the second largest variance in the dataset. [160] The approach does three things at once. It reduces the number of dimensions. It boosts the signal-to-noise ratio. It orthogonalizes the components so each one can be linked to a separate physical process. [160] The team applied PCA to poloidal magnetic field data. These measurements came from the Wilcox Solar Observatory. The data covered cycles 21 through 24. The accuracy was better than 0.5 Gauss. [160] The poloidal field runs north to south. It threads the Sun pole to pole like a bar magnet. The dynamo winds this field into an east-west toroidal field. That toroidal field erupts as sunspots. Then the dynamo rebuilds the poloidal field with reversed polarity each cycle. The analysis calculated the covariance matrix of the magnetic field data. It treated the variance as the eigenvalues of magnetic oscillations. This yielded the eigenvalues of the Sun's own magnetic oscillations. [161] The sets of eigenvalues and eigenvectors came from observed magnetic synoptic maps. The researchers sorted them by the variance of the data contributing to each eigenvector. [11]

This process revealed that the eigenvalues and corresponding eigenvectors come in pairs, with the first two eigenvalues covering 39% of the observed magnetic data variance, the next two covering 18%, and all four pairs covering about 95% of the magnetic data variance. [11] The first pair of two largest eigenvalues,

with the maximum variances of the data corresponding to the two largest eigenvectors, were considered to be the Principal Components. [160] These PCs are considered the main dipole dynamo waves of the solar poloidal magnetic field. [160] Using PCA, researchers managed to derive the eigenvalues of the Sun's own magnetic oscillations, showing clearly at least four noticeable pairs with large eigenvalues covering 96% of the total data variance. [161] The first two highest eigenvalues were used to build eigenvectors for the two principal components, or coherent magnetic waves, corresponding to these eigenvalues. [160] This is equivalent to deriving different wavelengths of white light after it is split in a prism. [150] Now these two magnetic waves can be assigned to unique physical processes. [161] By applying Parker's model for two layers with meridional circulation, researchers derived that these PC waves correspond very closely to the waves generated by dipole magnetic sources. [160] Principal Component Analysis (PCA) of synoptic magnetic maps from cycles 21–24 yields eigenvectors that cover the majority of magnetic data variance. The leading eigenvectors are thus interpreted as coherent dipole dynamo waves, suggesting that the solar poloidal field is dominated by a small number of distinct physical modes. [11][160][161][165][163]

Principal Component Analysis isolates the dominant eigenvalues. These values capture the maximum variance in the solar background magnetic field. [160] The researchers extrapolated these principal components backward in time. They revealed two grand cycles, each lasting 350 years. These long waves sit on top of the familiar 22-year cycles. The reconstruction reproduces historical features, including the Maunder and Dalton minima. [160] This approach confirms a specific mechanism. The interaction of dynamo waves with close frequencies leads to beating effects. These beats are responsible for the grand cycles. The method provides a confident prediction of solar activity on a millennium timescale. [160] The two principal components originate in opposite hemispheres. They travel with an increasing phase shift. This shift defines the active hemisphere for odd and even cycles. [160] This stability reassures us about the health of the dynamo machine. Variations in wave frequencies cause a beating effect. This effect produces grand cycles and grand minima. They occur every 350–400 years. [171]

Converting the eigenvector summary curve into a modulus summary curve is necessary to detect the 11-year solar cycle, as the raw eigenvector data alone does not clearly resolve this periodicity without such transformation. This mathematical step ensures that the oscillatory nature of the magnetic waves is properly captured, allowing the superposition of these principal components

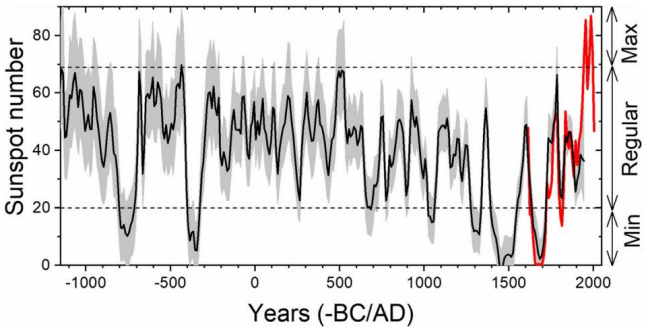


Figure 4.4: The graph displays a reconstruction of solar activity over the past 3000 years, plotting sunspot number against time in years (BC/AD). It shows persistent deviations from typical solar cycle amplitudes, with shaded regions indicating grand maxima (above the dashed upper line) and grand minima (below the dashed lower line). The plot highlights the Maunder Minimum (1645–1715) and Dalton Minimum (1790–1830) as periods of low activity, followed by a rise to the modern maximum, with solar cycles 24 and 25 appearing below average. The data reveals no regular pattern in the occurrence of extreme solar activity phases. [175]

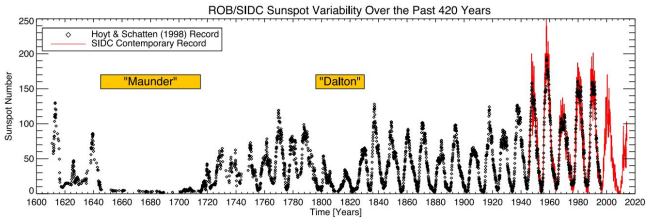


Figure 4.5: This line plot displays the total sunspot number from 1600 to 2020, showing solar activity over the past 420 years. The data, sourced from WDC-SILSO, reveals a dominant 11-year cycle and two extended periods of low activity labeled "Maunder" (1645–1715) and "Dalton" (1790–1830), representing grand minima. The plot compares the Huyt & Schatten historical record (black dots) with the SIDC contemporary record (red line), highlighting the long-term variability of solar output. [174]

to reconstruct the historical sunspot envelope and predict future solar activity minima. [132][11][166][160][171]

Solar activity does not pulse from a single oscillator. The data decompose into multiple waves, each rising from a distinct magnetic source deep inside the Sun. [172] One of these waves is a quadruple mode. It originates in the inner layer at the bottom of the Solar Convective Zone. That zone is the Sun's outer third by radius. Here, energy moves outward through churning convection rather than by radiation. The dynamo operates at this base. Theoretical evaluations indicate that this quadruple wave accounts for the centennial oscillations seen in the summary curve. [173] This mechanism helps restore historical features that dipole-only models missed. It captures the Dalton minimum at the beginning of the nineteenth century. It also captures another Gleissberg minimum at the start of the twentieth century. [173] The dipole and quadruple waves do not just coexist. They interfere. This beating effect naturally produces an envelope wave. Its period is approximately 100 years. This aligns with the observed centennial

cycle. [161]

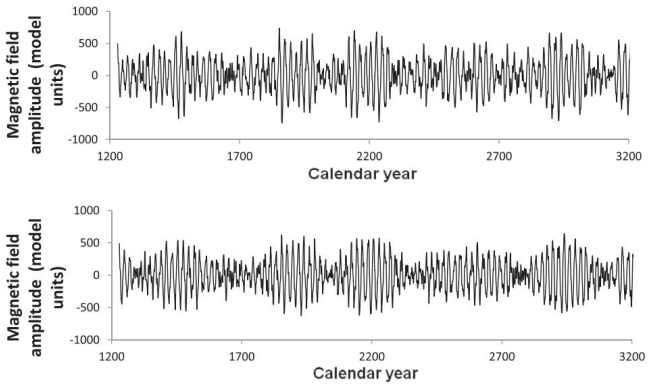


Figure 4.6: The figure displays two time-series plots of magnetic field amplitude (in model units) over a millennium (1200–3200 calendar years), comparing a model derived from dipolar magnetic fields (bottom plot) with an updated model incorporating both dipolar and quadrupolar magnetic field effects (top plot). Both curves exhibit oscillatory behavior with varying amplitude and frequency, showing that the in [173]

4.3 Isotope validation

Delaygue and Bard looked at Beryllium-10 records from Central Antarctica, specifically at the South Pole and Dome Fuji stations. [67] They covered the last millennium to see how ice-core deposition relates to production rates. Radiocarbon signals get smeared by the global carbon cycle. Beryllium-10 offers a more direct proxy. As an aerosol-borne isotope, it leaves the atmosphere relatively fast, within a few years. It then settles into natural archives like polar ice sheets. Because of this short atmospheric residence time, Beryllium-10 directly reflects cosmic ray intensity variations. There is almost no attenuation. The delay is only 1–2 years. [56]

Radiocarbon suffers from a different problem. The global carbon cycle smears the signal. It also delays it. The atmospheric concentration of ^{14}C does not jump in step with production. It lags behind. This phase lag measures how far the recorded signal trails the cause. We express it as a fraction of a cycle, where 360° is the whole thing. The lag ranges between 0 and 90°. Shorter periods suffer larger delays. For centennial variations, the lag is approximately 45°. That means atmospheric ^{14}C concentration lags production by roughly 12 years. [67] This specific lag aligns with the delay estimated by Bard et al. between the South Pole ^{10}Be record and the IntCal04 ^{14}C record. [67] Some models predict even larger lags. They point to stratospheric transfer times. But we lack adequate observations to fully validate these predictions. [67] The uncertainty in reconstructed ^{14}C due to carbon inventory remains a critical factor. Different box models show varying attenuations and time lags. These differences complicate the direct interpretation of high-frequency solar signals in tree-ring data. [176]

Ice cores trap beryllium-10 (^{10}Be), a rare isotope forged when galactic cosmic rays smash into atmospheric oxygen and nitrogen. [177] The solar wind's magnetic field pushes those cosmic rays away. So when the Sun is active, fewer rays reach Earth, and less ^{10}Be forms. The ice records this inverse relationship: high sunspot numbers mean low ^{10}Be concentrations. [177] To check solar models during the Maunder Minimum (1645–1715), scientists compared predictions with ^{10}Be data from two distant ice cores, Dye3 and NGRIP, separated by more than 1000 km. [178] The NGRIP record shows an inverted phase relation during that grand minimum. Earlier studies did not use this feature. Its presence suggests the ^{10}Be cycling was a genuine solar modulation effect, not a terrestrial artifact. [178][177][179] This agreement between spatially separated proxies and sunspot reconstructions supports using cosmogenic isotopes to hindcast solar variability and validate dynamo models. [178][177][179] Yet discrepancies remain. Simulated ^{14} levels deviate from IntCal04 data by several percent in specific centuries. These errors often stem from anomalies in the South Pole or Dome Fuji ^{10} records. [67]

Cosmogenic isotopes such as beryllium-10 and carbon-14 serve as proxies for past cosmic-ray flux, offering a record that extends far beyond the era of neutron monitors. [148] Both the monitors and the isotopes are counting the same thing. When a galactic cosmic ray strikes the upper atmosphere it shatters air nuclei into a shower of secondary particles, mostly neutrons; ground-based neutron monitors have counted that secondary flux directly since the 1950s, while those same neutrons produce ^{14}C on striking nitrogen and ^{10}Be by spalling nitrogen and oxygen. The isotopes are therefore the pre-instrumental extension of the neutron-monitor record. Consequently, extracting the solar component from the ^{14}C record becomes significantly more difficult for the modern period, as the anthropogenic trend competes with and often overwhelms the subtle variations driven by solar activity. Thus, the isotope validation section concludes that the two-wave model's robustness is best confirmed in the pre-industrial record, where anthropogenic noise is absent, while the modern era requires careful deconvolution of fossil-fuel-induced isotopic shifts to assess the model's accuracy.

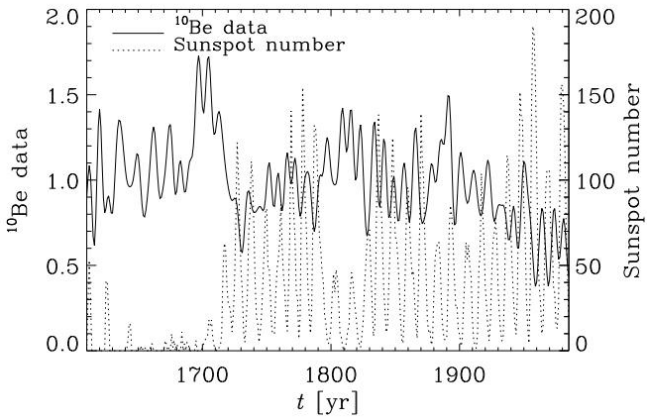


Figure 4.7: The figure displays a time series plot comparing beryllium-10 (^{10}Be) data (solid line, left y-axis in units of 10^{12}) with sunspot number (dotted line, right y-axis) over the period 1700–1985 years before present. The ^{10}Be data, derived from a 300 m shallow core at Dye 3, Greenland, shows high-frequency variability with a general trend of decreasing concentration from the early 1700s to the late 1 [179]

4.4 The 2020–2053 Modern Grand Solar Minimum prediction

The double-dynamo analysis suggests the Sun slipped into a modern Grand Solar Minimum in 2020. This quiet phase, marked by reduced activity, may stretch on until 2053. Other methods point to the same outcome. Velasco Herrera and colleagues applied a Bayesian algorithm — a statistical tool that updates probabilities as new data arrives — to averaged sunspot numbers. Their work also places the modern Grand Solar Minimum within cycles 25 through 27. [166][180][181] Further confirmation came from Kitiashvili and Obridko et al. They used the same WSO synoptic magnetic field data to extract spectra of the zonal harmonics in the solar background magnetic field. Feeding these into 3D solar dynamo models, they saw the same approach toward a Grand Solar Minimum. The current quiet Sun stems from a weakened magnetic field. This reduction arises when the two dynamo magnetic waves interfere with each other, cancelling out rather than reinforcing one another.

The two waves drift in and out of step because they run at slightly different frequencies. When they fall out of phase, the crest of one meets the trough of the other. They largely cancel each other out. The combined field becomes far weaker than either wave alone. This is destructive interference — the same physics that creates silence where two sound waves overlap. During this Grand Solar Minimum, solar irradiance — the total power of sunlight reaching Earth — will drop by about 3 W/m^2. That is a reduction of 0.22%. [180] This dip works against another trend. Orbital solar inertial motion effects tend to push irradiance up. The two forces pull in opposite directions. Their interplay defines the thermal baseline for the coming decades. [180]

Statistical analysis of past grand maxima suggests a 1-in-12 probability of a Maunder-like grand minimum occurring within

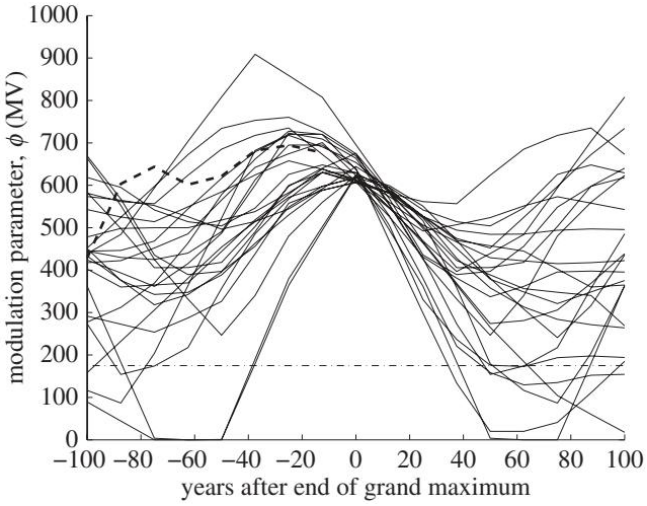


Figure 4.8: The chart displays a superposed epoch analysis of the heliospheric modulation parameter (in MV) over 9000 years, with 24 individual case trajectories aligned at t = 0—the point when drops below 600 MV, marking the end of a grand solar maximum. Each line represents a separate historical event, showing a general decline in following the peak, with the thick dashed line highlighting the recent 100-year trend. A horizontal dot-dashed line at 175 MV indicates a reference level from prior analysis, and the convergence of trajectories around t = 0 reveals a consistent pattern in the post-maximum decay of solar modulation. [188]

50 years. This estimate derives from a superposed epoch analysis of the modulation parameter at the end of the previous grand solar maxima in the last 9300 years, based on the composite reconstruction of the modulation parameter from Steinhilber et al.. [182][181][166][156][183] Furthermore, Owens et al. created a data set for solar wind parameters dating back to 1617 to investigate Maunder minimum conditions and find the most probable coronal magnetic field configuration for this period. This configuration could be used for any past or future grand minima. [182]

Predicting the amplitude of solar cycles remains highly uncertain, with models for Cycle 24 showing wide disagreement. This uncertainty stems from the fact that cycle prediction is a fairly model-dependent affair, as evidenced by contradictory forecasts for Solar Cycle 24. [184][185][186][181] While Dikpati et al. predicted it would be the strongest cycle in fifty years, Choudhuri et al. concluded it would be the weakest in a century. [185] These divergent outcomes highlight that there are still many uncertainties in solar dynamo models, making it worthwhile to analyze the physical basis of solar cycle prediction carefully rather than having too much faith in predictions from any particular model. [131] The community-wide panels convened to construct consensus opinions on upcoming cycles often receive a broad range of submissions that cover almost all potential physically reasonable outcomes. [186] Consequently, the strength of every solar cycle a few years before its onset cannot be determined with precision, demonstrating the inherent difficulty in forecasting solar activity. Consequently, the modest irradiance decline predicted for the upcoming Modern Grand Solar Minimum implies a limited direct radiative cooling effect, consistent with the model results assuming small TSI variation.

Simple energy-balance calculations link changes in Total Solar Irradiance — the total power output of the Sun — to Earth's effective temperature. [153] The predicted drop in TSI is about 3 W/m^2, or 0.22%. Spread over the spinning globe and corrected for reflection, this yields a direct radiative cooling of only one or two tenths of a degree. The effect is real, but modest. That is why this book's argument does not rest on irradiance arithmetic alone. The chapters that follow lay out the amplifiers. Chapter 6 covers cosmic-ray cloud seeding. Chapter 7 covers volcanic coupling. These mechanisms turn a two-tenths-of-a-degree nudge into Little Ice Age winters. Wherever this book quotes a larger cooling, it is a claim about that amplified response, not about the bare radiative term.

Solar activity has been falling since cycle 21. That decline tracks the weakening of the solar background magnetic field, a sign that the grand solar minimum — GSM — is approaching. [181] Other researchers have confirmed these predictions for cycles 25 through 27. [181] We can test such forecasts against a long view. That view combines the sunspot number record from the last 400 years with paleoreconstructions spanning the Holocene. Together, they provide critical observational constraints for dynamo models. [119]

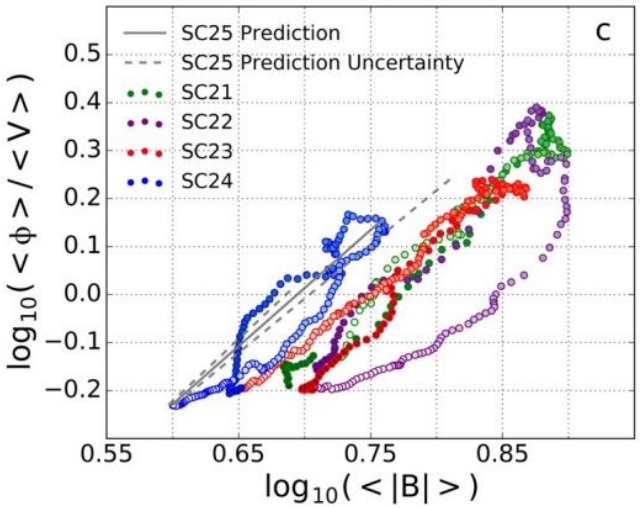


Figure 4.9: >) on the x-axis and $\log_{10}(<>/<V>)$ on the y-axis, showing data for solar cycles SC21 through SC24 and a prediction for SC25. The data points for each cycle are color-coded, with SC25 represented by a gray solid line and its uncertainty by a gray dashed line, based on a predicted maximum magnetic field strength of B_Max = 5.74 ś 0.80. The plot illustrates a transition toward a potential modern secular minimum, with SC24 and the SC25 prediction aligning with lower activity levels. [182]

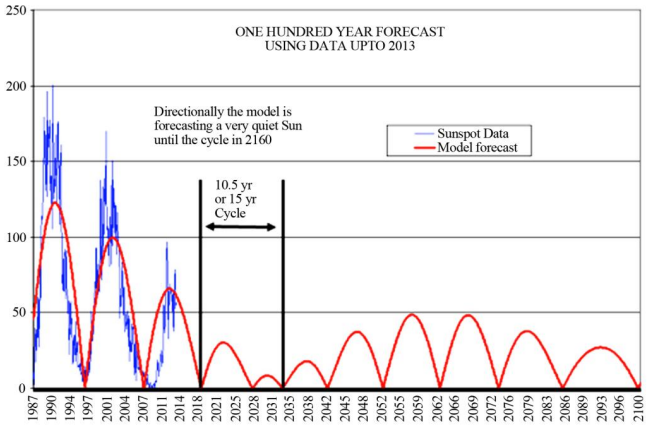


Figure 4.10: The figure displays a time-series plot comparing monthly sunspot numbers from 1987 to 2013 (blue line) against a model forecast of the absolute value of solar activity (red line) extending to 2100. The x-axis spans years from 1987 to 2100, with the y-axis representing sunspot numbers up to 250. The model forecast, derived using data up to 2013, predicts a prolonged period of low solar activity, in [187]

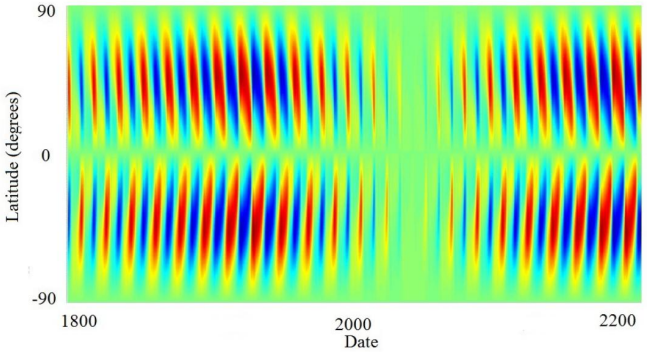


Figure 4.11: This figure displays a butterfly diagram illustrating the simulated toroidal magnetic field over time and latitude, based on a double layer dynamo model. The top plot covers the period from 1800 to 2200, showing the evolution of magnetic field strength (indicated by color, with red/yellow representing high intensity and blue representing low intensity) at different latitudes, with distinct bands o [189]

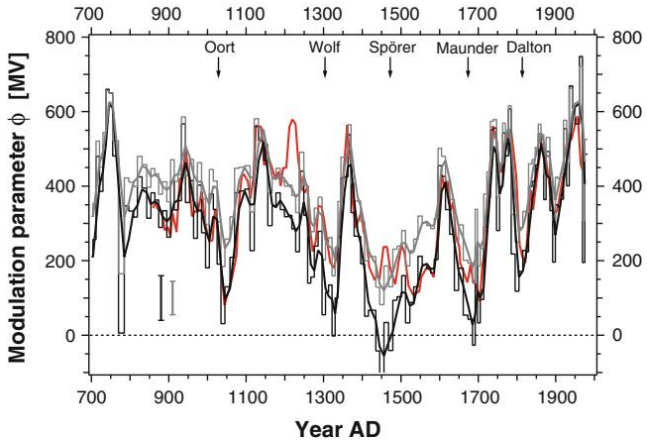


Figure 4.12: The figure displays the solar modulation parameter reconstructed from Antarctic ^{10}Be data using a ^{14}C-adjusted chronology, plotted against calendar year AD from 700 to 1900. It compares two production models: a purely local production (grey lines) and a model with 70% contribution from middle latitudes (black lines), with bold lines representing 1-2-1 box-filtered smoothed versions for compariso [190]

4.5 Flare physics — the same magnetic field

To grasp the magnetic architecture behind long-term solar variability, we must anchor our view in the physics of the solar dynamo. This engine generates the 11-year Schwabe cycle. [44] The classical Parker model, proposed in 1955, shows how this cycle arises from a self-exciting loop of magnetic field generation. [128] Large-scale circulation patterns also matter. Ribes and Mein discovered azimuthal rolls in 1984. These are giant convective cells wrapped around the Sun's rotation axis. They act like rolling bands of fluid circling the globe parallel to the equator. They modulate surface rotation. They appear to regulate the internal shear that drives the dynamo.

The Babcock–Leighton models show how the Sun's internal plumbing sets its rhythm. Meridional circulation — the slow, steady drift of plasma from the equator toward the poles — moves magnetic flux from the surface down to the tachocline. That layer — a thin shear zone at the base of the convection zone, where the Sun's rotation shifts from differential above to near-uniform below — winds up the toroidal field. [185][191] The large-scale poloidal field is not born deep inside. It regenerates at the surface, from the decay of tilted sunspot pairs. Those tilted bipolar regions generate the field, which the circulation then carries poleward and downward. This advective process is the heart of the flux transport dynamo framework. The speed of that flow sets the dynamo period. A direct link exists between flow speed and cycle length. [142] Models suggest that random fluctuations in the alpha-effect cannot trigger grand minima. A strong decrease in meridional circulation can. [191] The variability of this transport mechanism provides the physical basis for the irregularities seen in the solar record. It connects the large-scale dynamo operation to the potential for Maunder-like grand minima. [191]

Cosmogenic isotope records show that grand minima do not arrive on a fixed schedule. Their irregular timing suggests that chance plays a necessary role in the dynamo. Models must include stochastic drivers to reproduce this long-term variability. [192][193][194][195][196] The evidence points to random fluctuations in the dynamo's driving parameters. These fluctuations generate both secular trends and extreme activity levels. For example, simulations of the fully non-linear flux-transport dynamo include random noise in two places. They vary the angular momentum transport process. They also vary the Babcock-Leighton mechanism. These random inputs produce periods that look like grand minima and maxima. [194] This result supports a specific view of solar behavior. It suggests that grand minima are a special

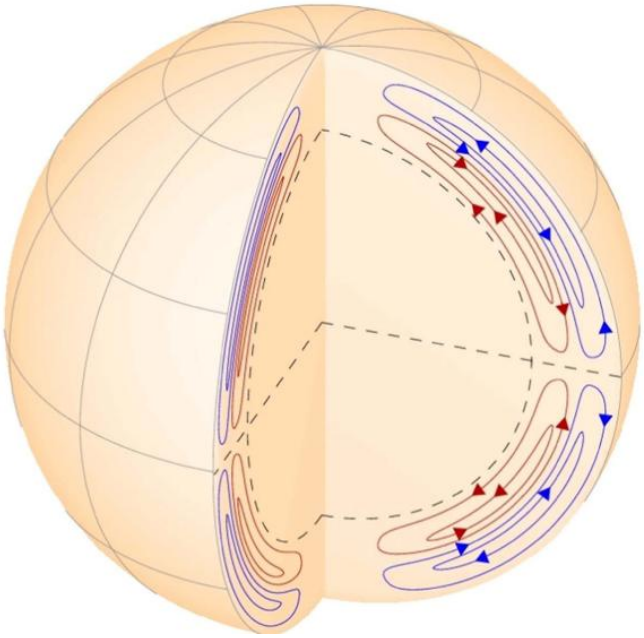


Figure 4.13: This figure illustrates a schematic model of the solar dynamo, depicting two opposing meridional circulation cells within the Sun's interior. The model, derived from HMI/SDO observations, shows flow patterns represented by blue and red arrows indicating upward and downward motions, respectively, along with nested streamlines illustrating the circulation. The opposing flows in the northern and southern hemispheres suggest a mechanism for generating the solar magnetic cycle, with the dashed lines indicating the solar equator and the grid representing latitude and longitude. [160]

state of the solar dynamo. They are distinct from normal or high activity phases. Chaotic or random processes within the solar interior drive them. [197] The same studies use a different tool to look at the atmosphere. They solve the time-dependent Fokker–Planck equation. This equation tracks how a whole population of particles spreads out in energy and direction. It accounts for repeated small collisions that nudge the particles, rather than following any single one. The solution reveals how electron beams precipitate into the solar atmosphere. It shows that magnetic convergence significantly alters energy deposition.

The flare work fits into a single research programme. The same magnetic fields that predict grand minima also control how deeply flares heat the Sun. We see this link in the 23 July 2002 flare. Sharp spikes in hard X-ray emissions — HXR, the high-energy photons that penetrate deep into the solar atmosphere — track changes in the photospheric magnetic field. This happens especially near the apparent magnetic neutral line. [198] A cross-correlation analysis shows a positive correlation of 0.5–0.6 between those magnetic shifts and the HXR light curves. The time lag stays under 1–2 minutes across all energy bands. [199] The magnetic flux changes in irreversible steps. It settles into a new steady state and never returns to its preflare values. This shows that restructuring the magnetic field starts the flare. [198] Later, we looked at the 2006 December 14 X-class flare. We used data from GONG, Hinode, and RHESSI. We saw extended ribbon emission moving through umbrae and penumbrae in both hemispheres. Energy deposited at the photosphere covered a smaller area than the overlying chromosphere. [200] These measurements revealed asymmetries in hard X-ray source intensity and size

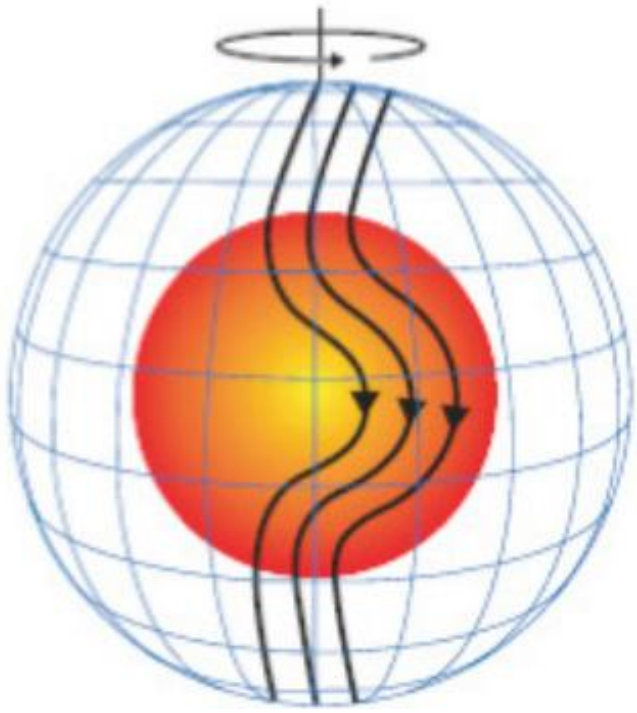


Figure 4.14: This schematic diagram illustrates the solar dynamo process, showing the Sun's internal structure with a red radiative core and a blue mesh representing the photosphere, separated by the convection zone. It depicts the generation of magnetic fields through differential rotation shearing poloidal field lines into toroidal fields at the base of the convection zone, followed by the buoyant rise of magnetic flux tubes that emerge at the surface as tilted bipolar regions. The diagram further shows the poleward transport of magnetic flux by meridional flow, which reverses the polar magnetic fields and returns some flux to the base of the convection zone, completing the cycle. [135]

between the Northern and Southern ribbons. They also showed strong impulsive changes in longitudinal magnetic flux at magnetic reversals. [200]

The 23 July 2002 flare offers a clear case study. We can watch the magnetic field shift in real time. Hard X-ray (HXR) emissions — the high-energy bursts from accelerated electrons — spike at the same moment. The timing is tight. The magnetic field changes in the photosphere — the visible surface layer — move in lockstep with the radiation. [198] The total magnetic flux shifted by about 1.2×10^{21} Mx during the event. This change concentrated near the apparent magnetic neutral line (AMNL) — the boundary where opposite magnetic polarities meet. The shift was not temporary. The field did not snap back to its old shape. It settled into a new, steady state. This step-like change matches theory. Models suggest that irreversible magnetic restructuring triggers the flare. [198] Cross-correlation analysis confirms the link. It measures how closely two signals follow each other. The correlation between magnetic variations at the AMNL and HXR light curves is positive, ranging from 0.5 to 0.6. The lag is short. The magnetic shift leads the radiation by no more than 1–2 minutes across all energy bands. [199] Complex wave patterns matter here. Quadruple and sextuple magnetic field components appear in the data. These interacting waves may create the conditions for magnetic reconnection. Reconnection releases the energy that accelerates particles. This mechanism could explain how the flare starts.

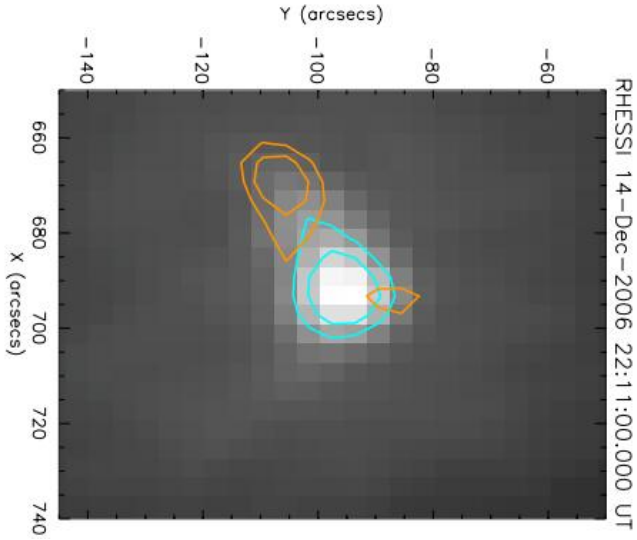


Figure 4.15: This image displays a time series of hard X-ray (HXR) solar flare observations from 22:08–22:15 UT on 14 December 2006, captured by RHESSI. The grayscale background represents 20–30 keV emission, with cyan contours outlining regions at 50% and 70% of the peak intensity. Overlaid orange contours indicate 40–100 keV emission at the same relative intensity levels, revealing the spatial distribution and energy-dependent structure of the flare emission across the solar surface. [200]

Chapter 5

The Sun's Inertial Motion

The Sun's barycentric orbit under Jupiter–Saturn–Uranus–Neptune forcing modulates insolation on decadal-to-centennial timescales via the Jose cycle and longer planetary-resonance beats.

5.1 How exoplanets reveal stellar wobble

We usually picture the Sun as a fixed anchor. It is not. The giant planets tug on it, and the star wobbles in response. [180] To map this motion, researchers build a mathematical model of the Sun–Jupiter–Saturn–Uranus–Neptune system. They use a semi-analytical approach, constructing an averaged Hamiltonian — a function that encodes the total energy and momentum of the system. [201] The Hori–Deprit method then smooths this Hamiltonian. It strips away short-period perturbations, the rapid jitters caused by planets lining up. These fast oscillations depend on mean longitude, the angular position of a planet along its orbit. Removing them clears the noise. The equations of motion become simpler. This allows for larger integration time steps, meaning the simulation can leap forward in time without losing accuracy. [202] The exclusion of short-period terms confirms a key point: we can isolate the long-term secular evolution of the system. We can separate the slow drift from the immediate gravitational tugs of individual planetary conjunctions. [201] The semi-analytical theory shows that the Sun's motion around the solar system barycentre — the center of mass of the whole system — follows stable, long-period cycles. One such cycle is the Jose cycle. It modulates the Sun–Earth distance on decadal-to-centennial timescales.

To handle the heavy algebra, researchers turn to computer algebra systems like Piranha. These tools perform the complex symbolic manipulations needed for high-order Hamiltonian expansions. The automation ensures that generating functions and averaged Hamiltonians are derived without error. This clean foundation enables numerical integration via methods such as the Everhart method. [203][203][201] The principle holds for our own Solar System. [204] The Sun does not sit still. It orbits the barycentre — the center of mass of the entire system. [205] The giant planets

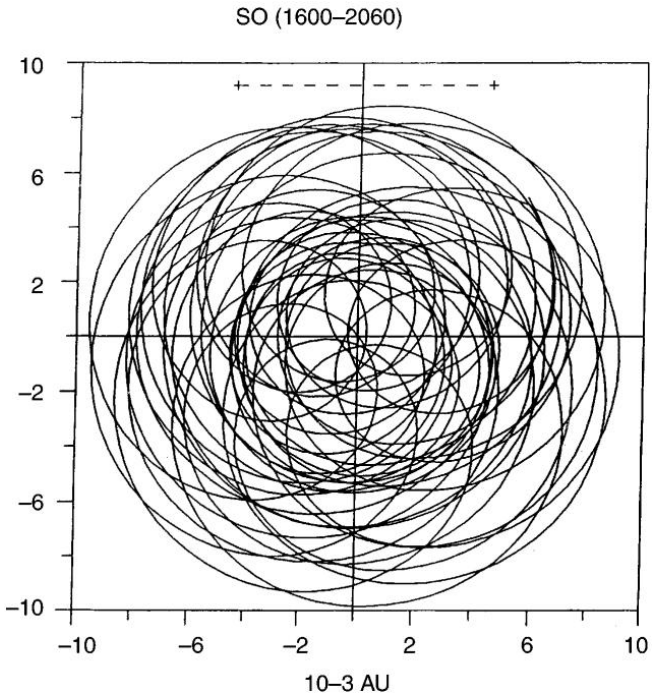


Figure 5.1: The figure displays a polar plot of the Sun's orbital path around the solar system barycenter from 1600 to 2060, with coordinates in units of 10^3 AU. The plot shows a complex, nested pattern of overlapping loops, indicating the Sun's motion due to gravitational interactions with the planets, primarily Jupiter and Saturn. A dashed horizontal line at the top represents the Sun's diameter, providing a scale reference for the orbital deviations. [201]

dominate this motion. Jupiter, Saturn, Uranus, and Neptune pull the Sun in complex paths. [201] Their combined gravity drives the star's wobble. [205] To verify these paths, scientists use numerical integration. [203] They compare different mathematical methods to ensure accuracy over long timescales. [202] One study compared the 15th-order Everhart method with the 11th-order Runge–Kutta method. [202] They integrated the equations of motion for the four giant planets. [202] This large motion affects the distance between the Sun and Earth. [172] Together, they shape the climate record.

The semi-analytical theory, constructed via the Hori–Deprit averaging method and Lie transformations, provides a framework for deriving averaged equations of motion from the Hamiltonian expanded in powers of planetary masses. However, the theory may be unacceptable near mean-motion resonances due to extreme growth in Hamiltonian terms, a limitation that suggests the need for complementary numerical simulations using symplectic integrators like NBI in such cases. Consequently, a hybrid strategy that combines semi-analytical insights with targeted numerical verification is likely to offer the most robust characterization of system dynamics. [203] Consequently, for systems exhibiting orbital flips or strong resonances, numerical simulations using symplectic integrators are required to complement analytical results when studying phenomena like orbital flips. The real evolution of a system, including the actual presence of flips, can only be studied using numerical methods that preserve the analytical properties of functions without accumulating the rounding errors

typical of purely numerical theories. [203][70]

However, this technique possesses an inherent geometric limitation: because the orbital inclination of the planetary system relative to our line of sight is generally unknown, the measured velocity amplitude yields only a lower limit on the planetary mass, expressed as $\sin$. For instance, studies of flaring stars have shown that while criteria like the Reduced Proper Motion (RUWE) can help filter out obvious binaries, they are less sensitive to close companions with semi-major axes below 0.1 astronomical units, meaning that some level of uncertainty regarding the true nature of the companion remains. [206] This limitation does not carry over when we turn the same tool inward to our own Sun: its motion about the solar system's centre of mass is computed directly from the known planetary masses and orbits, with no inclination ambiguity and no M sin i lower bound. [207] Just as we detect the wobble of distant stars to infer the presence of unseen planets, we can calculate the Sun's motion around the Solar System barycentre due to the gravitational influence of the giant planets. [172]

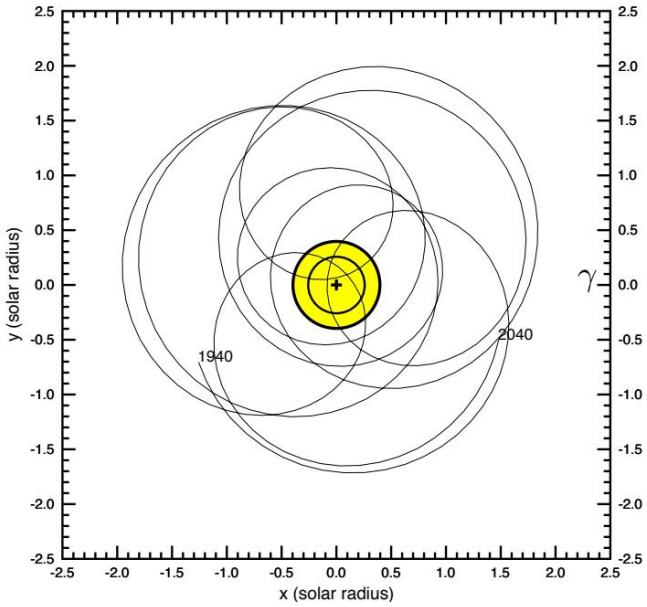


Figure 5.2: This figure plots the orbit of the Sun's center relative to the solar system barycenter (SSB) in the ecliptic plane from 1940 to 2040, with coordinates in solar radii. The Sun is represented by a yellow circle at the origin, and its path traces multiple overlapping loops around the SSB, indicating complex orbital motion. A larger concentric circle at radius 0.65 solar radii marks the boundary with [208]

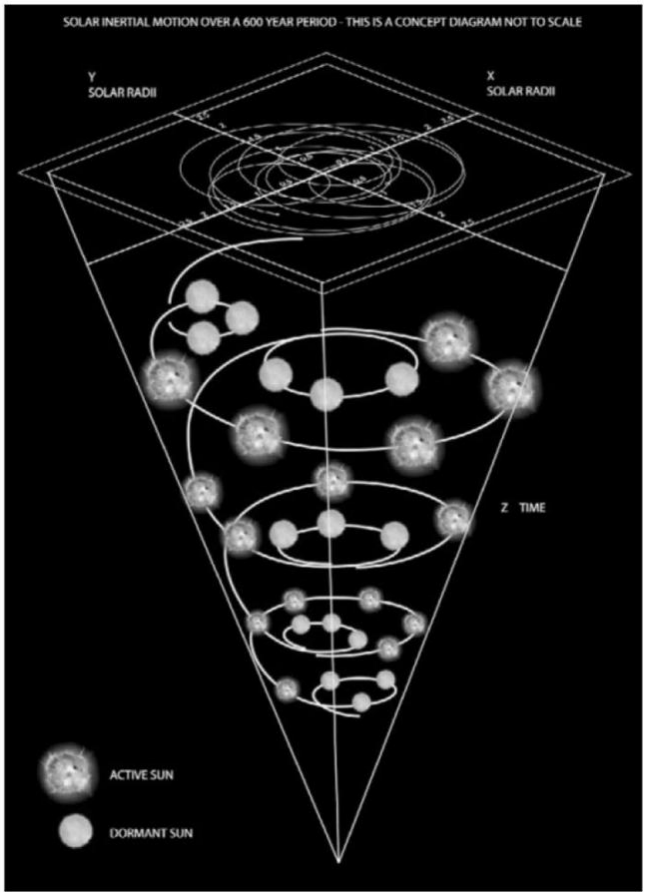


Figure 5.3: This concept diagram illustrates the Sun's inertial motion over a 600-year period, showing its trajectory around the solar system barycenter as a series of expanding spiral orbits. The plot uses a three-dimensional coordinate system with X, Y, and Z (time) axes, where the Sun's path forms a conical structure composed of three complete 179-year cycles, each containing approximately eight 22-year so [209]

5.2 Solar inertial motion (SIM)

The Sun does not sit still at the center of the System. It wobbles around the barycentre — the shared center of mass for all the planets and the star. That path is not a smooth ellipse. Jupiter and Saturn pull hard on the Sun. Their gravity twists the solar trajectory into a complex shape. [180] This motion creates specific patterns of solar acceleration. Those patterns may have profound implications for solar activity. [205] We can measure the normal component of that acceleration, denoted as . The data shows exceptional increases at specific epochs. One explanation points to an inversion of angular momentum. This happens when the Sun's orbit becomes retrograde. [205] In that moment, the angular momentum vector, L, aligns with the planetary acceleration direction. The vector points in the opposite sense. Thus, represents the maximum projection of L in the solar acceleration direction. [205] These changes are driven by orbital libration. They are not caused by an impulsive change in planetary acceleration. The planetary acceleration remains near the ecliptical plane. [205]

However, these features are significant because they indicate that at times of angular momentum inversions, L is almost anti-

parallel to the acceleration vector, with the angle between them oscillating between approximately 130 and 179 degrees. Crucially, these radial impulses never occurred before 1632 during the last millennium, even though similar planetary configurations did happen, demonstrating that these impulses arise only at epochs of orbital inversions and are responsible for particular phenomena. The periods of inversion were characterized by a unique geometry of planetary acceleration with respect to the Sun-barycentre system, where the radial component of solar acceleration had an exceptional magnitude and the L vector was anti-parallel to acceleration. [205] However, further investigation is required to determine whether this relationship is causal or merely coincidental.

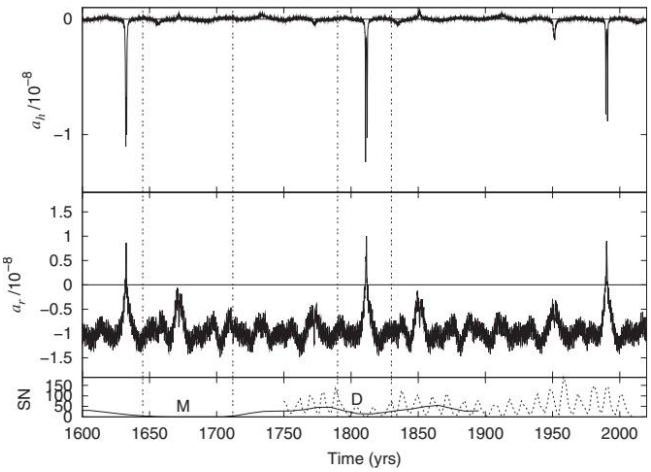


Figure 5.4: The chart displays three time-series plots from 1600 to 2000 CE: the normal acceleration a_h (top), radial acceleration a_r (middle), and sunspot number (SN, bottom). The sunspot number is shown as a solid line from a ^{14}C reconstruction (Solanki et al., 2004) and a dashed line representing observed-smoothed data. Vertical dashed lines mark the Maunder (M) and Dalton (D) Minima. Impulses in both acceleration components are clearly visible during the Maunder Minimum, the Dalton Minimum, and at the peak of solar cycle 22. The accelerations are in units of 10^{-8} astronomical units per day squared, with the sunspot number scaled from 0 to 1500. [212]

The new ephemeris — a precise map of planetary positions — shows that orbital inversions do not march to a steady drum. They cluster in irregular groups of three to nine events, defying the strict rhythm of the Jose-period. [210] These retrograde intervals follow a bimillennial cycle, averaging roughly 2.2 kyr. Yet within those long stretches, the inversions do not arrive at regular Jose-period intervals. [210] Some gaps are short, about 140 yr. For instance, the span between 2168 and 2308 shows this pattern, as does the interval between -2458 and -2318. [210] The Jose-period starting at -2458 holds firm, with another inversion at -2279. But an intermediate lapse occurs at -2318. This event arrives 39.26 yr before the expected inversion at -2279. [210] Before the retrograde interval of -2994, all inversions within each bimillennial cycle did occur at the Jose-period. [210] The reason for these shorter periods is straightforward. The Jose-period tracks the Uranus–Neptune synodic period of ˜171 yr. At each

such interval, Jupiter tends to quasi-conjoin with the other giants. [210] However, these quasi-alignments do not always trigger solar retrograde motion. The ever-changing planetary positions and velocities at these moments often prevent the effect. [210]

The Sun does not move in a smooth circle around the barycentre — the shared center of mass for the whole solar system. Its path contains sharp radial impulses, sudden kicks in speed. These impulses line up with major periods of reduced solar activity. [205] One such impulse marks the start of the Maunder Minimum. Another begins the Dalton Minimum. This alignment confirms a phenomenological link between the giant planets' barycentric motion and long-term solar cycle behavior. [70][205] The most recent impulse coincided with the peak of cycle 22. It preceded the current prolonged minimum of solar activity. Observational data show an apparent phase synchronization between sunspot numbers and the inclination of the orbital plane of the solar system barycenter. The correlation coefficients shift from 0.76 to -0.52 after the radial impulse. [205]

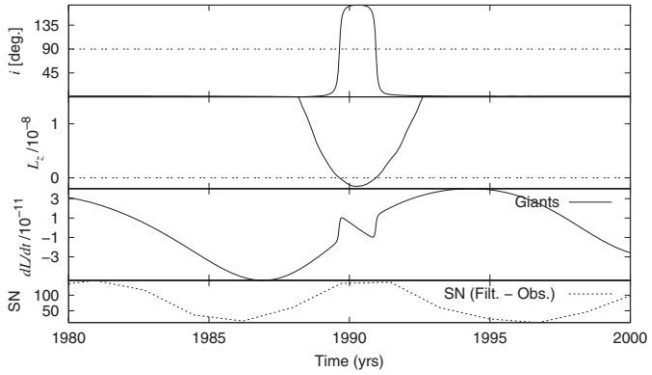


Figure 5.5: The chart displays four time series from 1980 to 2000: OSO inclination (i) in degrees, the Lz component of angular momentum in 10^8 AU^2Mday^1, the rate of change of angular momentum (dL/dt) for giant planets in 10^{11} AU^2Mday^2, and the sunspot number (SN) in a filtered-observed form. The inclination i exceeds 90° around 1990, indicating retrograde motion. A strong anticorrelation is evident between dL/dt and SN, with dL/dt peaking during the sunspot minimum of cycle 22, which is prolonged compared to previous cycles. [212]

Analysis of the Sun's barycentric dynamics reveals distinct impulsive events that correlate with major shifts in solar activity. [205] Specifically, a radial impulse in the Sun's velocity occurred at the maximum of Solar Cycle 22, before the present extended minimum. This timing is significant because it coincides with a violation of the Gleissberg–Ohl rule involving cycles 22 and 23. [205] Although the nature of the current prolonged minimum remains unconfirmed, the accumulation of spotless days is comparable to that seen near the Dalton Minimum. [211] The radial component, which points toward or away from the barycentre, exhibits particularly dramatic changes during episodes of planetary quasi-alignments. [210] During these intervals, the Sun's path undergoes orbital inversions, where the direction of its motion relative to the barycentre reverses. [205]

The sudden changes in radial acceleration are so significant that they dominate the overall coplanar acceleration, which is the vector sum of the radial and tangential components. [205] These spikes in acceleration occur when the Sun fails to loop the barycentre, a phenomenon that happens when the barycentre lies outside the Sun's orbital path. [205] This geometric configuration is a direct result of the specific alignments of the planets, which exert a combined gravitational force that pulls the Sun in a particular direction. [205] The magnitude of these acceleration spikes is much larger than the average values observed during other phases of the solar inertial motion. [205] The exceptional magnitude of the radial acceleration during retrograde intervals provides a clear signature of the planetary forcing on the Sun's motion. [205] The separation of these two influences allows for a more precise understanding of the factors that drive solar variability. [124]

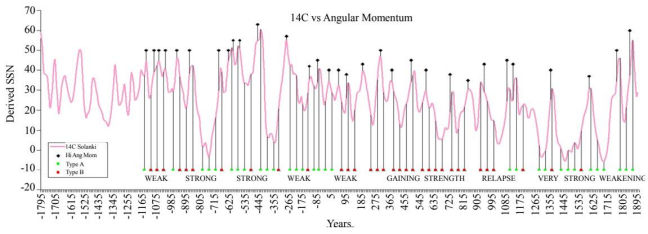


Figure 5.6: This figure plots derived sunspot number (SSN) against time in years, showing a pink line representing the 14C Solanki data and vertical bars indicating individual AMP (Angular Momentum Perturbation) events categorized as Hi Ang Mom, Type A, or Type B. The x-axis spans from approximately 1795 BCE to 1895 CE, with labeled periods such as WEAK, STRONG, GAINING STRENGTH, and RELAPSE, illustrating the [213]

5.3 The Jose cycle and longer beats

Power spectra of the sunspot record demonstrate that the 11-year Schwabe sunspot cycle is made up by three interfering cycles, which can be interpreted as due to the 9.93-year spring tidal cycle between Jupiter and Saturn, the 11.86-year Jupiter orbital tidal cycle, and a central oscillation of about 10.87 years that is almost, but not precisely, the average between the two tidal cycles and may emerge from the solar dynamo cycle as a collective synchronization harmonic. [214] This structure suggests that the 11-year Schwabe sunspot cycle consists of three periods linked to planetary orbital periods, including the Jupiter/Saturn spring period. Scafetta [11, 12] also noted that there are gravitational recurrence patterns of about 11.07-11.08 years due to the Mercury-Venus system and the Venus-Earth-Jupiter system, which correspond to the average solar cycle length. [214][127] Thus, numerous planetary tidal oscillations resonate around the 11-year Schwabe solar cycle, as postulated by Wolf. Taking these considerations into

account, a simple solar model was developed by Scafetta involving just three harmonics, namely the two Jupiter/Saturn tidal cycles and a hypothetical solar dynamo cycle with a 10.87-year period. [214] This model reproduces a varying 11-year cycle that correlates approximately with the Schwabe sunspot cycle, and produces beats at about 61 years, 115 years, 130 years and 983 years, which are synchronous with major solar and climatic multidecadal, secular and millennial oscillations observed throughout the Holocene. [214] The model recovers the Roman Warm period, Dark Ages Cold Period, Medieval Warm Period, Little Ice Age, and Current Warm Period. [125]

Instead of linking the periods of Sun's long-term cycles to corresponding periods of planetary influences, another concept is pursued in which long-term cycles emerge as beat periods between the basic Hale/Schwabe cycle with the typical synodic periods of Jupiter with other Jovian planets. [127] The beat period of 193 years, as resulting from the 22.14-year Hale cycle and the 19.86-year synodic cycle of Jupiter and Saturn, has been noticed by several authors. [127] The aim is to corroborate how such beat periods actually emerge in a specific solar dynamo model, which had already demonstrated synchronization of the Schwabe cycle with the 11.07 years tidal period, based on the resonance of the intrinsic helicity oscillations of the current-driven m = 1 Tayler instability with the m = 2 tidal forcing. [127] The geometry of this solar orbit is essentially planar, with the Sun moving in the plane of the solar system, allowing for a clear separation into ordered and disordered orbital types. [70] This millennial-scale variability is further confirmed by analyses of the solar background magnetic field baseline, which reveal weak oscillations with a period of 2000 ś 95 years. [172] This millennial-scale oscillation is characterized by clustered occurrences of grand minima and maxima around its lows and highs, respectively, indicating a solar origin rather than purely climatic or geomagnetic variability. [113] The correspondence between the semi-Hallstatt cycle and the Eddy cycle indicates that the longer Hallstatt period is composed of two ˜1000-year oscillations, corresponding to the Eddy cycle. This interpretation implies that the ˜2200-year Hallstatt cycle may not be a fundamental solar mode, but rather an emergent property of two superimposed ˜1000-year Eddy cycles. [36][8][113][15][111]

The Holocene — the warm stretch since the last ice age — holds a long record of solar activity. When researchers look for a steady rhythm in the arrival of grand minima, they find none. The timing seems driven by stochastic processes — random, chaotic fluctuations — rather than by long-term cycles. [156][215][136][172] The search for a beat in the rate of these extremes yields only a faint signal. A weak, marginally significant quasi-periodicity

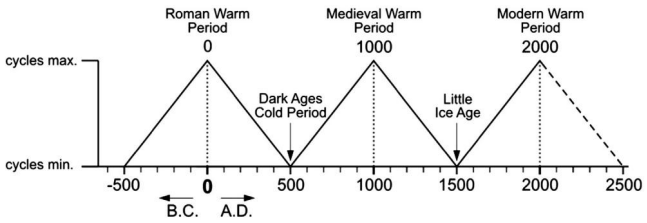


Figure 5.7: The figure illustrates a schematic sketch of the 1000-year Eddy solar activity cycle, showing a repeating triangular pattern of solar maxima and minima over time. The x-axis represents time in years before and after the Common Era (B.C. and A.D.), with labeled historical warm periods—Roman Warm Period, Medieval Warm Period, and Modern Warm Period—corresponding to solar maxima, and cold periods—Dark Ages Cold Period and Little Ice Age—aligning with solar minima. The current position is at the peak of the modern maximum, indicating that solar activity is expected to decline over the coming centuries, reaching a minimum around 2500. [8]

of 2000–2400 years appears, a span already familiar from ^{14}C data. No other periodicities show up in the grand minima record. [216] The story changes slightly for grand maxima. In the SN-S data, a marginal hint of a 1200-year periodicity and its harmonics emerges. The SN-L series, however, remains silent. [216] This contrast suggests the 2400-year signal does not modulate solar activity as a whole. It likely marks the clustering of grand minima alone. [216] [124]

The Sun rarely sits at its extremes. For most of the last few millennia, it has hovered at moderate activity levels. The data come from two sources: cosmogenic isotopes trapped in natural terrestrial archives — ice and tree rings — and historical sunspot counts. Together, they show that the Sun spends only about one-sixth of its time in a Grand minimum state. The rest of the time, it is either moderate or briefly flaring into Grand maximum activity. [215] These extremes do not follow a steady clock. Their arrival is driven by stochastic processes — random, chaotic fluctuations — rather than by long-term cycles. [44] Yet randomness does not mean uniformity. When researchers look at how these events cluster, a pattern emerges. The clustering aligns with a well-known period in radiocarbon data. Damon and Sonett, along with Vasiliev and Dergachev, noted this span. It matches the marginally significant quasi-periodicity found in the analysis. [216] The story differs for the peaks. The SN-L series shows no periodic features in the rate of grand maxima. The SN-S data, however, offers a marginal hint of a 1200-year periodicity and its harmonics. [216] This contrast clarifies the picture. The 2400-year periodicity is likely related to the clustering of grand minima. It does not appear to modulate solar activity as a whole. [216]

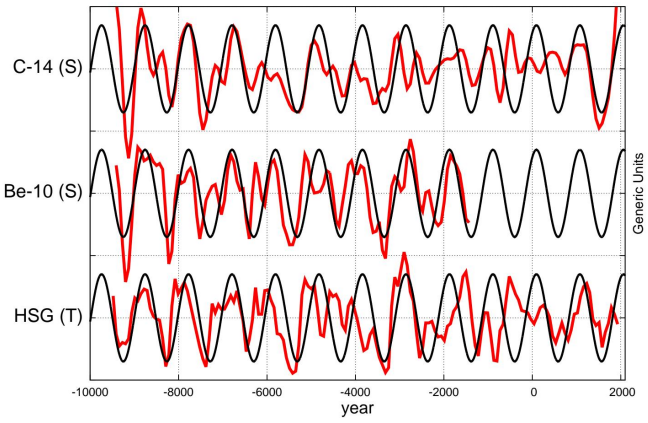


Figure 5.8: The figure displays three time-series plots spanning the Holocene, comparing solar activity proxies (carbon-14 and beryllium-10) and a global temperature proxy (HSG) against a modeled solar harmonic function. The top two panels show the C-14 (S) and Be-10 (S) records, while the bottom panel shows the HSG (T) record, all plotted against a common calendar year axis from -10,000 to 2000. A black harmonic function with a period of 983.4 years and a phase of 2059.7 A.D. is overlaid on each series, illustrating a strong millennial-scale oscillation. The plots reveal a relatively good correlation between the solar and climate records and the modeled harmonic, with correlation coefficients of 0.43 for C-14, 0.30 for HSG, and 0.57 for Be-10, all statistically significant ($P < 0.1\%$). [125]

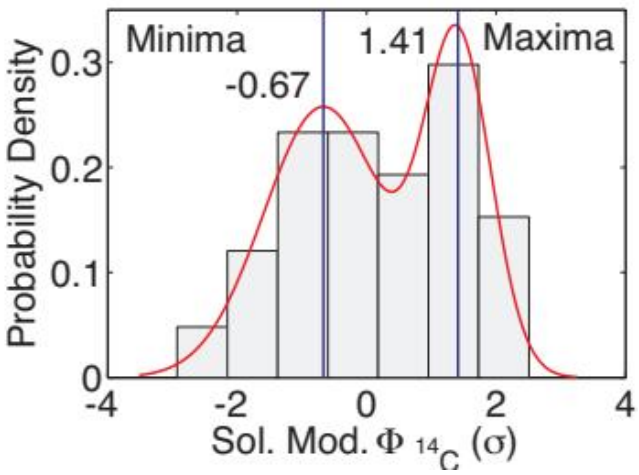


Figure 5.9: The image displays two overlapping histograms of solar modulation potential ($_{14}$) reconstructed from GRIPI^{10}Be and IntCal13^{14}C data over the Holocene, with probability density plotted against $_{14}$ (). A bimodal Gaussian distribution is fitted to the combined data, shown as a red line, highlighting two distinct modes: a minimum at -0.67 and a maximum at 1.41. Vertical lines and text labels identify the threshold values used to classify grand minima and grand maxima in solar activity. [217]

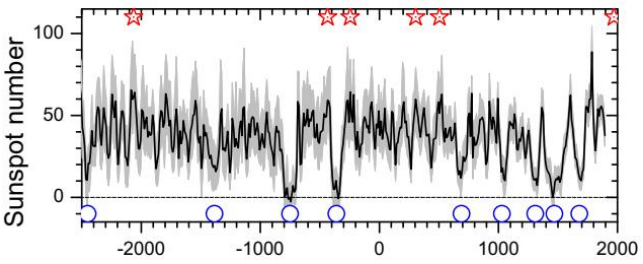


Figure 5.10: This figure displays decadal sunspot activity reconstructed from ^{14}C data over the Holocene, with the y-axis showing sunspot number and the x-axis representing time in years before present. The plot reveals a fluctuating solar activity pattern, with blue circles marking grand minima and red stars indicating grand maxima, highlighting periods of significantly reduced and enhanced solar output, respectively. [113]

5.4 Harmonic analysis — Yndestad and Abdussamatov

To isolate the long-term gravitational influences of the giant planets on the Sun's motion, researchers must first strip away the rapid, short-period oscillations that dominate immediate orbital dynamics. [201] This separation is achieved through semi-analytical planetary motion theory, which relies on advanced mathematical techniques to average the Hamiltonian of the system. The Hori–Deprit method, a cornerstone of this approach, uses Lie transformations to systematically eliminate short-period perturbations from the equations of motion. By removing these high-frequency noise terms, the method allows for a much larger time step in the numerical integration of the equations of motion, making it feasible to model the slow, secular evolution of planetary orbits over centuries or millennia. [203] In recent implementations, such as those using the computer algebra system Piranha, the Hamiltonian of the four-planetary problem is expanded into a Poisson series in osculating elements of the second Poincare system. [203] The transformation between the original osculating elements and the new averaged elements is defined by change-variable functions derived from the second approximation of the Hori–Deprit method. [203]

The algorithm proceeds by deriving second-order terms, $_2$ and $_2$, through the same procedural logic applied to first-order terms, maintaining consistency across the expansion hierarchy. [203] Crucially, the calculation of Poisson brackets, such as $-_2, _1 + _1''$, involves decomposing the expression into constituent parts like $-_2, _1''$ and $-_2, _1''$, with partial derivatives of $_2$ serving as change-variable functions computed by the _(2) script. This semi-analytical approach, constructed with computer algebra systems like Piranha to handle complex symbolic manipulations, contrasts sharply with purely numerical theories that yield only single trajectories and accumulate rounding errors.

Instead, semi-analytical theories show insights into phase space properties and long-term stability, establishing a clearer view of the system's dynamical behavior over extended periods. Applications to the Sun–Jupiter–Saturn–Uranus–Neptune system demonstrate the quasi-periodic nature of planetary motion up to 10 Gyr, with numerical integration of the averaged equations using Gragg–Bulirsch–Stoer and Everhart methods showing excellent agreement with numerical motion theories. [202][201][203] Specifically, simulations of the Sun–Jupiter–Saturn–Uranus–Neptune system over 100 Myr utilized the modified 15th-order Cowell–Störmer integrator and the symplectic Wisdom–Holman integrator, initialized with barycentric coordinates from the DE

430 ephemeris. [201] The results demonstrate that the osculating orbital elements derived from averaged equations maintain strong qualitative agreement with these direct numerical methods. [203]

The orbital evolution of the Sun–Jupiter–Saturn–Uranus–Neptune system on long time scales was studied using a Hamiltonian expansion into the Poisson series in elements of Poincaré second system, constructed up to third degree in the small parameter. [201] The estimation accuracy of this Hamiltonian expansion was evaluated by orbital elements of the Solar System's giant planets, reaching about 10^{12}. [201] The averaged Hamiltonian and the equations of motion in averaged Poincaré elements were constructed by the Hori-Deprit method up to third degree of the small parameter, with functions for the change of variables obtained in second approximation to transform between osculating and averaged orbital elements. [203]

These constructed analytical equations of motion were applied to study the orbital evolution of the Solar System's giant planets on long time scales with high precision, showing that the amplitudes and periods of the planetary motion are in good agreement with numerical theories. [201] The short-periodic perturbations of the orbital eccentricities and inclinations save small values over the entire interval of the integration. [202] Furthermore, the integration of the equations of motion with slightly different initial values of Uranus' semi-major axis showed that the Lyapunov time for the orbits of giant planets is about 10–30 Myr. If the difference between the perturbing functions in the first and second approximations exceeds an amount obviously larger than the small parameter, this may testify to the presence of a resonance whose strength increases with this difference. [202]

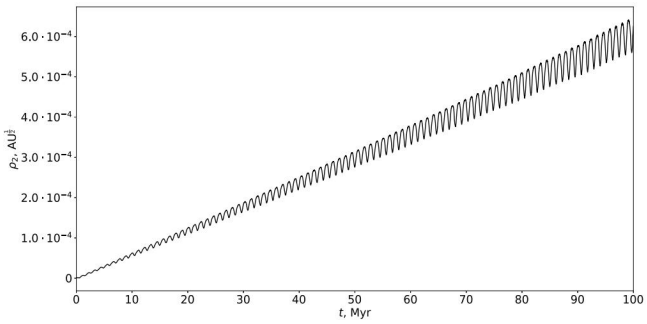


Figure 5.11: The plot shows the time evolution of the ρ_{2} metric, a measure of orbital divergence, for two Uranus-like orbits initialized with a semi-major axis difference of $2 \cdot 10^{-6}$ AU. The metric, scaled in AU$^{1/2}$, increases over 100 million years (Myr), exhibiting a steady growth with superimposed high-frequency oscillations, indicating chaotic divergence in the system's dynamics. [201]

The construction of semi-analytical theories for the orbital evolution of planetary systems, primarily focusing on the Sun–Jupiter–Saturn–Uranus–Neptune system and specific extrasolar systems such as HD 39194, HD 141399, and HD 160691, relies heavily on the Hori–Deprit averaging method. This framework uti-

lizes Lie transformations to derive averaged equations of motion from the Hamiltonian expanded in powers of planetary masses, contrasting with purely numerical theories that provide only single trajectories and accumulate rounding errors. The process involves computer algebra systems, specifically Piranha, to handle complex symbolic manipulations for high-order approximations, expanding the Hamiltonian using Jacobi coordinates and the second system of Poincaré elements. [203] However, for extrasolar systems, the theory may be unacceptable near mean-motion resonances due to extreme growth in Hamiltonian terms. The real evolution of a system in this case, including the real presence of flips, can be studied only using numerical methods, confirming that symplectic integrators are essential for cases involving mean-motion resonances or orbital flips where analytical series diverge. Thus, the semi-analytical approach is best suited for secular evolution far from resonances, whereas numerical integration remains indispensable for capturing chaotic dynamics and resonance crossings. [218][202][201]

5.5 How planetary forcing reaches Earth's climate

Three separate signals line up in a way that suggests they are not random noise. [218] First, the solar system crosses spiral arms of the galaxy. Combining eight measurements of HI — neutral hydrogen gas that traces those arms — yields a predicted crossing period of 134.6 ś 22 Myr. [218] Second, meteorites record cosmic ray flux variations. The Fe/Ni — iron to nickel — ratios in them point to a period of 143.6 ś 10 Myr. [218] Third, Earth's glaciations recur with an average period of 145.5 ś 6.7 Myr. [218] These values align closely. A best-fit analysis comparing the predicted location of the spiral arms to the glaciations yields a periodicity of 143.65 Myr. [218] This suggests that the phase of all three signals fits the predictions. [218]

Specifically, the average mid-point of glaciations lags by 33.6 ś 20 Myr after the spiral arm crossing, consistent with the predicted lag of 31.6 ś 8 Myr. [218] Furthermore, the CR exposure ages of iron meteorites cluster around troughs in the glaciations, reinforcing the link between increased cosmic ray flux and reduced global temperature. This alignment suggests a non-random phenomenon for the appearance of glaciations with high statistical significance, indicating a potential connection between galactic structure and Earth's climate history. Consequently, the data suggest that galactic environmental factors may play a significant role in modulating terrestrial climate cycles. [218] Thus, the SIM

topology provides a potential mechanical basis for understanding how planetary forcing modulates insolation over long timescales, independent of internal solar dynamo processes.

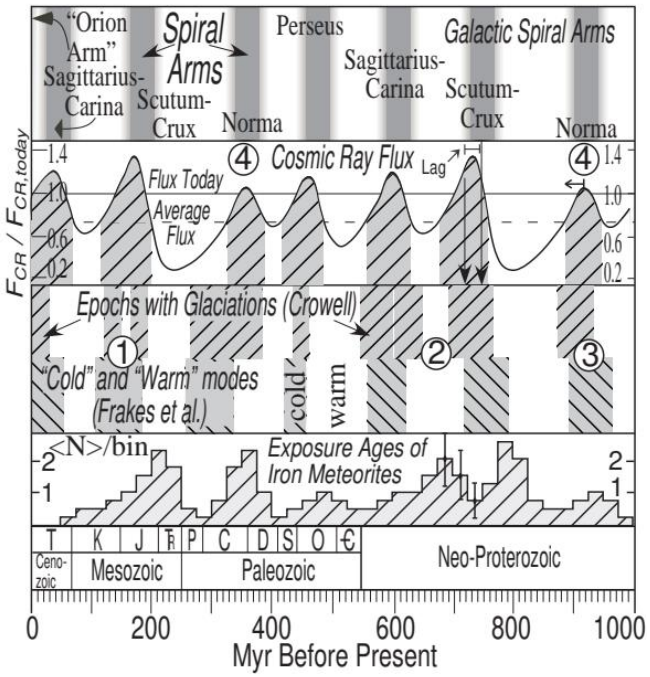


Figure 5.12: This figure presents a multi-panel analysis of the past 1000 million years, showing the correlation between galactic spiral arm crossings, cosmic ray flux (CRF), and geological evidence of ice ages. Panel A illustrates the timing of past Galactic spiral arm crossings, with the average CRF (Panel B) lagging behind these events, as indicated by hatched regions representing predicted intervals of intense cosmic ray flux (IAEs). Panel C displays geological records of ice ages (IAEs) from two studies—Crowell (25) and Frakes et al. (26)—and shows a qualitative alignment between the predicted CRF peaks and observed glacial epochs, suggesting a potential link between galactic dynamics and Earth's climate cycles. [221]

The solar wind — the stream of charged particles streaming from the Sun — pushes against the Earth's magnetosphere. That push suggests the planet's rotation rate changes during solar minima. [219] The interaction tweaks the Earth's total moment of inertia — its resistance to spinning faster or slower — and the angular momentum of the atmosphere. The solid interior adjusts its spin to compensate, a shift we measure as tiny changes in the length of the day. [220] Those rotational shifts ripple outward into ocean circulation and climate. The effect is most visible in the North Atlantic. There, periods when the Earth speeds up during grand solar minima may steer the main surface currents and shift the direction of the Gulf Stream. [219] This chain of cause and effect — solar wind hitting the magnetosphere, altering rotation, then stirring the oceans — fits the observed rises and falls in sea level in the Indian Ocean. [187]

The Earth's rotation speed wobbles twice each year, and that wobble tracks solar activity. This link supports the idea that zonal winds — the east-west air currents circling the globe — alter the planet's spin rate. The Maunder Minimum offers a likely recent example. Eddy noted in 1976 that this period lacked visible sunspots. It serves as a case where reduced solar activity produced a noticeable effect on the climate system. [46] These findings challenge the notion that solar minima had negligible impact. They suggest that reduced solar activity significantly altered the thermal structure of the North Atlantic. That shift

influenced global climate dynamics during these historical periods. [51]

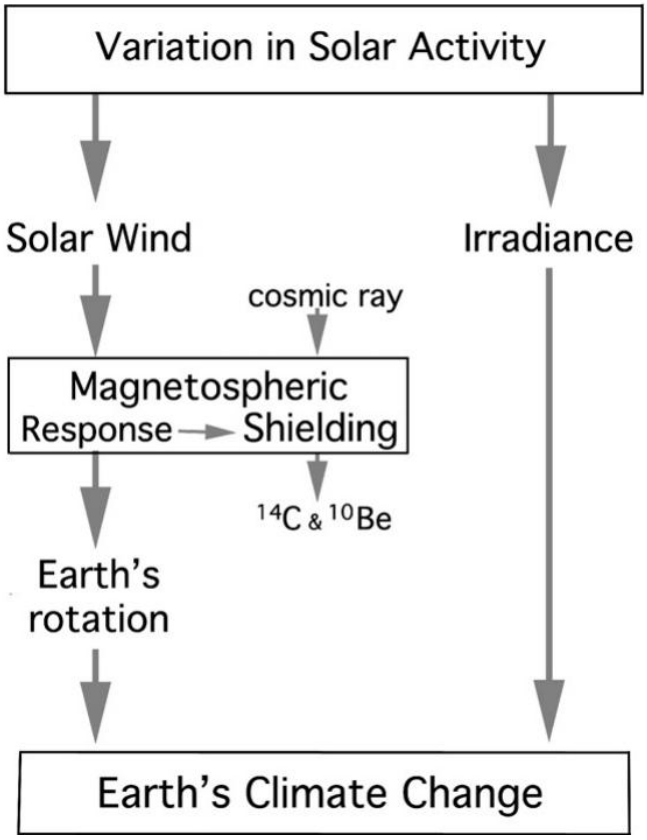


Figure 5.13: The diagram illustrates two pathways by which variations in solar activity influence Earth's climate. The left pathway shows solar wind modulating magnetospheric shielding, which affects Earth's rotation and subsequently climate change. The right pathway depicts solar irradiance directly impacting climate. The diagram highlights that while solar irradiance variations are small, solar wind effects are large, particularly through magnetospheric interactions that alter Earth's rotation and influence climate systems like the Gulf Stream. The flowchart also indicates that cosmic rays and cosmogenic nuclides (^{14}C & ^{10}Be) are linked to shielding changes. [219]

The timing of solar cycles suggests a New Grand Solar Minimum — a prolonged dip in solar output — may arrive by 2030–2040. This falls squarely inside the 2020–2053 window this book adopts. Multiple independent analyses support this prediction. [187] Dr. Theodor Landscheidt's research at the Schroeter Institute for Research in Cycles of Solar Activity points to a long period of cool climate. Its coldest phase would hit around 2030. That date sits again within the 2020–2053 window. It aligns closely with the author's own calculations for the bottom of the next solar hibernation. [49] Peter Harris concludes there is a 94 percent probability of imminent global cooling. [49] For the centuries preceding modern instrumentation, researchers have turned to cosmogenic radionuclides — isotopes created by cosmic rays, specifically ^{10}Be and ^{14}C — preserved in ice cores and tree rings. They use these frozen and wooden archives to reconstruct long-term trends in solar activity. [44]

These isotopes are produced in the Earth's atmosphere by nuclear reactions of cosmic ray particles with atmospheric nitrogen and oxygen, serving as a natural neutron monitor for cosmic radiation intensity. [56] However, it is crucial to recognize that these records do not measure total solar irradiance directly; instead, they reflect the modulation of galactic cosmic rays by the heliospheric

magnetic field. Studies of Antarctic ice cores from the South Pole and Dome Fuji stations indicate that ^{10}Be variations provide a valuable proxy of solar activity, though complex production pathways and atmospheric transport processes impede quantitative interpretation. [67] Thus, while the planetary forcing mechanism provides the external trigger, the cosmogenic record confirms that the Sun's magnetic response, not just its geometric position, is the variable that couples to Earth's climate system.

Chapter 6

The Cloud Hypothesis: Cosmic Rays and Climate

Galactic cosmic rays seed low-cloud condensation nuclei via ion-induced aerosol nucleation; the Sun modulates this flux; this controls albedo and surface temperature.

6.1 How cosmic rays reach the lower atmosphere

Before galactic cosmic rays can influence Earth's climate, they must first navigate the vast expanse of the heliosphere, the region of space dominated by the Sun's outflowing magnetized solar wind. [44] The solar wind is not merely a stream of plasma; it carries the Sun's magnetic field, known as the interplanetary magnetic field, which permeates interplanetary space. [222] The strength of this shielding varies with solar activity, modulating the flux of incoming galactic cosmic radiation that reaches the inner solar system. [168] When the Sun's magnetic field is strong, particularly during solar maximum, it effectively deflects these charged particles, preventing them from penetrating deeply into the planetary system. [223] Conversely, during periods of low solar activity, such as the Maunder Minimum, the weakened magnetic field allows greater penetration of galactic cosmic rays. [14] This modulation mechanism suggests that the interplanetary magnetic field carried by the solar wind shields the heliosphere from galactic cosmic radiation. The variability in this shielding is crucial because it determines the intensity of cosmic rays that eventually collide with Earth's atmosphere. [224][223][225][122][226][64] It is within these denser layers that atmospheric ionization occurs, creating the conditions necessary for potential cloud-seeding effects. [227]

The Sun does not just shine; it pushes. That solar wind, carrying the magnetic field, acts as a shield against the high-energy particles streaming in from the galaxy. [228][102][229][103][223][230] This protection breathes with the solar cycle. When solar activity is high, the shield strengthens, and fewer cosmic rays manage to reach Earth. [130] When the Sun is quiet, the shield weakens, and more particles pour through. [231] Those incoming particles are

mostly protons and alpha particles, born in distant supernovae. They do not drift harmlessly through the sky. They smash into air molecules. The collisions shatter the air, spawning a shower of secondary particles. This cascade includes neutrons, heavy ions, gamma rays, and X-rays. [232] The atmosphere absorbs most of this violence, keeping the surface safe from destructive radiation. But the shower does not vanish. It penetrates deep enough to alter chemistry in the lower atmosphere. That chemical change is the crucial link. It may explain how cosmic rays influence cloud formation. [223]

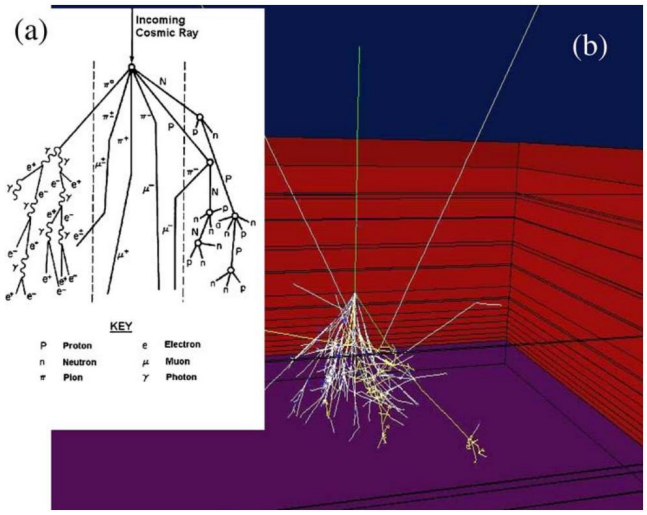


Figure 6.1: The figure presents a two-panel visualization of cosmic ray air showers. Panel (a) shows a schematic diagram illustrating the cascade of secondary particles—protons, neutrons, pions, muons, electrons, and photons—generated when an incoming cosmic ray interacts with atmospheric nuclei, with a key defining the particle symbols. Panel (b) displays a three-dimensional simulation of 10 cosmic ray showers initiated by 10 protons at 10 GeV, rendered using the ATMOCOSMICS code, showing the development and propagation of particle tracks through atmospheric layers. [241]

When energetic cosmic rays strike the Earth's atmosphere, they initiate a complicated nucleonic-muon-electromagnetic cascade that ionizes the ambient air across various altitudes. [228][111] Modeling of cosmogenic isotope production, such as ^{7}, reveals that the most effective energy for particle interaction shifts from approximately 1 GeV/nucleon in the stratosphere to about 3 GeV/nucleon in the lower troposphere as altitude decreases. [233] This process releases secondary particles, including protons, neutrons, and muons, which penetrate deeper into the atmospheric layers. [111] The cascading effect continues until particle energy falls too low for further collisions, generally ending around 16 kilometers above the surface in the lower atmosphere. [223] Within this region, below 16 km, muons and electrons from high-energy collisions are the primary contributors to charged particle intensity. The ions produced within the troposphere by these cosmic rays serve as an important element of aerosol production. [234][228][223][224][235] Specifically, ionization contributes to the gas-particle formation of ultra-fine aerosols, smaller than 20 nanometers, which build into cloud condensation nuclei. [236] Consequently, water vapor condenses into larger water droplets that form clouds, linking the initial cosmic-ray impact to the final cloud structure. These ions are critical because they serve

as likely candidates responsible for observed correlations between cosmic ray intensities and cloud or aerosol parameters. [237]

Consequently, ion chambers at the top of the atmosphere show a very much larger modulation with the solar cycle than instruments at sea-level, with a change in ionization at 10 mb bound to be approximately a 50 per cent reduction between sunspot minimum and sunspot maximum. In controlled chamber experiments simulating conditions found in the lower troposphere over oceans, researchers observed that the production of new aerosol particles is proportional to the negative ion density. [238] These experiments utilized a mercury discharge lamp to initiate photochemical reactions, producing sulfuric acid through the photolysis of ozone and subsequent reactions with sulfur dioxide, oxygen, and water. [238] Ionization was achieved through cosmic radiation, natural radon decay, and a 35 MBq Cs-137 gamma source, allowing for precise measurement of ion pair production rates ranging from approximately 3.7 to 35 cm^3 s^1. [239] These findings suggest that ions are active in continuously generating a reservoir of small thermodynamically stable clusters that can rapidly grow in the presence of condensable vapors. [238] This ion-mediated chemistry provides a plausible explanation for nucleation events that cannot be accounted for by classical nucleation theory alone. [238] Further field studies are therefore needed to quantify the relative importance of ion-induced nucleation in the global aerosol budget. [240]

6.2 Forbush decreases — the natural experiment

To see how this mechanism works, we look to ^{1} Ceti. This young solar twin offers a crucial case study for how solar activity affected the climate during the early history of the Earth. [229] When solar ejections are directed toward the Earth, they trigger sudden reductions in the influx of galactic cosmic rays. These drops happen over time scales ranging from hours to days, a phenomenon known as Forbush decreases. These temporary dips in cosmic ray flux are not merely theoretical curiosities. They serve as natural experiments that allow scientists to observe the immediate atmospheric response to changes in ionization. [229][230][236][218][64] Such large Forbush decreases are too rare in the modern era to have a significant ongoing effect on the Earth's climate. Their impact may have been far more profound in the distant past. [229]

Four billion years ago, when life started to evolve on the Earth, coronal mass ejections were expected to be much more common on the early Sun, suggesting that the reduction in galactic cosmic

ray influx originating from Forbush decreases could have been significant compared to the reduction from the Sun's more effective shielding at that time. [229] By using the flare rate of ^{1} Ceti to estimate the coronal mass ejection rate, scientists can gauge how common these events would have been on an Earth-like planet around such a young star, offering a window into the climatic conditions that shaped the origins of life. [229]

Forbush decreases act as natural experiments. These sudden drops in cosmic ray flux, caused by coronal mass ejections, let us test hypotheses about solar influences on Earth's weather and clouds. They are ideal for isolating the link between cosmic rays and clouds because they produce a sharp, transient signal lasting for a week or two. [103][64][230] Observations using three independent cloud satellite datasets and one aerosol dataset reveal a clear response in clouds and aerosols to these decreases. [242] The data shows that reductions in the cosmic ray flux translate into changes in cloud properties. The timing difference between the cosmic ray minimum and the cloud response reflects the time it takes for aerosols to grow into cloud condensation nuclei. [242]

Coronal mass ejections hurl clouds of plasma from the Sun. These clouds sweep past Earth and sweep away galactic cosmic rays. The result is a sudden drop in cosmic ray flux. Physicists call these sharp declines Forbush decreases. [236] They last for about a week. Such rare events offer a clean test. They let us check the causal chain from solar activity to cloud formation. [242] Researchers looked at the five strongest Forbush decreases between 1990 and 2005. They used three independent cloud satellite datasets and one aerosol dataset. The data show clear signals in low cloud liquid water content. [243][64][229][236][103] There is a distinct delay of five to seven days. The cosmic rays hit their minimum first. The clouds and radiative forcing respond later. This lag matches the time needed for aerosols to grow. The observed reduction in cloud properties confirms the mechanism. It is most visible in low liquid clouds over the oceans. The entire chain is active in the Earth's atmosphere. Cosmic rays affect aerosols, which then affect clouds. [243] Isolating these strong events helps. It maximizes the signal-to-noise ratio. The analysis establishes a statistically significant linear relationship. The strength of the Forbush decreases links directly to the globally averaged shortwave radiation response. [243]

When coronal mass ejections directed toward Earth cause sudden, week-long drops in galactic cosmic ray influx known as Forbush decreases, they provide a natural experiment to test atmospheric responses. [236] Specifically, these observations demonstrate that Forbush decreases are associated with changes in the relative abundance of fine atmospheric aerosols, establishing a link from

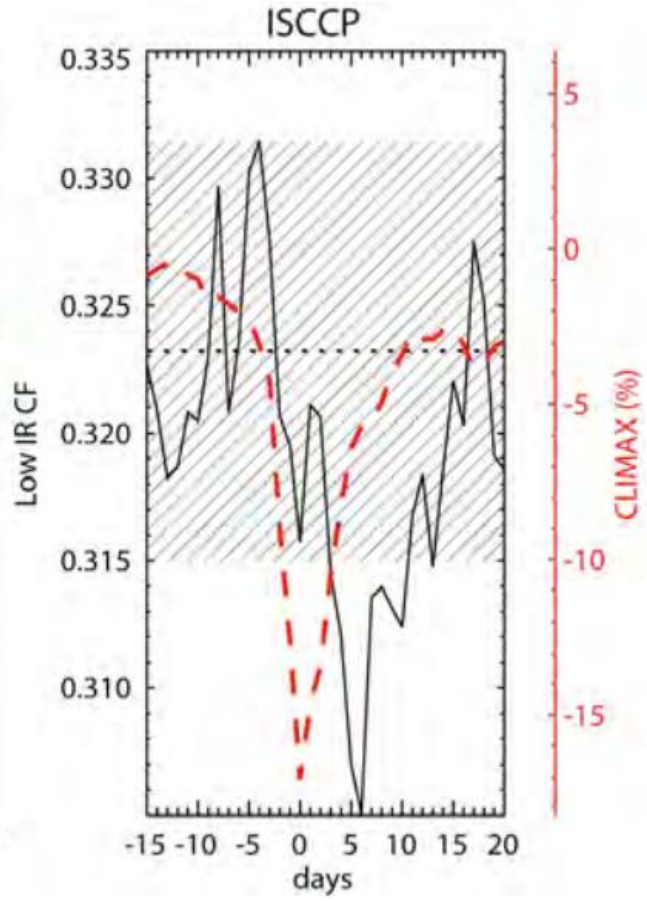


Figure 6.2: This figure displays the daily average low infrared-detected cloud fraction (Low IR CF) from ISCCP data (left y-axis, black line) and the CLIMAX cosmic ray flux (right y-axis, red dashed line) relative to Forbush decreases, averaged over five strong events from 1987 to 2005. The data shows a significant drop in low IR cloud fraction around day 0, coinciding with the minimum in cosmic ray flux, with the cloud fraction recovering in the days following the event. [224]

solar activity through cosmic rays to aerosols and finally to clouds. The delay between the cosmic ray minimum and the cloud parameter minimum reflects the time required for aerosols to grow into cloud condensation nuclei. [244][64][229][236][103][218] During these influential recent events, liquid water in the oceanic atmosphere decreased by as much as seven percent, confirming that the whole chain of effects is active in the real atmosphere. [242] This discernible response supports the hypothesis that cosmic ray ionization controls the number of cloud condensation nuclei, thereby affecting Earth's climate. [236]

Statistical work on these events shows clear atmospheric signals, especially near the poles. [243] Pudovkin and Veretenenko saw mean cloud cover drop after Forbush decreases north of 60°N. Roldugin and Tinsley found changes in atmospheric transparency — how much light passes through the air — above 55°N. These observations suggest that the sudden drop in ionizing radiation links to measurable shifts in cloud properties and optical depth. [245][230][64][103][218][229] Later, Kniveton and Tinsley, along with Todd and Kniveton, looked at zonal mean total cloud anomalies — average cloud cover across latitude bands. They found these anomalies tied to Forbush decreases in both polar and equatorial regions. These findings suggest that the primary effect of cosmic

rays may relate to vorticity — the spin of air masses — and cyclogenesis, the birth of storms. This link appears strongest during cold seasons in high-latitude areas. [218][230][229][103][64]

Forbush decreases serve as a natural experiment. They isolate the cosmic ray–cloud mechanism from long-term solar trends. [236] Coronal mass ejections send plasma clouds past Earth. These clouds cause sudden, short-term drops in cosmic ray flux. The drop lasts a week or two. The data reveal a clear, reproducible response in both clouds and aerosols. The timing of the minima is offset. It matches the time required for aerosols to grow into cloud condensation nuclei. [236] This latitudinal gradient aligns with theoretical expectations for cosmic ray penetration. [103] Crucially, the magnitude of the observed responses suggests a link. The cosmic ray–cloud connection could explain approximately 1 W/m^2 of solar cycle forcing. This estimate is consistent with crude calculations. A 3% variation in cloud cover during an average 11-year solar cycle corresponds to a radiative forcing of 0.8 to 1.7 W/m^2. [103] Consequently, the physical link appears robust. Its global climatic significance requires further quantification.

6.3 Chamber evidence — SKY and CLOUD

To move beyond statistical correlations and establish a physical basis for the cosmic-ray cloud hypothesis, researchers have turned to controlled laboratory environments that replicate the complex chemistry of the lower atmosphere. [246] The pivotal SKY experiment, conducted at the Danish National Space Center in Copenhagen, was designed to isolate the specific role of ionization in aerosol formation by using natural cosmic rays and gamma rays to simulate atmospheric ionization under conditions representative of Earth's atmosphere over the oceans. This experimental setup allowed scientists to introduce trace amounts of ozone, sulfur dioxide, and water vapor into an eight-cubic-meter reaction chamber, where ultraviolet light initiated photochemical reactions to produce sulfuric acid, a key precursor for cloud condensation nuclei. [52][247] By varying the ionization levels using cesium-137 gamma sources, the researchers could directly observe the response of aerosol concentrations to changes in ion density. [247]

Controlled chamber experiments bridge the gap between theory and physical mechanism. They show exactly how ionization drives aerosol growth, moving the discussion beyond speculation. [236] The SKY experiment, run at the Danish National Space Institute, tested this directly. It found that electrons released by cosmic rays act as catalysts. These electrons accelerate the formation of stable

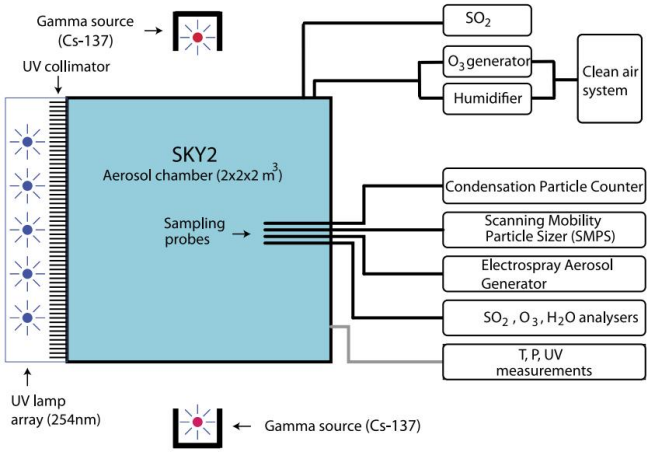


Figure 6.3: The figure illustrates the schematic of the SKY2 aerosol chamber experiment, a 2»2»2 m^3 reaction chamber equipped with a UV collimator and lamp array (254 nm) for simulating solar radiation. It shows the integration of a gamma source (Cs-137), a clean air system with SO_2, O_3, and humidity controls, and various measurement instruments including a Condensation Particle Counter, Scanning Mobility Particle Sizer, and analyzers for SO_2, O_3, and H_2O. Sampling probes extract air from the chamber for real-time monitoring of aerosol properties and gas concentrations, enabling the study of atmospheric chemistry under controlled conditions. [247]

clusters made of sulphuric acid and water. Without ionization, the molecular clusters simply failed to grow. They never reached the size needed to supply significant numbers of cloud condensation nuclei larger than 50 nm in diameter. [240][247][64][52] But when the chamber air was exposed to ionizing radiation, simulating cosmic rays, the picture changed. The clusters grew much faster. They quickly reached the sizes where they help water droplets form and make clouds. This result contradicts earlier numerical modelling results. It indicates that an important part of the ion-mechanism was missing from the theory. [247] The solution involves a so-far-ignored contribution to growth from the mass of the ions themselves. [236]

Researchers left the messy correlations of the real world behind. They moved into controlled laboratory chambers to isolate the microphysical mechanism. [246] This design strips away other atmospheric variables. It leaves only the ionization effects to be studied. [236] Inside these boxes, the air mimics the lower troposphere. The experiments show that ions do trigger nucleation there. They help trace gases, like sulfuric acid, form tiny aerosols. [240] When the ionization goes up, the number of these new particles rises too. This provides a direct physical link. It connects cosmic ray flux to aerosol production. [236] The result confirms the viability of the ion-aerosol mechanism. Cosmic rays can seed the particles needed for cloud droplets. This validates the core premise of the Svensmark hypothesis in a controlled setting. However, the real atmosphere is far more complex. Laboratory conditions may not capture natural aerosol processing fully. [103][64] The magnitude of this effect outdoors remains uncertain. The mechanism is physically plausible, yes. But its climatic significance is still debated.

Researchers moved the debate from the sky into the lab to see if cosmic rays could actually start clouds. [246] They wanted a controlled setting where they could watch the first step of nucleation happen in real time. The experiments confirmed that ions do help form tiny particles. But forming a particle is not the same as making a cloud. The path from a speck of matter to a cloud condensation nucleus — a particle large enough to catch water vapor and grow into a droplet — is long and difficult. [247] Computer models of aerosols suggested the journey would be hard. They predicted that extra particles would compete for the available gases. This competition would slow growth down. It would also make it likely that a small particle would get swallowed by a larger one before it ever reached the size needed for CCN. That scenario challenged the idea of a direct link between nucleation and cloud formation. [247] The lab results told a different story. In chambers where ultraviolet light created aerosols from ozone, sulfur dioxide, and water vapor, gamma-ray ionization consistently boosted production. [247] This boost did not fade away. It remained steady from the very first nucleation stage all the way up to diameters larger than 50 nm. That size range is exactly where particles become effective cloud condensation nuclei. [247] The outcome was not predicted by theory. It points to a missing process in current models. One possibility is that ions help form sulfuric acid within small clusters, giving them a growth advantage. [247] By showing that ions help particles reach the cloud-condensing size, the SKY data supports the mechanism. It suggests galactic cosmic rays could modulate cloud cover. That, in turn, could influence global surface temperature. [246]

The models paint a crowded picture. Existing aerosols compete for the available gases. This competition slows the growth of new particles. It also raises the chance that a small particle will be swallowed by a larger one before it reaches CCN size. [247] The chamber experiments tell a different story. They show that ions can seed the formation of aerosol particles. These particles are essential precursors for cloud condensation nuclei. [236] But the path from these initial nucleation events to observable cloud droplets remains unclear. Researchers are still asking how efficient this process is in the real atmosphere. The consistency across different cloud records suggests that the correlation is not merely an artifact of data persistence. Yet the precise causal link remains contested. [103] The chamber experiments confirm the microphysical possibility of ion-induced nucleation. They do not prove it is a dominant climate forcing mechanism. The debate centers on the satellite records. Are the observed correlations robust enough to support the hypothesis? The hypothesis claims that galactic cosmic rays play a significant role in modulating global cloud cover. This modulation would, by extension, influence surface

temperature. [103]

6.4 Heliospheric modulation and global temperature

The relationship between solar activity and global surface temperature is not merely a matter of direct irradiance but involves complex modulation mechanisms that amplify the Sun's influence on Earth's climate system. [248] While Total Solar Irradiance (TSI) varies only slightly over the solar cycle, its impact on surface temperatures appears to be significantly enhanced by other factors, particularly those linked to cosmic rays and cloud formation. [64] The evidence thus points to a more nuanced understanding of solar-climate interactions, where the Sun's magnetic activity and its effect on cosmic rays are key drivers of surface temperature variability. [103] In these records, solar changes lead temperature anomalies, a pattern consistent with both climate modeling and other climate and solar variability studies. [1] The climatic effect of the de Vries solar cycle is thus well established across multiple paleoclimate archives, including Central Asian ice-cores, Asian and South American monsoon-record speleothems, Mesoamerican lake-sediment cores used as drought proxies, and Alpine glaciers. [1] These diverse datasets collectively support the existence of a significant delay between solar forcing and terrestrial thermal response. [1]

Surface temperatures do not jump in step with the Sun. There is a delay of approximately 11 years between changes in Total Solar Irradiance and the corresponding shifts in heat. [8] This lag suggests that the atmosphere or oceans are doing more than just absorbing light. Complex feedback processes may be amplifying the signal, rather than a simple radiative response. [8] The picture widens further when we look at the galaxy. Temporal correlations link three distinct things. They connect expected spiral arm crossings, the variable cosmic-ray flux observed in iron meteorites, and the appearance of ice ages. [218] This basic evidence supports a view where Earth's climate is affected by our changing location in the Milky Way. The mechanism works by way of a variable cosmic-ray flux. [218] Closer to home, the ice tells a different story. The data confirms that Greenland's interior ice sheet experienced a growth trend starting as far back as 1992. It gained mass by a net 11 billion tons per year. The uncertainty is plus or minus three billion tons per year. [49] This finding comes from Dr. H. Jay Zwally et al. in a 2005 article in the journal Glaciology. [49]

The mid-century cooling trend, specifically the global cooling from 1945 to 1977, occurred during a period of increasing post-

1945 CO2 emissions. This divergence demonstrates that rising greenhouse gas concentrations were not the dominant driver of surface temperatures during this interval. [8] The coincidence of two warming periods in this oscillation with the Modern Solar Maximum suggests that natural forcing and internal variability made a significant contribution to observed warming. [1] Consequently, the natural contribution to observed warming should come at the expense of considerably reducing the anthropogenic contribution. Furthermore, there is very solid evidence that periods of low solar activity in the past, identified by a higher rate of cosmogenic isotopes production such as ^{14}C and ^{10}Be, have a high degree of correlation with periods of climate deterioration manifested mainly as temperature decrease and precipitation changes. 2500-yr Bray cycle, with comparison of climate and solar variability records leading to the important observation that the period of the cycle correlates with the amplitude of the climate effect observed. [1] In general, the longer the cycle period, the more profound effect it appears to have on climate. [1]

6.5 Shaviv and the spiral-arm record

The Phanerozoic eon — the last 570 Myr of Earth's history — shows no steady warming or cooling trend. Instead, the climate record alternates between cool and warm intervals. [1] This variability may include a 150-Myr periodicity, a pattern first identified by G.E. [1]

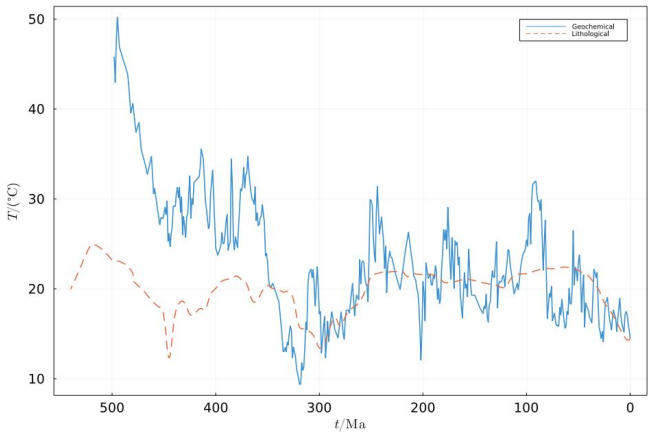


Figure 6.4: The figure displays two time-series reconstructions of temperature (°C) over the past 500 million years, plotted against time in millions of years (Ma). The solid blue line represents a geochemical reconstruction, while the dashed orange line shows a lithological reconstruction. Both reconstructions exhibit fluctuating temperature trends, with the geochemical data showing significantly higher temperatures in the early Phanerozoic compared to the lithological data, particularly before 500 Ma. [252]

Reconstructions of local supernova rates over the past 500 Myr, derived from open cluster ages and trajectories, demonstrate that cosmic ray flux variations on million-year timescales are determined by the local galactic environment rather than solar activity. Monte Carlo simulations combining open cluster dynamics with stellar evolution reveal that nearby supernovae

cause significant spikes in Galactic cosmic ray flux, inducing atmospheric ionization changes larger than those caused by solar activity. [230][218]

The alignment between galactic structure and Earth's climate history suggests a deep connection between cosmic-ray flux and long-term glaciation. [218] This periodicity excludes random phenomena for glaciation appearance with high statistical significance, supporting the hypothesis that galactic environment drives Earth's ice age epochs. [218]

The Phanerozoic temperature record displays a c. [1] 150-Myr periodicity, a pattern first reported by G.E. [1] However, the spiral-arm climate hypothesis remains controversial because the solar system's past path, speed, and the position of the galactic arms in the distant past are not well constrained.

On geological timescales exceeding a million years, cosmic-ray variations are determined by the local galactic environment, with density expected to be higher when Earth resides within dense galactic spiral arms. [218] However, interpreting this correlation is not straightforward, as it assumes the constancy of other drivers and climate type throughout millions of years. During the Phanerozoic period, cold glacial periods coincided with high local supernova frequency and high cosmic rays, while warm climates appeared when the flux was low. [249] The CRF record exhibits a clear variability signal with a periodicity of 143ś10 Myr, which is consistent in phase with the predicted CR diffusion model incorporating spiral arms. [250] The concentration of trace elements in pyrite serves as a proxy for nutrient availability in the oceans, correlating closely with cosmic ray changes throughout the Phanerozoic. [249]

Nutrients like phosphorus limit how much life can grow. When cosmic rays shift the climate, they squeeze that biological energy flow. [249] The studies show this chain holds up over millions of years. Supernovae drive the climate, which moves the nutrients, which feeds the biosphere. [249] Ice ages follow a rhythm too. Their timing matches a cosmic ray signal with a periodicity of 143 ś 10 Myr. This rhythm agrees in phase with the predicted diffusion model for the Milky Way's spiral arms. [251] That alignment offers a qualitative link. It points to cosmic rays as a driver of climatic variability. The long-timescale question of climate sensitivity finds an answer here. Galactic cosmic rays persistently influence Earth's biosphere and climate. This supports the view that cosmic ray modulation is a primary factor. It shapes global temperature and productivity fluctuations.

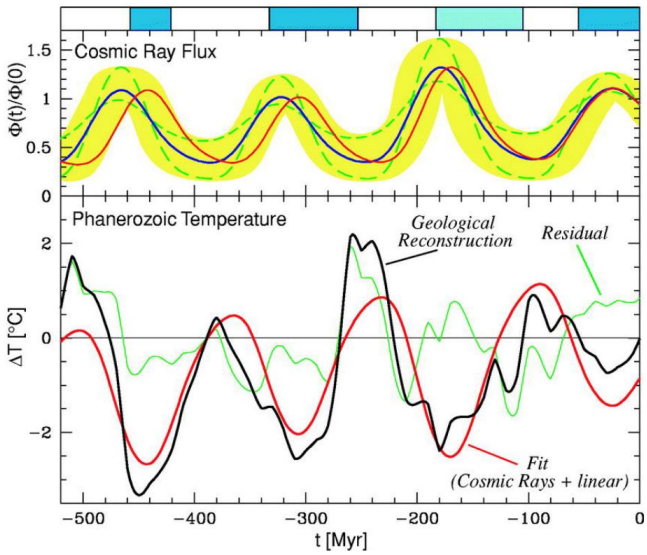


Figure 6.5: The figure displays two time-series plots spanning the past 500 million years, showing reconstructed cosmic ray flux (top panel) and tropical ocean temperature (bottom panel) in degrees Celsius. The top panel, labeled "Cosmic Ray Flux," presents multiple curves representing different reconstructions of flux variations, with a yellow shaded band indicating uncertainty; the bottom panel, labeled "Phanerozoic Temperature," compares a black curve of geological reconstruction with a red fit curve that includes a linear trend and a component attributed to cosmic rays. A horizontal bar at the top marks the timing of four major ice ages: Ordovician/Silurian, Carboniferous/Permian, Jurassic/Cretaceous, and Pleistocene. The data suggest a correlation between periods of elevated cosmic ray flux and cooler global temperatures, particularly during the identified ice ages. [254]

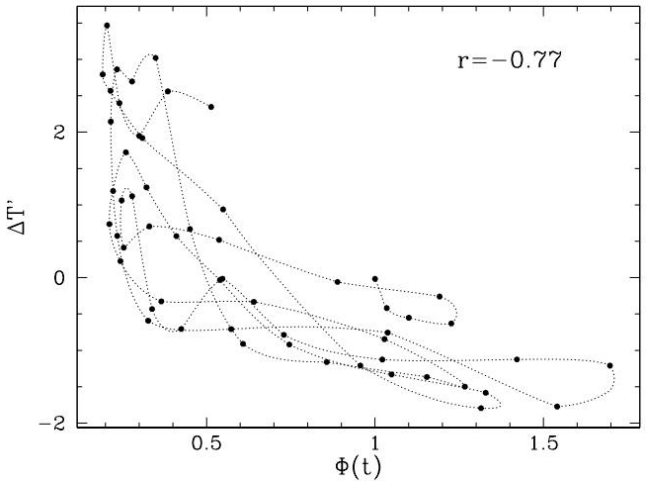


Figure 6.6: This scatter plot displays the reconstructed temperature anomaly T (in °C) against the cosmic ray flux (CRF) proxy (t) (in arbitrary units) over the Phanerozoic eon, with data points spaced at 10 Ma intervals and smoothed using a 50 Ma moving average. The plot shows a strong negative correlation (r = -0.77) between the two variables, indicating that higher cosmic ray flux corresponds to lower reconstructed temperatures. The data points form multiple overlapping trajectories, suggesting complex temporal dynamics, and the high correlation supports the use of this relationship to estimate global climate sensitivity. [253]

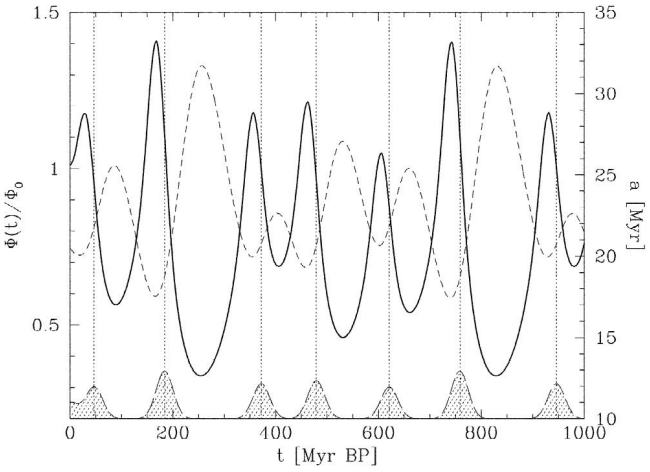


Figure 6.7: The plot shows the cosmic-ray flux ((t)/$_0$, solid line) and cosmic-ray age (a, in Myr, dashed line) as functions of time (t, in Myr BP) for a diffusion coefficient D = 10^{28} cm^2/s and a scale height l_H = 2 kpc. The flux exhibits periodic peaks that are phase-lagged behind the spiral arm crossings, which are indicated by vertical dashed lines and correspond to the locations of spiral arms defined by the Taylor and Cordes free electron density model. The shaded regions at the bottom represent the relative amplitude and width of these spiral arms, and the flux distribution is skewed toward later times, consistent with a delay between supernova explosions and the subsequent propagation of cosmic rays through the interstellar medium. [218]

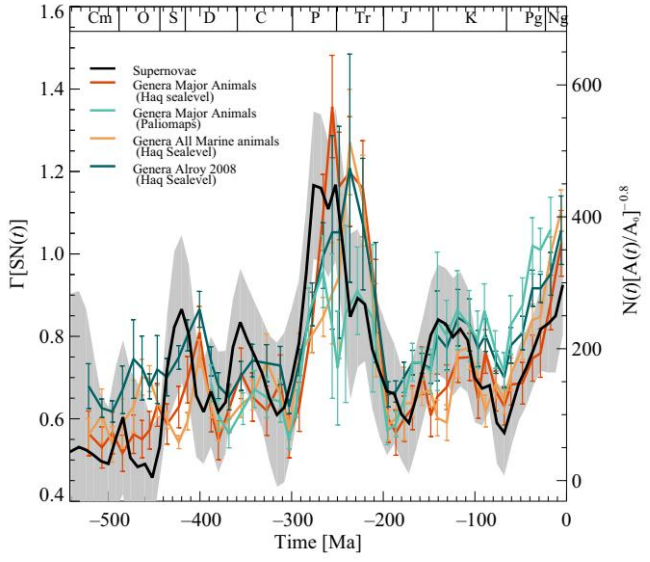


Figure 6.8: The figure displays a time-series comparison of supernova rate variations and marine animal diversity over the past 500 million years. The black curve, representing supernova activity, is derived from Equation (4) and shows fluctuations with a gray shaded region indicating 1- uncertainty from Monte Carlo simulation. Multiple curves depict marine animal diversity: orange and teal lines show major marine animal genera normalized to shallow marine margin area using data from Haq et al. and Haq & Schutter, and Cao et al., respectively; a dark green line represents the genera-level diversity of marine invertebrates from Alroy et al.; and another dark green line shows all marine animals normalized to shallow marine area using Haq et al. and Haq & Schutter. Error bars on the genera curves reflect minimum 1- uncertainty due to unavailable area estimates. The data suggest a correlation between supernova activity and marine biodiversity trends, particularly during major extinction and diversification events. [249]

Chapter 7

The Underground Connection: Volcanism and the Sun

Grand minima have coincided with anomalously intense volcanism; plausible mechanisms — lithospheric stress, isostatic rebound, deep-Earth degassing — are testable and matter for the coming minimum.

7.1 When the Sun goes quiet, the Earth gets loud

Tree rings trap carbon-14, while ice cores from Greenland and the Antarctic lock away beryllium-10. [56][46][46][255][65] Researchers read these isotopic archives to track how the Sun's activity shifts over centuries. They find that the star does not burn steadily. It dips into long, quiet stretches called grand minima. When the Sun's magnetic shield weakens during these hibernations, cosmic rays—high-energy particles from deep space—pour through more easily. This surge is not just a theory. Geological records capture the influx directly. [256] The signal matches across different isotopes and distant locations. This consistency suggests that local quirks do not drive the pattern. The variations appear global, linked tightly to solar modulation. [249] The Maunder Minimum offers a clear example. Visible sunspots vanished from the solar surface. Radionuclide production spiked in their place. This signature marks a period of reduced solar activity. [44]

Holocene reconstructions indicate that grand minima are not periodic but appear as the result of chaotic or stochastic processes within clusters separated by 2000–2500 years. Analysis of radiocarbon data reveals a weak, marginally significant quasi-periodicity of 2000–2400 years, a well-known period in ^{14}C records that likely relates to the clustering of grand minima rather than to a long-term modulation of solar activity. [33][1][156][216] This pattern suggests that the occurrence of grand minima and maxima is defined by stochastic or chaotic processes, with no clear periodicities observed in the occurrence of grand maxima. [257] The observed effect of the 2500-year Bray solar cycle is to result in long Spörer-type solar grand minima or clusters of such

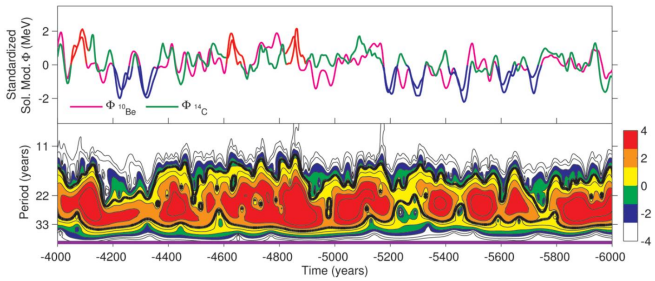


Figure 7.1: The image displays two panels: the top panel shows standardized solar modulation potential time series for cosmogenic isotopes ^{10}Be (pink line) and ^{14}C (green line), with blue and red lines indicating identified grand minima and maxima, respectively. The bottom panel presents a local cross-wavelet spectrum of high-pass filtered ^{10}Be and ^{14}C data, with a cutoff frequency of 1/30 year^{1}, highlighting periods of strong coherence between the two proxies during identified grand minima; the color scale indicates wavelet power, and the purple line marks dates in BC. [166]

minima at its lows. [216] These climatic shifts, registered mainly as significant reductions in winter temperatures and increases in precipitation in the North Atlantic region, have historically coincided with societal disruptions, including food crises and population decreases. [216] The biological and temperature subdivisions of the Holocene display transitions related to the lows of the Bray cycle, suggesting that climate-related disruptions have been quasi-periodic drivers of societal change. [216] Thus, while the timing of individual grand minima may be stochastic, their clustering within the broader 2000–2500 year cycle provides a structural framework for understanding long-term solar variability and its associated climatic impacts.

The Sun's output has not been steady. Across the Holocene — the ten thousand years from 10,000 B.C. to today — reconstructions show the solar cycle varies greatly in strength. [1] Some cycles churn out many sunspots. Others produce very few. These quiet stretches mark distinct epochs of suppressed activity, known as solar Grand Minima. [258] We define a Grand Minimum as a period when the smoothed sunspot number falls below 15 for at least two consecutive decades. [257] Detailed analysis of these records reveals a surprising frequency. The Sun spends about 17 percent of its time in this Grand Minima state. This finding suggests that grand minima are not rare anomalies. Instead, they appear to be a recurring feature of solar behavior over the past ten millennia. [111][1] The energetic opposite, solar Grand Maxima, behaves differently. Those intense states are typically short-lived, lasting in the order of 50 years.

Sunspot records reveal a longer rhythm, a quasi-period of 90 ś 10 years. We call this the Wolf-Gleissberg cycle. It stands out as the most prominent of the extended solar cycles. Wavelet power spectrum analysis confirms this periodicity. Researchers

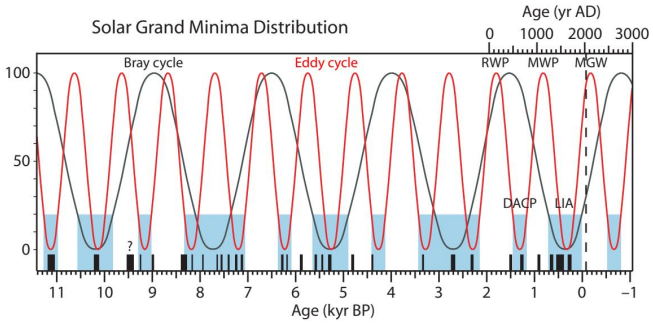


Figure 7.2: This figure displays the distribution of 30 Solar Grand Minima (SGM) during the Holocene, plotted against age in kiloyears before present (kyr BP) and age in years AD. Black boxes represent SGM events, with their thickness indicating duration, and are shown to cluster within the blue-shaded regions corresponding to the lowest 20% of the 2500-year Bray cycle (black sinusoid) and 1000-year Eddy cycle (red sinusoid). The graph illustrates that 54% of the Holocene falls within these low solar activity phases, with the present time marked by a dashed line. Periods of significant climate change, including the Roman Warm Period (RWP), Dark Ages Cold Period (DACP), Medieval Warm Period (MWP), Little Ice Age (LIA), and Modern Global Warming (MGW), are labeled, showing their alignment with solar cycles. A question mark indicates a debated SGM potentially linked to a supernova-induced cosmic ray increase. [1]

examined sunspot data from 1700 to 2020. The mean total wavelet period came to Tsa = 4*22.5 = 90.0 years. [258][220][19][259] Fast Fourier Transform (FFT) computations tell a similar story. They scanned the full sunspot number time series. They also checked subsets: the first half, the second half, and the middle half. The 87.6-year Gleissberg peak appeared sharp and prevalent across all these intervals. It is absent in recent data, however. [123] Earlier hypotheses, such as those by Stothers, suggested an 11-year periodicity in volcanic activity. Recent analyses look deeper. They examined 3,829 eruptions with a Volcanic Explosivity Index (VEI) of 2 or greater. A dominant 22-year period emerged. This aligns with the solar background magnetic field (SBMF) cycle. [259] The evidence suggests a specific timing. More volcanic eruptions occur during the maximum phases of the doubled solar cycles. This happens when the solar background magnetic field possesses a southern polarity. [181] This correlation is not uniform across all historical periods. A rather high positive correlation between the number of volcanic eruptions and the southern polarity of the SBMF was established for the period 1868–1950. A much smaller negative correlation was observed during 1750–1868. [11]

The proposed link involves increased electromagnetic interaction between the SBMF and the terrestrial magnetic field, causing geomagnetic disturbances that can lead to shifts of the crusts, most

powerful earthquakes, and volcanic eruptions. [260] The reduced correlation between volcanic eruptions and solar activity indices recorded during the period 1750–1868 can be associated with a geomagnetic jerk and the related migration of the North pole towards lower latitudes. [260] Differences in eruption frequencies over the phases of solar cycles may also relate to differences in solar activity indices defined by sunspots and eigen vectors of magnetic fields related to different types of solar magnetic fields, specifically the toroidal and poloidal fields. [181] The lack of correlation in the period 1950–1980 is linked to open air nuclear bomb testings that distorted the effects of the solar magnetic field. [181] In summary, the increase of volcanic eruptions established during solar cycles with the southern polarity of the SBMF emphasizes the importance of solar-terrestrial interaction in volcanic eruptions. [259] Hence, despite links between volcano occurrences and solar activity not being clear yet, the consequences of volcanic eruptions for the terrestrial atmosphere during cycle 26 with the southern polarity of the solar magnetic field can be expected to be noticeable during the modern Grand Solar Minimum (2020–2053).

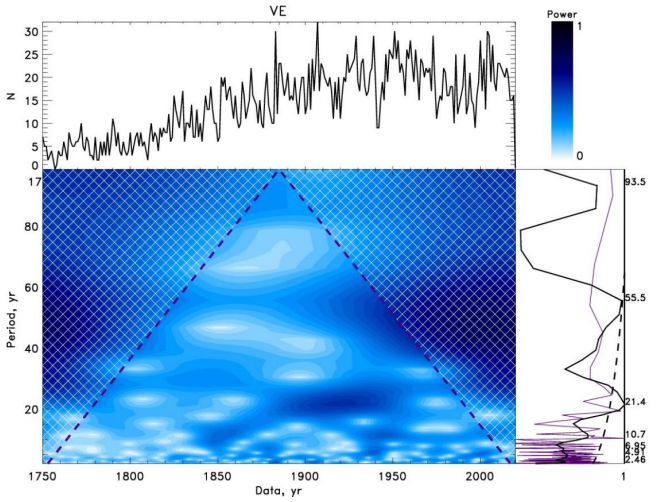


Figure 7.3: The figure displays a wavelet analysis of volcanic eruptions from 1750 to 2020. The top panel shows the annual eruption count time series, while the bottom left panel presents the wavelet power spectrum, revealing dominant periodicities in eruption frequency over time, with the Cone of Influence marked by a dashed line. The bottom right panel compares the global wavelet spectrum (solid black line) and Fourier spectrum (indigo line), with the 95% confidence interval for the global wavelet spectrum indicated by a dashed line. [11]

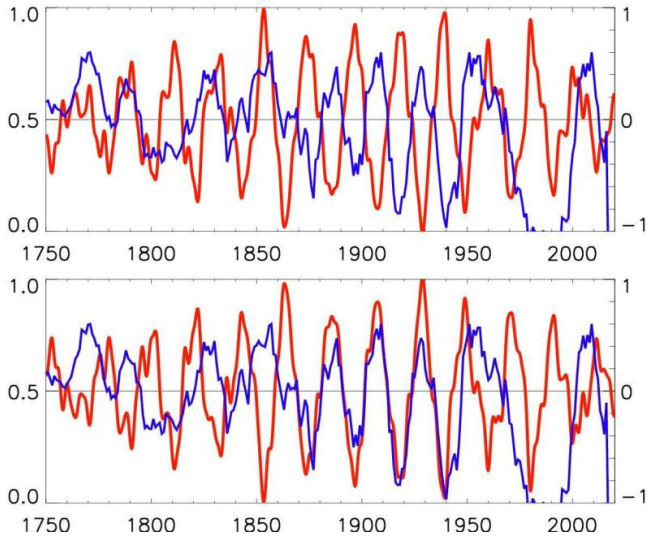


Figure 7.4: The figure displays two time-series plots from 1750 to 2000, comparing the normalized number of volcanic eruptions (blue curves, left y-axis) with the normalized eigen vectors of the solar background magnetic field (red curves, right y-axis). The top plot shows the eruption count versus the summary eigen vector curve, where positive values indicate northern polarity and negative values indicate southern polarity of the solar magnetic field. The bottom plot presents the same eruption data against an inverted eigen vector curve, with positive values corresponding to southern polarity and negative to northern polarity. Both plots exhibit correlated oscillatory patterns, suggesting a potential relationship between solar magnetic field dynamics and volcanic activity, with correlation coefficients detailed in the source paper. [11]

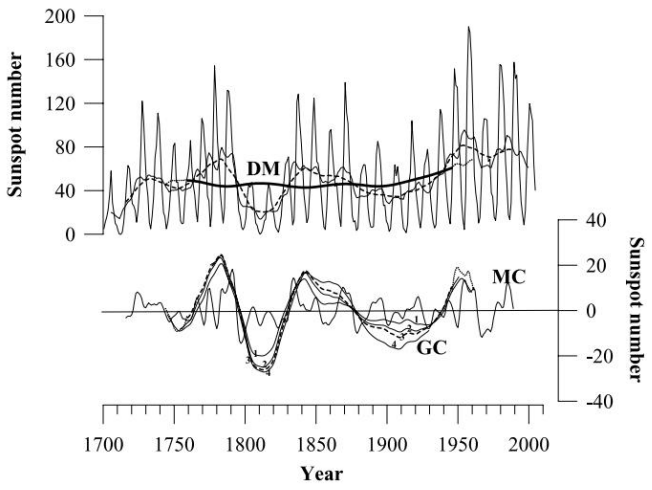


Figure 7.5: The figure displays two panels analyzing sunspot number data from 1700 to 2000. The top panel shows the raw sunspot number time series (thin curve) alongside successive running averages: an 11-year average (thick curve), a 22-year average (dashed curve), and an 88-year average (short, thick curve), with a dotted extension of the R88 signal; the Dalton Minimum (DM) is marked. The bottom panel presents filtered signals of the Hale cycle (solid curve, MC) and the Gleissberg cycle (dashed curve, GC), with a dotted extension of the GC signal, illustrating long-term oscillations in solar activity. [136]

7.2 The Maunder-era eruptions

The eruption began on February 19 and raged until mid-March. It remains the largest explosive event in the Andes, rated VEI 6. Geologic evidence matches early Spanish chronicles to confirm this magnitude. [261][262][263][264] Those accounts describe a sustained Plinian column — a towering shaft of gas and rock — rising 27–35 km. The blast ejected 3.1 km^3 of dacitic pumice. Ash drifted 200–500 km to south Peru, west Bolivia, and north Chile. Strong winds pushed finer particles more than 500 km west, out into the Pacific Ocean. [261] The eruption's high discharge stemmed from a disrupted hydrothermal system. This system lay within an amphitheater formed before AD 1600. Volumetric eruption rates reached between 5.4–6.6 » 10^4 and 1 » 10^5 m^3/s. [261]

The dry air of the Central Andes preserves tephra — the fragmented rock and glass ejected by volcanoes — with unusual clarity. This arid landscape acts as a natural archive. It allows researchers to trace how far the eruption's material traveled. [262] Scientists measured the thickness of the Plinian pumice fall at 260 sites across roughly 95,000 km^2. From these data, they reconstructed a bulk volume of 7.87 km^3 for that specific layer. [261] That figure likely underestimates the total. It ignores deposits thinner than 1 cm. When the later, post-Plinian tephra is added, the total bulk volume rises to 11.4–12.1 km^3. [261] The chemical fingerprint of the glass in that tephra also matches glass found in Antarctic ice. [265]

The glass in that tephra carries a chemical signature. It matches the glass found in Antarctic ice. This link ties the AD 1600 Huaynaputina eruption to those deposits. It sharpens our estimates of stratospheric loading. [265]

The Huaynaputina volcano in southern Peru erupted in AD 1600. It was one of the biggest explosive events in history. We know this because the glass in its tephra matches the acidity spikes in Antarctic ice. [265] That match links the eruption to the ice record. It suggests the stratosphere filled with enough dust to cool the globe. [265] The cooling was likely severe. Tree rings from the Swiss and Austrian Alps show very low temperatures in AD 1601. [266] Wood density data from thirteen sites along the northern tree line of North America confirm this signal. [266] Frost rings appear in the western USA. They also show up near Bush Lake in Canada. The Polar Urals hold similar marks. [267] These biological traces support the idea of widespread cooling. [267] Historical records back up the science. People in England and Italy wrote about an unusually cold summer. Russia, Latvia,

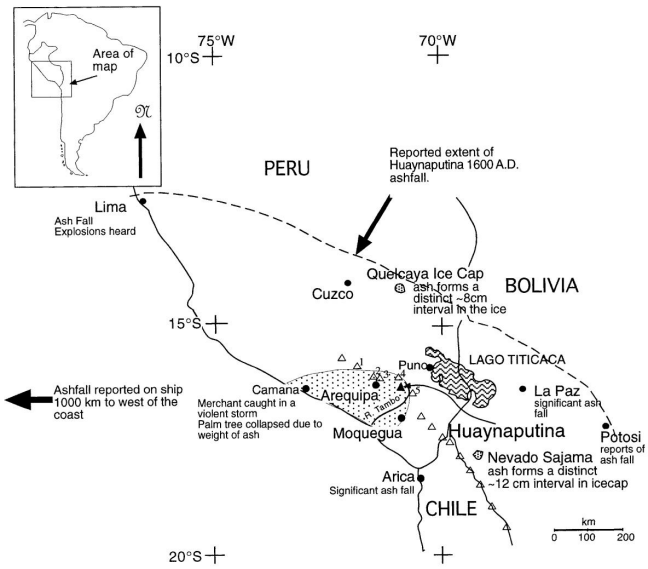


Figure 7.6: This map illustrates the regional context of Volcán Huaynaputina in southern Peru, showing the extent of its 1600 A.D. ashfall across Peru, Bolivia, and northern Chile. It highlights the distribution of volcanic ash deposits, including the stage-I pumice fall (stippled area) dispersed primarily west-southwest, and identifies key locations with ashfall evidence such as ice cap layers in the Queucaya and Nevado Sajama ice caps, historic reports from Lima and Potosí, and a ship log recording ashfall 1,000 km west of the coast. The map also marks active volcanoes in the Central Volcanic Zone, including Sabancaya, Chachani, Misti, Ubinas, and Ticsani. [181]

and Estonia endured a severe winter. Killing frost destroyed crops in northern China. [266]

The ecological aftermath of the AD 1600 Huaynaputina eruption provides a precise chronometer for studying rapid biological colonization in the northern Atacama desert. [268] On the deep pumice substrates near Omate, Moquegua, Peru, floristic inventories demonstrate that approximately 59 angiosperm species established themselves within the last 400 years. This unique vegetation type, dominated by therophytes and chamaephytes, exhibits a floristic composition with the highest similarity to the coastal Lomas de Tacna rather than geographically closer Sierra formations, despite stark climatic differences. [268][269] The presence of nine species representing highly disjunct populations, with nearest living relatives located 200 to over 700 km away, confirms that long-distance dispersal events were the primary colonization mechanism on the denuded substrate. [268] Morphological analysis further establishes that four taxa have undergone considerable divergence from their source populations, with two potentially representing neoendemics, proving that speciation can occur rapidly on suitable target areas. [268] These findings highlight how the specific edaphic and climatic filters of the Omate pumice slopes precluded establishment from adjoining habitats while allowing successful colonization from remote source areas, offering insights into the speed of phyto-diversity processes following major explosive volcanic events. [268]

The 1600 AD Huaynaputina eruption left a blank slate in the northern Atacama desert. [268] That fresh pumice is now a natural laboratory for watching life return. Over the last 400 years, vascular plants have taken root on the slopes near Omate, Moquegua, Peru. [268] The resulting community is unlike anything

else nearby. It looks most like the coastal Lomas de Tacna, not the geographically closer Sierra formations. A Sørensen index of 24 at the species level quantifies this link between the Omate sites and the Lomas de Tacna. [268][268] That similarity is nearly twice as high as for any other compared sites. The reason lies in the ground itself. The porous pumice soaks up rain only in the top layers. The subsoil stays dry all year. This mimics the harsh water limits of the coastal Lomas, rather than the moisture-retaining soils of the Sierra. [268] So the Lomas act as the recruiting ground for this unique Andean vegetation type. They do this despite significant altitudinal and geographical barriers. This strong ecological link shows how substrate properties can override simple proximity. It highlights the role of long-distance dispersal mechanisms in repopulating denuded volcanic landscapes. [269]

Crucially, nine species on these slopes represent highly disjunct populations, with their nearest known living populations located 200 to greater than 700 kilometers away in central Peru, Chile, Bolivia, or Argentina. These disjunctions suggest recent long-distance dispersal as the primary colonization mechanism, given that the substrate was denuded in 1600 AD. [268] Abiotic conditions, including soil type and climate, appear to limit establishment from neighboring vegetation. [268] Morphological analysis reveals that four taxa exhibit clear differences from populations elsewhere, with two potentially representing neoendemics, indicating rapid morphological divergence over the 400-year period. [268] Rodent midden data suggest no dramatic late Holocene climatic changes since 1600 AD, though a strong El Niño event in 1652 AD may have facilitated Lomas flora expansion and subsequent dispersal to Omate. [268] This young, annual-dominated community contrasts with the shrub-dominated flora on adjacent rocky soils, identifying the Omate pumice slopes as the first recorded Andean vegetation type dominated by annuals and floristically akin to coastal Lomas. This unique assemblage likely reflects a specific post-eruption colonization trajectory rather than a stable equilibrium state. [268] Consequently, the site serves as a critical natural experiment for understanding rapid ecological succession in extreme volcanic environments.

7.3 Tambora and the Year Without a Summer

The April 1815 eruption of Mount Tambora stands as a defining event in the instrumental record, classified at an intensity of 7 on the volcanic explosivity index, a relative measure of volcanic explosiveness that ranges from 0 to 8. [270] This aerosol umbrella, six times the size of Mount Pinatubo's 1991 cloud, disrupted

normal patterns of temperature and precipitation across the hemispheres by entering the meridional currents of the global climate system. [83] The subsequent year of 1816 has been termed the "Year Without a Summer," a period marked by significant climate anomalies and harvest failures across Europe and North America. [271] The dust veil increased visual extinction in the stratosphere by 1.4 ś 0.2 mag at northern middle latitudes, implying a worldwide stratospheric aerosol load of ˜2.0 » 10ˆ14 g, in near agreement with values estimated from Greenland ice acidities. [80] The relation between volcanism and climate depends on eruptive scale, with volcanic ejecta and gases penetrating high enough to reach the stratosphere where sulfate aerosols form and spread aloft by winds and meridional currents. [83] The telltale sulfate imprint left on the ice for paleoclimatologists to discover more than a century and a half later confirms the global reach of this atmospheric perturbation. [272]

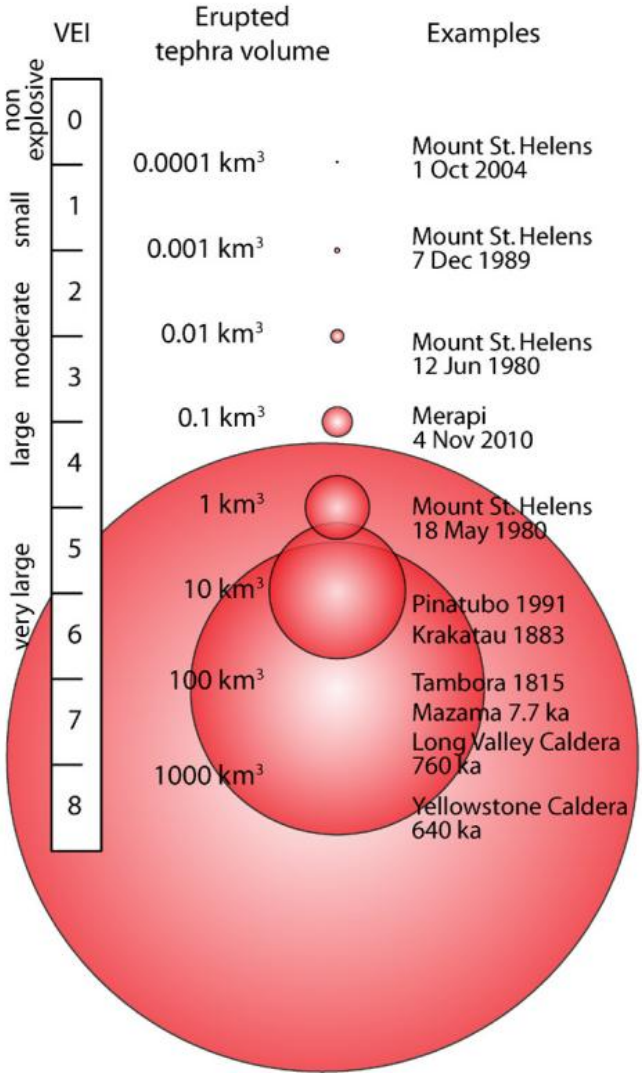


Figure 7.7: The image displays a logarithmic scale of the Volcanic Explosivity Index (VEI), illustrating the relationship between eruption magnitude and erupted tephra volume in cubic kilometers. It uses a series of concentric circles to represent increasing volumes from 0.0001 km^3 to 1000 km^3, with each circle corresponding to a VEI level from 0 to 8. The chart includes examples of historical eruptions, such as Mount St. Helens at VEI 5 and the Yellowstone Caldera (640 ka) at VEI 8, showing how specific events map to their respective explosive magnitudes and volumes. [277]

Tambora's 1815 blast hurled roughly 150 km^3 of ash and pumice into the sky. That volume equals about 50 km^3 of dense-rock-

equivalent magma. The resulting dust veil thickened the atmosphere, raising visual extinction by 1.4 ś 0.2 magnitudes at northern middle latitudes. [80] Those sulfate aerosols scattered incoming sunlight, dimming the Earth's surface. This scattering drove a global cooling of 0.4 to 0.8°C between 1815 and 1818. The chill hit hardest in eastern North America and central and western Europe. There, cold and wet weather dominated the late spring and summer of 1816. [273][80][75] People called that stretch the "Year Without A Summer." The weather caused severe famine and deep social distress. [274] The Dalton Minimum added a small extra chill, but the volcano did the heavy lifting. [85] Tambora's impact exceeded any other known eruption in the past 10,000 years. That scale makes it a precise calibration standard for studying older explosive events. [80] Crops failed widely, worsening the hardship left by the Napoleonic wars. [274] Late grape harvests in France and frost damage rings in trees in the western United States and South Africa confirm the cold. [75] A dot marks Geneva on the map. It sits inside a region of negative SLP anomaly. [275]

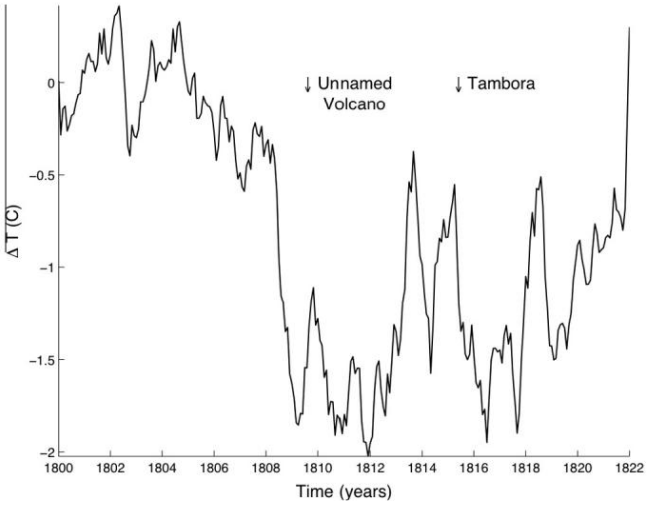


Figure 7.8: This line graph shows land temperature anomalies (T in °C) from 1800 to 1822, based on data from the Berkeley Earth Project, illustrating the cooling during the Dalton (CGC) minimum. The plot reveals a significant temperature decline beginning in 1809, prior to the eruptions of the unnamed volcano and Tambora (marked by arrows), with the most pronounced cooling occurring around 1812. Temperature fluctuations of approximately 1.5°C are evident between 1815 and 1820, highlighting the period's climatic instability. [24]

The wet chill of 1816 compounded the misery left by the Napoleonic Wars. That weather produced famine, disease, and social unrest. [75] Manley's data suggest that central England's summer of 1816 ran about 1.5°C cooler than the summer of 1815. Kelly and colleagues reconstructed the pressure maps for that same period. Their charts show negative pressure anomalies dominating Europe from early 1816. [75] That atmospheric shift may have bent the track of middle-latitude cyclones southward. It dumped cold, wet air over England. The damp spread across much of western Europe. [83] The cold reached further west. Hudson's Bay Company posts on the eastern side of Hudson Bay kept detailed records. They logged the summers of 1816 and 1817 as possibly the coldest in the modern record. Tree rings from northern and western Quebec seem to support that finding. [75]

New Haven, Connecticut, kept a weather ledger that stretches back to 1780. According to that archive, the summer of 1816 was the coldest until 1968. [271] Frost returned again and again across New England. It struck from late spring through summer, killing crops and causing severe food shortages. [82] In Pennsylvania, corn rotted on the stalk, frozen hard by the cold. Newspapers in England called 1816 a year without a summer. [40] Corn failed across America. Grain failed across Europe. These widespread crop losses demonstrate the devastating impact of the 1816 climate anomalies. The resulting socioeconomic disruptions appear to have been significantly exacerbated by these climatic conditions. [276][75][40][83]

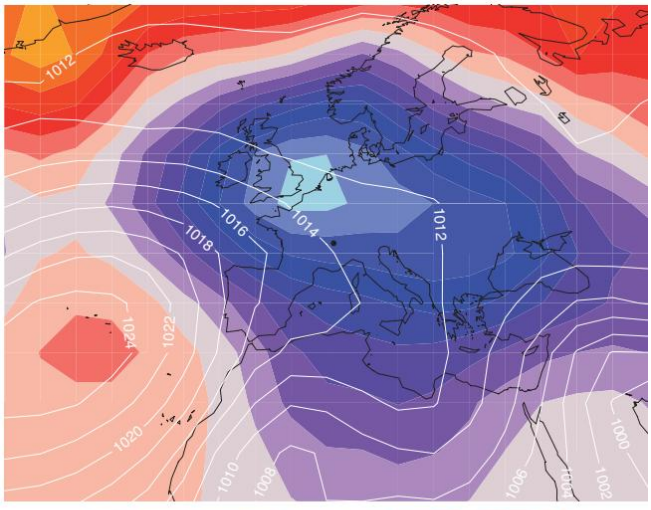


Figure 7.9: This figure displays a map of sea-level pressure (SLP) anomalies for summer 1816 (June–August) relative to a reference period, with absolute SLP values shown as white contour lines. The anomaly field, color-coded in hPa, reveals a large negative anomaly centered over northern Europe, indicating lower-than-average pressure, while positive anomalies are present over the Atlantic and parts of eastern Europe. The dot marks Geneva, located within a region of negative SLP anomaly. The data illustrates the atmospheric circulation pattern associated with the "Year Without a Summer" following the 1815 eruption of Mount Tambora. [275]

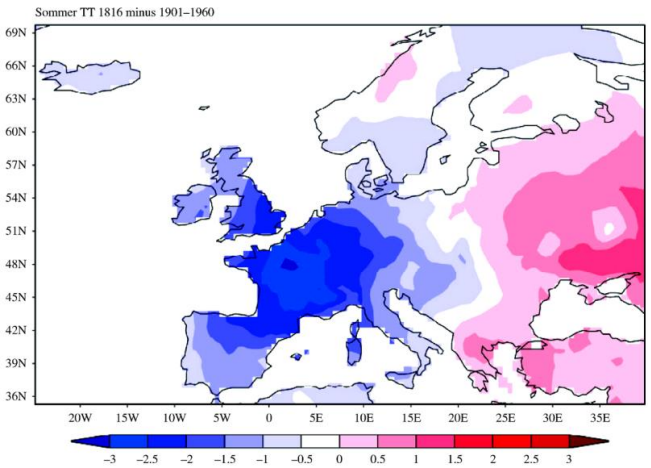


Figure 7.10: This figure displays a map of Europe showing the deviation in summer temperature in 1816 from the 1901–1960 average, illustrating the anomalous cooling during the 'Year without a Summer'. The color scale, ranging from dark blue (-3°C) to dark red (+3°C), indicates regions of significant cooling (blue) across Western and Central Europe and warming (red) in Eastern Europe and parts of Russia. [278]

Western Europe endured a summer of 1816 that was cool and exceedingly wet. This weather compounded the aftereffects of the Napoleonic Wars. The result was famine, disease, and social unrest. [75] Post called this period "The Last Great Subsistence Crisis in the Western World." The atmosphere behaved strangely.

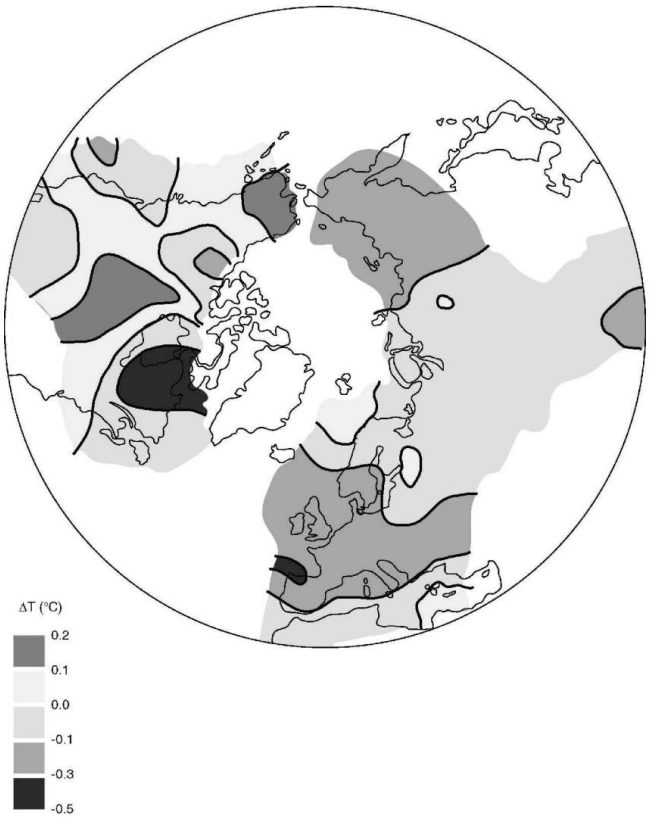


Figure 7.11: This figure displays a gridded map of reconstructed surface temperature anomalies (T in °C) for summer 1816, derived from latewood density in tree rings across the Northern Hemisphere. The data, based on Briffa et al., shows widespread negative anomalies, with the most severe cooling (down to -0.5°C) concentrated over northern Europe and parts of Siberia, while milder cooling (around -0.1 to -0.3°C) extends across much of the continent and into North America. [274]

Negative pressure anomalies — regions of low atmospheric weight that steer storms — dominated Europe beginning in early 1816. These anomalies shifted the tracks of middle-latitude cyclones southward. [75] Data from Manley indicate that the summer months of 1816 in central England were about 1.5°C cooler than during the summer of 1815. [75] In North America, the cold was even more extreme. Records from Hudson's Bay Company posts on the eastern side of Hudson Bay show that the summers of 1816 and 1817 were the coldest of any in the modern record. Tree-ring data from northern and western Quebec support this finding. [75] Repeated frosts in New England caused crop failures. These failures resulted in poor harvests and food shortages. [82] The resulting food insecurity and social distress following the 1816 harvest failures contributed to outbreaks of typhus and other diseases in Europe. [274]

By September 1817, the typhus epidemic had reached its peak. Doctors in Dublin warned of impending ruin. Their colleagues in Edinburgh expressed alarm at the fever spreading across the British Isles. [83] This anomalous cooling followed the spectacular April 1815 eruption of Tambora volcano on Sumbawa Island in Indonesia. The eruption ejected approximately 150 km^3 of ash and pumice. This volume equals about 50 km^3 of dense rock equivalent magma. The column rose an estimated 50 km into the stratosphere. Ash covered an area exceeding 4 » 10^5 km^2.

Darkness lasted for up to two days at distances of 600 km from the source. [75] Yet Tambora alone cannot explain the severity of the 1816 cooling. European temperature measurements during the Dalton Minimum showed a decline in place well before the eruption. The lowest temperatures were recorded prior to 1816. This trend appears in the European temperature profile done by David Archibald in his work, The Past and Future Climate.

7.4 Hunga Tonga — the eruption that warmed the world

The January 2022 eruption of Hunga Tonga–Hunga Ha'apai stands apart in our modern records. It was not sulfur dioxide that defined this event, but water. An unprecedented volume of water vapour shot straight into the stratosphere. NASA's Aura satellite watched from above. Balloons launched by the National Oceanic and Atmospheric Administration (NOAA) near Reunion Island measured the plume from below. Together, they confirmed that roughly 150 Tg of water vapour blasted about 60 km into the air. This single injection increased the global stratospheric burden by 10%. It remains the largest stratospheric perturbation of water vapour observed in the satellite era, a record spanning more than 30 years. [279][280][281] Classic explosive eruptions like Pinatubo or Tambora are defined by sulfate aerosols. Those particles scatter sunlight and induce temporary cooling. Hunga's primary radiative forcing agent was water instead. The immediate atmospheric response included strong cooling in the Southern Hemisphere mid-latitude stratosphere. This cooling strengthened the mid-latitude jet. It also slowed the Brewer–Dobson Circulation. At the same time, the eruption perturbed polar ozone chemistry. Increased HOx and polar stratospheric cloud formation drove these changes. Satellite records show the dark patch of high humidity spreading globally. It moved from the Southern Hemisphere to the north over the course of a year.

What made Hunga different was the ratio of water to sulfur. TROPOMI satellite-based measurements of SO_2 concentrations in the atmosphere establish that the total stratospheric SO_2 mass was approximately 0.4 Tg, a figure consistent with other estimates of ˜0.5 Tg that confirm the eruption injected only a modest amount of sulfur dioxide.[282][281][283] This disparity is critical because SO_2 oxidizes into sulfate aerosols that reflect sunlight and cool the surface, whereas stratospheric water vapour acts as a greenhouse gas that warms it. Atmospheric physics demonstrates that stratospheric water vapour effectively alters radiative forcing and influences global surface temperature once

it enters the stratosphere.[1][284][281][285][181] Consequently, the Hunga event produced a transient natural warming pulse rather than the classic volcanic winter associated with Pinatubo-type eruptions — a thermal anomaly that acted in direct opposition to the traditional volcanic winter narrative.

How long will the pulse last? For the first two years, the stratospheric burden hardly changed. That stability left the residence time of the volcanically injected water vapour uncertain. Early estimates varied widely. Some projections suggested a return to baseline conditions as early as 2025. Others predicted a lingering presence for more than a decade. The Microwave Limb Sounder — the MLS instrument aboard NASA's Aura satellite — has provided continuous observations of the Hunga-enhanced water since the eruption. Recent data show a substantial decline from 2024 to early 2025. That marks the largest drop since the event. Comparison with 3-D numerical model simulations shows that the long-term removal of the Hunga water has entered a new phase. Stratosphere-troposphere exchange is playing an increasingly important role. It exceeded Antarctic dehydration in 2024.

The water leaves the stratosphere through three main routes. Ice crystals in polar stratospheric clouds — frozen layers that form in the extreme cold — settle out of the air. Air masses also sink from the stratosphere into the lower atmosphere at middle and high latitudes. A tiny fraction is destroyed higher up, in the mesosphere, by sunlight. The remaining excess water is now decaying steadily. The e-folding time — the period required for the amount to drop by a factor of — is 3 years. This trajectory suggests the perturbation will return to the pre-Hunga range of variability around 2030. That quantifies the residence time of the Hunga stratospheric water vapour perturbation at 9 years. [281] The decay estimate is statistically well-constrained. Combining the formal fitting uncertainty of the exponential fit to the MLS time series through July 2025 with the spread arising from natural variability yields a total two-sigma uncertainty of roughly 0.29 years.

This transient natural warming pulse contributed to the global temperature surge observed in 2023 and 2024, challenging narratives that attribute recent heat solely to anthropogenic carbon dioxide. Unlike the persistent cooling shadow cast by sulfate aerosols, which can linger for years and mask underlying solar trends, the radiative impact of stratospheric water vapour is inherently temporary, governed by the atmospheric residence time of the molecule itself. As the vapour dissipates toward 2030, the radiative forcing will wane, allowing the underlying climate drivers — solar irradiance and cosmic-ray modulation among

them — to reassert their influence on global surface temperatures. Understanding the timeline of this decay is critical for disentangling natural variability from long-term climate trends, particularly in assessing the compounding effects of solar minima and volcanic activity.

7.5 Mechanisms — why might the Sun affect the Earth's crust?

John Eddy spotted a link in the 1970s. He saw that solar activity and the European climate moved together over the previous millennium. The Little Ice Age — a cold stretch from 1300 to 1850 AD — arrived while the Sun was particularly inactive. The Medieval Warm Period — a warmer span from 1000 to 1200 AD — happened while the Sun was active. [64] New temperature reconstructions for the extratropical Northern Hemisphere over the last two millennia show a similar pattern. They track the assumed low-frequency variability in solar forcing of the last millennium reasonably well. Several periods of especially low solar activity stand out in the data. This includes the Wolf Minimum, which lasted from AD 1645 to 1715. [2] Figure 5a shows recent temperature reconstructions for the last 1000 years. Figure 5b displays cosmic ray reconstructions. These rely on ice cores from Antarctica and an ice core from Greenland. The two records show a remarkable correlation. Changes in temperature match changes in cosmic rays driven by solar activity. [64]

Historical data associate the European Maunder Minimum winter cooling with enhanced northeasterly advection of continental air, consistent with an anomalous negative NAO, and reconstructions of large-scale surface temperature patterns from networks of diverse proxy information, such as tree rings, ice cores, corals, and historical records, provide empirical estimates of the large-scale climate response to solar forcing. [286] When filtered to isolate the multidecadal-to-centennial time scales associated with the Maunder Minimum, the empirical regression shows a clear AO/NAO-type pattern of alternating cold land and warm ocean temperature anomalies, indicating that solar forcing affects regional scales much more strongly than global or hemispheric scales. [286] Ocean sediments show a decreased SST of 1° to 2°C in the Sargasso Sea during the 16th to 19th centuries, which is consistent with a reduced NAO but not with uniform basin-wide cooling, while other evidence suggests colder North Atlantic temperatures during those centuries, including evidence for increased sea ice around Iceland. [286]

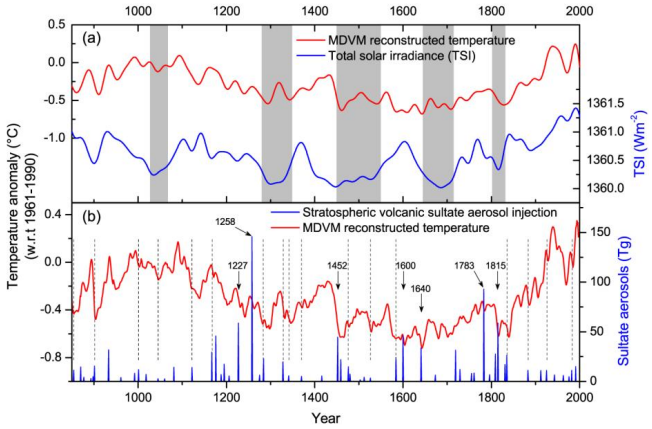


Figure 7.12: The figure presents a comparison of MDVM reconstructed temperature anomalies (red lines) with external forcing factors over the past two millennia. Panel (a) shows the reconstructed total solar irradiance (TSI) variations (blue line), with 30-year low-pass filtered data and shaded regions indicating the timing of great solar minima. Panel (b) displays reconstructed stratospheric volcanic sulfate aerosol injection (blue bars) in the Northern Hemisphere, with labeled major eruptions, alongside the MDVM temperature reconstruction. The plots illustrate the temporal relationship between climate variability and solar and volcanic forcing, highlighting periods of significant cooling associated with volcanic events and solar minima. [291]

The link between the Sun and our weather depends on a tiny physical step. It connects cosmic ray ionization — the creation of charged particles in the air — to the way clouds form. [287] This connection may explain reported oscillations in the troposphere and stratosphere. It supports the idea that the Sun's control over cosmic rays changes cloud cover, and thereby the climate. [103] We can test this by comparing the clean radionuclide record with shifts in the geomagnetic dipole field strength — the main axis of Earth's magnetic field. That comparison shows geomagnetic shielding drives variability over thousands of years. Stronger fields mean less cosmic radiation reaches us. Solar modulation dominates on shorter, multidecadal to centennial scales. Radiation peaks match grand solar minima. But the Sun's influence fades over longer periods. [56][230][11][220][288][181] Researchers at the GeoForschungsZentrum (GFZ) in Potsdam dug deeper into these magnetic shifts. They measured field strength at the Kolbeinsey Ridge in the Iceland Sea, going back 300000 years. [223] The data suggests a strong field shields Earth from galactic cosmic rays. Weak fields near reversals let those rays bombard the equator. [223]

Ice sheets in North America shifted their patterns with every major flip of the Earth's magnetic field. [289] These shifts tracked changes in the land's topography. The link suggests that geomagnetic reversals line up with cold spells in the ancient climate record. The match is not tight, but it is there. A closer look at the last millennium shows a weak, steady link between Northern hemisphere temperatures and the strength of the magnetic field. [230] This hints that cosmic rays help drive climate changes. The

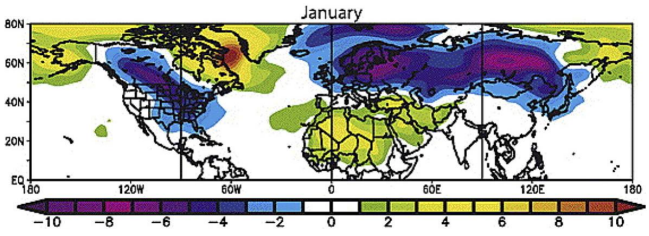


Figure 7.13: This figure displays a global map of surface temperature anomalies for January, illustrating the pattern associated with the negative phase of the North Annular Mode, which corresponds to periods of reduced solar output. The map uses a color scale from -10°C (dark purple) to +10°C (dark red), showing significant cooling (purple/blue) over the Arctic and northern North America, with warming (yellow/-green) in mid-latitudes and tropical regions. This pattern closely matches the temperature anomalies observed during the late Little Ice Age (1650–1850). [290]

last two warm interglacial periods ended suddenly. The magnetic field was weak then, near a reversal. This happened roughly 70000 and 180000 years ago. [223] The timing suggests that a weakening field can boost global cooling. A physical mechanism strong enough to do this exists. It points to a deeper connection. The inverse link between solar cycle length and long-term temperature shifts may stem from how the Sun modulates cosmic-ray flux over long periods. [103] The atmospheric evidence is indirect. Yet it supports the broader idea. Solar variability plays a significant role in shaping Earth's climate and geological activity.

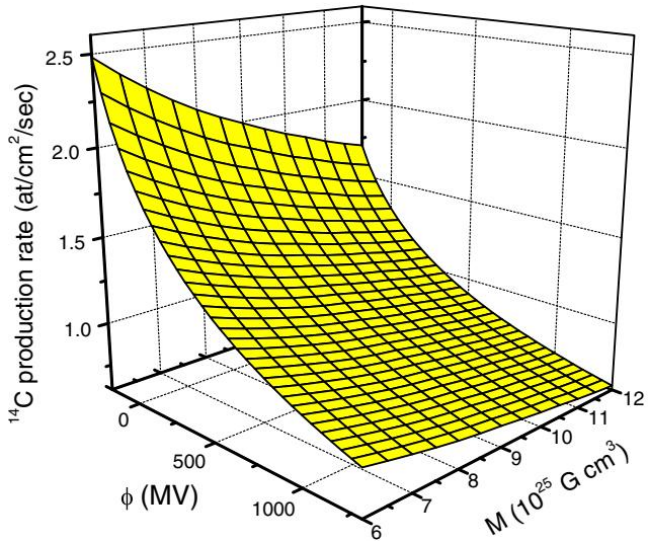


Figure 7.14: A 3D surface plot shows the globally-averaged production rate of carbon-14 (^{14}C) in atoms per square centimeter per second as a function of modulation potential (, in MV) on the x-axis and geomagnetic dipole moment (M, in 10^{25} G cm^3) on the y-axis. The surface, colored yellow, decreases monotonically with increasing and M, indicating that higher solar modulation and stronger geomagnetic fields reduce cosmic-ray-induced ^{14}C production. The plot illustrates the combined influence of solar activity and Earth's magnetic field on cosmogenic nuclide generation. [44]

7.6 What if the next minimum brings the next big eruption?

The Smithsonian Institution's Global Volcanism Program — the archive that catalogs 1,408 Holocene volcanoes and 9,928

eruptions — provides the data for such analyses. [181] Yet the record is incomplete. It varies by era and by eruption size. Newhall and Self note that dates for the biggest blasts, those with a Volcanic Explosivity Index (VEI) of 5 or more, only become reliable around 1800. That index measures the size of an explosion. The record fills in around 1900 for VEI 4 events. It does not fill in for VEI 3 events until around 1960. [220] This temporal bias explains the spike in recorded VEI 3 eruptions since 1800. We likely see more small eruptions because we are better at spotting them. It does not necessarily signal an actual increase in worldwide volcanism. [220] The historical record is spotty, especially before the sixteenth century. Any analysis of long-term trends must account for these gaps. When examining eruption frequency from 1700 to 2020, researchers applied smoothing filters to remove random noise. They assumed the data gaps were random too. [166] But the pre-modern record is incomplete. Many significant eruptions may have gone unrecorded. They may remain unknown to science. This uncertainty is critical when projecting future hazards. [82] Establishing these geological baselines suggests that future large-scale eruptions might coincide with solar minima. This highlights the need for rigorous hazard assessment in regions like Peru, where populations live near active volcanic structures.

Separating volcanic signals from the background noise of solar radiation and oceanic oscillations remains difficult. The Icelandic Laki eruption of June–August 1783 illustrates this challenge perfectly. It was a massive blast, yet it failed to trigger immediate global cooling. A strong El Niño event in 1782–1783 likely masked the volcanic signal. That warm ocean phase diluted the cooling effect. [292][220][49][76][1] Large eruptions can still punch through this variability to leave marks in sensitive regions like Europe. But each event must be judged on its own terms. [292] Huaynaputina offers a different lesson. Before AD 1600, its fumarolic activity was mild. Historical accounts say Indian people climbed the volcano to make offerings. They sought to appease it. The rock record agrees with these stories. The pumice-fall deposit from AD 1600 contains few lithic fragments. This suggests the vent was already open. The plinian column could therefore rise quickly. [261] We learn to manage disasters through repetition. Without repeated experiences, coping measures do not evolve. The National Hurricane Center saw this after the 2004 and 2005 hurricane seasons. They noted a stark gap in understanding. Those who have never experienced a direct hit by a major hurricane seem incapable of envisaging what one is like. [39]

Furthermore, those who have experienced such events ‘only remember the worst effects of a hurricane for about seven years.’

Consequently, predictions that the risk of a significant event is substantial do not, historically, generate the collective will necessary for us to make investments in resiliency. This holds true even when science indicates quite clearly that the event is quite likely to happen eventually and that the consequences of being unprepared will be severe. [39] As Clive Hamilton observed, 'Sometimes facing up to the truth is just too hard. [39] When the facts are distressing it is easier to reframe or ignore them.' [39] Geological Survey national volcanic threat assessment demonstrates the utility of this kind of risk analysis by ranking volcanoes into five relative threat groupings based on a 24-factor schema. [293] This methodology accounts for the highly variable knowledge of eruptive histories of more than 160 active U.S. volcanoes, as well as the diversity of eruptive styles and geographic settings. [293] By prioritizing where to focus volcanic risk mitigation through research, monitoring, hazard assessment, and community engagement, the framework serves as an effective communication tool for engaging stakeholders and the public. [293] The adaptation of this threat assessment methodology by groups in Chile, New Zealand, Argentina, the Caribbean region, and Peru, along with its inclusion in the United Nations Office for Disaster Risk Reduction Global Assessment Report for Risk Reduction 2015, suggests the broad applicability of such structured risk management frameworks. [293]

Pinpointing the odds of a volcanic outlier is hard. The data needed to constrain those probability tails is often missing. Newhall and Self note that the frequency record for past volcanism has significant shortcomings. [294][166][220][295][296][262] It is generally incomplete. Ice cores tell one story. For the last 1000 years, the decadal rate of all eruptions captured in ice has remained approximately uniform. [294] Other sources tell another. Their estimates show a marked increase in eruptive frequency as they approach the present. [294] This apparent rise is largely attributed to the advent of satellite observations. [294] Satellites catalogue smaller eruptions globally. They do not signal an actual increase in worldwide volcanism. [294] Extensive ice core samples reflect the occurrence of large eruptions. They fail to capture the small ones. [294] Recent short-term observations are the reverse. They accurately represent small, more frequent eruptions. But the repose times of the larger eruptions are beyond the length of the record. [294] The result is a gap in the middle. The relative frequencies of eruptions for the period 0–999 AD are much less than for the period 1000–2000 AD. [294] It remains unclear whether this reflects an actual lull in volcanism. Or it may reflect a failure of the record to capture or preserve the events.

The geological record of Vesuvius reveals that prehistoric erup-

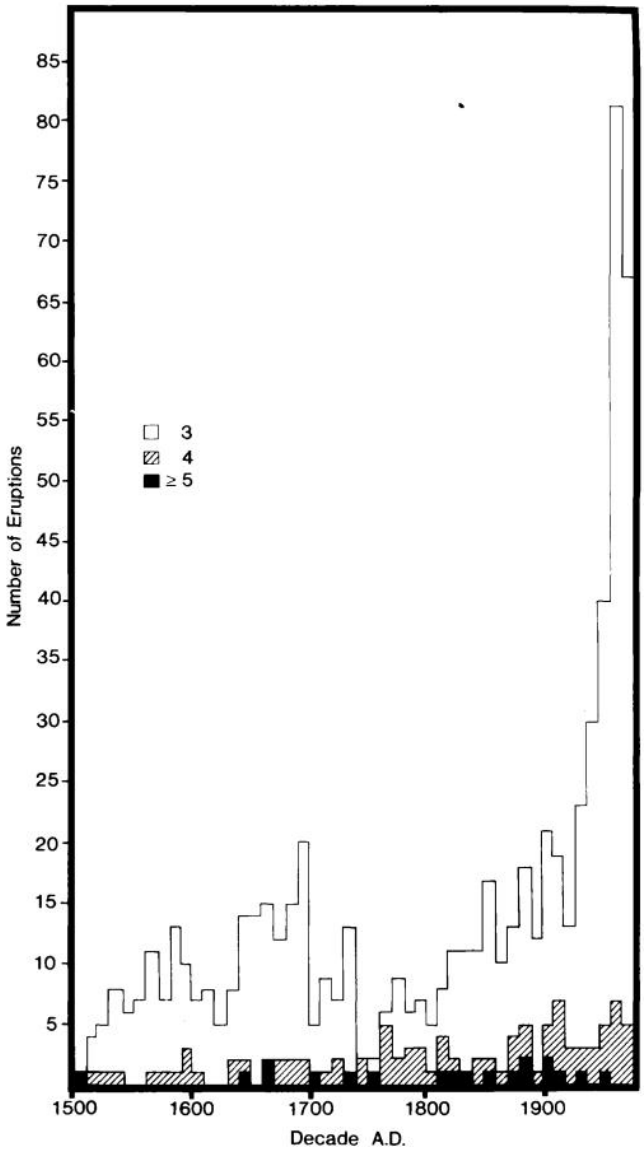


Figure 7.15: This bar chart displays the number of volcanic eruptions by Volcanic Explosivity Index (VEI) from 1500 to 1950 A.D., categorized into VEI 3 (white bars), VEI 4 (hatched bars), and VEI 5 (black bars). The data shows a sharp increase in the frequency of VEI 3 eruptions throughout the period, particularly after 1800, while the number of VEI 5 eruptions remains low and relatively stable, with only slight increases over time. [277]

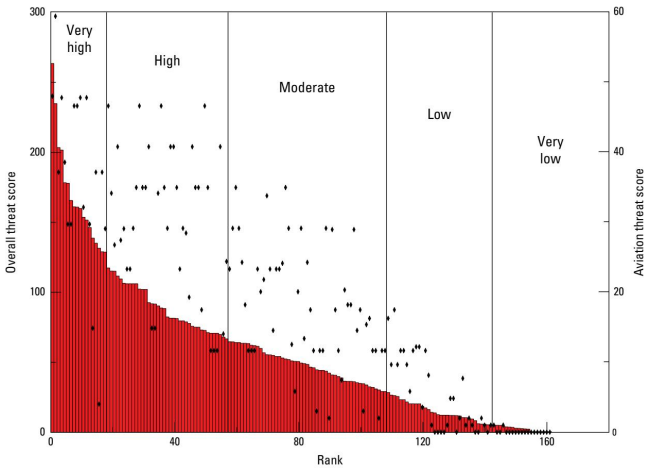


Figure 7.16: The figure displays a composite visualization of volcanic threat assessments for U.S. volcanoes, combining a ranked histogram of overall threat scores with scatter points for aviation threat scores. The left y-axis shows overall threat scores (0–300) plotted as a red histogram against rank (0–160), with vertical bands labeling threat categories: Very high, High, Moderate, Low, and Very low. Black diamond markers represent aviation threat scores (right y-axis, 0–60) plotted against the same rank order, showing a general decrease in both threat metrics with increasing rank. [293]

tions, specifically the Pomici di Base and Avellino Pumice events occurring 22,000 and 4,300 years ago respectively, were accompanied by debris avalanches that reached the coast. [82] This historical evidence suggests that future large-scale flank failures of volcanoes like Vesuvius raise implications for tsunami hazards associated with debris avalanches reaching the coast. Structural failure of the volcanic edifice could also occur, triggering landslides and potentially caldera formation, while mixing of ground water and magma within the conduit during the waning stages of an eruption could produce hydrovolcanic explosions. [82][293][277] The difficulty of reconciling purely statistical analyses of eruption frequency and clustering with what the geological record tells us about magma-reservoir processes means no one knows when Vesuvius will reawaken. [82] The 2018 update to the U.S. [293] This assessment framework underscores the need to monitor specific physical indicators, such as whether a volcano has produced a tsunami within the Holocene or has hydrothermal explosion potential due to extensive thermal features. [293]

Chapter 8

There Is No Such Thing as Settled Science

Warming did occur, but the dominant driver was solar activity — not anthropogenic CO_2 — and the natural CO_2 budget plus low climate sensitivity make a CO_2-only attribution untenable.

8.1 Warming happened — but who did it?

The twentieth century witnessed a pronounced warming trend, a fact that serves as the foundational premise for the dominant narrative attributing recent climate change primarily to anthropogenic carbon dioxide emissions. [249] In a pivotal study, Schurer et al. compared the expected signatures of high and low solar forcing against an ensemble of surface air temperature reconstructions for the past thousand years, carefully accounting for internal climate variability, volcanic eruptions, and uncertainties in both proxy data and model outputs. [297] Consequently, the mainstream interpretation holds that the warming observed in the Northern Hemisphere cannot be explained by solar cycles alone, setting the stage for a debate that centers on whether the current attribution models have adequately separated natural multi-decadal oscillations from anthropogenic signals or if they have inadvertently dismissed a more substantial solar contribution due to an underestimation of total solar irradiance variability and its potential amplification mechanisms.

The study weighs the different forces at work. Volcanic eruptions and greenhouse gases explain most of the climate shifts before the twentieth century. Solar forcing plays a much smaller role. [297] The researchers calculated a strict boundary for that role. The 95% upper limit on the solar scaling factor rules out a large solar contribution from the Maunder Minimum to the present. That contribution cannot be greater than about 0.15 K. This limit holds even if we account for missing solar–ozone feedbacks. Those feedbacks would mostly shift regional temperatures. They would not significantly boost the hemispheric mean response. [297] The authors draw a sharp conclusion from this. For solar forcing to drive the warming strongly, the real-world climate sensitivity to

it would have to be almost an order of magnitude smaller than in climate models. They consider this scenario highly unlikely. Thus, the evidence shows that solar forcing is not a strong driver of large-scale Northern Hemispheric temperature variability over the past millennium. This undermines the claim that solar activity alone accounts for the observed warming trend.

The global mean annual surface temperature increased 0.55°C from 1860 to 1990, a period coinciding with a steady rise in overall solar activity levels. [298] While standard climate models incorporating small total solar irradiance (TSI) changes of approximately 0.1% attribute recent warming primarily to anthropogenic greenhouse gases, this consensus view faces significant challenges from alternative reconstructions. [64] Temperature records derived from boreholes, such as the study by Huang et al., provide robust evidence for a 1.0–1.5 K difference between the Medieval Warm Period and the Little Ice Age, contradicting reconstructions that show minimal variation. [64] Consequently, some studies utilizing high solar variability estimates, which propose TSI changes of the order of 0.4%, argue that solar variability may have been the dominant cause of long-term warming since the 19th century. This perspective highlights the possibility that irradiance from the quiet Sun varies significantly in time, offering a natural explanation for the warming trend that does not rely solely on industrial CO_2 emissions. [64][31][1][46]

The twentieth century's unusual warmth stems from a specific alignment. Two peaks in the 65-year oscillation — a long-term cycle that shifts heat around the climate system — arrived within the same century. At the same time, solar activity reached an unusually high level. This combination suppressed the cooling expected in the mid-century and amplified the LTCW. [1] If we view this oscillation as a mechanism that redistributes heat from its cold phases to its warm ones, the accounting changes. This interpretation assigns only 10–20% of the twentieth century's temperature rise to GHGs. The remaining 80–90% falls to solar activity. This 80–90% figure sits at the top end of the solar-attribution estimates presented across this book. It spans from the high-variability TSI reconstructions, which make the Sun the dominant cause of warming since the nineteenth century, up to this near-total attribution. Every one of these estimates places the Sun, not carbon dioxide, in the driver's seat. The MSM illustrates this intensity. It was a period of 70 years with above-average solar activity. This represents the longest such stretch in the 320-year sunspot record. [1] The fact that the Modern Maximum coincides with the biggest period of warming in 600 years should not be dismissed as an unrelated coincidence. [1] A test of this interpretation is about to take place. [62] Extrapolation of the

forcings indicates we have entered, for the first time since 1900, a period when low solar activity coincides with a low in the 65-year oscillation. [1]

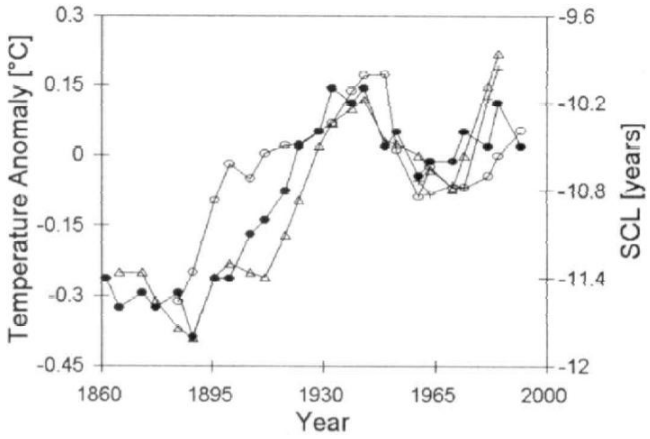


Figure 8.1: The chart displays temperature anomalies in degrees Celsius (left y-axis) and solar cycle length (SCL) in years (right y-axis) as functions of year from 1860 to 2000. Multiple time series, marked with different symbols, show temperature anomalies generally increasing from the late 19th century, with notable fluctuations, while SCL exhibits a decreasing trend over the same period, suggesting a potential inverse relationship between solar activity and global temperature anomalies. [299]

The official consensus within climate science, as articulated by Working Group I of the Intergovernmental Panel on Climate Change (IPCC), maintains that solar activity exerts only a limited influence on terrestrial climate dynamics. [8] However, this consensus overlooks abundant empirical evidence suggesting that the Sun has had a large influence on climate over the Holocene period, with temperature changes between periods of low and high solar activity reaching the order of 1–2 K. Such large variations are inconsistent with the consensus and herald a real and solid connection between solar activity and Earth's climate, challenging the notion that solar effects are insignificant. [64]

The historical record tells a different story. It suggests recent warming is not a unique anomaly caused only by industry. [298] Look at the Wolf Minimum. Radiocarbon dating of pine tree rings reveals a steady climate cycle of about 210 years. This rhythm lines up with those grand solar dips. [19] That match strengthens the case for a solar link to temperature changes. It also questions the idea that twentieth-century warming is entirely new. [94]

8.2 The natural CO_2 budget

The usual story puts human emissions at the center of climate change. That view often misses the order of events in the deep past. Temperature shifts came first. Carbon dioxide followed. [7] This sequence is not a small glitch in the data. It is a pattern in the paleoclimate record. Over the last 420 kyr, CO_2 variations broadly tracked Antarctic temperature. They lagged behind by several centuries to a millennium. [7] The data suggest that

atmospheric CO_2 concentrations lag temperature increases by 800 ś 400 years during glacial terminations. Take Termination III, for example. That warming event stretched over a 5000-yr period. The CO_2 increase arrived 800 ś 200 years after the Northern Hemisphere deglaciation. [300][7][301][302] Ice core data indicate that temperature leads CO_2. This fact challenges the assumption that rising CO_2 is the sole or primary cause of recent warming. [302] Think of the ocean as a vast reservoir. It releases gas as it warms. This process is governed by Henry's law. [8] The lag seen in the ice cores fits this picture. Temperature changes may drive the carbon cycle, not the other way around. [300] Thus, the natural CO_2 budget, shaped by solar forcing and oceanic response, offers a coherent explanation for the observed CO_2 increases without requiring an exclusive attribution to human activity.

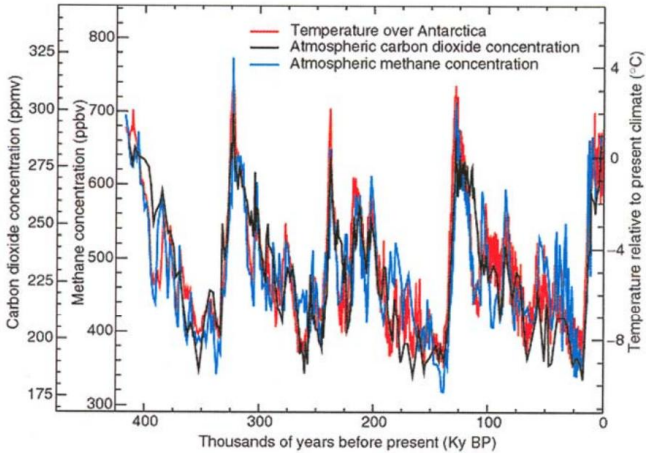


Figure 8.2: A line graph displays four hundred thousand years of proxy data from ice cores, showing temperature over Antarctica (red, right y-axis in °C relative to present climate), atmospheric carbon dioxide concentration (black, left y-axis in ppmv), and atmospheric methane concentration (blue, left y-axis in ppbv), all plotted against time in thousands of years before present (Ky BP). The data reveal strong correlations between temperature and greenhouse gas levels, with both CO_2 and CH_4 concentrations fluctuating in phase with temperature changes across multiple glacial-interglacial cycles. [302]

The oceans hold a vast stock of carbon dioxide, roughly 50 times more than the atmosphere contains. [302] That reservoir is not static, however. Its capacity to hold gas depends strictly on temperature. The historical record confirms this dynamic. During glacial terminations, temperature changes arrive first. Carbon dioxide shifts follow 400 to 1,000 years later. [303] This lag indicates that terrestrial temperature drives atmospheric carbon dioxide levels, rather than the reverse. The rise since the Little Ice Age fits this pattern. Solar heating warms the ocean. Warm water holds less gas. It releases the excess into the air. Carbon isotopic ratios do show fossil fuel burning. But that source accounts for only 1 to 5 percent of the total increase. [304] The data suggest that the dominant driver is the thermal response of the oceans. Natural climate cycles, not anthropogenic emissions, appear to lead the way.

Modern observational studies suggest that atmospheric CO_2

changes lag global surface temperature changes by approximately 9 to 12 months. This temporal sequence is consistent with the mechanism where temperature controls the CO_2 level, as evidenced by MacRae who found that atmospheric CO_2 changes lag atmospheric temperature changes by about nine months. [1][301][52] Furthermore, Humlum et al. show that CO_2 increases consistently follow temperature increases by about 9 to 12 months, indicating that the correlation between cause and effect data proves there is no observable cause-effect relationship in the opposite direction. The lack of a statistically significant correlation between the rate of human carbon emissions and the rate of change of global surface temperature, even using time lags up to 20 years as found by Munshi, supports the view that temperature drives CO_2 rather than vice versa. [301] This aligns with the broader finding that CO_2 increases do not correlate with human CO_2 emissions but instead follow temperature increases, reinforcing the hypothesis that earth's temperature is driving atmospheric carbon dioxide levels. [301] Thus, the observed lag and correlation patterns indicate that natural processes, particularly ocean outgassing driven by surface temperature, play a dominant role in atmospheric CO_2 variations. However, this foundation appears unstable when scrutinizing the historical measurement series.

Charles Keeling trusted the French chemist Reiset's late-19th-century measurements as the most accurate available. [10] That trust overlooked a methodological flaw. Reiset dried the air with sulphuric acid before analysis. The acid absorbs some of the CO_2, dragging the results down by about 20 ppm. This bias was known since 1848, and the Belgian chemist W. Spring tested it quantitatively in 1883. [10] The corrected average for the century's end was 312 ppm, not the 294 ppm that fit Keeling's impression of pre-industrial levels. If the baseline was not 280 ppm, the argument that human CO_2 causes all the increase above that threshold loses its empirical grounding. [305] Beck's reconstruction from chemical data supports this view. It shows levels reaching 440 ppm in 1820 and again in 1945. These peaks contradict the low proxy ice-core values that have dominated the discourse. These findings suggest that natural fluctuations may have played a more significant role than currently acknowledged. [305][10][7] Consequently, the attribution of recent CO_2 rises exclusively to anthropogenic sources remains open to debate. However, ice-core data from Siegenthaler and Joos indicate a different pattern. Natural CO_2 increased by 17 ppm, or 6 percent, before 1900. Human emissions totaled only 5 ppm at that time. This contradicts the assumption of constant natural variability.

Beck's chemical reconstruction paints a different picture. It shows

CO_2 levels hitting 440 ppm in 1820, then rising to that same height again in 1945. These peaks sit far above the values derived from ice cores alone. Jaworoski argues that ice cores fail to capture the true atmospheric history. He concludes that natural processes produce 97 percent of the CO_2 in the air. [305] The ice record does link carbon dioxide and temperature, but the order matters. Temperature changes always come first. CO_2 levels follow after a lag of 400 to 1000 years. [52] This sequence suggests that Earth's temperature drives atmospheric CO_2, not the other way around. The oceans hold the key. They store far more carbon dioxide than the atmosphere does. [16] Carbon dioxide dissolves in water, but less of it stays dissolved as water warms. So, when the oceans warm, they release CO_2 into the air. [52] This physical mechanism suggests that temperature-driven outgassing explains most of the CO_2 rise since 1750. The oceans have warmed since the Little Ice Age, pushing gas upward. [301] The observed climate changes fit this pattern. They align with shifts in albedo and the associated warming and cooling of the seas. This supports the view that we are seeing a natural cycle. It is a cycle visible in palaeoclimate data for most of the last 10000 years. [304]

At annual and 2-7 year time scales, the concentration of CO2 in the atmosphere is strongly driven by the ocean, and at longer time scales, greenhouse gas concentrations lag behind temperature. [304] Carbon isotopic ratios indicate that while there is a contribution from the burning of fossil fuels, it is of the order of 1-5 percent of the increase, implying that the warming of the oceans is a major contributor to the observed rise in CO2. [304] Furthermore, the Earth's atmosphere is fairly stable and resilient; carbon dioxide levels during the Ordovician period were approximately 5,000 ppm, yet these high levels did not throw the world into runaway global warming. If exceptionally high carbon dioxide levels did not cause runaway global warming in the past, it is reasonable to question why minimal levels of 387 ppm would do so in the future, reinforcing the conclusion that the available evidence indicates climate change is predominantly natural and occurs mostly in response to variations in solar heating of the oceans. Consequently, the attribution of recent warming primarily to anthropogenic emissions appears to be an oversimplification of a complex, naturally driven system. [52][304][303][302][306][305]

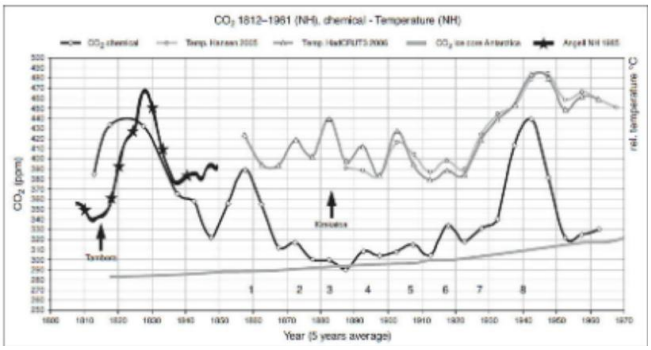


Figure 8.3: This line graph displays over 90,000 direct chemical measurements of atmospheric CO_2 concentrations (ppm) from 1812 to 1961, plotted as a 5-year moving average against the year. The primary black line shows CO_2 levels, which exhibit significant short-term fluctuations and a general upward trend, particularly after the 1940s. The graph also includes several other data series for comparison: temperature reconstructions (e.g., Harari 2005, 166KCFRITS 2006), CO_2 data from Antarctica, and a temperature record from Argel NH 1885, all plotted on a secondary right-hand y-axis in relative temperature units. The data reveals a complex pattern of CO_2 variability, with notable peaks around 1910 and 1940, and a marked increase in the mid-20th century. [307]

8.3 The surface temperature record under a magnifying glass

We must look closely at the global surface temperature record. [101] The main worry is how cities skew land-based readings. China shows the problem clearly. Rapid urbanization has turned many rural stations into urban sites. This suggests that urbanization bias persists across many records. [148] Scientists use homogenization algorithms to fix this. These statistical methods smooth out artificial warming spikes. But this correction may spread warmer urban temperatures across wider areas. That process could inflate the Global Surface Air Temperature (GSAT) estimates used in recent assessments.

The standard defense of global temperature datasets relies on statistical homogenization techniques, such as the Menne & Williams algorithm, which are designed to remove non-climatic biases from raw station records. [148] Proponents argue that these automated methods substantially reduce urbanization bias, thereby rendering the combined urban and rural data representative of true hemispheric trends. [101] However, this confidence is challenged by evidence suggesting that the algorithm performs poorly when a substantial fraction of neighboring stations share similar non-climatic biases. In such scenarios, the method can lead to "urban blending," a process where the urbanization bias of heavily urbanized stations is not removed but rather averaged with neighbors. [148] Consequently, if rural stations are few, they may have artificial urbanization bias introduced into their records,

effectively aliasing the urban signal onto rural trends. Critics dispute homogenization methodologies, arguing they may inadvertently cause 'urban blending' that aliases urban bias onto rural stations. This implies that the homogenized Global Historical Climatology Network may retain significant systematic errors, particularly in regions where siting biases are widespread, undermining the assumption that statistical adjustments fully correct for the urban heat island effect. [148][51][101]

The integrity of the terrestrial temperature record since 1900 faces scrutiny from urban heat-island effects, which may distort the apparent warming trend. [8] Analysis of 5x5 degree grid boxes by Jones and Moberg reveals that statistically significant warming trends are present in only 10–20% of available boxes, with most land-area warming concentrated near large cities and urban centers rather than being uniformly distributed. [308] This spatial correlation suggests that urbanization and land-use change, rather than greenhouse gases, drive the most pronounced local increases. [308] Further evidence indicates that standard adjustments for these non-climatic factors are insufficient. [8] Ross McKitrick and Patrick Michaels demonstrated a strong correlation between urbanization indicators and "urban adjusted" temperatures, concluding that fully correcting the surface temperature data for such extraneous factors reduces the estimated 1980–2002 global average temperature trend over land by about half. [8]

Jos de Laat and Ahilleas Maurellis mapped warming against industrial growth. The patterns matched closely, suggesting a large upward bias in the global trend. [8] The Urbana, Illinois station offers a concrete case. As the university campus expanded around the thermometer from 1900 to 1983, the local air warmed by 0.9°C. When researchers moved the instrument to a rural site, that heat vanished. [8] These examples imply that current adjustments for urban heat islands may be inadequate. If so, up to half of the apparent land warming since 1900 could be an artifact of city growth. [308][8][309] Consequently, the true scale of human-caused warming might be smaller than the record suggests, provided these localized biases remain uncorrected. [308][8][309]

The integrity of the surface temperature record hinges on whether urbanization has introduced a measurable warming bias, a question that remains contentious despite widespread assertions to the contrary. [148] While some analyses suggest minimal impact, empirical comparisons between urban and rural stations reveal significant temperature differences that contradict claims of no statistically significant urbanization impact. This discrepancy is not merely theoretical; it manifests in concrete data from diverse

global locations. [8][148][101] For instance, Ren et al. noted that annual urbanization-induced warming at Beijing and Wuhan stations accounted for about 65–80% of the overall warming in 1961–2000, demonstrating that local anthropogenic effects can dominate regional trends. [148] Similar nocturnal warming and daytime cooling patterns were observed in California's Central Valley by Christy et al., where increased irrigation suppressed daytime temperatures via evaporative cooling while warming nights through increased heat capacity. [8] These findings, echoed in studies across China, Europe, and even remote villages like Barrow, Alaska, confirm that urban heat-island effects are pervasive and often greatest at night and in higher latitudes during winter. [8] Consequently, the assertion that current surface air temperature records are free from urbanization-induced bias is undermined by numerous studies showing significant warming in urbanized areas, necessitating careful scrutiny of homogenization procedures that may inadvertently retain these artificial signals rather than removing them.

Building a temperature map from rural stations alone acts as a safety check. It sidesteps the messy adjustments that homogenization procedures apply to mixed urban and rural data. [101][148] This method matters most where rural stations are thick on the ground. There, the gap between raw readings and adjusted ones can change how much warming we think has happened. The idea is simple. Raw rural records might show the climate's true shift better than blended datasets. [101] Homogenization tries to fix non-climatic errors, but it can create new uncertainties instead. [148] The resulting rural-only maps suggest a different story. Their temperature trends often diverge from those in standard global datasets. This split forces us to look closely at our data sources. It also demands scrutiny of the processing methods behind climate studies. Choosing raw rural data over homogenized global records can lead to different interpretations of history. [101]

We must look closely at the surface temperature record, especially where development is rapid. [148] China offers a clear example. Since 1953, observers there appear to have kept strict schedules. Earlier records do not show that same consistency. [148] Menne & Williams applied net adjustments to the data. It is plausible that some of these corrections fix time-of-observation bias. Yet the evidence suggests such biases are quite modest for the Chinese network. [148] Tang & Ren tried to account for this bias. They used a combination of maximum and minimum temperature records. Their reconstruction looked quite similar to the gridded mean average. This was true even when they used the non-homogenized dataset. [148] This similarity suggests that net biases

from changes in time of observation are quite modest for the Chinese network. [148] Still, this does not rule out the possibility that the relatively large pre-1950s Menne & Williams adjustments are correctly removing some other non-climatic biases. Station moves could introduce such errors. On the other hand, the number of fully rural stations in an area was low pre-1951. Homogenization algorithms like the Easterling & Peterson 1995 algorithm used by Li et al. will lead to urban blending in such cases. [148]

This process means that the urbanization bias will tend to be distributed amongst all stations, both urban and rural, to generate a uniform "homogenous" blend. [148] Indeed, the magnitude of the adjustments for the pre-1951 period is actually greatest for the fully rural subset, and the homogenization algorithm reduces the warmth of the mid-20th century warm period, effectively introducing a warming trend into the fully rural subset. This pattern is consistent with urban blending. [148] If the homogenization algorithm has indeed introduced urban blending, then this would have reduced the reliability of the station records, rather than improved it. [148] Consequently, homogenization adjustments in Chinese records pre-1951 are greatest for rural subsets, potentially introducing artificial warming trends via urban blending. This mechanism explains why Li et al. failed to identify much urbanization bias in their analysis, as the algorithm effectively masks the very signal it seeks to correct. [148] The implication is that the rural-only composites, often cited as cleaner proxies for natural variability, may themselves be contaminated by the statistical artifacts of homogenization. [148] When urban blending occurs, the distinction between rural and urban stations blurs, and the resulting composite inherits the urban heat island bias. [148] This does not negate the warming itself, but it does complicate the attribution of that warming to specific drivers. [310] The lesson from the Chinese records is that homogenization is not a neutral process; it can actively reshape the temperature trend, especially in periods with sparse rural coverage. [148]

8.4 TSI vs. CO_2 — the Connolly–Soon attribution

Central to this alternative view is the realization that the deep ocean carbon stores are so vast that carbon sinks can be considered unlimited in terms of anthropogenic emissions, a fact supported by large ^{13} excursions associated with the formation of large igneous provinces that formed over tens of thousands of years. [1] By recognizing that constant current emissions lead to a new equilibrium at 240 ppm above the present value, we see that

the system is self-regulating through deep ocean carbon stores. [1] Thus, the focus shifts from panic over emissions to understanding the solar and natural cycle drivers that truly govern our climate, setting the stage for a more accurate assessment of future warming trends and the potential return of cooler conditions.

Greenland's temperature history offers a sharp test for human influence. The island warmed and cooled over the past 500 years, long before we pumped large amounts of CO_2 into the air. Those early swings could not have been caused by us. Merged data from 1784 to 2005 show the warmest stretch arrived in the pre-World War II era, specifically the 1930s and 1940s. This peak came before the massive global industrialization of the last 70 years and the emission of most greenhouse gases. [49][311][7][2][312] Later, southern Greenland cooled by 1.29°C between 1958 and 2001, adding to the ice sheet's mass balance. These shifts were driven by natural variability, not industrial emissions. That rules out CO_2 as the primary driver for the observed changes in the Greenland record. [8]

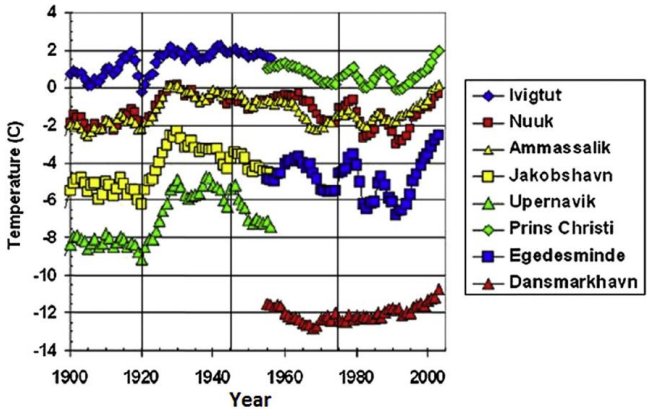


Figure 8.4: This line graph displays annual five-year average temperatures (°C) from 1900 to 2005 for eight Greenland weather stations: Ivigtut, Nuuk, Ammassalik, Jakobshavn, Upernavik, Prins Christi, Egedesminde, and Dansmarkhavn. The data shows that temperature trends vary significantly by location, with the 1995–2005 period exhibiting warming comparable to the 1920–1930 peak, but not surpassing it. [8]

The mid-century cooling trend from 1945 to 1977, which occurred despite a significant post-1945 increase in CO_2 emissions, demonstrates that rising greenhouse gases were not the sole determinant of surface temperatures during that era. This period of cooling, juxtaposed against increasing anthropogenic forcing, challenges the assumption that CO_2 dominates short-term climate variability. [8] Instead, it suggests that natural factors, such as solar activity and internal climatic oscillations, played a substantial role in modulating global temperatures. [1] The coincidence of this cooling with specific phases of the ˜65-year oscillation and solar cycles indicates that these natural drivers can counteract greenhouse warming on decadal timescales. [1] Consequently, the temperature record from 1945 to 1977 provides critical evidence that the climate system's response to forcing is more complex than simple CO_2-driven warming, highlighting the need to account for natural variability in attribution studies.

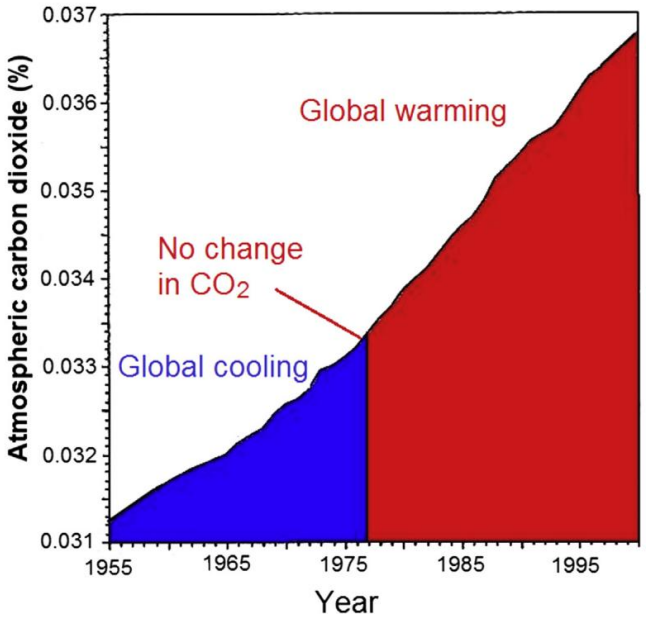


Figure 8.5: A stacked area chart shows atmospheric carbon dioxide concentration (in percent) from 1955 to 2000, with the y-axis representing CO_2 levels and the x-axis representing the year. The data is divided into two periods: a blue area labeled "Global cooling" (1955–1977) and a red area labeled "Global warming" (1978–2000). The chart illustrates that atmospheric CO_2 concentration increased steadily throughout the entire period, with no discontinuity or change in trend at the 1977–1978 transition point, supporting the caption's claim of "no change in CO_2" at the shift from cooling to warming. [8]

The attribution debate hinges on whether solar variability or greenhouse gases drove the twentieth-century warming. [249] While standard models assign a minor role to the Sun, alternative analyses suggest a much larger solar contribution. [248]

The gap between predicted and observed warming suggests the IPCC's central estimate of 3.0 C for doubling sensitivity may be far too large. [313]

The attribution debate hinges on which forcing best explains the observed warming. [1] The unusual warming of the 20th century is mainly due to the coincidence of two highs in the 65-yr oscillation and an unusually high level of solar activity that reduced mid-century cooling. [1] If this interpretation holds, the overwhelming share of the modern temperature increase belongs to the Sun rather than to greenhouse gases — the quantitative split was set out at the opening of this chapter. [1] This apparent success demonstrates that the models rely on several adjustable parameters, chosen specifically to produce agreement with the observed global average surface temperature, rather than robust physical constraints.

Climate sensitivity measures the warming caused by doubling greenhouse gas forcing. The true value could easily be three times larger than the current best guess. [314][7][1][313][46] The IPCC presents a narrow range of 1.5 to 4.5 degrees Celsius. This precision feels earned, but the underlying uncertainty remains vast. Aerosol forcing adds another layer of doubt. The cloud-reflective effect alone carries an uncertainty of at least 200%. Models use this shaky input to build attribution graphs. By tweaking these adjustable parameters, the simulations can match

the predicted warming. This fine-tuning hides a deeper problem. The projections fail to catch the actual temperature variations of the past 100 years. They miss the cyclicities that the data clearly show. [7] Relying on such flexible inputs suggests a troubling conclusion. The attribution of warming to anthropogenic causes is not unequivocally tied to physical evidence. It rests instead on model assumptions. These assumptions can be scaled to fit the data. [1]

The Sun leaves a mark on the climate that survives long after the thermometer arrives. This link between solar modulation — the variation in solar energy reaching Earth — and terrestrial weather stretches back far beyond the instrumental era. [64] John Eddy's early observations anchored this long-term trend. He traced the correlation between solar activity and European climate over the previous millennium. [64] This alignment suggests that the Sun's influence is not a short-term anomaly. It points to a persistent driver operating on decadal to millennial timescales. [64] Such a deep history challenges the notion that recent warming stems solely from anthropogenic factors. Instead, it points to a natural cycle that has governed Earth's climate for centuries. [1]

8.5 Natural cycles as confounders — Scafetta, AMO, PDO

The Barents Sea offers a clear case of this kind of forcing. Long-term temperature records there show steady rhythms tied to lunar mechanics. [315] If similar cycles run across the globe, they might explain much of the warming we see. That possibility weakens the idea that CO_2 is the main driver. [310] Wavelet analysis of Arctic ice extent data reveals dominant cycles of roughly 18 and 74 years. These match patterns in polar motion and North Atlantic water records. [316] The 74-year cycle linked to polar position shifts correlates with cold Arctic water outflow. This suggests lunar gravity steers the release of cold water from the Arctic Ocean into the Greenland Sea. The gap between the polar-position cycle and Greenland ice extent is about 18.5 years. That lag shows Arctic water circulation takes time to adjust. [317][316] This delay supports the view that the Arctic system does not react instantly to forcing. Instead, it blends signals over decades. [90]

Cod in the North Arctic do not follow a simple, steady path. Their population dynamics shift with ecology and fishing pressure, creating a complex, non-linear system. This system tracks temperature cycles with striking precision. The key periods are 6.2 years, 18.6 years, and 55.8 years. These numbers are not random. They

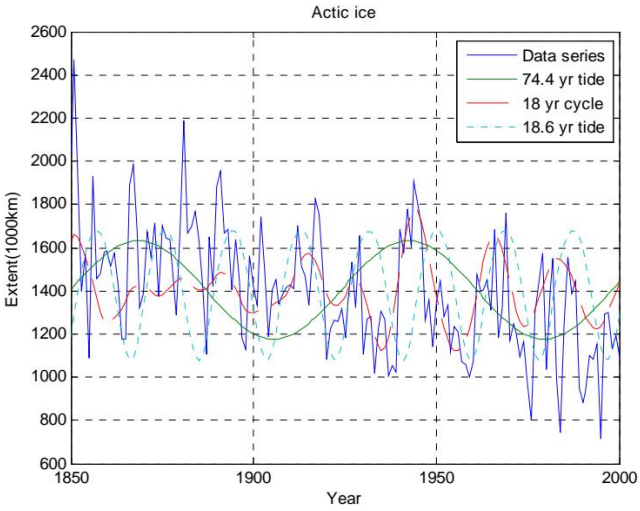


Figure 8.6: The graph plots Arctic ice extent (in 1000 km^2) from 1850 to 2000, showing the observed data series alongside three modeled tidal cycles: a 74.4-year harmonic lunar nodal tide (green), an 18-year wavelet cycle (red), and the astronomical 18.6-year lunar nodal tide (dashed cyan). The data series exhibits significant variability, with the 74.4-year and 18.6-year cycles showing similar long-term oscillations, while the 18-year cycle appears to track shorter-term fluctuations, suggesting a potential influence of lunar tidal forces on Arctic ice variability. [316]

derive from 18.6 divided by 3, and 3 multiplied by 18.6. [318] These cycles likely stem from changes in Earth's nutation, making them deterministic rather than chaotic. The 6.2-year rhythm affects how many young cod survive and grow. The longer 18.6 and 55.8-year cycles shape overall growth rates and maximum biomass. [318] If the system is deterministic, we might manage it. A control strategy could handle these temperature-driven dynamics. This opens the door to simpler models for forecasting future biomass. [318] We can even predict long-term temperature fluctuations using Multi-Layer Feedforward Networks. This suggests Arctic temperature and biomass follow predictable patterns, not random noise. The standard climatological baseline, such as the Roemmich-Gilson climatology, takes a different view. It treats the ocean as an Eulerian field. This means averaging measurements at fixed geographic locations over time. [319]

However, ocean temperature is fundamentally a Lagrangian property, characteristic of specific water masses that move, mix, and transform as they are advected by currents. A water mass at 30° N, 150° W in January 2005 and another at the same coordinates in January 2018 are not the same physical entity; they possess different histories, source regions, and thermodynamic states. [319] Averaging their temperatures produces a statistical artifact rather than a meaningful physical baseline. [319] This Eulerian-Lagrangian mismatch is compounded by the temporal arbitrariness of the chosen averaging period. [319] The baseline is derived from smoothing measurements over the 2004–2018 period, a 15-year window that is physically arbitrary. [319] Major ocean processes, including mesoscale eddies, seasonal convection cycles, the El Niño-Southern Oscillation, the Pacific Decadal Oscillation, and Atlantic Multidecadal Variability, operate on timescales incommensurate with this averaging period. [319] Consequently, the resulting climatology reflects the specific dynamical state of

the ocean during 2004–2018, including whatever phase each oscillatory process occupied, rather than any physically meaningful equilibrium state. Furthermore, changing float density and persistent spatial sampling gaps in polar domains introduce systematic biases, particularly when constructing climatological reference states.

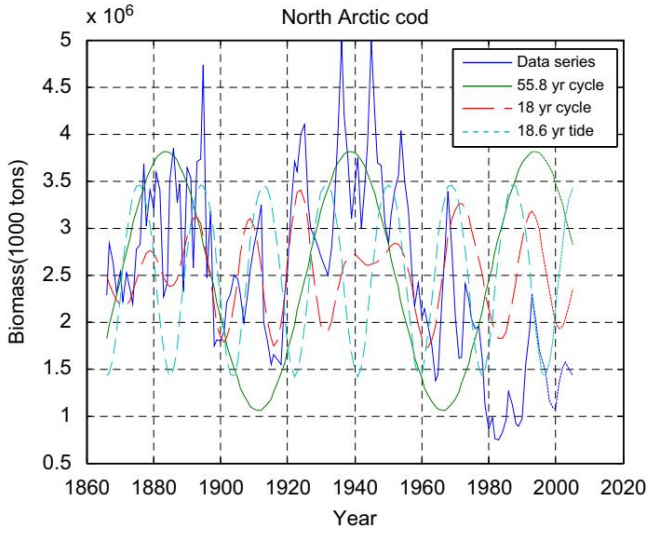


Figure 8.7: The figure displays the biomass of Northeast Arctic cod (in 1000-ton units) from 1866 to 2005 as a blue line, alongside three modeled cycles: a 55.8-year cycle (green), an 18-year wavelet cycle (red), and an 18.6-year tide cycle (cyan). The 55.8-year and 18.6-year cycles are scaled to align with the biomass data, illustrating their phase relationships to the observed fluctuations. The plot reveals that the biomass time series exhibits periodic oscillations that correspond closely to the superharmonic 55.8-year cycle and the astronomic 18.6-year tide cycle, with the 18-year wavelet cycle also showing a similar but less dominant periodicity. [320]

The reliability of the Earth Energy Imbalance (EEI) assessment is called into question by the physical validity of the underlying Argo-float-based estimates of global Ocean Heat Content (OHC). [319] Rather than canceling out globally, these displacements are governed by local, non-stationary processes such as eddies, fronts, and turbulent shear, which introduce incoherent regional errors into Eulerian gridded fields. [319] When these errors accumulate, they create a time-dependent methodological bias in OHC trends, particularly when combined with interannual circulation variability like ENSO or PDO shifts. [319] A rough scaling suggests this effect could shift global EEI estimates by on the order of 0.02–0.1 W m^2, a range comparable to or exceeding some published ensemble spreads that do not account for this foundational data-assignment flaw. [319]

Furthermore, similar artifacts arise from how the reference climatology is constructed, where temperature profiles measured at different times during each month are pooled together and statistically fitted. Consequently, the confidence in EEI trends derived from these datasets is undermined by these unresolved methodological uncertainties. This uncertainty is not merely theoretical; it is embedded in the very metrics used to quantify the planet's energy state. [319] When these errors are synthesized, the resulting uncertainty is far larger than officially reported. [319] Consequently, the apparent energy accumulation driving

the warming narrative may be an artifact of interpolation in unsampled volumes and framework discrepancies rather than a robust physical signal.

Chapter 9

What Can We Do? Preparation for the Next Minimum

Take the Dalton and Maunder baselines as the operating analogue; every preparedness recommendation here improves resilience to extreme weather of any kind, even if the Grand Solar Minimum forecasts are wrong.

9.1 The historical baseline — what cold periods look like

The historical record confirms that these epochs were not merely mild winters. They were extended periods of significant global cooling. This cooling triggered widespread famine, epidemic disease, and profound agricultural failure. [232] The evidence demonstrates that the primary threat was not just the cold itself. It was the cascading failures in food production and public health that followed. [321] As noted in analyses of past solar minima, humanity has faced this danger before. The manner in which we survived offers a template for future preparedness. We adapted in housing, travel, and agriculture. [303] The conditions of a small ice age constrain agricultural production. This leads to famines that require long-term food storage. We also need alternative heat sources to mitigate the massive power outages caused by ice and snow storms. [303]

We need to know exactly how a renewed Little Ice Age would hit us. The historical texts give us that specific picture. They show the real-world consequences of reduced solar activity. This knowledge is essential for building a robust plan. Our infrastructure and individual households must be resilient enough to withstand the severe difficulties. The record from the past offers a concrete test case. Observers at St. Fort Reliance recorded the temperature. This post stood 400 miles southeast of Fort Yukon. The mercury dropped to 69 F (56 C). That figure confirms the extreme thermal lows experienced in the region. [40] The local people said no winter of such severity had ever been known by them. This highlights the unprecedented nature of the event. [40] The consequences were dire. Migrating birds arrived eight to ten days late. The

natives narrowly escaped starvation. In some cases, they were compelled to eat their dogs. They also ate the tanned sealskin covers of their boats. [40]

In the Gulf of Alaska and the Yukon, oral accounts link extreme cold to surging glaciers. The Lowell and Malaspina glaciers moved during the 19th century. Ethnographers John Swanton and Frederica de Laguna recorded these narratives. The stories depict the ice as sentient. The glaciers respond to human behavior. They surge or flood in reaction. [322]

The historical record of the late Little Ice Age reveals that climatic stress often compounded with other societal shocks, creating devastating feedback loops for vulnerable populations. [43] In northwestern North America, the convergence of environmental hardship and biological catastrophe proved particularly lethal for indigenous communities. [43] The mid-19th century smallpox epidemic, for instance, caused breaks in cultural memory and massive loss of life, forcing survivors to migrate to settlements like Guseix or Neskataheen. [39] This historical baseline establishes that cold periods do not merely lower temperatures; they destabilize the ecological and social foundations upon which human survival depends. [43] For instance, the Kaskawulsh Glacier advanced between 1405/1430 and 1440/1625, leaving spruce logs in its end moraine. [322] In most glacierized regions, the positions of glacier termini have been observed only sporadically for less than a century, meaning that although dominant recession is commonly inferred, data are generally inadequate to construct long and detailed time series. [322] Because minor fluctuations encompassing only a few years may point to important brief climatic reversals, these discontinuous records provide limited information, other than generalized long-term trends. [322]

Most data from North America represent sporadic observations of this type, mainly confined to the last hundred years, with the earliest useful observations of Alaskan glacier termini made in the late 18th century, but repetitive surveys of selected glaciers did not begin until the 1930s. [322] By contrast, glacier observations in the European Alps extend back to the early part of the Little Ice Age, where some of the largest, most-accessible glaciers have been observed at frequent intervals since the 17th or 18th centuries. In a few cases, fluctuations of glacier termini during the past 2 centuries have been reconstructed in considerable detail using a combination of written descriptions, drawings, paintings, maps, and photographs. [322] For this reason, and because the Alps lie relatively close to Greenland where the long ice-core acidity record has been obtained, special attention is directed toward the fluctuations of these glaciers. Curves depicting the variations of glaciers in Greenland, Scandinavia, and Iceland commonly contain

many fewer control points than the best Alpine examples and are therefore judged less reliable. [322] In these areas, historical observations have been supplemented by lichenometric dating of recent glacier variations. [322]

9.2 Grid and energy resilience

While terrestrial weather and human errors already account for $75-180bn annually in economic costs from power outages, the potential impact of geomagnetic storms represents a catastrophic risk to the infrastructure's core components. [323] These storms are severe disturbances caused by solar storms in the upper layers of our atmosphere that induce currents in long conductors on the Earth's surface, such as power lines. [323] The resulting geomagnetically induced currents can overload the electric grid system to trigger voltage collapse, or worse, damage a significant number of expensive extra-high voltage transformers. [323] This specific mechanism suggests that massive solar storms can severely damage electrical grid components via geomagnetically induced currents. The economic costs of such an event would be catastrophic, particularly because large transformer repairs and replacements occur on the timescale of weeks to months. [323][324][325] Therefore, understanding the likelihood of extreme geomagnetic storms and the specific vulnerabilities of the North American power grid is essential for assessing the regions at highest risk from this complex natural hazard. The implications for the insurance industry and society generally highlight that preparedness must address not just the frequency of outages, but the duration and severity of those caused by the physical destruction of key infrastructure. [323]

The North American grid hides a sharp fragility. [323] Solar storms push currents into long conductors, like power lines. Those currents can overload the system and destroy expensive extra-high voltage transformers. [323] Replacing such massive equipment takes months or years. The result may be long-term blackouts and chronic supply shortages. This prolonged disruption argues for robust resilience strategies. [323][303][326][327] One proposal is a national electrical power grid control center. Such a hub would monitor transformers across the country. It would also help balance electrical loads from region to region. That balancing act is essential to spare at-risk transformers from destruction during intense geomagnetic storms. [326]

The 2008 Chinese winter storm offers a stark warning about infrastructure fragility. Extreme weather can paralyze transport networks, halting the flow of essential goods. When roads freeze

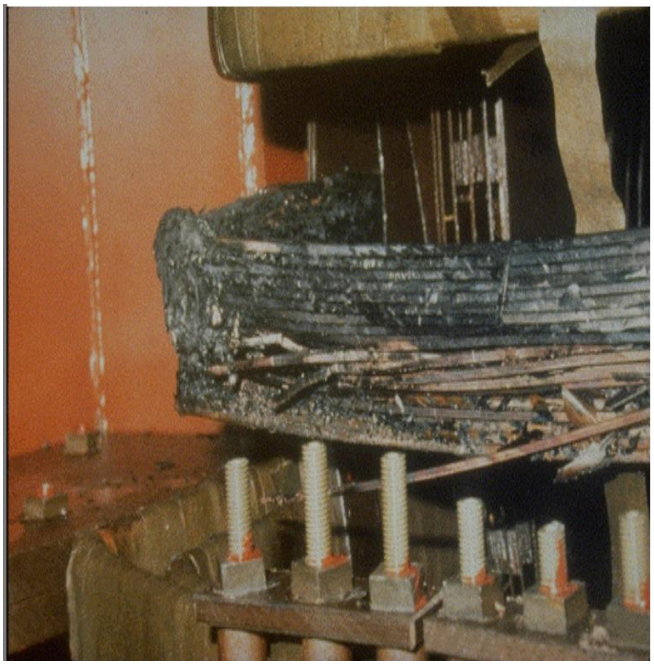


Figure 9.1: The image shows a severely damaged generator step-up transformer, with its internal insulation and windings charred and melted, likely due to the 13–14 March 1989 geomagnetic storm. The exposed core and terminal bushings exhibit extensive thermal degradation, indicating failure from induced geomagnetically driven currents. This visual evidence illustrates the vulnerability of high-voltage electrical infrastructure to space weather events. [329]

under heavy snow and sleet, coal shipments stop entirely. Power plants then face critical fuel shortages, with reserves dropping to emergency levels sufficient for only eight days of generation. [53][49][52][40][87] This disruption triggered cascading blackouts affecting over thirty million people. City water systems also failed, as they require electricity to pump water to homes. [53] To prevent similar failures, plants must stockpile fuel, including coal, fuel oil, and LPG. Supplies must be ready by September 15 each year. [53] This preparation often requires constructing additional storage facilities. [328] The 2008 crisis suggests that extreme winter weather can paralyze transport. It causes critical fuel shortages for power plants. Without robust fuel reserves, the grid remains vulnerable. Hardened transmission lines help too. Cold, snow, and logistical collapse compound the risk. [53][49][52][40][87]

Extreme cold exposes critical vulnerabilities in residential heating systems, particularly when power outages coincide with subzero temperatures. [53] Consequently, distributed-generation and microgrid systems offer a vital redundancy, ensuring that local power can keep heating systems operational even if the central grid fails.

A power cut does more than darken a room. It triggers a chain reaction that knocks out essential services, one after another. [329] In cities, water infrastructure depends entirely on electricity. When the grid goes down, municipal pumps stop turning. Water stops flowing to homes within days. Sewer systems lose their power too. Raw sewage spills into rivers and lakes instead of being treated. [329] This interdependence means that a long outage is a major disaster. Transportation grinds to a halt. Gas

stations cannot pump fuel without power. Life becomes difficult, if not impossible, for months or even years. [52] Restoring the grid is slow work. Most EHV transformers — the massive devices that step voltage up or down for long-distance transmission — are large and costly items. They take a year or more to manufacture. A massive blackout could therefore extend through many months while replacements are built. [52] This threat of a master reset reveals that our technological world is vulnerable. We need robust preparedness to prevent the loss of essential means of response and recovery during extreme weather events.

The structural integrity of long-distance power transmission systems is inherently compromised by the physics of electrical resistance and current flow. [323] As distance increases, so does the total resistance along each transmission line, while the current carried by the line also increases with distance, meaning the total risk rises with the total path length. [323] Because higher voltage lines offer less resistance, larger currents flow relative to lower voltage lines under identical surface electric fields. [323] Consequently, grids with low reserve capacity and long transmission lines appear to be significantly more susceptible to equipment damage and widespread blackouts during extreme geomagnetic events. This heightened susceptibility suggests that infrastructure planning must account for these cumulative risks to mitigate potential cascading failures. [329][323][323]

Long transmission lines are fragile, so we need power closer to home. [330] When a high-voltage transformer breaks, it does not simply get swapped out. Replacement units take five to sixteen months to arrive, leaving whole regions in the dark for an extended period. [323] In cold climates, that darkness is lethal. Modern homes rely on electricity for heat, so when the grid fails, the warmth slowly leaks away. The house becomes unlivable unless you have a backup heat source that does not depend on the grid. [53] Our dependence on energy is so vast that we must plan for fuel security now, not later. We can learn from people who already survive extreme cold. In Antarctica and northern Minnesota, communities know how to keep warm when the weather turns severe. [303] These lessons help us prepare for the harder problems that follow global cooling, including famines and epidemics. Storing food for the long term and finding alternative ways to heat our homes are not just survival tactics. They are part of a broader strategy for resilience. This strategy admits that severe weather may last for a long time. [52] Our ability to withstand such conditions depends on two things. First, our energy infrastructure must be robust enough to hold together. Second, individuals must be ready to adapt to a colder future.

9.3 Food security and agriculture

Analysis of extreme impact events suggests that a massive asteroid or comet strike would produce a global catastrophe, where unfavorable weather conditions and acid rain would severely retard food production, processing, and distribution. The infrastructure required to sustain modern populations would take a significant hit, with broken transportation lines inhibiting the movement of grains from processing centers to population hubs. [331][49][303][88][75] This damage to government, finance, communications, and energy systems would place recovery efforts into shambles, leading to starvation and famines in the general population. [331] A weakened population resulting from such starvation becomes vulnerable to disease, epidemics, and plagues, compounding the initial disaster. [274] The Plan de Preparación para el Gran Mínimo Solar highlights that a Grand Solar Minimum produces an era of great difficulties, including significant global cooling, great famines, and great epidemics. [303] Just as humanity survived the last such episode approximately 300 years ago through adaptation, we must prepare for the constraints on agricultural production that a small ice age imposes. [303] The conditions of a small ice age will constrain agricultural production, leading to famines, and necessitating preparation for long-term food storage. [53] Furthermore, great ice and snow storms produce massive cuts in electricity, making alternative heat sources essential. By studying survival methods in extremely cold climates like Fairbanks, Alaska, International Falls, Minnesota, and Antarctica, we can adapt our clothing, travel, and home designs. [303]

Recovery stalls when infrastructure breaks, and that delay brings widespread suffering. [328] We need systems that do not rely on a single central hub. Decentralized food and energy networks can survive sudden hits and long cold spells alike. Schneider calls this the "Genesis Strategy." It means building reserves while harvests are good, so people can eat when they are not. Maher and Baum echo this idea for global catastrophes. [332] We already have some of these reserves in place. FDR's grain reserve sits in government silos. The Church of Latter Day Saints keeps household supplies for its members. These stores could theoretically feed people for four to seven months. [332] But stockpiling has a cost. It is expensive for populations before the disaster arrives. It can even make food security worse right now. Resources go into storage instead of immediate consumption. This hurts most when hundreds of millions already face hunger. The scale of the threat also matters. Volcanic winters may last years or decades. Stockpiles are at best a partial solution. It may be infeasible to produce enough

reserves to feed the global population for such extended periods. [332][83] Relying on stockpiling alone appears insufficient to mitigate long-term risks. We likely need complementary strategies. [332][83]

The historical record of the 1810s, identified as probably the coldest period in the past five centuries, illustrates how sustained cooling from volcanic eruptions like Tambora and the 1809 Unknown devastated human agriculture and food supply. [83] To mitigate these risks, the Plan de Preparación para el Gran Mínimo Solar emphasizes adaptation strategies observed in extreme cold regions like Fairbanks, Alaska, and the Antarctic. [303] These methods include preparing for long-term food storage and developing alternative heat sources, recognizing that severe cold constrains agricultural production and leads to famine. [303] By studying how individuals survived the last Little Ice Age through changes in clothing, travel, and home design, we can better prepare for the significant difficulties and epidemics associated with future grand solar minima. [303] The primary expense lies not in immediate procurement but in the research, development, and deployment of alternative food practices that can function when sunlight is blocked. [332] Consequently, food stockpiles should serve only as a temporary stopgap measure while this alternative production infrastructure is scaled up to meet demand. Household grain storage — covered in the preparedness sections of this chapter — rules out reliance on grocery stores, which are insufficient and will be quickly exhausted during large impact events where basic infrastructure is destroyed. [328] This method suggests a viable pathway for extending the shelf life of potatoes and beets by destroying insects and microorganisms while simultaneously preventing sprouting. [232]

Furthermore, repeated studies indicate that irradiation cannot mask off-flavors or the smell of spoiled foods, ensuring that safety improvements do not compromise quality. Consequently, resilience requires local self-sufficiency in food, meaning that regions must develop their own capacity for production and distribution. The available options—food stockpiles, traditional agriculture, and foods produced from alternative energy sources—each carry distinct advantages and disadvantages. [332] Stockpiles are versatile but expensive, while agriculture is efficient but less viable in severe catastrophe scenarios. [332] Alternative foods, such as those derived from biomass or fossil fuels, are inexpensive pre-catastrophe but require significant scaling post-catastrophe and may face issues of social acceptability. [332] Therefore, the optimal portfolio typically includes some of each option, adjusted for local constraints. This approach ensures that food supply resilience is integrated into broader risk reduction strategies

without attempting to maximize resilience at the expense of other important objectives, including catastrophe prevention. [332] By recognizing that food supply resilience requires not just the food itself but also the accompanying systems of production and distribution, planners can design more robust and adaptable food systems. [332] Ultimately, the goal is to create a flexible and resilient food system that can withstand the shocks of a changing climate, regardless of the specific mechanisms driving that change.

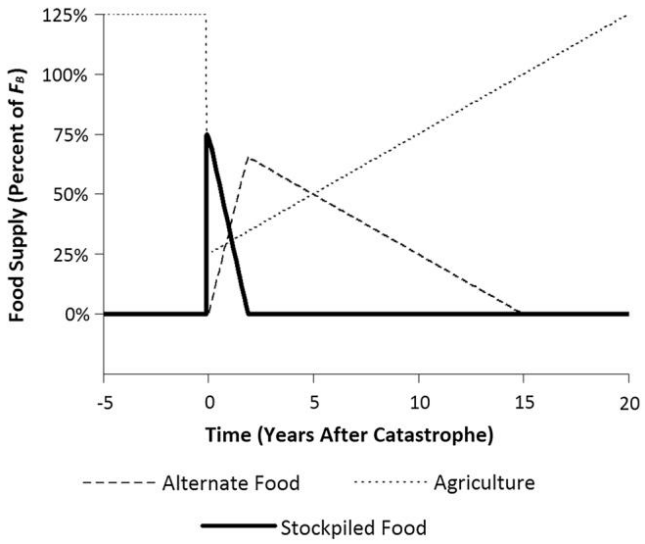


Figure 9.2: The figure displays a line graph showing the percentage of food supply (F) over time (years after a catastrophe), illustrating the contributions of stockpiled food, agriculture, and alternative food. Stockpiled food provides 100% of the supply at year 0, then drops to 0% by year 3. Agriculture begins at 0% and increases linearly, surpassing stockpiled food around year 5. Alternative food starts at 0% and rises sharply, exceeding agriculture by year 10. The graph demonstrates the transition from reliance on stored food to sustained production from agriculture and alternative sources in a post-catastrophe scenario. [332]

9.4 Water, sanitation, and the built environment

In places where winter bites hard, keeping water moving through outdoor pipes is a matter of survival. Standard insulation often cannot stop the freeze when temperatures plunge well below zero. [53] We rely on electric heat tape to help, but that protection vanishes the moment the power fails. If the lights go out for even a few hours during extreme cold, the pipes freeze solid and may burst. The damage goes far beyond a broken pipe. Without flowing water, sanitation systems stop working. You cannot flush toilets or manage human waste, which quickly becomes a severe health hazard. [53][232][330] Power loss also chokes the heating itself. Fuel oil can coagulate into a substance resembling Jell-O, clogging the lines. The furnace then sits idle, even after electricity returns. Documented cases show how a one-hour blackout can turn into a desperate struggle for warmth.

Therefore, any comprehensive preparedness strategy must account for the possibility that electric pipe protection will not suffice, necessitating backup plans for water storage, waste management, and alternative heating sources that do not rely on the grid. To

mitigate this, shoveling snow or placing mulch over underground pipe runs can reduce freezing threats, leveraging the insulating properties of fresh snow, which is approximately equal to a six-inch-layer of fiberglass insulation with an R-value of R-19. This simple intervention supports resilience by preventing the clogging of buried fuel oil lines and the shifting of house foundations during Little Ice Age conditions. [53]

The insulation properties of snow are critical for understanding heat retention in extreme cold. [53] Ten inches of fresh fluffy snow provides insulation equivalent to a six-inch layer of fiberglass (R-19). This demonstrates that natural snow cover can significantly mitigate heat loss from buildings, provided the snow remains fresh and contains about 7 percent water. [53] However, historical accounts from severe cold periods reveal that even with thick stone walls, small windows, and constant fires, indoor temperatures could drop so low that ice formed on interior walls and bed-places, requiring daily removal with a hatchet. In modern contexts, a brief power outage during extreme cold can cause fuel oil to coagulate, rendering furnaces useless and turning a minor inconvenience into a life-threatening struggle. [232] Therefore, while snow offers substantial thermal resistance, reliable backup heating systems and robust building envelopes remain essential for survival during prolonged freezing events, ensuring that internal heat is retained when external conditions become hostile. Consequently, households must prepare manual filtration systems and approaches to treat contaminated tap water or surface ground water. Alternatively, filtering large contaminants using bleached cotton cheese cloth and treating the water with liquid bleach can kill dangerous bacteria. [330] Storing several bottles of bleach and a roll of cheesecloth ensures that individuals can disinfect water using 1/4 teaspoon of regular household bleach per gallon, allowing the mixture to sit for 30 minutes before drinking. [330]

In such emergencies, boiling water may be impossible if electricity is unavailable, making chemical disinfection a critical survival skill. [330] The available evidence demonstrates that non-scented household bleach can disinfect water by killing dangerous bacteria. This method relies on standard liquid bleach containing between 5 percent and 6 percent chlorine, applied at precise dosages—such as one-quarter teaspoon per gallon—to ensure safety without introducing harmful additives like perfumes or dyes. [330] By storing several bottles of this bleach alongside filtration materials like bleached cotton cheese cloth, individuals can effectively treat contaminated tap water, rainwater, or water from rivers and lakes. [330] Consequently, disaster preparedness plans for prolonged loss of clean water and electricity suggest that manual filtration

systems and sanitation systems are recommended for long-term survival without utilities. This approach is consistent with the observation that while vast quantities of water may remain available during a disaster, they are often highly polluted, necessitating independent purification methods such as slow sand filtration or ceramic filters to prevent disease. [328] By integrating these manual systems with grain storage and processing capabilities, individuals can mitigate the risks associated with the destruction of basic infrastructure. [328] Therefore, the implementation of manual water purification and sanitation protocols serves as a critical buffer, ensuring that households maintain hygiene and health even when the broader societal framework fails.

9.5 Household and regional preparedness

The danger is not just a thought experiment. It includes two very different kinds of trouble. One is the sudden, violent strike of a massive solar storm. The other is the slow, grinding chill of a Little Ice Age scenario. Both require plans made in advance, before the trouble arrives. [303] The first line of defense targets the narrow window around a major solar storm. You would stockpile batteries and fill your vehicle's tank with gasoline or diesel. You would secure alternative cooking fuels, such as charcoal or propane. You would also ensure a ninety-day supply of prescription medications. [52] These steps aim to keep basic life functioning during the acute phase of infrastructure failure. [330] The goal is to ease the misery and hardship that may be encountered. This turns the abstract threat of solar variability into a manageable set of logistical challenges. We can address these challenges through deliberate, informed action.

Immediate reactive preparations for an imminent major solar storm or electrical blackout establish the necessity of stocking batteries, fuel, cash, water, non-perishable food, and prescription medications. These measures are likely to mitigate the immediate risks associated with prolonged power outages. [52][303][328] Consequently, individuals may find themselves better prepared to handle the ensuing logistical challenges. Similarly, obtaining a long-term food supply becomes a primary challenge once grocery stores are exhausted, establishing raw grains like corn, wheat, and soybeans as among the most storable bulk food sources for sustaining populations through extended crises. [232] One ton of grain can supply roughly one person's needs for three years, suggesting that, in principle, U.S. grain output could feed its population if protected from damage. [330] Individuals and families are advised to purchase and store grain supplies prior

to an impact event, utilizing farm cooperatives and Feed & Grain stores for bulk shipments. [328] Whole corn kernels are recommended over cracked corn to extend shelf life and facilitate cleaning before processing, ensuring that households maintain a reliable caloric intake when traditional supply chains fail. [330]

The Solar Grand Minima Preparedness Plan establishes that individual survival during a Little Ice Age depends on adapting to severe cold, long-term food storage, and alternative heat sources. Historical precedents from Fairbanks, International Falls, and Antarctica demonstrate that adaptation requires changes in clothing, travel, and home design to withstand significant global cooling and famine. [303] At the individual level, preparations must include water storage, treatment, sanitation, and security measures to survive months or years without grid support. [52]

The Plan de Preparación para el Gran Mínimo Solar emphasizes that survival during a small ice age depends on adaptation, drawing lessons from communities in Fairbanks, International Falls, and Antarctica. [303] While government strategies address agriculture and energy, individual resilience requires long-term food storage to counter agricultural constraints and alternative heat sources for massive power outages caused by ice storms. [52] The emphasis on adaptation underscores that personal readiness is not merely optional but essential for navigating the severe climatic difficulties associated with a grand solar minimum. [303]

Grocery shelves empty fast when a large-scale disaster strikes. [53] Households must therefore secure a durable food supply before that happens. Raw grains offer the most viable long-term source for sustaining individuals. Corn is an abundant choice in the United States, and its high caloric density makes it a natural fit for storage. [328] This approach eliminates the need for constant food rotation. Families can maintain a stable reserve of basic staples like rice, beans, and wheat. They keep these items in metalized bags within Superpails. [53]

The Dalton and Maunder eras offer a stark warning. [321] They suggest what happens when the Sun goes quiet. Those periods brought severe cold and agricultural constraints that lasted for years. Surviving a prolonged solar minimum today may mean adapting to those same harsh conditions. We must therefore rethink how we keep food safe. Traditional methods rely on continuous refrigeration or complex supply chains that can break down. We need preservation techniques that withstand long-term storage without those supports. [53] This shift supports a broader point about preparedness. Every action we take, from building-envelope retrofits to indoor-agriculture scaling, may build resilience. These measures help us handle extreme weather

of any kind. It does not matter what the ultimate climate driver is. The goal is to close the resilience gap. Government action often cannot fill that gap in time. Adopting irradiation and other preservation technologies may help bridge the divide. These tools ensure communities are equipped for the challenge. They prepare us for the sustained sub-zero conditions predicted by solar minimum forecasts.

9.6 The precautionary closing argument

The precautionary principle, which we met at the start, asks us to prepare for severe disruption even when the odds remain unclear. [29] These recommendations are not speculative hedging. They are essential upgrades to our collective immune system. Every step that improves resilience acts as a buffer against the unknown. This includes installing current-blocking capacitors on the grid. It also means storing water and food at the household level.

Remember where this book began: on the ice of the Thames, in the winters when the river froze solid for two months and Londoners walked upon it; when John Evelyn swore no man alive had known England so cold; when an army marched across a frozen sea. That world was not a fable, and it was not long ago. It was simply the last time the Sun went quiet — and the people it caught hardest were the ones who had forgotten that cold was possible. The quiet Sun is returning on its own schedule, indifferent to our committees and our forecasts. The goal is not to fear the cold, but to respect it, and to build a society that can withstand it. [53] The time for debate is over; the time for preparation is now. [49]

Bibliography

[1] J. Vinós. *Climate of the Past, Present and Future*. Vinós, J. (2022). Climate of the Past, Present and Future. 2022.

[2] Fredrik Charpentier Ljungqvist. "A new reconstruction of temperature variability in the extra-tropical northern hemisphere during the last two millennia". In: *Geografiska Annaler: Series A, Physical Geography* (2010). DOI: 10.1111/j.1468-0459.2010.00399.x.

[3] H.F. et al. Diaz. *Spatial and Temporal Characteristics of Climate in Medieval Times Revisited*. Diaz, H.F., et al. (2011). Spatial and Temporal Characteristics of Climate in Medieval Times Revisited. https://doi.org/10.1175/bams-d-10-05003.1. 2011. DOI: 10.1175/bams-d-10-05003.1.

[4] H. Mackay et al. "The 852/3 CE Mount Churchill eruption: examining the potential climatic and societal impacts and the timing of the Medieval Climate Anomaly in the North Atlantic Region". In: *Climate of the Past* (2022). DOI: 10.5194/cp-2021-170.

[5] Ken Hyland. "Hedging in Scientific Research Articles". In: *Pragmatics & Beyond New Series* (1998). DOI: 10.1075/pbns.54.

[6] Robert Tardif et al. "Last Millennium Reanalysis with an expanded proxy database and seasonal proxy modeling". In: *Climate of the Past* 15.4 (2019), pp. 1251–1273. DOI: 10.5194/cp-15-1251-2019.

[7] K.P. Heiss. *Global Warming – Global Winter - What sayeth the Data: Open Questions and New Theories*. Heiss, K.P. (2007). Global Warming – Global Winter - What sayeth the Data: Open Questions and New Theories. 2007.

[8] DON J. EASTERBROOK. "Evidence-Based Climate Science". In: (2011). DOI: 10.1016/c2010-0-67154-9.

[9] Berry. "Edwin X Berry". In: (2023). DOI: 10.53234/scc2023xx/xx.

[10] E.G. Beck. *Evidence of Variability of Atmospheric CO2 Concentration During the 20th Century*. Beck, E.G. (2008). Evidence of Variability of Atmospheric CO2 Concentration During the 20th Century. 2008.

[11] V.I.Z. Valentina. *Links of Terrestrial Volcanic Eruptions to Solar Activity and Solar Magnetic Field*. Valentina, V.I.Z. (2023). Links of Terrestrial Volcanic Eruptions to Solar Activity and Solar Magnetic Field. 2023.

[12] Bharati Kakad et al. "Diminishing activity of recent solar cycles (22–24) and their impact on geospace". In: *Journal of Space Weather and Space Climate* 9 (2019), A1. DOI: 10.1051/swsc/2018048.

[13] R. H. Cameron, J. Jiang, and M. Schüssler. "Solar Cycle 25: Another Moderate Cycle?" In: *The Astrophysical Journal Letters* 823.2 (2016), p. L22. DOI: 10.3847/2041-8205/823/2/122.

[14] Valentina Zharkova. "Modern Grand Solar Minimum Will Lead to Terrestrial Cooling". In: *Understanding and Tackling Obesity:* (2020), pp. 45–68. DOI: 10.1080/23328940.2020.1796243.

[15] V. V. Zharkova et al. “Periodicities of solar activity and solar radiation derived from observations and their links with the terrestrial environment”. In: *arXiv (Cornell University)* (2023). DOI: 10.48550/arxiv.2301.07480.

[16] H.I. Abdussamatov. “The New Little Ice Age Has Started”. In: *Evidence-Based Climate Science* (2016), pp. 307–328. DOI: 10.1016/b978-0-12-804588-6.00017-3.

[17] Habibullo I. Abdussamatov. “The Additional Criterion for the Determination of the Time of Minimum of a Solar Cycle”. In: *Journal of Electromagnetic Analysis and Applications* 02.03 (2010), pp. 128–132. DOI: 10.4236/jemaa.2010.23019.

[18] C. de Jager. “Solar Forcing of Climate”. In: *Space Sciences Series of ISSI* (2012), pp. 113–119. DOI: 10.1007/978-94-007-4327-4_9.

[19] H. Yndestad. *The Kola Temperature variability*. Yndestad, H. (2020). The Kola Temperature variability. 2020.

[20] N.A. Krivova, L.E.A. Vieira, and S.K. Solanki. *Reconstruction of solar spectral irradiance since the Maunder minimum*. Krivova, N.A., Vieira, L.E.A., & Solanki, S.K. (2010). Reconstruction of solar spectral irradiance since the Maunder minimum. https://-doi.org/10.1029/2010ja015431. 2010. DOI: 10.1029/2010ja015431.

[21] Geoff J. Sharp. “Are Uranus & Neptune Responsible for Solar Grand Minima and Solar Cycle Modulation?” In: *International Journal of Astronomy and Astrophysics* 03.03 (2013), pp. 260–273. DOI: 10.4236/ijaa.2013.33031.

[22] H. Douglas Lightfoot and Gerald Ratzer. “The Sun Versus CO2 as the Cause of Climate Change Projected to 2050”. In: *Journal of Basic & Applied Sciences* 18 (2022), pp. 16–25. DOI: 10.29169/1927-5129.2022.18.03.

[23] V.M. Velasco Herrera, W. Soon, and D.R. Legates. “Does Machine Learning reconstruct missing sunspots and forecast a new solar minimum?” In: *Advances in Space Research* 68.3 (2021), pp. 1485–1501. DOI: 10.1016/j.asr.2021.03.023.

[24] Alexander Ruzmaikin and Joan Feynman. “The Earth’s climate at minima of Centennial Gleissberg Cycles”. In: *Advances in Space Research* 56.8 (2015), pp. 1590–1599. DOI: 10.1016/j.asr.2015.07.010.

[25] Helge Goessling, Thomas Rackow, and Thomas Jung. “Recent global temperature surge intensified by record-low planetary albedo”. In: (2025). DOI: 10.5194/egusphere-egu25-15920.

[26] Sam White et al. “The 1600CE Huaynaputina eruption as a possible trigger for persistent cooling in the North Atlantic region”. In: *Climate of the Past* 18.4 (2022), pp. 739–757. DOI: 10.5194/cp-18-739-2022.

[27] Eduardo Moreno-Chamarro et al. “An abrupt weakening of the subpolar gyre as trigger of Little Ice Age-type episodes”. In: *Climate Dynamics* 48.3-4 (2016), pp. 727–744. DOI: 10.1007/s00382-016-3106-7.

[28] Zhangqi Dai et al. “Atlantic Multidecadal Variability Response to External Forcing during the Past Two Millennia”. In: *Journal of Climate* 35.24 (2022), pp. 8103–8115. DOI: 10.1175/jcli-d-21-0986.1.

[29] F.U. et al. Jehn. *Focus of the IPCC Assessment Reports Has Shifted to Lower Temperatures*. Jehn, F.U., et al. (2022). Focus of the IPCC Assessment Reports Has Shifted to Lower Temperatures. https://doi.org/10.1029/2022ef002876. 2022. DOI: 10.1029/2022ef002876.

[30] Ilya G. Usoskin et al. “The Maunder minimum (1645–1715) was indeed a grand minimum: A reassessment of multiple datasets”. In: *Astronomy & Astrophysics* 581 (2015), A95. DOI: 10.1051/0004-6361/201526652.

[31] J. Lean, J. Beer, and R. Bradley. *Reconstruction of solar irradiance since 1610 Implications for climate change*. Lean, J., Beer, J., & Bradley, R. (2007). Reconstruction of solar irradiance since 1610 Implications for climate change. 2007.

[32] Minze Stuiver, Pieter M. Grootes, and Thomas F. Braziunas. “The GISP2 18O Climate Record of the Past 16,500 Years and the Role of the Sun, Ocean, and Volcanoes”. In: *Quaternary Research* 44.3 (1995), pp. 341–354. DOI: 10.1006/qres.1995.1079.

[33] U. Heikkilä, J. Beer, and J. Feichter. “Modeling cosmogenic radionuclides 10 Be and 7 Be during the Maunder Minimum using the ECHAM5-HAM General Circulation Model”. In: *Atmospheric Chemistry and Physics* 8.10 (2008), pp. 2797–2809. DOI: 10.5194/acp-8-2797-2008.

[34] C.V. Field, G.A. Schmidt, and D.T. Shindell. *Interpreting 10Be changes during the Maunder Minimum*. Field, C.V., Schmidt, G.A., & Shindell, D.T. (2009). Interpreting 10Be changes during the Maunder Minimum. https://doi.org/10.1029/2008jd010578. 2009. DOI: 10.1029/2008jd010578.

[35] Nadezhda Zolotova and Mikhail Vokhmyanin. “Long-Lived Sunspots in Historical Records: A Case Study Analysis from 1660 to 1676”. In: *Solar Physics* 300.2 (2025). DOI: 10.1007/s11207-025-02432-0.

[36] Z. V.V and J. ShepherdS. *Erratum - baseline magnetic eld oscillations: possible SIM effects on solar irradiance and temperature at Earth*. V.V, Z., & ShepherdS., J. (2020). Erratum - baseline magnetic eld oscillations: possible SIM effects on solar irradiance and temperature at Earth. 2020.

[37] K. Scherer and H. Fichtner. “Constraints on the heliospheric magnetic field variation during the Maunder Minimum from cosmic ray modulation modelling”. In: *Astronomy & Astrophysics* 413.2 (2003), pp. L11–L14. DOI: 10.1051/0004-6361:20034636.

[38] John A. Eddy. “The Maunder Minimum”. In: *Science* 192.4245 (1976), pp. 1189–1202. DOI: 10.1126/science.192.4245.1189.

[39] G. Parker. *Global Crisis*. Parker, G. (2017). Global Crisis. 2017.

[40] J. Marusek. *A Chronological Listing of Early Weather Events*. Marusek, J. (2014). A Chronological Listing of Early Weather Events. 2014.

[41] Heli Huhtamaa and Samuli Helama. “Distant impact: tropical volcanic eruptions and climate-driven agricultural crises in seventeenth-century Ostrobothnia, Finland”. In: *Journal of Historical Geography* 57 (2017), pp. 40–51. DOI: 10.1016/j.jhg.2017.05.011.

[42] G. Parker’s. *Global Crisis: War, Climate Change and Catastrophe in the Seventeenth Century*. Parker’s, G. (2017). Global Crisis: War, Climate Change and Catastrophe in the Seventeenth Century. 2017.

[43] Dagomar Degroot. “Climate change and society in the 15th to 18th centuries”. In: *WIREs Climate Change* 9.3 (2018). DOI: 10.1002/wcc.518.

[44] Ilya G. Usoskin. “A history of solar activity over millennia”. In: *Living Reviews in Solar Physics* 14.1 (2017). DOI: 10.1007/s41116-017-0006-9.

[45] Kyle Augustson et al. “Grand Minima and Equatorward Propagation in a Cycling Stellar Convective Dynamo”. In: *The Astrophysical Journal* 809.2 (2015), p. 149. DOI: 10.1088/0004-637x/809/2/149.

[46] D. et al. Rind. *The Relative Importance of Solar and Anthropogenic Forcing of Climate Change between the Maunder Minimum and the Present*. Rind, D., et al. (2004). The Relative Importance of Solar and Anthropogenic Forcing of Climate Change between the Maunder Minimum and the Present. https://doi.org/10.1175/1520-0442(2004)017<0906:triosa>2.0.co;2. 2004. DOI: 10.1175/1520-0442(2004)017<0906:triosa>2.0.co;2.

[47] K. Scherer et al. “Interstellar-Terrestrial Relations: Variable Cosmic Environments, The Dynamic Heliosphere, and Their Imprints on Terrestrial Archives and Climate”. In: *Space Science Reviews* 127.1-4 (2007), pp. 327–465. DOI: 10.1007/s11214-006-9126-6.

[48] H. Douglas Lightfoot and Gerald Ratzer. “Significant Errors Identified in the IPCC Reports”. In: *Journal of Basic & Applied Sciences* 21 (2025), pp. 167–175. DOI: 10.29169/1927-5129.2025.21.18.

[49] J.L. Casey. *Dark Winter: How the Sun Is Causing a 30-Year Cold Spell*. Casey, J.L. (2016). Dark Winter: How the Sun Is Causing a 30-Year Cold Spell. 2016.

[50] G. Shanmugam. “200 Years of Fossil Fuels and Climate Change (1900-2100)”. In: *The London, Edinburgh, and Dublin Philosophical Magazine and Journal of Science* 27.184 (1864), pp. 476–477. DOI: 10.1080/14786446408643701.

[51] Quirin Schiermeier. “IPCC: The climate chairman”. In: *Nature* 501.7467 (2013), pp. 303–305. DOI: 10.1038/501303a.

[52] J. Marusek. *The Sun is Undergoing a State Change*. Marusek, J. (2010). The Sun is Undergoing a State Change. 2010.

[53] Peet James. “Plan, Plan, Plan”. In: *Verification Plans* (2004), pp. 1–10. DOI: 10.1007/978-1-4615-0473-3_1.

[54] *The Approaching New Grand Solar Minimum and Little Ice Age Climate Conditions*. The Approaching New Grand Solar Minimum and Little Ice Age Climate Conditions.

[55] *The Sun’s Role in Climate Change*. The Sun’s Role in Climate Change.

[56] Friedhelm Steinhilber et al. “9,400 Years of Cosmic Radiation and Solar Activity from Ice Cores and Tree Rings”. In: (2012). DOI: 10.1073/pnas.1118965109.

[57] Mélanie Baroni et al. “Volcanic and solar activity, and atmospheric circulation influences on cosmogenic 10Be fallout at Vostok and Concordia (Antarctica) over the last 60years”. In: *Geochimica et Cosmochimica Acta* 75.22 (2011), pp. 7132–7145. DOI: 10.1016/j.gca.2011.09.002.

[58] Anna Sturevik-Storm et al. “10Be climate fingerprints during the Eemian in the NEEM ice core, Greenland”. In: *Scientific Reports* 4.1 (2014). DOI: 10.1038/srep06408.

[59] M. Vonmoos, J. Beer, and R. Muscheler. *Large variations in Holocene solar activity: Constraints from 10Be in the Greenland Ice Core Project ice core*. Vonmoos, M., Beer, J., & Muscheler, R. (2006). Large variations in Holocene solar activity: Constraints from 10Be in the Greenland Ice Core Project ice core. https://doi.org/10.1029/2005ja011500. 2006. DOI: 10.1029/2005ja011500.

[60] S. Duhau and C. de Jager. “The Solar Dynamo and Its Phase Transitions during the Last Millennium”. In: *Solar Physics* 250.1 (2008), pp. 1–15. DOI: 10.1007/s11207-008-9212-x.

[61] Jane K. Willenbring and Friedhelm von Blanckenburg. “Meteoric cosmogenic Beryllium-10 adsorbed to river sediment and soil: Applications for Earth-surface dynamics”. In: *Earth-Science Reviews* 98.1-2 (2010), pp. 105–122. DOI: 10.1016/j.earscirev.2009.10.008.

[62] Frédéric Clette et al. “Revisiting the Sunspot Number”. In: *Space Science Reviews* 186.1-4 (2014), pp. 35–103. DOI: 10.1007/s11214-014-0074-2.

[63] J. B. Pedro et al. “High-resolution records of the beryllium-10 solar activity proxy in ice from Law Dome, East Antarctica: measurement, reproducibility and principal trends”. In: *Climate of the Past* 7.3 (2011), pp. 707–721. DOI: 10.5194/cp-7-707-2011.

[64] H. Svensmark. *The Sun’s Role in Climate Change*. Svensmark, H. (2019). The Sun’s Role in Climate Change. 2019.

[65] S. K. Solanki et al. “Unusual activity of the Sun during recent decades compared to the previous 11,000 years”. In: *Nature* 431.7012 (2004), pp. 1084–1087. DOI: 10.1038/nature02995.

[66] Rhodes W. Fairbridge and James H. Shirley. “Prolonged minima and the 179-yr cycle of the solar inertial motion”. In: *Solar Physics* 110.1 (1987), pp. 191–210. DOI: 10.1007/bf00148211.

[67] Gilles Delaygue and Edouard Bard. “An Antarctic view of Beryllium-10 and solar activity for the past millennium”. In: *Climate Dynamics* (2011). DOI: 10.1007/s00382-010-0795-1.

[68] Michael Dee et al. “Radiocarbon evidence over the apparent grand solar minimum around 400 BCE”. In: *Radiocarbon* 67.2 (2025), pp. 265–274. DOI: 10.1017/rdc.2024.132.

[69] Charlotte L Pearson et al. “Dendrochronology and Radiocarbon Dating”. In: *Radiocarbon* 64.3 (2021), pp. 569–588. DOI: 10.1017/rdc.2021.97.

[70] I. Charvátová. “Can Origin of the 2400-Year Cycle of Solar Activity Be Caused by Solar Inertial Motion?” In: (2000). DOI: 10.1007/s00585-000-0399-x.

[71] T. J. Heaton et al. “Extreme solar storms and the quest for exact dating with radiocarbon”. In: *Nature* 633.8029 (2024), pp. 306–317. DOI: 10.1038/s41586-024-07679-4.

[72] *Features of great minima in solar activity during the last 1000 years*. Features of great minima in solar activity during the last 1000 years.

[73] Ryuho Kataoka and Shin’ya Nakano. “Auroral zone over the last 3000 years”. In: *Journal of Space Weather and Space Climate* 11 (2021), p. 46. DOI: 10.1051/swsc/2021030.

[74] Sam M. Silverman and Hisashi Hayakawa. “The Dalton Minimum and John Dalton’s Auroral Observations”. In: *Journal of Space Weather and Space Climate* 11 (2021), p. 17. DOI: 10.1051/swsc/2020082.

[75] M.R. et al. Rampino. *Volcanic Winters*. Rampino, M.R., et al. (2002). Volcanic Winters. 2002.

[76] B. Langmann. *On the Role of Climate Forcing by Volcanic Sulphate and Volcanic Ash*. Langmann, B. (2015). On the Role of Climate Forcing by Volcanic Sulphate and Volcanic Ash. 2015.

[77] Joan Feynman. “Has solar variability caused climate change that affected human culture?” In: *Advances in Space Research* 40.7 (2007), pp. 1173–1180. DOI: 10.1016/j.asr.2007.01.077.

[78] Christoph C. Raible et al. “Tambora 1815 as a test case for high impact volcanic eruptions: Earth system effects”. In: *WIREs Climate Change* 7.4 (2016), pp. 569–589. DOI: 10.1002/wcc.407.

[79] K. R. Briffa et al. “Influence of volcanic eruptions on Northern Hemisphere summer temperature over the past 600 years”. In: (1998). DOI: 10.1038/30943.

[80] Richard B. Stothers. “The great Tambora eruption in 1815 and its aftermath”. In: *Deep Sea Research Part B. Oceanographic Literature Review* 31.12 (1984), p. 910. DOI: 10.1016/0198-0254(84)93639-2.

[81] Rosanne D’Arrigo, Rob Wilson, and Alexander Tudhope. “The impact of volcanic forcing on tropical temperatures during the past four centuries”. In: *Nature Geoscience* 2.1 (2008), pp. 51–56. DOI: 10.1038/ngeo393.

[82] Clive Oppenheimer. “Eruptions that Shook the World”. In: (2011). DOI: 10.1017/cbo9780511978012.

[83] G.D. Wood. *X Contents*. Wood, G.D. (2019). X Contents. 2019.

[84] M. Mactaggart. “Blast from the past”. In: *The Computer Bulletin* 44.2 (2002), pp. 20–21. DOI: 10.1093/combul/44.2.20.

[85] J. G. Anet et al. “Impact of solar versus volcanic activity variations on tropospheric temperatures and precipitation during the Dalton Minimum”. In: *Climate of the Past* 10.3 (2014), pp. 921–938. DOI: 10.5194/cp-10-921-2014.

[86] Werner K. Schmutz. “Changes in the Total Solar Irradiance and climatic effects”. In: *Journal of Space Weather and Space Climate* 11 (2021), p. 40. DOI: 10.1051/swsc/2021016.

[87] Eric Sigg. “New England”. In: *T. S. Eliot in Context* (2011), pp. 17–24. DOI: 10.1017/cbo9780511973673.003.

[88] J. Marusek. *EPA Comments*. Marusek, J. (2009). EPA Comments. 2009.

[89] James O’Reilly. “Just Over the Horizon”. In: *Network Storage* (2017), pp. 245–251. DOI: 10.1016/b978-0-12-803863-5.00014-5.

[90] Joanna Slawinska and Alan Robock. “Impact of Volcanic Eruptions on Decadal to Centennial Fluctuations of Arctic Sea Ice Extent during the Last Millennium and on Initiation of the Little Ice Age”. In: *Journal of Climate* 31.6 (2018), pp. 2145–2167. DOI: 10.1175/jcli-d-16-0498.1.

[91] H. Douglas Lightfoot and Gerald Ratzer. “The Sun Versus CO2 as the Cause of Climate Change Projected to 2050”. In: *Journal of Basic & Applied Sciences* 18 (2022), pp. 16–25. DOI: 10.29169/1927-5129.2022.18.03.

[92] Johannes Preiser-Kapeller. “The Medieval Climate Anomaly, the Oort Minimum, and Socio-Political Dynamics in the Eastern Mediterranean and the Byzantine Empire, 10th to 12th Century”. In: *A Companion to the Environmental History of Byzantium* (2024), pp. 405–488. DOI: 10.1163/9789004689350_017.

[93] Yochanan Kushnir and Mordechai Stein. “Medieval Climate in the Eastern Mediterranean: Instability and Evidence of Solar Forcing”. In: *Atmosphere* 10.1 (2019), p. 29. DOI: 10.3390/atmos10010029.

[94] PAGES 2k Consortium. “Continental-scale temperature variability during the past two millennia”. In: *Nature Geoscience* 6.5 (2013), pp. 339–346. DOI: 10.1038/ngeo1797.

[95] Pei Xing et al. “The Extratropical Northern Hemisphere Temperature Reconstruction during the Last Millennium Based on a Novel Method”. In: *PLOS ONE* 11.1 (2016), e0146776. DOI: 10.1371/journal.pone.0146776.

[96] Celia Martin-Puertas et al. “Regional atmospheric circulation shifts induced by a grand solar minimum”. In: *Nature Geoscience* 5.6 (2012), pp. 397–401. DOI: 10.1038/ngeo1460.

[97] Adam Izdebski, Lee Mordechai, and Sam White. “The Social Burden of Resilience: A Historical Perspective”. In: *Human Ecology* 46.3 (2018), pp. 291–303. DOI: 10.1007/s10745-018-0002-2.

[98] G Chiodo et al. “The impact of a future solar minimum on climate change projections in the Northern Hemisphere”. In: *Environmental Research Letters* 11.3 (2016), p. 034015. DOI: 10.1088/1748-9326/11/3/034015.

[99] A.C. et al. Maycock. *Possible impacts of a future grand solar minimum on climate: Stratospheric and global circulation changes*. Maycock, A.C., et al. (2015). Possible impacts of a future grand solar minimum on climate: Stratospheric and global circulation changes. https://doi.org/10.1002/2014jd022022. 2015. DOI: 10.1002/2014jd022022.

[100] Nicola Scafetta and Richard C. Willson. “ACRIM total solar irradiance satellite composite validation versus TSI proxy models”. In: *Astrophysics and Space Science* 350.2 (2014), pp. 421–442. DOI: 10.1007/s10509-013-1775-9.

[101] P. K. Choudhury and M. Abou El-Nasr. “Invited reviews”. In: *Journal of Electromagnetic Waves and Applications* (2021). DOI: 10.1080/09205071.2014.937931.

[102] Nigel D. Marsh and Henrik Svensmark. “Low Cloud Properties Influenced by Cosmic Rays”. In: *Physical Review Letters* 85.23 (2000), pp. 5004–5007. DOI: 10.1103/physrevlett.85.5004.

[103] Henrik Svensmark and Eigil Friis-Christensen. “Variation of cosmic ray flux and global cloud coverage—a missing link in solar-climate relationships”. In: *Journal of Atmospheric and Solar-Terrestrial Physics* 59.11 (1997), pp. 1225–1232. DOI: 10.1016/s1364-6826(97)00001-1.

[104] Stephen C. Porter. “Pattern and Forcing of Northern Hemisphere Glacier Variations During the Last Millennium”. In: *Quaternary Research* 26.1 (1986), pp. 27–48. DOI: 10.1016/0033-5894(86)90082-7.

[105] J.R. et al. McConnell. *Extreme climate after massive eruption of Alaska’s Okmok volcano in 43 BCE and effects on the late Roman Republic and*. McConnell, J.R., et al. (2020). Extreme climate after massive eruption of Alaska’s Okmok volcano in 43 BCE and effects on the late Roman Republic and.... https://doi.org/10.1073/pnas.2002722117/-/dcsupplemental. 2020. DOI: 10.1073/pnas.2002722117/-/dcsupplemental.

[106] Karoly Nemeth, Shane J. Cronin, and James D.L. White. “Kuwae Caldera and Climate Confusion”. In: *The Open Geology Journal* 1.1 (2007), pp. 7–11. DOI: 10.2174/1874262900701010007.

[107] Anne S. Palmer et al. “High-precision dating of volcanic events (A.D. 1301–1995) using ice cores from Law Dome, Antarctica”. In: *Journal of Geophysical Research: Atmospheres* 106.D22 (2001), pp. 28089–28095. DOI: 10.1029/2001jd000330.

[108] C. T. Plummer et al. “An independently dated 2000-yr volcanic record from Law Dome, East Antarctica, including a new perspective on the dating of the 1450s CE eruption of Kuwae, Vanuatu”. In: *Climate of the Past* 8.6 (2012), pp. 1929–1940. DOI: 10.5194/cp-8-1929-2012.

[109] E. Walter Maunder. “A Prolonged Sunspot Minimum”. In: (1894). DOI: 10.1038/scientificamerican09011894-15569bsupp.

[110] Hisashi Hayakawa et al. “Daniel Mögling’s Sunspot Observations in 1626–1629: A Manuscript Reference for the Solar Activity before the Maunder Minimum”. In: *The Astrophysical Journal* 909.2 (2021), p. 194. DOI: 10.3847/1538-4357/abdd34.

[111] Ilya G. Usoskin. “A history of solar activity over millennia”. In: *Living Reviews in Solar Physics* 20.1 (2023). DOI: 10.1007/s41116-023-00036-z.

[112] N. V. Zolotova and D. I. Ponyavin. “How Deep Was the Maunder Minimum?” In: *Solar Physics* 291.9-10 (2016), pp. 2869–2890. DOI: 10.1007/s11207-016-0908-z.

[113] Ilya G. Usoskin. “A History of Solar Activity over Millennia”. In: *Living Reviews in Solar Physics* 10 (2013). DOI: 10.12942/lrsp-2013-1.

[114] J.M. Vaquero and R.M. Trigo. “Redefining the limit dates for the Maunder Minimum”. In: *New Astronomy* 34 (2015), pp. 120–122. DOI: 10.1016/j.newast.2014.06.002.

[115] Leif Svalgaard and Kenneth H. Schatten. “Reconstruction of the Sunspot Group Number: The Backbone Method”. In: *Solar Physics* 291.9-10 (2016), pp. 2653–2684. DOI: 10.1007/s11207-015-0815-8.

[116] Leif Svalgaard. “Several Populations of Sunspot Group Numbers – Resolving a Conundrum”. In: (2021). DOI: 10.5194/egusphere-egu21-282.

[117] Leif Svalgaard. “Solar activity – past, present, future”. In: *Journal of Space Weather and Space Climate* 3 (2013), A24. DOI: 10.1051/swsc/2013046.

[118] Ilya G. Usoskin et al. “The Maunder minimum (1645–1715) was indeed a grand minimum: A reassessment of multiple datasets”. In: *Astronomy & Astrophysics* 581 (2015), A95. DOI: 10.1051/0004-6361/201526652.

[119] Akash Biswas et al. “Long-Term Modulation of Solar Cycles”. In: *Space Science Reviews* 219.3 (2023). DOI: 10.1007/s11214-023-00968-w.

[120] Anna V. Shapiro et al. “Solar-cycle irradiance variations over the last four billion years”. In: *Astronomy & Astrophysics* 636 (2020), A83. DOI: 10.1051/0004-6361/201937128.

[121] Marius Potgieter. “Solar Modulation of Cosmic Rays”. In: *Living Reviews in Solar Physics* 10 (2013). DOI: 10.12942/lrsp-2013-3.

[122] F.B. McDonald, W.R. Webber, and D.V. Reames. *Unusual time histories of galactic and anomalous cosmic rays at 1 AU over the deep solar minimum of cycle 23/24*. McDonald, F.B., Webber, W.R., & Reames, D.V. (2010). Unusual time histories of galactic and anomalous cosmic rays at 1 AU over the deep solar minimum of cycle 23/24. https://-doi.org/10.1029/2010gl044218. 2010. DOI: 10.1029/2010gl044218.

[123] Antonio Vecchio et al. “Solar activity cycles and grand minima occurrence”. In: (2019). DOI: 10.1393/ncc/i2019-19015-0.

[124] R. H. Cameron and M. Schüssler. “Understanding Solar Cycle Variability”. In: *The Astrophysical Journal* 843.2 (2017), p. 111. DOI: 10.3847/1538-4357/aa767a.

[125] Nicola Scafetta. "Multi-scale harmonic model for solar and climate cyclical variation throughout the Holocene based on Jupiter–Saturn tidal frequencies plus the 11-year solar dynamo cycle". In: *Journal of Atmospheric and Solar-Terrestrial Physics* 80 (2012), pp. 296–311. DOI: 10.1016/j.jastp.2012.02.016.

[126] Jamie M. Jasinski and Marco Velli. "The Sun Reversed Its Decades-long Weakening Trend in 2008". In: *The Astrophysical Journal Letters* 990.2 (2025), p. L55. DOI: 10.3847/2041-8213/adf3a6.

[127] F. Stefani et al. "Schwabe, Gleissberg, Suess-de Vries: Towards a consistent model of planetary synchronization of solar cycles". In: *Magnetohydrodynamics* 56.2-3 (2020), pp. 269–280. DOI: 10.22364/mhd.56.2-3.18.

[128] E. Popova, V. Zharkova, and S. Zharkov. "Probing latitudinal variations of the solar magnetic field in cycles 21–23 by Parker's Two-Layer Dynamo Model with meridional circulation". In: *Annales Geophysicae* 31.11 (2013), pp. 2023–2038. DOI: 10.5194/angeo-31-2023-2013.

[129] Scott W. McIntosh et al. "Uniting the Sun's Hale magnetic cycle and "extended solar cycle" paradigms". In: *Frontiers in Astronomy and Space Sciences* 9 (2022). DOI: 10.3389/fspas.2022.923049.

[130] David H. Hathaway. "The Solar Cycle". In: *Living Reviews in Solar Physics* 12.1 (2015). DOI: 10.1007/lrsp-2015-4.

[131] Kristóf Petrovay. "Solar cycle prediction". In: *Living Reviews in Solar Physics* 17.1 (2020). DOI: 10.1007/s41116-020-0022-z.

[132] V N Obridko, A S Shibalova, and D D Sokoloff. "The extended solar cycle and asymmetry of the large-scale magnetic field". In: *Monthly Notices of the Royal Astronomical Society* 523.1 (2023), pp. 982–990. DOI: 10.1093/mnras/stad1515.

[133] Aimee Norton et al. "Solar Cycle Observations". In: *Space Science Reviews* 219.8 (2023). DOI: 10.1007/s11214-023-01008-3.

[134] Raisa Leussu et al. "Properties of sunspot cycles and hemispheric wings since the 19th century". In: *Astronomy & Astrophysics* 592 (2016), A160. DOI: 10.1051/0004-6361/201628335.

[135] Gordon J. D. Petrie. "Solar Magnetism in the Polar Regions". In: *Living Reviews in Solar Physics* 12.1 (2015). DOI: 10.1007/lrsp-2015-5.

[136] C. Demetrescu and V. Dobrica. *Signature of Hale and Gleissberg solar cycles in the geomagnetic activity*. Demetrescu, C., & Dobrica, V. (2008). Signature of Hale and Gleissberg solar cycles in the geomagnetic activity. https://doi.org/10.1029/2007ja012570. 2008. DOI: 10.1029/2007ja012570.

[137] S. V. Berdyugina and I. G. Usoskin. "Active longitudes in sunspot activity: Century scale persistence". In: *Astronomy & Astrophysics* 405.3 (2003), pp. 1121–1128. DOI: 10.1051/0004-6361:20030748.

[138] Leif Svalgaard and Yohsuke Kamide. "Asymmetric Solar Polar Field Reversals". In: *The Astrophysical Journal* 763.1 (2012), p. 23. DOI: 10.1088/0004-637x/763/1/23.

[139] L. Zhang, K. Mursula, and I. Usoskin. "Consistent long-term variation in the hemispheric asymmetry of solar rotation". In: *Astronomy & Astrophysics* 552 (2013), A84. DOI: 10.1051/0004-6361/201220693.

[140] N. V. Zolotova and D. I. Ponyavin. “Was the unusual solar cycle at the end of the XVIII century a result of phase asynchronization?” In: *Astronomy & Astrophysics* 470.3 (2007), pp. L17–L20. DOI: 10.1051/0004-6361:20077681.

[141] A. Vecchio et al. “Connection between solar activity cycles and grand minima generation”. In: *Astronomy & Astrophysics* 599 (2017), A58. DOI: 10.1051/0004-6361/201629758.

[142] Paul Charbonneau. “Multiperiodicity, Chaos, and Intermittency in a Reduced Model of the Solar Cycle”. In: *Solar Physics* 199.2 (2001), pp. 385–404. DOI: 10.1023/a:1010387509792.

[143] *Solar activity over nine millennia: A consistent multi-proxy reconstruction.* Solar activity over nine millennia: A consistent multi-proxy reconstruction.

[144] Leif Svalgaard, Marco Cagnotti, and Sergio Cortesi. “The Effect of Sunspot Weighting”. In: *Solar Physics* 292.2 (2017). DOI: 10.1007/s11207-016-1024-9.

[145] Leif Svalgaard. “A Recount of Sunspot Groups on Staudach’s Drawings”. In: *Solar Physics* 292.1 (2016). DOI: 10.1007/s11207-016-1023-x.

[146] F. Clette et al. “Recalibration of the Sunspot-Number: Status Report”. In: *Solar Physics* 298.3 (2023). DOI: 10.1007/s11207-023-02136-3.

[147] C.-J. Wu et al. “Solar total and spectral irradiance reconstruction over the last 9000 years”. In: *Astronomy & Astrophysics* 620 (2018), A120. DOI: 10.1051/0004-6361/201832956.

[148] Willie Soon, Ronan Connolly, and Michael Connolly. “Re-evaluating the role of solar variability on Northern Hemisphere temperature trends since the 19th century”. In: *Earth-Science Reviews* 150 (2015), pp. 409–452. DOI: 10.1016/j.earscirev.2015.08.010.

[149] Greg Kopp. “Solar irradiance measurements”. In: *Living Reviews in Solar Physics* 22.1 (2025). DOI: 10.1007/s41116-025-00040-5.

[150] J. J. Butler et al. “Sources of Differences in On-Orbital Total Solar Irradiance Measurements and Description of a Proposed Laboratory Intercomparison”. In: *Journal of Research of the National Institute of Standards and Technology* 113.4 (2008), p. 187. DOI: 10.6028/jres.113.014.

[151] W. Finsterle et al. “The total solar irradiance during the recent solar minimum period measured by SOHO/VIRGO”. In: *Scientific Reports* 11.1 (2021). DOI: 10.1038/s41598-021-87108-y.

[152] Theodosios Chatzistergos, Natalie A. Krivova, and Kok Leng Yeo. “Long-term changes in solar activity and irradiance”. In: *Journal of Atmospheric and Solar-Terrestrial Physics* 252 (2023), p. 106150. DOI: 10.1016/j.jastp.2023.106150.

[153] Habibullo I. Abdussamatov. “Bicentennial Decrease of the Total Solar Irradiance Leads to Unbalanced Thermal Budget of the Earth and the Little Ice Age”. In: *Applied Physics Research* 4.1 (2012). DOI: 10.5539/apr.v4n1p178.

[154] LiBo Liu et al. “Solar activity effects of the ionosphere: A brief review”. In: *Chinese Science Bulletin* 56.12 (2011), pp. 1202–1211. DOI: 10.1007/s11434-010-4226-9.

[155] R. Jurdana-epi et al. “A relationship between the solar rotation and activity in the period 1998–2006 analysed by tracing small bright coronal structures in SOHO-EIT images”. In: *Astronomy & Astrophysics* 534 (2011), A17. DOI: 10.1051/0004-6361/201014357.

[156] I. G. Usoskin, S. K. Solanki, and G. A. Kovaltsov. “Grand minima and maxima of solar activity: new observational constraints”. In: *Astronomy & Astrophysics* 471.1 (2007), pp. 301–309. DOI: 10.1051/0004-6361:20077704.

[157] I. Cnossen and J. Matzka. *Changes in solar quiet magnetic variations since the Maunder Minimum: A comparison of historical observations and mod*. Cnossen, I., & Matzka, J. (2016). Changes in solar quiet magnetic variations since the Maunder Minimum: A comparison of historical observations and mod.... https://doi.org/10.1002/2016ja023211. 2016. DOI: 10.1002/2016ja023211.

[158] L. Jian, C. Russell, and J. Luhmann. *Comparing Solar Minimum 23/24 with Historical Solar Wind Records at 1 AU*. Jian, L., Russell, C., & Luhmann, J. (2012). Comparing Solar Minimum 23/24 with Historical Solar Wind Records at 1 AU. https://doi.org/10.1007/s11207-011-9737-2. 2012. DOI: 10.1007/s11207-011-9737-2.

[159] Frédéric Clette et al. "Revisiting the Sunspot Number". In: *Space Science Reviews* 186.1-4 (2014), pp. 35–103. DOI: 10.1007/s11214-014-0074-2.

[160] V. V. Zharkova et al. "Heartbeat of the Sun from Principal Component Analysis and prediction of solar activity on a millenium timescale". In: *Scientific Reports* 5.1 (2015). DOI: 10.1038/srep15689.

[161] V. Zharkova et al. "Reply to comment on the paper " on a role of quadruple component of magnetic field in defining solar activity in grand cycles" by Usoskin (2017)". In: *Journal of Atmospheric and Solar-Terrestrial Physics* 176 (2018), pp. 72–82. DOI: 10.1016/j.jastp.2017.09.019.

[162] Simon J. Shepherd, Sergei I. Zharkov, and Valentina V. Zharkova. "Prediction of Solar Activity from Solar Background Magnetic Field Variations in Cycles 21-23". In: *The Astrophysical Journal* 795.1 (2014), p. 46. DOI: 10.1088/0004-637x/795/1/46.

[163] V. V. Zharkova, S. J. Shepherd, and S. I. Zharkov. "Principal component analysis of background and sunspot magnetic field variations during solar cycles 21-23". In: *Monthly Notices of the Royal Astronomical Society* 424.4 (2012), pp. 2943–2953. DOI: 10.1111/j.1365-2966.2012.21436.x.

[164] Philip H. Scherrer et al. "The mean magnetic field of the Sun: Observations at Stanford". In: (1977). DOI: 10.1007/bf00159925.

[165] Ashok Ambastha. "Solar Magnetic Field and Activity Cycles". In: *Physics of the Invisible Sun* (2020), pp. 83–114. DOI: 10.1201/9781003005674-4.

[166] Vasilieva and Zharkova. *Terrestrial volcanic eruptions and their possible links with solar activity*. Vasilieva, & Zharkova (2022). Terrestrial volcanic eruptions and their possible links with solar activity. 2022.

[167] V. V. Zharkova et al. "RETRACTED ARTICLE: Oscillations of the baseline of solar magnetic field and solar irradiance on a millennial timescale". In: *Scientific Reports* 9.1 (2019). DOI: 10.1038/s41598-019-45584-3.

[168] M. Lockwood. *Twenty-three cycles of changing open solar magnetic flux*. Lockwood, M. (2003). Twenty-three cycles of changing open solar magnetic flux. https://doi.org/10.1029/2002ja009431. 2003. DOI: 10.1029/2002ja009431.

[169] V N Obridko et al. "Solar large-scale magnetic field and cycle patterns in solar dynamo". In: *Monthly Notices of the Royal Astronomical Society* 504.4 (2021), pp. 4990–5000. DOI: 10.1093/mnras/stab1062.

[170] V V Zharkova et al. "Comparison of solar activity proxies: eigenvectors versus averaged sunspot numbers". In: *Monthly Notices of the Royal Astronomical Society* 521.4 (2023), pp. 6247–6265. DOI: 10.1093/mnras/stad1001.

[171] V. V. Zharkova et al. “Reinforcing a Double Dynamo Model with Solar-Terrestrial Activity in the Past Three Millennia”. In: *Proceedings of the International Astronomical Union* 13.S335 (2017), pp. 211–215. DOI: 10.1017/s1743921317010912.

[172] Valentina Zharkova. “Millennial Oscillations of Solar Irradiance and Magnetic Field in 600–2600”. In: *Solar System Planets and Exoplanets* (2021). DOI: 10.5772/intechopen.96450.

[173] E. Popova et al. “On a role of quadruple component of magnetic field in defining solar activity in grand cycles”. In: *Journal of Atmospheric and Solar-Terrestrial Physics* 176 (2018), pp. 61–68. DOI: 10.1016/j.jastp.2017.05.006.

[174] Scott W. McIntosh and Robert J. Leamon. “Deciphering solar magnetic activity: on grand minima in solar activity”. In: *Frontiers in Astronomy and Space Sciences* 2 (2015). DOI: 10.3389/fspas.2015.00002.

[175] *Solar evolution and extrema: current state of understanding of long-term solar variability and its planetary impacts.* Solar evolution and extrema: current state of understanding of long-term solar variability and its planetary impacts.

[176] Raimund Muscheler et al. “Solar activity during the last 1000 yr inferred from radionuclide records”. In: *Quaternary Science Reviews* 26.1-2 (2007), pp. 82–97. DOI: 10.1016/j.quascirev.2006.07.012.

[177] Jürg Beer, Steven Tobias, and Nigel Weiss. “An Active Sun Throughout the Maunder Minimum”. In: *Solar Physics* 181.1 (1998), pp. 237–249. DOI: 10.1023/a:1005026001784.

[178] M.J. Owens, I. Usoskin, and M. Lockwood. *Heliospheric modulation of galactic cosmic rays during grand solar minima: Past and future variations.* Owens, M.J., Usoskin, I., & Lockwood, M. (2012). Heliospheric modulation of galactic cosmic rays during grand solar minima: Past and future variations. https://doi.org/10.1029/2012gl053151. 2012. DOI: 10.1029/2012gl053151.

[179] A. Brandenburg and E.A. Spiegel. “Modeling a Maunder minimum”. In: *Astronomische Nachrichten* 329.4 (2008), pp. 351–358. DOI: 10.1002/asna.200810973.

[180] P.V. Zharkova. *Solar Activity, Solar Irradiance and Earth’s Temperature.* Zharkova, P.V. (2020). Solar Activity, Solar Irradiance and Earth’s Temperature. 2020.

[181] I. VASILIEVA and V.V. ZHARKOVA. *Terrestrial Volcanic Eruptions and Their Possible Links with Solar Activity.* VASILIEVA, I., & ZHARKOVA, V.V. (2022). Terrestrial Volcanic Eruptions and Their Possible Links with Solar Activity. 2022.

[182] F. et al. Rahmanifard. *Evidence From Galactic Cosmic Rays That the Sun Has Likely Entered a Secular Minimum in Solar Activity.* Rahmanifard, F., et al. (2022). Evidence From Galactic Cosmic Rays That the Sun Has Likely Entered a Secular Minimum in Solar Activity. https://doi.org/10.1029/2021sw002796. 2022. DOI: 10.1029/2021sw002796.

[183] J.A. et al. Abreu. *For how long will the current grand maximum of solar activity persist?* Abreu, J.A., et al. (2008). For how long will the current grand maximum of solar activity persist?. https://doi.org/10.1029/2008gl035442. 2008. DOI: 10.1029/2008gl035442.

[184] R. Braja et al. “On solar cycle predictions and reconstructions”. In: *Astronomy & Astrophysics* 496.3 (2009), pp. 855–861. DOI: 10.1051/0004-6361:200810862.

[185] J. Jiang, P. Chatterjee, and A. R. Choudhuri. “Solar activity forecast with a dynamo model”. In: *Monthly Notices of the Royal Astronomical Society* 381.4 (2007), pp. 1527–1542. DOI: 10.1111/j.1365-2966.2007.12267.x.

[186] Scott W. McIntosh et al. “Overlapping Magnetic Activity Cycles and the Sunspot Number: Forecasting Sunspot Cycle 25 Amplitude”. In: *Solar Physics* 295.12 (2020). DOI: 10.1007/s11207-020-01723-y.

[187] Nils-Axel Mörner. “The Approaching New Grand Solar Minimum and Little Ice Age Climate Conditions”. In: *Natural Science* 07.11 (2015), pp. 510–518. DOI: 10.4236/ns.2015.711052.

[188] Mike Lockwood. “Solar change and climate: an update in the light of the current exceptional solar minimum”. In: *Proceedings of the Royal Society A: Mathematical, Physical and Engineering Sciences* 466.2114 (2009), pp. 303–329. DOI: 10.1098/rspa.2009.0519.

[189] V. V. Zharkova et al. “Reinforcing a Double Dynamo Model with Solar-Terrestrial Activity in the Past Three Millennia”. In: *Proceedings of the International Astronomical Union* 13.S335 (2017), pp. 211–215. DOI: 10.1017/s1743921317010912.

[190] Gilles Delaygue and Edouard Bard. “An Antarctic view of Beryllium-10 and solar activity for the past millennium”. In: *Climate Dynamics* (2011). DOI: 10.1007/s00382-010-0795-1.

[191] Bidya Binay Karak. “Importance of Meridional Circulation in Flux Transport Dynamo: The Possibility of a Maunder-Like Grand Minimum”. In: *The Astrophysical Journal* 724.2 (2010), pp. 1021–1029. DOI: 10.1088/0004-637x/724/2/1021.

[192] Dibyendu Nandy et al. “Solar evolution and extrema: current state of understanding of long-term solar variability and its planetary impacts”. In: *Progress in Earth and Planetary Science* 8.1 (2021). DOI: 10.1186/s40645-021-00430-x.

[193] Dmitry Sokoloff et al. “Sunspot cycles and Grand Minima”. In: *Proceedings of the International Astronomical Union* 5.S264 (2009), pp. 111–119. DOI: 10.1017/s1743921309992511.

[194] F. Inceoglu, R. Arlt, and M. Rempel. “The Nature of Grand Minima and Maxima from Fully Nonlinear Flux Transport Dynamos”. In: *The Astrophysical Journal* (2018). DOI: 10.3847/1538-4357/aa8d68.

[195] Teimuraz V. Zaqarashvili et al. “Long-Term Variation in the Sun’s Activity Caused by Magnetic Rossby Waves in the Tachocline”. In: *The Astrophysical Journal* 805.2 (2015), p. L14. DOI: 10.1088/2041-8205/805/2/l14.

[196] Rodolfo Gustavo Cionco and Willie Soon. “A phenomenological study of the timing of solar activity minima of the last millennium through a physical modeling of the Sun–Planets Interaction”. In: *New Astronomy* 34 (2015), pp. 164–171. DOI: 10.1016/j.newast.2014.07.001.

[197] T. V. Siversky and V. V. Zharkova. “Stationary and impulsive injection of electron beams in converging magnetic field”. In: *Astronomy & Astrophysics* 504.3 (2009), pp. 1057–1070. DOI: 10.1051/0004-6361/200912341.

[198] V. V. Zharkova et al. “Recent Advances in Understanding Particle Acceleration Processes in Solar Flares”. In: *Space Science Reviews* 159.1-4 (2011), pp. 357–420. DOI: 10.1007/s11214-011-9803-y.

[199] V. Zharkova. *Electron and Proton Kinetics and Dynamics in Flaring Atmospheres*. Zharkova, V. (2012). Electron and Proton Kinetics and Dynamics in Flaring Atmospheres. 2012.

[200] S. A. Matthews, S. Zharkov, and V. V. Zharkova. "Anatomy of a Solar Flare: Measurements of the 2006 December 14 X-Class Flare with Gong,hinode, Andrhessi". In: *The Astrophysical Journal* 739.2 (2011), p. 71. DOI: 10.1088/0004-637x/739/2/71.

[201] Alexander Perminov and Eduard Kuznetsov. "The orbital evolution of the Sun–Jupiter–Saturn–Uranus–Ne system on long time scales". In: *Astrophysics and Space Science* 365.8 (2020). DOI: 10.1007/s10509-020-03855-w.

[202] A.S. Perminov and E.D. Kuznetsov. *Orbital Evolution of the Sun–Jupiter–Saturn–Uranus–Neptune Four-Planet System on Long-Time Scales*. Perminov, A.S., & Kuznetsov, E.D. (2018). Orbital Evolution of the Sun–Jupiter–Saturn–Uranus–Neptune Four-Planet System on Long-Time Scales. https://doi.org/10.1134/s0038094618010070. 2018. DOI: 10.1134/s0038094618010070.

[203] A. S. Perminov and E. D. Kuznetsov. "The Implementation of Hori–Deprit Method to the Construction Averaged Planetary Motion Theory by Means of Computer Algebra System Piranha". In: *Mathematics in Computer Science* 14.2 (2019), pp. 305–316. DOI: 10.1007/s11786-019-00441-4.

[204] J. H. Jeans. "A Theory of Stellar Evolution". In: *Monthly Notices of the Royal Astronomical Society* 85.9 (1925), pp. 914–933. DOI: 10.1093/mnras/85.9.914.

[205] Gustavo. "Cionco-Compagnucci-R-man-fig.captions-R". In: (2012). DOI: 10.1016/j.asr.2012.07.013.

[206] Valeriy Vasilyev et al. "Sun-like stars produce superflares roughly once per century". In: *Science* 386.6727 (2024), pp. 1301–1305. DOI: 10.1126/science.adl5441.

[207] Hugh S. Hudson. "Carrington Events". In: *Annual Review of Astronomy and Astrophysics* 59.1 (2021), pp. 445–477. DOI: 10.1146/annurev-astro-112420-023324.

[208] Harald Yndestad and Jan-Erik Solheim. "The influence of solar system oscillation on the variability of the total solar irradiance". In: *New Astronomy* 51 (2017), pp. 135–152. DOI: 10.1016/j.newast.2016.08.020.

[209] V. V. Zharkova et al. "RETRACTED ARTICLE: Oscillations of the baseline of solar magnetic field and solar irradiance on a millennial timescale". In: *Scientific Reports* 9.1 (2019). DOI: 10.1038/s41598-019-45584-3.

[210] Rodolfo G. Cionco and Dmitry A. Pavlov. "Solar barycentric dynamics from a new solar-planetary ephemeris". In: *Astronomy & Astrophysics* 615 (2018), A153. DOI: 10.1051/0004-6361/201732349.

[211] M. Lindholm Nielsen and H. Kjeldsen. "Is Cycle 24 the Beginning of a Dalton-Like Minimum?" In: *Solar Physics* 270.1 (2011), pp. 385–392. DOI: 10.1007/s11207-011-9733-6.

[212] R.G. Cionco and R.H. Compagnucci. *A new imminent grand minimum?* Cionco, R.G., & Compagnucci, R.H. (2011). A new imminent grand minimum?. https://doi.org/10.1017/s174392131200516 2011. DOI: 10.1017/s1743921312005169.

[213] Geoff J. Sharp. "Are Uranus & Neptune Responsible for Solar Grand Minima and Solar Cycle Modulation?" In: *International Journal of Astronomy and Astrophysics* 03.03 (2013), pp. 260–273. DOI: 10.4236/ijaa.2013.33031.

[214] N. Scafetta. *Solar and Planetary Oscillation Control on Climate Change: Hind-Cast, Forecast and a Comparison with the Cmip5 Gcms*. Scafetta, N. (2013). Solar and Planetary Oscillation Control on Climate Change: Hind-Cast, Forecast and a Comparison with the Cmip5 Gcms. https://doi.org/10.1260/0958-305x.24.3-4.455. 2013. DOI: 10.1260/0958-305x.24.3-4.455.

[215] Ilya G. Usoskin, Sami K. Solanki, and Gennady A. Kovaltsov. "Grand minima of solar activity during the last millennia". In: *Proceedings of the International Astronomical Union* 7.S286 (2011), pp. 372–382. DOI: 10.1017/s174392131200511x.

[216] I. G. Usoskin, S. K. Solanki, and G. A. Kovaltsov. "Grand minima and maxima of solar activity: new observational constraints". In: *Astronomy & Astrophysics* 471.1 (2007), pp. 301–309. DOI: 10.1051/0004-6361:20077704.

[217] F. Inceoglu et al. "Grand solar minima and maxima deduced from10Be and14C: magnetic dynamo configuration and polarity reversal". In: *Astronomy & Astrophysics* 577 (2015), A20. DOI: 10.1051/0004-6361/201424212.

[218] Nir J. Shaviv. "The spiral structure of the Milky Way, cosmic rays, and ice age epochs on Earth". In: *New Astronomy* 8.1 (2003), pp. 39–77. DOI: 10.1016/s1384-1076(02)00193-8.

[219] Nils-Axel Mörner. "Solar Minima, Earth's rotation and Little Ice Ages in the past and in the future". In: *Global and Planetary Change* 72.4 (2010), pp. 282–293. DOI: 10.1016/j.gloplacha.2010.01.004.

[220] R.B. Stothers. *Volcanic Eruptions and Solar Activity*. Stothers, R.B. (2007). Volcanic Eruptions and Solar Activity. 2007.

[221] *Cosmic Ray Diffusion from the Galactic Spiral Arms, Iron Meteorites, and a Possible Climatic Connection*. Cosmic Ray Diffusion from the Galactic Spiral Arms, Iron Meteorites, and a Possible Climatic Connection.

[222] Rainer Schwenn. "Space Weather: The Solar Perspective". In: *Living Reviews in Solar Physics* 3 (2006). DOI: 10.12942/lrsp-2006-2.

[223] J.A. Marusek. *Supernovae – The Force Behind Great Ice Ages*. Marusek, J.A. (2005). Supernovae – The Force Behind Great Ice Ages. 2005.

[224] Wolfgang Kundt. "Cosmic rays, clouds and climate". In: *Europhysics News* 46.3 (2015), pp. 31–31. DOI: 10.1051/epn/2015306.

[225] Henrik Svensmark. "Cosmic rays, clouds and climate". In: *Europhysics News* 46.2 (2015), pp. 26–29. DOI: 10.1051/epn/2015204.

[226] Mathew J. Owens et al. "A Geomagnetic Estimate of Heliospheric Modulation Potential Over the Last 175 Years". In: (2024). DOI: 10.21203/rs.3.rs-4165343/v1.

[227] Nigel Marsh and Henrik Svensmark. "Solar Influence on Earth's Climate". In: *Space Science Reviews* 107.1-2 (2003), pp. 317–325. DOI: 10.1023/a:1025573117134.

[228] I. G. Usoskin et al. "Ionization effect of solar particle GLE events in low and middle atmosphere". In: (2010). DOI: 10.5194/acpd-10-30381-2010.

[229] C. Karoff and H. Svensmark. *How did the Sun affect the climate when life evolved on the Earth? A case study on the young solar twin Kappa-1 Ceti*. Karoff, C., & Svensmark, H. (2018). How did the Sun affect the climate when life evolved on the Earth? A case study on the young solar twin Kappa-1 Ceti. 2018.

[230] Ilya G. Usoskin and Gennady A. Kovaltsov. "Link Between Cosmic Rays and Clouds on Different Time Scales". In: (2006). DOI: 10.1142/9789812707185_0026.

[231] Pete Riley et al. "Inferring the Structure of the Solar Corona and Inner Heliosphere During the Maunder Minimum Using Global Thermodynamic Magnetohydrodynamic Simulations". In: *The Astrophysical Journal* 802.2 (2015), p. 105. DOI: 10.1088/0004-637x/802/2/105.

[232] K. et al. Conlon. *Supernova Disaster Preparedness Plan*. Conlon, K., et al. (2014). Supernova Disaster Preparedness Plan. 2014.

[233] I.G. Usoskin and G.A. Kovaltsov. *Production of cosmogenic 7Be isotope in the atmosphere: Full 3-D modeling*. Usoskin, I.G., & Kovaltsov, G.A. (2008). Production of cosmogenic 7Be isotope in the atmosphere: Full 3-D modeling. https://doi.org/10.1029/2007jd009725. 2008. DOI: 10.1029/2007jd009725.

[234] A. Gil. *Heliospheric modulation of galactic cosmic rays: Effective energy of ground-based detectors*. Gil, A. (2017). Heliospheric modulation of galactic cosmic rays: Effective energy of ground-based detectors. 2017.

[235] James Cook. "The rise of the Mass cycle". In: *The Cyclic Mass* (2019), pp. 19–39. DOI: 10.4324/9781351042383-2.

[236] H. Svensmark et al. "Increased ionization supports growth of aerosols into cloud condensation nuclei". In: *Nature Communications* 8.1 (2017). DOI: 10.1038/s41467-017-02082-2.

[237] N. Bork et al. "Structures and reaction rates of the gaseous oxidation of SO 2 by an O 3 - (H 2 O) 0-5 cluster – a density functional theory investigation". In: *Atmospheric Chemistry and Physics* 12.8 (2012), pp. 3639–3652. DOI: 10.5194/acp-12-3639-2012.

[238] Henrik Svensmark et al. "Experimental evidence for the role of ions in particle nucleation under atmospheric conditions". In: *Proceedings of the Royal Society A: Mathematical, Physical and Engineering Sciences* 463.2078 (2006), pp. 385–396. DOI: 10.1098/rspa.2006.1773.

[239] Martin B. Enghoff et al. "Evidence for the Role of Ions in Aerosol Nucleation". In: *The Journal of Physical Chemistry A* 112.41 (2008), pp. 10305–10309. DOI: 10.1021/jp806852d.

[240] M. B. Enghoff and H. Svensmark. "The role of atmospheric ions in aerosol nucleation – a review". In: *Atmospheric Chemistry and Physics* 8.16 (2008), pp. 4911–4923. DOI: 10.5194/acp-8-4911-2008.

[241] *Interstellar-Terrestrial Relations: Variable Cosmic Environments, The Dynamic Heliosphere, and Their Imprints on Terrestrial Archives and Climate*. Interstellar-Terrestrial Relations: Variable Cosmic Environments, The Dynamic Heliosphere, and Their Imprints on Terrestrial Archives and Climate.

[242] H. Svensmark, T. Bondo, and J. Svensmark. *Cosmic ray decreases affect atmospheric aerosols and clouds*. Svensmark, H., Bondo, T., & Svensmark, J. (2009). Cosmic ray decreases affect atmospheric aerosols and clouds. https://doi.org/10.1029/2009gl038429. 2009. DOI: 10.1029/2009gl038429.

[243] Henrik Svensmark et al. "Atmospheric ionization and cloud radiative forcing". In: *Scientific Reports* 11.1 (2021). DOI: 10.1038/s41598-021-99033-1.

[244] Henrik Svensmark. "Evidence of nearby supernovae affecting life on Earth". In: *Monthly Notices of the Royal Astronomical Society* 423.2 (2012), pp. 1234–1253. DOI: 10.1111/j.1365-2966.2012.20953.x.

[245] I. Mironova and I. Usoskin. *Possible effect of extreme solar energetic particle events of September-October 1989 on polar stratospheric aerosols:* Mironova, I., & Usoskin, I. (2013). Possible effect of extreme solar energetic particle events of September-October 1989 on polar stratospheric aerosols:.... https://doi.org/10.5194/acp-13-8543-2013. 2013. DOI: 10.5194/acp-13-8543-2013.

[246] Henrik Svensmark. "Cosmoclimatology: a new theory emerges". In: *Astronomy & Geophysics* 48.1 (2007), pp. 1.18–1.24. DOI: 10.1111/j.1468-4004.2007.48118.x.

[247] Henrik Svensmark, Martin B. Enghoff, and Jens Olaf Pepke Pedersen. "Response of cloud condensation nuclei (>50 nm) to changes in ion-nucleation". In: *Physics Letters A* 377.37 (2013), pp. 2343–2347. DOI: 10.1016/j.physleta.2013.07.004.

[248] Valentina Zharkova. "Modern Grand Solar Minimum Will Lead to Terrestrial Cooling". In: *Understanding and Tackling Obesity:* (2020), pp. 45–68. DOI: 10.1080/23328940.2020.1796243.

[249] K. Scherer et al. "Interstellar-Terrestrial Relations: Variable Cosmic Environments, The Dynamic Heliosphere, and Their Imprints on Terrestrial Archives and Climate". In: *Space Science Reviews* 127.1-4 (2007), pp. 327–465. DOI: 10.1007/s11214-006-9126-6.

[250] Henrik Svensmark. "A persistent influence of supernovae on biodiversity over the Phanerozoic". In: *Ecology and Evolution* 13.3 (2023). DOI: 10.1002/ece3.9898.

[251] N.J. Shaviv. *Cosmic Ray Diffusion from the Galactic Spiral Arms, Iron Meteorites, and a Possible Climatic Connection.* Shaviv, N.J. (2002). Cosmic Ray Diffusion from the Galactic Spiral Arms, Iron Meteorites, and a Possible Climatic Connection. https://-doi.org/10.1103/physrevlett.89.051102. 2002. DOI: 10.1103/physrevlett.89.051102.

[252] *Climate Modes of the Phanerozoic.* Climate Modes of the Phanerozoic.

[253] *On climate response to changes in the cosmic ray flux and radiative budget.* On climate response to changes in the cosmic ray flux and radiative budget.

[254] *Supernovae – The Force Behind Great Ice Ages.* Supernovae – The Force Behind Great Ice Ages.

[255] U. Heikkilä, J. Beer, and J. Feichter. "Modeling cosmogenic radionuclides 10 Be and 7 Be during the Maunder Minimum using the ECHAM5-HAM General Circulation Model". In: (2007). DOI: 10.5194/acpd-7-15341-2007.

[256] Harald Yndestad. "Jovian Planets and Lunar Nodal Cycles in the Earth's Climate Variability". In: *Frontiers in Astronomy and Space Sciences* 9 (2022). DOI: 10.3389/fspas.2022.839794.

[257] D. Moss et al. "Solar Grand Minima and Random Fluctuations in Dynamo Parameters". In: *Solar Physics* 250.2 (2008), pp. 221–234. DOI: 10.1007/s11207-008-9202-z.

[258] Seung Bum Kye. "Uses of the Little Ice Age Theory in the Korean Academia of Korean History". In: *The Korean Society of the History of Historiography* 46 (2022), pp. 11–48. DOI: 10.29186/kjhh.2022.46.11.

[259] Leif. *The modulation potential series is not very useful as a proxy for solar activity since the modulation potential is a.* Leif (2018). The modulation potential series is not very useful as a proxy for solar activity since the modulation potential is a .... 2018.

[260] Valentina V. Zharkova and Irina Vasilieva. “Links of Terrestrial Environment with Solar Activity and Solar and Planetary Orbital Motion”. In: *Atmospheric and Climate Sciences* 15.01 (2025), pp. 72–105. DOI: 10.4236/acs.2025.151004.

[261] J.-C Thouret et al. “Reconstruction of the AD 1600 Huaynaputina eruption based on the correlation of geologic evidence with early Spanish chronicles 1 1Data Repository at http://www.elsevier.com/locate/jvolgeores see ‘Electronic Supplements’.” In: *Journal of Volcanology and Geothermal Research* 115.3-4 (2002), pp. 529–570. DOI: 10.1016/s0377-0273(01)00323-7.

[262] J.-M. Prival et al. “New insights into eruption source parameters of the 1600 CE Huaynaputina Plinian eruption, Peru”. In: *Bulletin of Volcanology* (2020). DOI: 10.1007/s00445-019-1340-7.

[263] W. et al. Báez. *Estratigrafía y evolución del Complejo Volcánico Cerro Blanco, Puna Austral, Argentina*. Báez, W., et al. (2015). Estratigrafía y evolución del Complejo Volcánico Cerro Blanco, Puna Austral, Argentina. 2015.

[264] R. I. Tilling. “Volcanism and associated hazards: the Andean perspective”. In: *Advances in Geosciences* 22 (2009), pp. 125–137. DOI: 10.5194/adgeo-22-125-2009.

[265] Shanaka L. de Silva and Gregory A. Zielinski. “Global influence of the AD 1600 eruption of Huaynaputina, Peru”. In: *Nature* 393.6684 (1998), pp. 455–458. DOI: 10.1038/30948.

[266] J. Fei, D.D. Zhang, and H.F. Lee. *1600 AD Huaynaputina Eruption (Peru), Abrupt Cooling, and Epidemics in China and Korea*. Fei, J., Zhang, D.D., & Lee, H.F. (2016). 1600 AD Huaynaputina Eruption (Peru), Abrupt Cooling, and Epidemics in China and Korea. 2016.

[267] Jie Fei and Jie Zhou. “The possible climatic impact in North China of the AD 1600 Huaynaputina eruption, Peru”. In: *International Journal of Climatology* 29.6 (2008), pp. 927–933. DOI: 10.1002/joc.1776.

[268] Christian Schwarzer et al. “400 Years for Long-Distance Dispersal and Divergence in the Northern Atacama Desert – Insights from the Huaynaputina Pumice Slopes of Moquegua, Peru”. In: *Journal of Arid Environments* 74.11 (2010), pp. 1540–1551. DOI: 10.1016/j.jaridenv.2010.05.034.

[269] Y.A. Vera. *Monitoreo sísmico temporal y caracterización geoquímica de fumarolas y fuentes termales del volcán Huaynaputina*. Vera, Y.A. (2011). Monitoreo sísmico temporal y caracterización geoquímica de fumarolas y fuentes termales del volcán Huaynaputina. 2011.

[270] Rudolf Brázdil et al. “Climatic effects and impacts of the 1815 eruption of Mount Tambora in the Czech Lands”. In: *Climate of the Past* 12.6 (2016), pp. 1361–1374. DOI: 10.5194/cp-12-1361-2016.

[271] Bernice de Jong Boers. “Mount Tambora in 1815: A Volcanic Eruption in Indonesia and Its Aftermath”. In: *Indonesia* 60 (1995), p. 37. DOI: 10.2307/3351140.

[272] J. et al. Cole-Dai. *Cold Decade (AD 1810–1819) Caused by Tambora (1815) and Another (1809) Stratospheric Volcanic Eruption*. Cole-Dai, J., et al. (2009). Cold Decade (AD 1810–1819) Caused by Tambora (1815) and Another (1809) Stratospheric Volcanic Eruption. https://doi.org/10.1029/2009gl040882. 2009. DOI: 10.1029/2009gl040882.

[273] Tom Bodenmann et al. “Perceiving, explaining, and observing climatic changes: An historical case study of the "year without a summer" 1816”. In: *Meteorologische Zeitschrift* 20.6 (2011), pp. 577–587. DOI: 10.1127/0941-2948/2011/0288.

[274] Clive Oppenheimer. “Climatic, environmental and human consequences of the largest known historic eruption: Tambora volcano (Indonesia) 1815”. In: *Progress in Physical Geography: Earth and Environment* 27.2 (2003), pp. 230–259. DOI: 10.1191/0309133303pp379ra.

[275] R. Auchmann et al. “Extreme climate, not extreme weather: the summer of 1816 in Geneva, Switzerland”. In: *Climate of the Past* 8.1 (2012), pp. 325–335. DOI: 10.5194/cp-8-325-2012.

[276] Stephanie Bearce and Eliza Bolli. “1816: The Year Without a Summer”. In: *Twisted True Tales from Science Disaster Discoveries* (2021), pp. 16–20. DOI: 10.4324/9781003239260-5.

[277] C. Newhall, S. Self, and A. Robock. *Anticipating future Volcanic Explosivity Index (VEI) 7 eruptions and their chilling impacts*. Newhall, C., Self, S., & Robock, A. (2018). Anticipating future Volcanic Explosivity Index (VEI) 7 eruptions and their chilling impacts. https://doi.org/10.1130/ges01513.1. 2018. DOI: 10.1130/ges01513.1.

[278] *Climatic Extremes, Recurrent Crises and Witch Hunts: Strategies of European Societies in Coping with Exogenous Shocks in the Late Sixteenth and Early Seventeenth Centuries*. Climatic Extremes, Recurrent Crises and Witch Hunts: Strategies of European Societies in Coping with Exogenous Shocks in the Late Sixteenth and Early Seventeenth Centuries.

[279] Martyn P. Chipperfield et al. “Ongoing large ozone depletion in the polar lower stratospheres: the role of increased water vapour”. In: *Faraday Discussions* 258 (2025), pp. 216–233. DOI: 10.1039/d4fd00163j.

[280] H. Douglas Lightfoot and Gerald Ratzer. “The Impact of the Hunga Tonga Volcanic Eruption on Earth’s Temperature”. In: *Journal of Basic & Applied Sciences* 21 (2025), pp. 136–140. DOI: 10.29169/1927-5129.2025.21.14.

[281] Xin Zhou et al. “Residence time of Hunga stratospheric water vapour perturbation quantified at 9 years”. In: (2026). DOI: 10.5194/egusphere-egu26-22524.

[282] Meng Zuo et al. “Volcanoes and Climate: Sizing up the Impact of the Recent Hunga Tonga-Hunga Ha’apai Volcanic Eruption from a Historical Perspective”. In: *Advances in Atmospheric Sciences* 39.12 (2022), pp. 1986–1993. DOI: 10.1007/s00376-022-2034-1.

[283] Lauren R. Marshall et al. “Volcanic effects on climate: recent advances and future avenues”. In: *Bulletin of Volcanology* 84.5 (2022). DOI: 10.1007/s00445-022-01559-3.

[284] S. Imran. *Radiation Transfer Calculations and Assessment of Global Warming by CO2*. Imran, S. (2017). Radiation Transfer Calculations and Assessment of Global Warming by CO2. 2017.

[285] R.E. Byrom and K.P. Shine. *Methane’s Solar Radiative Forcing*. Byrom, R.E., & Shine, K.P. (2022). Methane’s Solar Radiative Forcing. https://doi.org/10.1029/2022gl098270. 2022. DOI: 10.1029/2022gl098270.

[286] Drew T. Shindell et al. “Solar Forcing of Regional Climate Change During the Maunder Minimum”. In: *Science* 294.5549 (2001), pp. 2149–2152. DOI: 10.1126/science.1064363.

[287] Nir J. Shaviv. “On climate response to changes in the cosmic ray flux and radiative budget”. In: *Journal of Geophysical Research: Space Physics* 110.A8 (2005). DOI: 10.1029/2004ja010866.

[288] Tomasz Goslar. "14C as an Indicator of Solar Variability". In: (2003). DOI: 10.22498/pages.11.2-3.12.

[289] Stuart A. Harris. "Comparison of Recently Proposed Causes of Climate Change". In: *Atmosphere* 14.8 (2023), p. 1244. DOI: 10.3390/atmos14081244.

[290] Joan Feynman. "Has solar variability caused climate change that affected human culture?" In: *Advances in Space Research* 40.7 (2007), pp. 1173–1180. DOI: 10.1016/j.asr.2007.01.077.

[291] *The Extratropical Northern Hemisphere Temperature Reconstruction during the Last Millennium Based on a Novel Method.* The Extratropical Northern Hemisphere Temperature Reconstruction during the Last Millennium Based on a Novel Method.

[292] Richard B. Stothers. "Climatic and Demographic Consequences of the Massive Volcanic Eruption of 1258". In: *Climatic Change* 45.2 (2000), pp. 361–374. DOI: 10.1023/a:1005523330643.

[293] John Ewert, Angela Diefenbach, and David Ramsey. "2018 Update to the U.S. Geological Survey National Volcanic Threat Assessment". In: *Scientific Investigations Report* (2018). DOI: 10.3133/sir20185140.

[294] G. M. MILES, R. G. GRAINGER, and E. J. HIGHWOOD. "Volcanic Aerosols". In: *Encyclopedia of Environmental Change* (2014). DOI: 10.4135/9781446247501.n4085.

[295] Isabel Serra et al. "Probability estimation of a Carrington-like geomagnetic storm". In: (2020). DOI: 10.5194/egusphere-egu2020-8763.

[296] S.C. Chapman, R.B. Horne, and N.W. Watkins. *Using the aa Index Over the Last 14 Solar Cycles to Characterize Extreme Geomagnetic Activity.* Chapman, S.C., Horne, R.B., & Watkins, N.W. (2020). Using the aa Index Over the Last 14 Solar Cycles to Characterize Extreme Geomagnetic Activity. https://doi.org/10.1029/2019gl086524. 2020. DOI: 10.1029/2019gl086524.

[297] Andrew P. Schurer, Simon F. B. Tett, and Gabriele C. Hegerl. "Small influence of solar variability on climate over the past millennium". In: *Nature Geoscience* 7.2 (2013), pp. 104–108. DOI: 10.1038/ngeo2040.

[298] Judith Lean, Juerg Beer, and Raymond Bradley. "Reconstruction of solar irradiance since 1610: Implications for climate change". In: *Geophysical Research Letters* 22.23 (1995), pp. 3195–3198. DOI: 10.1029/95gl03093.

[299] Theodor Landscheidt. "New Little ICE Age Instead of Global Warming?" In: *Energy & Environment* 14.2-3 (2003), pp. 327–350. DOI: 10.1260/095830503765184646.

[300] N. Marsh and H. Svensmark. *Galactic cosmic ray and El Niño–Southern Oscillation trends in International Satellite Cloud Climatology Project D2 l.* Marsh, N., & Svensmark, H. (2003). Galactic cosmic ray and El Niño–Southern Oscillation trends in International Satellite Cloud Climatology Project D2 l.... https://doi.org/10.1029/2001jd001264. 2003. DOI: 10.1029/2001jd001264.

[301] Berry. "The Impact of Human CO2 on Atmospheric CO2". In: (2022). DOI: 10.53234/scc202112/13.

[302] Stuart Licht, Baohui Wang, and Hongjun Wu. "STEP—A Solar Chemical Process to End Anthropogenic Global Warming. II: Experimental Results". In: *The Journal of Physical Chemistry C* 115.23 (2011), pp. 11803–11821. DOI: 10.1021/jp111781a.

[303] J.A. Marusek. *El sol y el cambio climatico*. Marusek, J.A. (2010). El sol y el cambio climatico. 2010.

[304] W.D. Lange. *Why I am a Climate Realist*. Lange, W.D. (2025). Why I am a Climate Realist. 2025.

[305] Edwin X Berry. "Human CO_2 Emissions Have Little Effect on Atmospheric CO_2". In: *International Journal of Atmospheric and Oceanic Sciences* 3.1 (2019), p. 13. DOI: 10.11648/j.ijaos.20190301.13.

[306] Hermann Harde. "How Natural CO2 Dominates the Increase in Atmospheric CO2". In: (2023). DOI: 10.53234/scc202301/21.

[307] *Miracle Tree: A Review on Multi-purposes of Moringa oleifera and Its Implication for Climate Change Mitigation*. Miracle Tree: A Review on Multi-purposes of Moringa oleifera and Its Implication for Climate Change Mitigation.

[308] C. Marusek. *Heat Island Effects*. Marusek, C. (2008). Heat Island Effects. 2008.

[309] Junji Nakamura and Masayoshi Ishida. "Global Warming and CO2 Emissions". In: *Blueprint for a Methanol Society* (2025), pp. 3–26. DOI: 10.1007/978-981-95-3465-4_1.

[310] Nicola Scafetta. "Empirical evidence for a celestial origin of the climate oscillations and its implications". In: *Journal of Atmospheric and Solar-Terrestrial Physics* 72.13 (2010), pp. 951–970. DOI: 10.1016/j.jastp.2010.04.015.

[311] Guobao Xu et al. "Century-scale temperature variability and onset of industrial-era warming in the Eastern Tibetan Plateau". In: *Climate Dynamics* (2019). DOI: 10.1007/s00382-019-04807-z.

[312] Alan Robock. "The "Little Ice Age": Northern Hemisphere Average Observations and Model Calculations". In: *Science* 206.4425 (1979), pp. 1402–1404. DOI: 10.1126/science.206.4425.1402.

[313] Tina. *A Primer on Carbon Dioxide and Climate*. Tina (2016). A Primer on Carbon Dioxide and Climate. 2016.

[314] C. Marusek. *Response to CCSP-Usp-Synthesis Report*. Marusek, C. (2008). Response to CCSP-Usp-Synthesis Report. 2008.

[315] Harald Yndestad. "Lunar-driven control of climate and Barents Sea Eco-System". In: *The Western Arctic Seas Encyclopedia* (2017), pp. 45–45. DOI: 10.1007/978-3-319-25582-8_20006.

[316] Harald Yndestad. "The Arctic Ocean as a Coupled Oscillating System to the Forced 18.6 Year Lunar Gravity Cycle". In: *Nonlinear Dynamics in Geosciences* (2006), pp. 281–290. DOI: 10.1007/978-0-387-34918-3_16.

[317] Harald Yndestad. "The influence of the lunar nodal cycle on Arctic climate". In: *ICES Journal of Marine Science* 63.3 (2006), pp. 401–420. DOI: 10.1016/j.icesjms.2005.07.015.

[318] H. Yndestad. *A General System Theory*. Yndestad, H. (2004). A General System Theory. 2004.

[319] Jonathan Cohler. "Leading Scientists Challenge Foundation of Climate Change Assessments, Revealing Fatal Flaws in Ocean Heat Content (OHC) Measurements". In: (2026). DOI: 10.5281/zenodo.18936064.

[320] Harald Yndestad. "The influence of long tides on ecosystem dynamics in the Barents Sea". In: *Deep Sea Research Part II: Topical Studies in Oceanography* 56.21-22 (2009), pp. 2108–2116. DOI: 10.1016/j.dsr2.2008.11.022.

[321] James Annable. "Analysis". In: *Challenge* 27.2 (1984), pp. 59–61. DOI: 10.1080/05775132.1984.11470925.

[322] Julie Cruikshank. "Glaciers and Climate Change: Perspectives from Oral Tradition". In: *ARCTIC* 54.4 (2001). DOI: 10.14430/arctic795.

[323] Lloyd's. *Solar Storm Risk to the North American Electric Grid*. Lloyd's (2013). Solar Storm Risk to the North American Electric Grid. 2013.

[324] Bruce T. Tsurutani et al. "Extreme changes in the dayside ionosphere during a Carrington-type magnetic storm". In: *Journal of Space Weather and Space Climate* 2 (2012), A05. DOI: 10.1051/swsc/2012004.

[325] Jeffrey J. Love et al. "On the uncertain intensity estimate of the 1859 Carrington storm". In: *Journal of Space Weather and Space Climate* 14 (2024), p. 21. DOI: 10.1051/swsc/2024015.

[326] Sam C. Sarkesian, John Allen Williams, and Stephen J. Cimbala. "U.S. National Security". In: (2002). DOI: 10.1515/9781685859145.

[327] Edward W. Cliver et al. "Extreme solar events". In: *Living Reviews in Solar Physics* 19.1 (2022). DOI: 10.1007/s41116-022-00033-8.

[328] J.A. Marusek. *Impact Disaster Preparedness Plan*. Marusek, J.A. (2007). Impact Disaster Preparedness Plan. 2007.

[329] Meraj Ahmed et al. "Transformer Protection Strategy During Solar Storm: Threat Analysis and Implementing Countermeasures". In: *2023 10th IEEE International Conference on Power Systems (ICPS)* (2023), pp. 1–6. DOI: 10.1109/icps60393.2023.10428848.

[330] K. et al. Conlon. *Solar Storm Disaster Preparedness Plan*. Conlon, K., et al. (2014). Solar Storm Disaster Preparedness Plan. 2014.

[331] J.A. Marusek. *Comet and Asteroid Threat Impact Analysis*. Marusek, J.A. (2006). Comet and Asteroid Threat Impact Analysis. 2006.

[332] Seth D. Baum et al. "Resilience to global food supply catastrophes". In: *Environment Systems and Decisions* 35.2 (2015), pp. 301–313. DOI: 10.1007/s10669-015-9549-2.